Dissertation Thesis

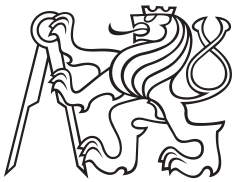

Czech Technical University in Prague

F4

Faculty of Nuclear Sciences and Physical Engineering
Department of Physics

Study of photoproduction at ALICE

Ing. Tomáš Herman

Supervisor: Mgr. Michal Broz, Ph.D.
Field of study: Nuclear Engineering
January 2024

Disertační práce

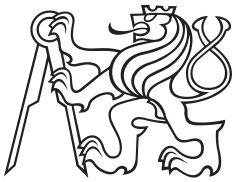

České
vysoké
učení technické
v Praze

F4

Fakulta jaderná a fyzikálně inženýrská
Katedra fyziky

Studium fotoprodukce na experimentu ALICE

Ing. Tomáš Herman

Školitel: Mgr. Michal Broz, Ph.D.
Obor: Jaderné inženýrství
Leden 2024

Acknowledgements

I would like to thank my supervisor, Michal Broz, and our group leader, Jesús Guillermo Contreras Nuño, for their guidance and invaluable advice during my studies. I want to extend my thanks to colleagues from the UPC Physics Analysis Group of ALICE with whom I collaborated and discussed my work. Additionally, I would like to express my gratitude to the entire MFT team, especially Stefano, Sarah, and Charlotte, for their help with my duties to the MFT and all they have taught me during that time. I also want to thank all of my colleagues and friends whom I met at the University, in ALICE, at CERN, or at conferences. It is thanks to all of these people that I managed to go through my Ph.D. studies; they helped to shape me as a scientist but also as a human being. However, the greatest appreciation has to go to my family and especially to my wife, Pavlínka, without whom none of this would be possible.

This work has been partially supported by the Department of Physics of the Faculty of Nuclear Sciences and Physical Engineering of the Czech Technical University in Prague and the grant 18-07880S from the Czech Science Foundation (GACR).

"You step into the road, and if you don't keep your feet, there is no knowing where you might be swept off to."

J.R.R. Tolkien

Prohlášení

Prohlašuji, že jsem tuto práci vypracoval samostatně a použil jsem pouze podklady uvedené v přiloženém seznamu.

Nemám závažný důvod proti použití tohoto díla ve smyslu §60 zákona č.121/2000 Sb., o právu autorském, o právech souvisejících s právem autorským a o změně některých zákonů (autorský zákon).

V Praze, 24. ledna 2024

Bibliographic Entry

Author	Ing. Tomáš Herman Czech Technical University in Prague, Faculty of Nuclear Sciences and Physical Engineering, Department of Physics

Title of Dissertation	Study of photoproduction at ALICE
Degree Programme	Applications of Natural Sciences
Field of Study	Nuclear Engineering

Supervisor	Mgr. Michal Broz, Ph.D. Czech Technical University in Prague, Faculty of Nuclear Sciences and Physical Engineering, Department of Physics

Academic Year	2023/2024
Number of Pages	222
Keywords	ALICE, photoproduction, ultra-peripheral collisions, MFT

Bibliografický záznam

Autor	Ing. Tomáš Herman České vysoké učení technické v Praze, Fakulta jaderná a fyzikálně inženýrská, Katedra fyziky
Název práce	Studium fotoprodukce na experimentu ALICE
Studijní program	Aplikace přírodních věd
Studijní obor	Jaderné inženýrství
Školitel	Mgr. Michal Broz, Ph.D. České vysoké učení technické v Praze, Fakulta jaderná a fyzikálně inženýrská, Katedra fyziky
Akademický rok	2023/2024
Počet stran	222
Klíčová slova	ALICE, fotoprodukce, ultra-periferní srážky, MFT

Abstract

This dissertation explores the coherent photonuclear production of J/ψ in ultra-peripheral Pb–Pb collisions at a center-of-mass energy per nucleon pair of $\sqrt{s_{\mathrm{NN}}} = 5.02$ TeV, utilizing data obtained by the ALICE detector. The cross section is examined as a function of electromagnetic dissociation (EMD) of Pb, revealing insights into the energy dependence of this process within the range $17 < W_{\gamma \mathrm{Pb,n}} < 920$ GeV, corresponding to three orders of magnitude in Bjorken-x $1.1 \times 10^{-5} < x < 3.3 \times 10^{-2}$. Additionally, the nuclear suppression factor is determined, unveiling substantial nuclear shadowing of the gluon distribution in Pb nuclei. These results offer insights into quantum chromodynamics at high energies, enhancing our understanding of the fundamental properties of nuclear matter.

Keywords: ALICE, photoproduction, ultra-peripheral collisions, MFT

Supervisor: Mgr. Michal Broz, Ph.D. Department of Physics, FNSPE CTU in Prague

Abstrakt

Tato disertační práce zkoumá koherentní fotoprodukci J/ψ v ultra-periferních srážkách Pb–Pb při těžišťové energii na nukleonový pár $\sqrt{s_{\mathrm{NN}}} = 5.02$ TeV, využívající data získaná detektorem ALICE. Účinný průřez je zkoumán jako funkce elektromagnetické disociace (EMD) olova, odhalující poznatky o energetické závislosti tohoto procesu v rozsahu $17 < W_{\gamma \mathrm{Pb,n}} < 920$ GeV, což odpovídá třem řádům v Bjorken-x $1.1 \times 10^{-5} < x < 3.3 \times 10^{-2}$. Kromě toho je určen jaderný faktor potlačení, odhalující významné stínění gluonové distribuční funkce v jádrech olova. Tyto výsledky poskytují vhled do kvantové chromodynamiky při vysokých energiích a rozšiřují naši znalost základních vlastností jaderné hmoty.

Klíčová slova: ALICE, fotoprodukce, ultra-periferní srážky, MFT

Překlad názvu: Studium fotoprodukce na experimentu ALICE

Contents

Figures

Tables

Preface

This dissertation thesis aims to provide a summary of my Ph.D. studies. A description of my research, technical, teaching, and extracurricular activities can be found in Chapter Author's Contribution.

An introduction to the physics of ultra-peripheral collisions (UPCs) is discussed in Chap. 1 of this thesis. The physics of UPCs is a very intriguing field as it addresses one of the fundamental questions of physics: the understanding of the elementary structure of matter. The ALICE detector and its subdetectors that were most important for the results presented in this thesis are described in Chap. 2. The measurement of the coherent J/ψ photoproduction cross section in Pb–Pb UPC events at a center-of-mass energy per nucleon pair of $\sqrt{s_{\mathrm{NN}}} = 5.02$ TeV, accompanied by neutron emission, was used to extract the energy dependence of the photonuclear cross section γPb. This analysis and its results are presented in Chap. 4 and represent the highest energy measurement of the γPb cross section available to date, extending the reach of the previous measurement by more than 300 GeV.

The upgrades of the ALICE detector during Long Shutdown 2, with a special focus on the Muon Forward Tracker and the architecture of the new data Quality Control (QC) system of ALICE and its implementation for the MFT, are described in Chap. 3.

Author's contribution

Research activities

The main focus of my research was the analysis of the neutron emission class differential measurement of the coherent J/ψ photoproduction cross section in Pb–Pb UPC events at a center-of-mass energy per nucleon pair of $\sqrt{s_{\mathrm{NN}}} = 5.02$ TeV. Using these data, the energy dependence of the photonuclear cross section of the $\gamma + \mathrm{Pb} \to J/\psi + \mathrm{Pb}$ process was extracted. The nuclear suppression factor was also extracted. These results represent the highest energy measurement of the γPb cross section available to date. Progress in the analysis has been regularly reported in the UPC Physics Analysis Group meetings and the Physics Working Group meetings of the ALICE collaboration. The results have been published in the Journal of High Energy Physics [1].

Technical activities

As part of my service task for the ALICE collaboration I started working on the development of the MFT QC software. I continued in its development in the role of the MFT QC coordinator where I was responsible for coordinating the work of the MFT QC team. The progress of the development was regularly reported on the weekly MFT Software and Physics meetings as well as on the weekly MFT Operation Board meetings.

In addition to the QC development, I also participated in the MFT expert on-call shifts during 2021, 2022, and 2023. The task of the MFT on-call shifter is to assist the central ALICE system shifters when there is a problem with the MFT detector. The on-call shifter has to be present at the ALICE Run Control Center or available on the phone to deal with any unusual situation concerning the MFT detector 24/7.

For the first half of 2022, I was assigned the role of the MFT System Run Coordinator (SRC). This is one of the most important positions of the MFT project. As the SRC, my responsibility was to ensure the smooth operation of the MFT detector, as well as to be the liaison with the Run Coordination of ALICE and the contact person for any problem with the operation of the MFT. I also trained the MFT on-call expert shifters, coordinated their shift assignments, and supervised them during their shifts.

As one of the most experienced MFT shifters, I had the opportunity to fulfill the MFT on-call shifter role during the crucial periods of heavy ions in 2022 and 2023. In 2021, I also took part in the central Detector Control System (DCS) shifts of ALICE. The DCS shifter is responsible for operating the ALICE detector systems during commissioning or data taking. I had the opportunity to fulfill this role during the pilot-beam period, which was the first time since the end of LHC Run 2 with a beam circulating in the LHC.

During the spring of 2021, I also had the opportunity to assist in the construction of the FDD detector, one of the ALICE upgrades during LS2. The construction was carried out in the Czech Republic due to constraints imposed by the COVID-19 pandemic, which prevented the construction from happening at CERN.

Conferences and workshops

I presented results on behalf of the ALICE collaboration in the following conferences and workshops:

- 34nd Rencontres de Blois, 2023, Blois, France
- Workshop on Discovery Physics at the LHC, 2022, Kruger, South Africa
- LHCC poster session, 2022, CERN, Switzerland
- Quark Matter, 2022, Krakow, Poland
- DIS, 2021, Virtual Event, Stony Brook, NY, USA
- Quark Matter, 2019, Wuhan, China
- Lepton Photon Interactions at High Energies, 2019, Toronto, Canada

Publications

Papers

- Energy dependence of coherent photonuclear production of J/ψ mesons in ultra-peripheral Pb–Pb collisions at $\sqrt{s_{\mathrm{NN}}} = 5.02$ TeV [1]
  - This paper is a direct outcome of my Ph.D. work and I participated in all of its stages as a leading author.
- ALICE upgrades during the LHC Long Shutdown 2 [2]
  - This paper provides a comprehensive summary of all ALICE upgrades during Long Shutdown 2. My contribution was to the MFT project, where I participated significantly during my Ph.D.

Proceedings

- J/ψ photoproduction results from ALICE [3]
- Latest ALICE results on J/ψ photoproduction in ultra-peripheral collisions at the LHC [4]
- Latest ALICE results on coherent J/ψ photoproduction in ultra-peripheral Pb–Pb collisions at the LHC [5]

Teaching activities

I was a supervisor specialist for the Bachelor thesis of Bc. Jakub Juracka. In addition, I taught for the total of four semesters in the laboratory classes PRA1 (2 semesters), PRA2 (1 semester), and PRAK (1 semester) as a laboratory assistant.

Extracurricular activities

- 2023: ECFA ECR CZ representative
  - One of three representatives of the Czech Republic in the early career panel of the European Committee for Future Accelerators

- 2019-2021: ALICE Junior Representative
  - One of three elected representatives of the ALICE junior community responsible for representing them in the ALICE Collaboration Board and Management Board
- 2019-2023: ALICE Junior Ambassador for Czech Republic
  - National contact point for juniors in the Czech Republic
- 2018-2023: EPS Young Minds Prague section
  - Member of the executive board

Chapter 1

Introduction to the physics of ultra-peripheral collisions

This chapter provides an introduction to the key concepts of the physics of ultra-peripheral collisions (UPCs). These concepts serve as the motivation for the analysis and results presented in this thesis. Relevant previous measurements as well as theoretical models compared to the results presented in Chap. 4 are also discussed.

Quantum chromodynamics (QCD) successfully describes the internal structure of hadrons across a wide kinematic range. Nevertheless, this task becomes significantly more intricate at high energy extremes. Therefore, it is crucial to validate theoretical predictions with experimental measurements and employ them to advance our comprehension of QCD and the internal makeup of hadronic matter. One of the effective tools for obtaining results that can constrain the existing theoretical predictions of the hadronic structure at high energies is through ultra-peripheral collisions (UPCs).

1.1 Parton distribution functions

The longitudinal parton composition of hadrons is described by universal parton distribution functions (PDFs). In the context of leading-order perturbative quantum chromodynamics (LO pQCD), these functions can be understood as representing the abundance of specific partons within the examined hadron. These PDFs are determined at specific values of Bjorken-x and scale Q^2. Bjorken-x is inversely proportional to the square root of the center-of-mass energy of the collision, denoted as $\sqrt{s}$. Consequently, PDFs measured at high-energy collisions correspond to low values of Bjorken-x. In the infinite-momentum frame, Bjorken-x takes on the interpretation of representing the fraction of the hadron's longitudinal momentum carried by the individual parton. The scale Q^2 is associated with the four-momentum transfer occurring during the collision between the observed hadron and the probing particle used for its examination.

1.2 Saturation

At low Bjorken-x, the parton content of nucleons is primarily composed of gluons, as observed by the HERA collaboration [6] and depicted in Fig. 1.1. The increase in the gluon PDF as Bjorken-x decreases can be interpreted as the manifestation of an increasing number of gluons with progressively lower momentum. This phenomenon can be described as gluons emitting other gluons, effectively splitting into two. Additionally, there exists a competing mechanism wherein two gluons with lower momenta combine to form a gluon with higher momenta.

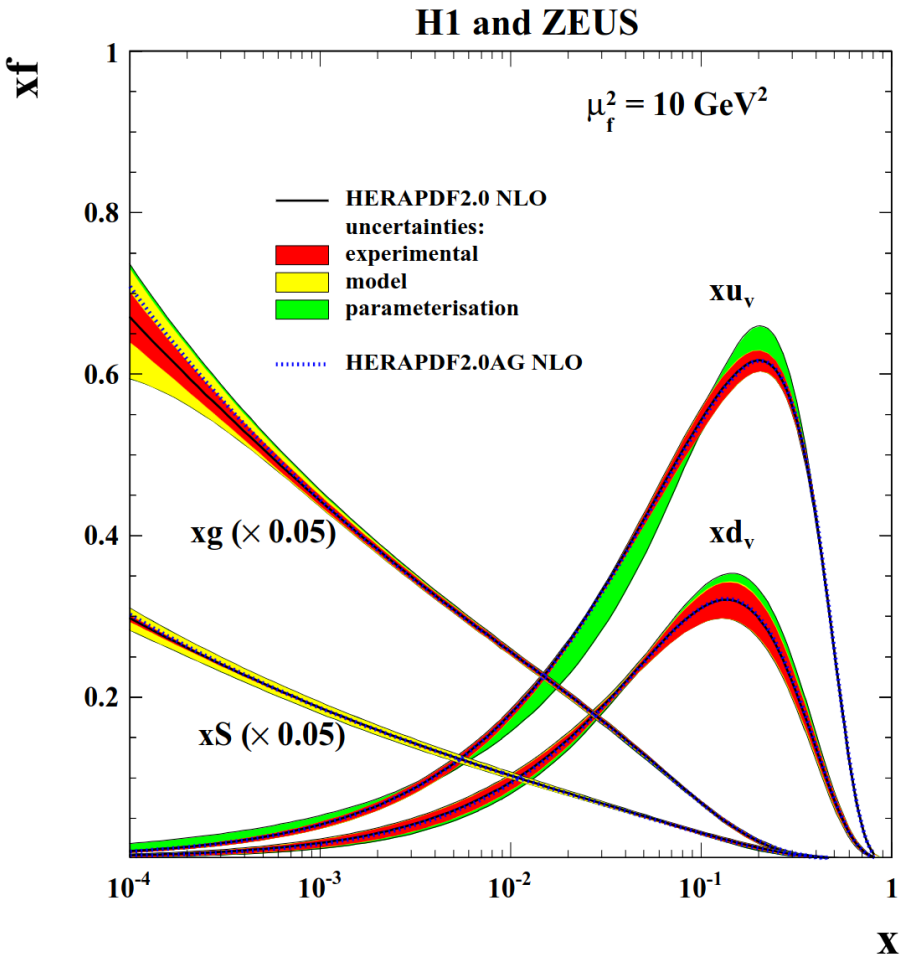

Figure 1.1: Parton distribution functions for valence quarks u (xu_v), valence quarks d (xd_v), sea quarks ($xS = 2x(\overline{U}+\overline{D})$), and gluons ($xg$) of HERAPDF2.0 NLO at scale $\mu_f^2 = 10$ GeV^2 measured by the HERA collaboration at DESY. The experimental, model, and parameterization uncertainties are shown separately. The sea quarks and gluon distributions are scaled down by a factor of 20. The dotted line labeled HERAPDF2.0AG NLO represents the results obtained using an alternative form of the gluon parametrization. Taken from [6].

To maintain unitarity and suppress the growth of the gluon PDF, it is anticipated that at significantly low Bjorken-x, a dynamic equilibrium state referred to as satu-

ration [7] will be achieved. In this state, gluons split and merge at equivalent rates, leading to the saturation of the gluon PDF. For a more comprehensive explanation see Ref. [8]. It is worth noting that while this phenomenon has been predicted, experimental results have thus far only provided preliminary indications of its potential onset.

1.3 Nuclear shadowing

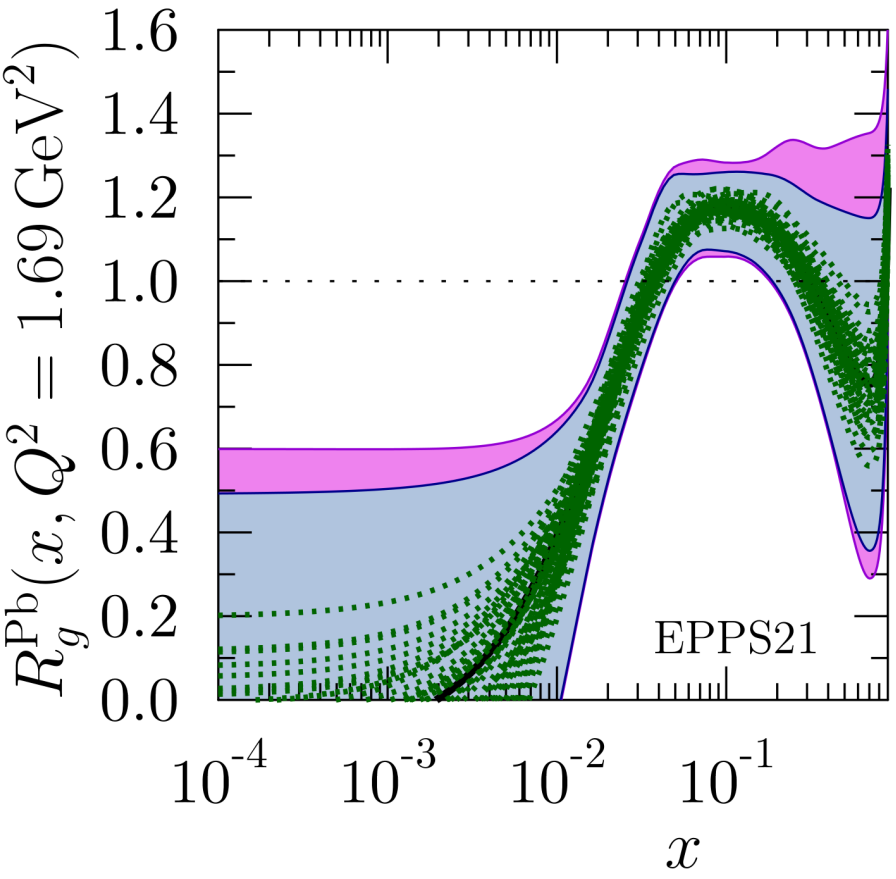

Figure 1.2: EPPS21 gluon nuclear modification factor for Lead R_g^{Pb} at $Q^2 = 1.69\,\mathrm{GeV}^2$ as a function of Bjorken-x. Taken from [9].

When examining the gluon PDF of a free nucleon ($g_N(x, Q^2)$) in comparison to the gluon PDF of nucleons bound in a nucleus ($g_A(x, Q^2)$), it becomes apparent that the ratio $R_g^{\mathrm{Pb}}(x, Q^2)$ does not exhibit a linear scaling relationship with the atomic number A.

$$R_g^{\mathrm{Pb}}(x, Q^2) = \frac{g_A(x, Q^2)}{A\ g_N(x, Q^2)} \tag{1.1}$$

The evolution of the $R_g^{\mathrm{Pb}}(x, Q^2)$ ratio with Bjorken-x can be observed in Fig. 1.2.

At low Bjorken-x, the value of the ratio $R_g^{\mathrm{Pb}}(x, Q^2)$ is less than one, and this phenomenon is commonly referred to as nuclear gluon shadowing [10]. The saturation phenomenon, as introduced in the previous section, is expected to depend on the atomic mass number as $A^{1/3}$ [11], as depicted in Fig. 1.3. It is anticipated that saturation should become more prominent at higher Bjorken-x in nuclei compared to free nucleons. Therefore, it is possible that one of the contributing factors to the observed shadowing effect is saturation.

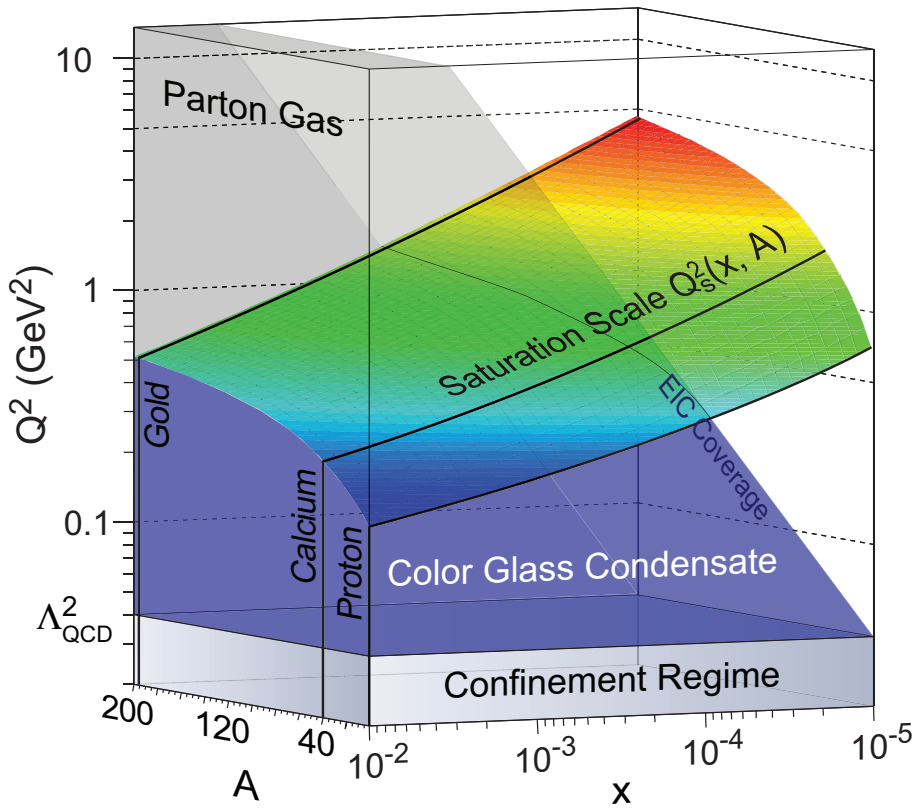

Figure 1.3: Figure showing the theoretical expectations for the saturation scale as a function of Bjorken-x and nuclear mass number (A). Taken from [12].

1.4 Photoproduction

The cross section for coherent vector meson photoproduction exhibits a strong sensitivity to the gluon PDFs. This sensitivity allows to use experimental measurements of this process to investigate phenomena of saturation and shadowing, which were discussed above. In LO pQCD, the cross section for coherent photoproduction is proportional to the square of the gluon PDF. Specifically, in the leading logarithmic approximation of pQCD, the cross section for exclusive J/ψ photoproduction on a proton target is [13, 14]

$$\frac{\mathrm{d}\sigma_{\gamma p\to \mathrm{J}/\psi p}(W_{\gamma p}, t=0)}{\mathrm{d}t} = C_p(\mu^2)[\alpha_s(\mu^2) x g_p(x,\mu^2)]^2\,, \tag{1.2}$$

where $W_{\gamma p}$ is the center-of-mass energy of the photon-proton system, t represents the Mandelstam variable, $\alpha_s(\mu^2)$ is the strong coupling constant, and $xg_p(x,\mu^2)$ represents the proton gluon parton distribution function at a light-cone momentum fraction x and resolution scale μ. The parameter $C_p(\mu^2)$ is a normalization factor. Taking a non-relativistic approximation for the J/ψ wave function, as was done in [13], yields $\mu^2 = M^2_{J/\psi}/4$ and

$$C_p(\mu^2) = \pi^3 \Gamma_{ee} M^3_{J/\psi}/(48\alpha_{\mathrm{e.m.}}\mu^8), \tag{1.3}$$

where $M_{J/\psi}$ is the J/ψ mass, Γ_{ee} is the J/ψ decay width to e^+e^- pair, and $\alpha_{\mathrm{e.m.}}$ is the electromagnetic coupling constant.

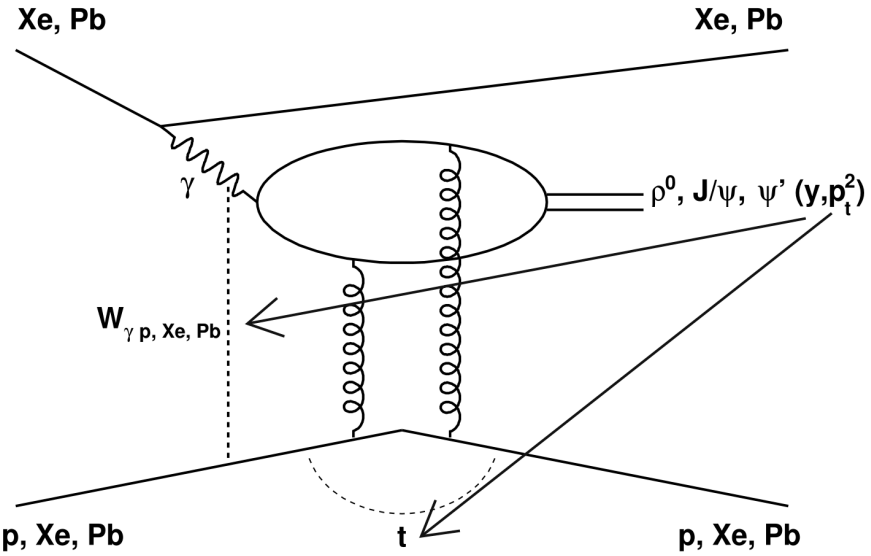

Figure 1.4: A diagram depicting the photoproduction of vector mesons in collision systems accessible at the LHC with the vector mesons ρ^0, J/ψ, ψ' observable by ALICE during Run 2. This diagram illustrates the kinematic variables of the vector mesons alongside the parameters describing the collision. Furthermore, it highlights a connection between the related variables.

Figure 1.4 illustrates a photoproduction diagram where a photon γ, emitted by one of the colliding particles, is interacting via gluons with the target particle. The number of photons emitted by a particle depends on the square of its electric charge. Therefore, in proton–nucleus collisions, the photon source is predominantly the nucleus. The energy of the emitted photon increases with the Lorentz boost of the source ion.

Photoproduction of vector mesons can be investigated in various collision systems. The collision systems and the vector mesons produced, which were accessible at the LHC during Run 2 with the ALICE detector, are also detailed in Fig. 1.4.

The diagram in Fig. 1.4 also depicts the center-of-mass energy of the photon-target system, denoted as W, the square of the momenta transferred in the collision, represented as t, and the rapidity y and transverse momentum p_{T} of the produced vector meson. The center-of-mass energy per nucleon of the photon-target system can be computed using natural units as

$$W^2_{\gamma \mathrm{p/Xe/Pb}} = M\sqrt{s_{\mathrm{NN}}}\, e^{-y}\,, \tag{1.4}$$

where $\sqrt{s_{\mathrm{NN}}}$ represents the center-of-mass energy per nucleon pair, M is the mass of the produced vector meson, and y denotes its rapidity in the laboratory frame when measured relative to the direction of the incoming target (p/Xe/Pb).

Vector meson photoproduction can be categorized into classes based on the average transverse momenta p_{T} of the produced vector meson. The average p_{T} is determined by the size of the target with which the photon interacts during the collision, and it is inversely dependent on the target size.

The first category, characterized by the lowest average p_{T}, corresponds to a situation in which the photon is interacting coherently with the entire target nucleus. In the case of lead ions, this corresponds to an average p_{T} of approximately 60 MeV/c for the produced vector meson:

- In ion–ion collisions, this process is referred to as coherent photoproduction. The target nucleus remains intact after this interaction.

The second category is characterized by the photon interacting with a single nucleon. The size of the nucleon leads to an average p_{T} of approximately 300 MeV/c for the produced vector meson:

- In proton–ion collisions, this process is referred to as exclusive photoproduction. The photon emitted by the lead nucleus interacts with the entire proton, which remains intact after the collision.
- In ion–ion collisions, this process is referred to as incoherent photoproduction. The photon emitted by one nucleus interacts only with a single nucleon in the target nucleus, and the nucleus breaks into fragments after the collision.

Finally, the last category, characterized by the highest average p_{T}, corresponds to the photon interacting with a single nucleon and exciting it. The average p_{T} of the produced vector mesons in this process exceeds 1 GeV/c:

- In proton–ion collisions, this process is referred to as dissociative photoproduction. The photon emitted by the nucleus interacts with the proton and excites it to a higher energy state, causing it to dissociate after the collision.

- In ion–ion collisions, this process is also referred to as dissociative photoproduction. The photon emitted by one nucleus interacts with a single nucleon in the target nucleus and excites it so that it dissociates and the nucleus breaks into fragments after the collision.

When the produced vector meson is being detected via its dilepton decay channel, there is another process that contributes to the measured signal, as it shares the same experimental signature. This contribution arises from the photoproduction of a lepton-antilepton pair in an interaction of two photons. A diagram of this process in a Pb–Pb collision system can be seen in Fig. 1.5.

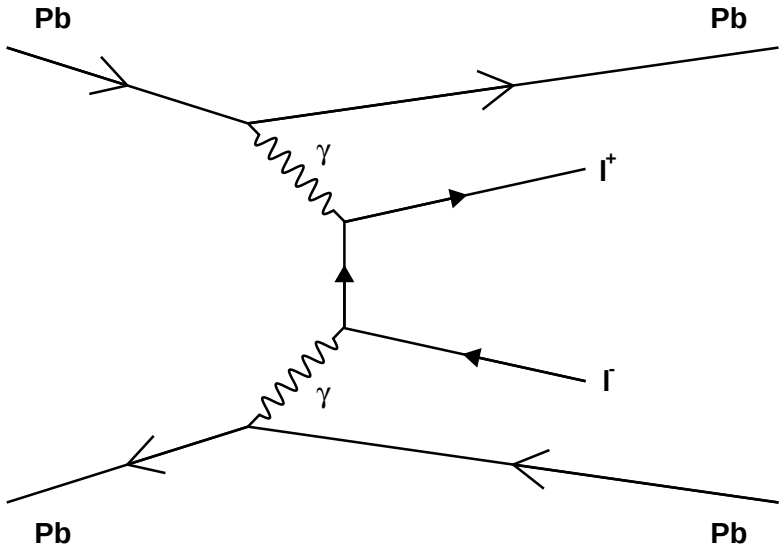

Figure 1.5: Diagram of dilepton photoproduction in a Pb–Pb collision system.

Additionally, when the vector meson has excited states, it is possible that these excited states can contribute to the measured signal of the ground state by decaying into the ground state. For the analysis of J/ψ as described in Chap. 4, such a contribution arises from the decay of $\psi' \to J/\psi + X$, where the decay products, denoted as X, are not detected. Only the produced J/ψ is detected, through the detection of its decay products. This contribution is then observed in the measured signal and is referred to as a feed-down contribution. The feed-down contribution exhibits a higher average p_T when compared to the primary J/ψ photoproduction.

1.5 Ultra-peripheral collisions

To accurately measure the cross section for vector meson photoproduction, it is imperative to mitigate the influence of inelastic hadronic interactions during the collision, as they introduce a significant background contribution. This suppression of hadronic interactions can be achieved in UPCs by ensuring that the impact parameter b of the two colliding particles is greater than the sum of their radii R. This configuration effectively suppresses the short-range strong interaction. A diagram of an ultra-peripheral collision can be seen in Fig. 1.6.

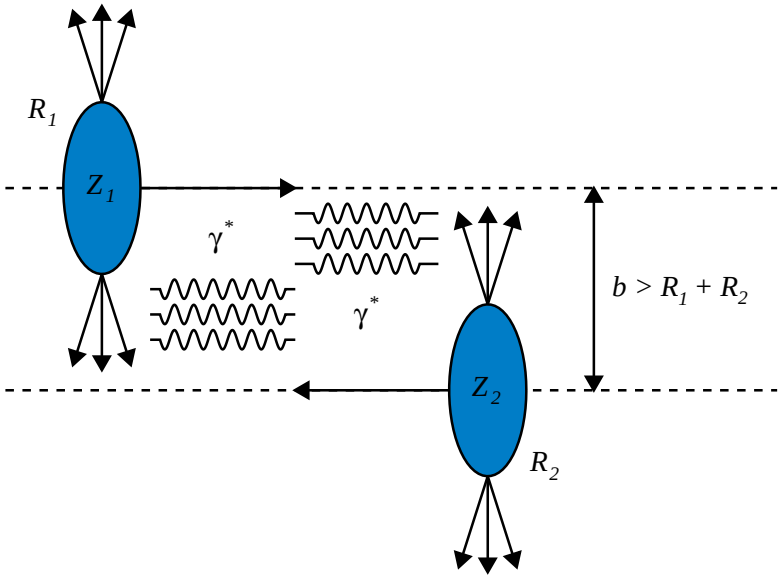

Figure 1.6: Diagram of an ultra-peripheral collision of two particles with charge Z_i, radius R_i and impact parameter b.

However, note that photoproduction contributes to the vector meson cross section also in collisions where $b < R_1 + R_2$, a phenomenon initially reported by ALICE [15]. This finding has been subsequently confirmed by STAR [16, 17], ALICE [18, 19], and LHCb [20].

The value of the Bjorken-x accessible in an UPC can be calculated, assuming natural units, as

$$x = \frac{M^2}{W^2_{\gamma \mathrm{p/Xe/Pb}}}, \tag{1.5}$$

where M represents the mass of the produced vector meson, and $W^2_{\gamma \mathrm{p/Xe/Pb}}$ denotes the center-of-mass energy per nucleon of the photon-target system, as described in Equation 1.4.

In an ion–ion collision, it is crucial to note that either of the ions can function as the source of the photon or the target. This leads to a change in the sign of the measured rapidity in Eq. 1.4. Given that the rapidity dependence is exponential, this sign change has a substantial impact on the resulting center-of-mass energy per nucleon and the corresponding Bjorken-x value. Consequently, the measured UPC cross section in a lead-lead system, denoted as σ_{PbPb}, is a combination of these two contributions [21].

$$\frac{\mathrm{d}\sigma_{\mathrm{PbPb}}}{\mathrm{d}y} = n_\gamma(y,\{b\})\sigma_{\gamma\mathrm{Pb}}(y) + n_\gamma(-y,\{b\})\sigma_{\gamma\mathrm{Pb}}(-y) \tag{1.6}$$

In this equation, $n_\gamma(y)$ represents the photon flux, which, when employing the equivalent photon approximation, see Ref. [22] for a review, represents the number of photons with energy k given by

$$k = \frac{M}{2}e^{-y}. \tag{1.7}$$

The value of the photon flux is obtained through integration over its distribution within a specified range of impact parameters $\{b\}$. The term $\sigma_{\gamma\mathrm{Pb}}(y)$ in Eq. 1.6 denotes the photonuclear cross section for vector meson production at a given rapidity y. Notably, for measurements at midrapidity ($y \sim 0$), the two $\sigma_{\gamma\mathrm{Pb}}$ contributions are nearly identical, but for forward measurements at higher rapidity values, they exhibit significant differences.

In the kinematic range of ALICE during LHC Run 2, the probed Bjorken-x values for the two $\sigma_{\gamma\mathrm{Pb}}$ contributions to the coherent J/ψ cross section σ_{PbPb} cover the range from 10^{-2} to 10^{-5}. The contribution with the lower Bjorken-x reaches approximately 40% of the total at $|y| = 2.5$ and only about 5% at $|y| = 4.0$. Given the limited knowledge of gluon PDFs in the range of Bjorken-x at 10^{-5}, there is significant interest in separating these two contributions to the cross section and examining them individually, particularly focusing on the contribution with the lower Bjorken-x value. Achieving this is the main contribution of this work.

For further details regarding photoproduction and the physics of UPCs refer to [22, 23, 24, 25].

1.6 Separating photonuclear cross section contributions

It is important to note that the two contributions present in Eq. 1.6 cannot be disentangled using a single measurement. To achieve separation and isolate the distinct $\sigma_{\gamma\mathrm{Pb}}$ contributions, at least two measurements at the same rapidity but with different photon flux values are required. Up to this point, two methods for achieving

this goal have been proposed. Both of these methods take advantage of the fact that the photon flux varies depending on the impact parameter of the γPb interaction.

The first method, which is extensively described in [26], relies on the measurement of the coherent J/ψ photoproduction cross section obtained from UPCs and from peripheral collisions. References concerning the presence of the photoproduction contribution to the vector meson cross section in peripheral collisions, are given in Sec. 1.5.

The second method, as discussed in [27, 28], uses the high intensity of the photon fluxes generated by the interacting ions. The high intensity significantly increases the likelihood of additional photon-induced interactions between the ions alongside the vector meson photoproduction. One potential outcome of this extra interaction is electromagnetic dissociation (EMD) [29] of one or both of the ions. EMD can lead to the emission of forward neutrons, which can be detected using forward hadronic calorimeters. Refer to Fig. 1.7 for an illustration of J/ψ photoproduction, accompanied by the EMD of one of the ions resulting from an additional photon exchange.

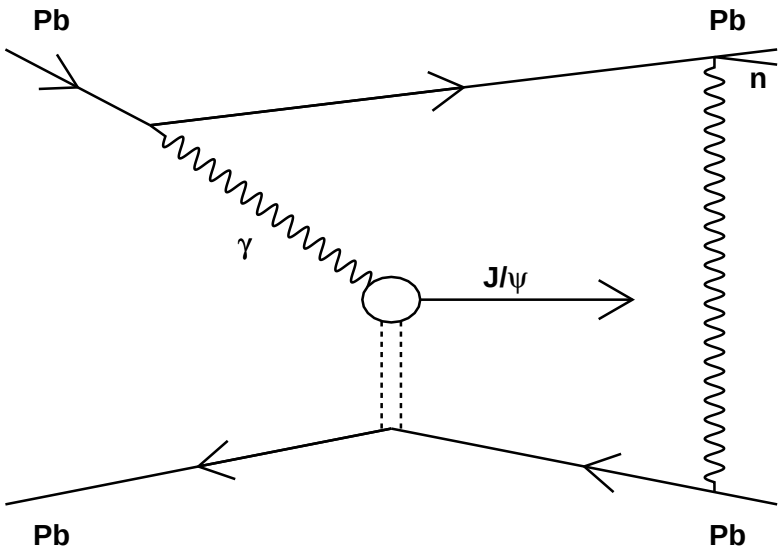

Figure 1.7: Diagram depicting J/ψ photoproduction in a Pb–Pb collision accompanied by an additional photon exchange between the interacting ions resulting in the EMD of one of the ions.

The classification of photoproduction events, based on the number of forward-emitted neutrons, implies sorting the events into distinct categories according to their impact parameter ranges. This categorization is due to the fact that photons with the highest energy are emitted at the lowest impact parameters. To induce the EMD of a nucleus, a photon with a minimum energy of approximately 10 MeV is required. Exploiting this observation, it becomes possible to categorize coherent J/ψ photoproduction events into classes characterized by the absence of EMD, the

presence of a single EMD, or the occurrence of mutual EMD. The following list of equations serves to describe these measured classes:

$$\frac{\mathrm{d}\sigma_{\mathrm{0n0n}}}{\mathrm{d}y} = n_\gamma(y,\mathrm{0n0n})\sigma_{\gamma\mathrm{Pb}}(y) + n_\gamma(-y,\mathrm{0n0n})\sigma_{\gamma\mathrm{Pb}}(-y)\,, \tag{1.8}$$

$$\frac{\mathrm{d}\sigma_{\mathrm{0nXn}}}{\mathrm{d}y} = n_\gamma(y,\mathrm{0nXn})\sigma_{\gamma\mathrm{Pb}}(y) + n_\gamma(-y,\mathrm{0nXn})\sigma_{\gamma\mathrm{Pb}}(-y)\,, \tag{1.9}$$

$$\frac{\mathrm{d}\sigma_{\mathrm{Xn0n}}}{\mathrm{d}y} = n_\gamma(y,\mathrm{Xn0n})\sigma_{\gamma\mathrm{Pb}}(y) + n_\gamma(-y,\mathrm{Xn0n})\sigma_{\gamma\mathrm{Pb}}(-y)\,, \tag{1.10}$$

$$\frac{\mathrm{d}\sigma_{\mathrm{XnXn}}}{\mathrm{d}y} = n_\gamma(y,\mathrm{XnXn})\sigma_{\gamma\mathrm{Pb}}(y) + n_\gamma(-y,\mathrm{XnXn})\sigma_{\gamma\mathrm{Pb}}(-y)\,. \tag{1.11}$$

The n_γ are the corresponding photon fluxes, which can be computed for each of the different neutron emission classes and the two possible signs for rapidity. $\sigma_{\gamma\mathrm{Pb}}(y)$ and $\sigma_{\gamma\mathrm{Pb}}(-y)$ are the two contributions to be extracted from Eq. 1.6. Finally, 0n0n, 0nXn, Xn0n, and XnXn denote the four different neutron emission classes, defined as:

- 0n0n: no neutrons on either side of ALICE;
- 0nXn: no neutrons in the direction of the A beam[1];
- Xn0n: no neutrons in the direction of the C beam[2];
- XnXn: neutrons on both sides of ALICE.

It is important to note that in an EMD process, not only neutrons can be emitted. Highly energetic photons can also produce charged particles, notably pions. These are then detected by ALICE, requiring the application of specific corrections for this effect. Further details regarding these corrections can be found in Sec. 4.8.

1.7 Previous measurements

The rapidity dependence of coherent J/ψ photoproduction has been measured at the LHC during both Run 1 and Run 2 by multiple experiments. In LHC Run 1, with center-of-mass energies per nucleon pair of $\sqrt{s_{\mathrm{NN}}} = 2.76$ TeV, the ALICE collaboration conducted measurements at both forward rapidity [30] and midrapidity [31]. Complementing these results, the CMS collaboration reported the cross section values within the intermediate rapidity range [32]. For a visual representation of the cross section values, please refer to Fig. 1.8.

[1] At the LHC, the A beam circulates in the anti-clockwise direction when the accelerator is viewed from above.

[2] At the LHC, the C beam circulates in the clockwise direction when the accelerator is viewed from above.

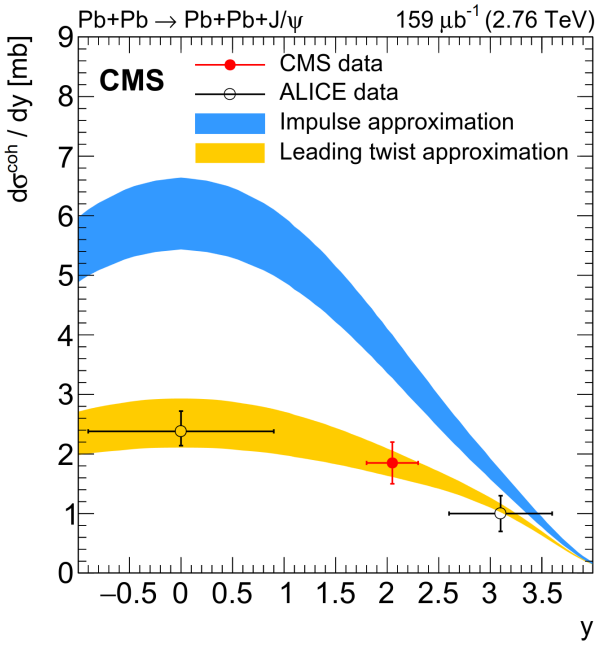

Figure 1.8: Differential cross section versus rapidity for coherent J/ψ photoproduction in Pb–Pb UPC at $\sqrt{s_{NN}} = 2.76$ TeV during LHC Run 1, as measured by ALICE and CMS. The vertical error bars encompass both statistical and systematic uncertainties, added in quadrature, while the horizontal bars represent the range of measurements in y. Additionally, calculations based on the impulse approximation and the leading twist approximation are also provided. Taken from [32].

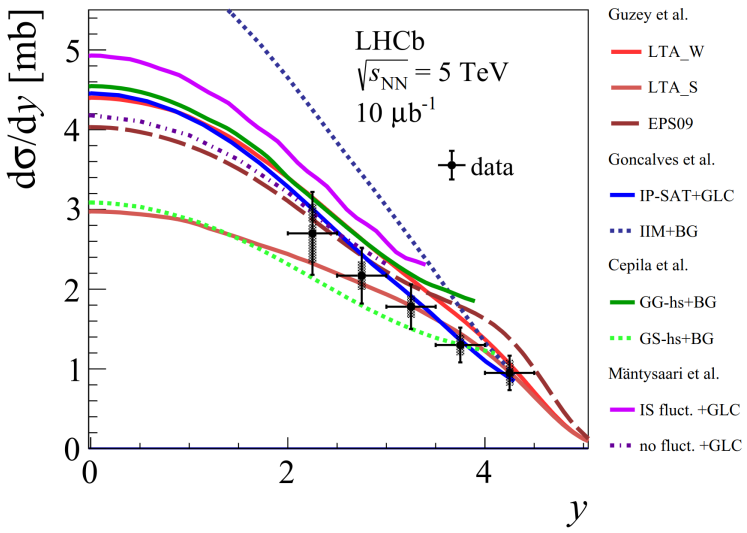

Figure 1.9: Differential cross section as a function of rapidity for coherent J/ψ production in Pb–Pb UPC events at $\sqrt{s_{NN}} = 5.02$ TeV during LHC Run 2, as measured by LHCb. Various phenomenological predictions are also provided. The measurements are represented as data points, with inner and outer error bars denoting statistical and total uncertainties, respectively. Taken from [33].

The Run 1 results demonstrated that it is possible to measure photon-induced processes using detectors and a hadron collider not initially intended for this purpose. Additionally, the precision of these first results was already sufficient to reject some of the theoretical models.

In LHC Run 2, operating at a center-of-mass energy of $\sqrt{s_{\mathrm{NN}}} = 5.02$ TeV, the LHCb collaboration published their results at forward rapidity [33], which can be found in Fig. 1.9. Moreover, the ALICE collaboration presented their findings at midrapidity [34, 35] and forward rapidity [36]. For graphical representations of the results, please refer to Fig. 1.10.

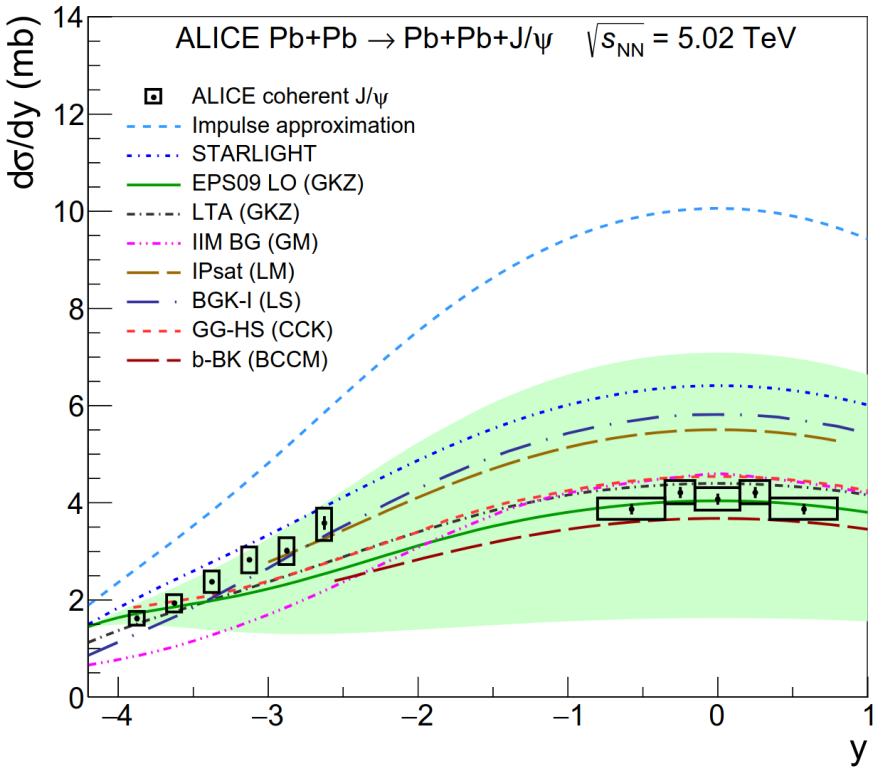

Figure 1.10: Measured differential cross section for coherent J/ψ photoproduction in Pb–Pb UPC events at $\sqrt{s_{\mathrm{NN}}} = 5.02$ TeV during LHC Run 2, as measured by ALICE. The error bars (boxes) represent statistical (systematic) uncertainties. Theoretical calculations are provided, with the green band indicating the uncertainties associated with the EPS09 LO calculation. Taken from [36].

The Run 2 results based on a significantly larger dataset, reduced the uncertainties associated with the measurement. This has facilitated the computation of the cross section in more rapidity bins and a broader overall range. Consequently, these findings have imposed more stringent constraints on existing theoretical predictions, as none of them has demonstrated the capacity to fully capture the shape of the data.

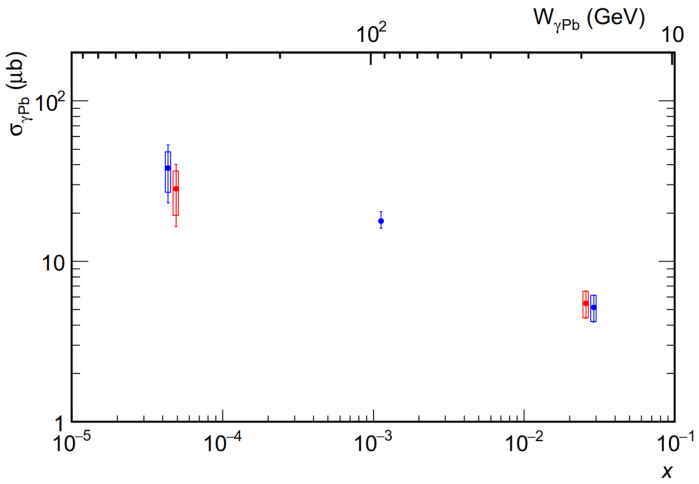

Figure 1.11: Cross section for coherent J/ψ photonuclear production off a lead nucleus as a function of $W_{\gamma \mathrm{Pb,n}}$ (upper axis) and x (lower axis). Statistical uncertainties are represented by a line and systematic uncertainties by the empty box, except for the middle cross section, where they are both represented by the bar. Blue symbols are evaluated at the center, while red symbols are evaluated at the mean of the rapidity ranges where the corresponding measurements were performed. Taken from [26].

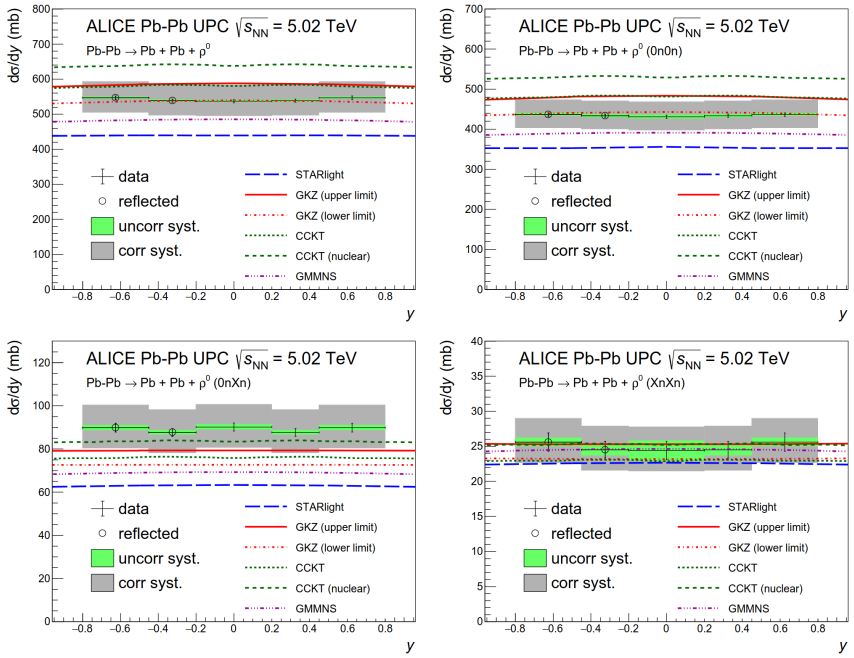

Figure 1.12: Cross section for the coherent photoproduction of ρ^0 vector mesons in Pb–Pb UPC as a function of rapidity for the integrated data set in EMD classes (top left) and for the 0n0n (top right), 0nXn (bottom left), and XnXn (bottom right) classes separately. The results are compared to predictions from various models. Taken from [37].

The availability of a wide range of experimental results at various J/ψ rapidity values is of paramount importance due to the exponential dependence on the center-of-mass energy per nucleon in the γPb system, as denoted in Eq. 1.4. The utilization of such an extensive data set enables the exploration of the γPb cross section across a broad energy spectrum.

The first attempt at this exploration was performed in Ref. [38] using the ALICE Run 1 results. The analysis was based on the fact that at mid rapidity, where $y = 0$, both contributions in Eq. 1.4 are the same. Therefore, by computing the corresponding photon flux $n_\gamma(y = 0)$, it is straightforward to extract the $\sigma_{\gamma\mathrm{Pb}}$ value from Eq. 1.4. The second technique employed in the paper is based on the fact that for the measurement at the highest rapidity, $|y| = 4.0$, the low Bjorken-x contribution accounts for only about 5% of the total UPC cross section. Therefore, neglecting this contribution, it is possible to obtain the $\sigma_{\gamma\mathrm{Pb}}$ value for the higher Bjorken-x contribution with a precision on the order of the size of the neglected contribution. Using the data at $y = 0$, the extracted $\sigma_{\gamma\mathrm{Pb}}$ corresponds to an energy of $W_{\gamma\mathrm{Pb,n}} = 92$ GeV, while the cross section extracted from the data at $|y| = 4.0$ corresponds to an energy of $W_{\gamma\mathrm{Pb,n}} = 20$ GeV.

Another attempt using the ALICE Run 1 data set was made in [26]. This result utilizes the first technique discussed in Sec. 1.6, i.e., combining the results from peripheral and ultra-peripheral measurements of coherent J/ψ photoproduction to extract the $\sigma_{\gamma\mathrm{Pb}}$ values at different center-of-mass energies. This approach yielded the γPb photonuclear cross section at energies $W_{\gamma\mathrm{Pb,n}}$ of 18 GeV, 92 GeV, and 470 GeV, as depicted in Fig. 1.11.

The second technique discussed in Sec. 1.6, which involves categorizing photoproduction events into EMD classes to extract $\sigma_{\gamma\mathrm{Pb}}$ at different $W_{\gamma\mathrm{Pb,n}}$ energies from Eq. 1.6, was initially employed in the measurement of coherent ρ^0 photoproduction at midrapidity by the ALICE collaboration [40, 37, 41] during LHC Run 2, see Fig. 1.12. Subsequently, this technique has also been utilized to measure the cross section for the $\gamma\gamma \to \mu^+\mu^-$ and $\gamma\gamma \to e^+e^-$ processes in UPCs by the CMS and ATLAS collaborations [42, 43, 39]. For the $\gamma\gamma \to e^+e^-$ ATLAS results, please see Fig. 1.13. The results obtained by ATLAS and CMS have been successfully described by the SuperChic Monte Carlo generator [44].

1.8 Theoretical models

When computing theoretical predictions for the values of coherent J/ψ photoproduction cross section σ_{PbPb}, two key components are required: the photonuclear cross section $\sigma_{\gamma\mathrm{Pb}}(y)$ and the photon flux $n_\gamma(y)$ as defined in Eq. 1.6. In addition to these primary contributions outlined in Eq. 1.6, there is also an interference term as discussed in [45]. It is worth noting that for the results presented in Chap. 4, the interference term can be safely omitted as its contribution to the total cross section, which is integrated over the accessible transverse momentum range, is negligible.

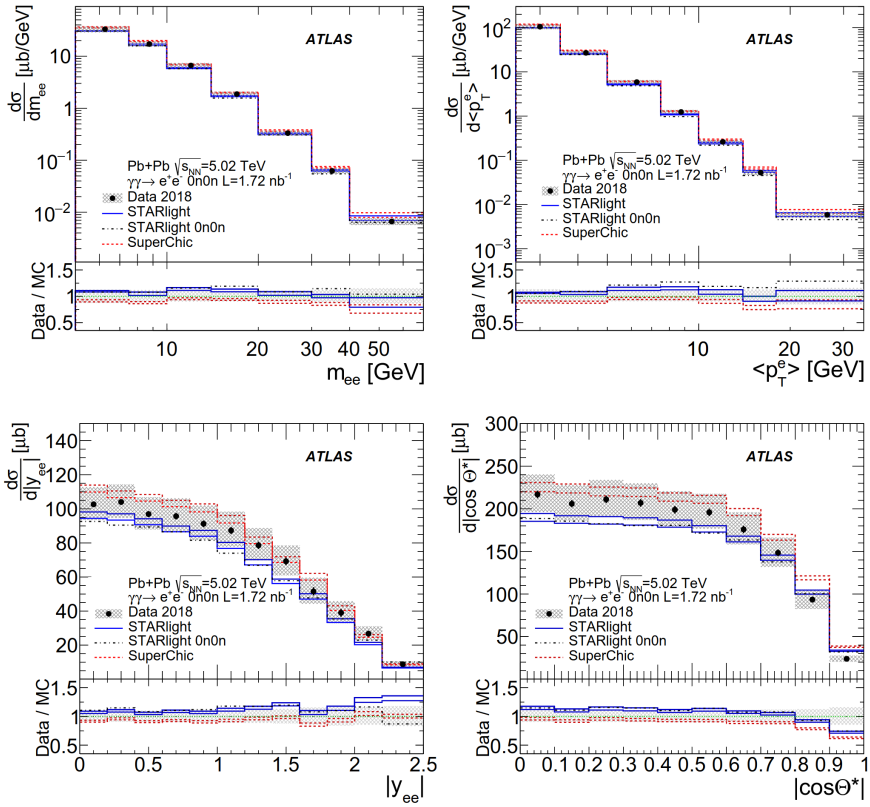

Figure 1.13: Fully corrected differential cross sections were measured for the 0n0n category in exclusive dielectron production as functions of m_{ee}, $< p_{\mathrm{T}}^{e} >$, $|y_{ee}|$, and $|\cos\theta^*|$. These cross sections were then compared with Monte Carlo (MC) predictions from Starlight (solid blue) and SuperChic v3.05 (dashed red). Each of these predictions is represented by two lines reflecting systematic variations. Furthermore, a dedicated prediction from Starlight for the 0n0n category (dashed-dotted black) is presented. The bottom panels display the ratios of data to predictions. The shaded area signifies the total uncertainty of the data, excluding the 2% luminosity uncertainty. Taken from [39].

1.8.1 Photon flux

The photon flux values are computed using the STARlight model [21, 27, 46] and the $\mathbf{n}^{\mathbf{O}}_{\mathbf{O}}\mathbf{n}$ model [47]. Both of these models assume the rest frame of the target nucleus for this computation, which simplifies the procedure. In this frame, the photon energy k is large, while the square of the momentum transferred in the collision $|t|$ is small. The photon flux of a lead ion accelerated to speeds close to the speed of light is determined using the Weizsäcker-Williams approach. The gamma factor of the lead is

$$\gamma = E_A/m_A \gg 1, \tag{1.12}$$

where E_A is the energy and m_A is the mass of the accelerated ion. The photon flux, in the point-like approximation, generated by this particle at a distance r is given by

$$\frac{\mathrm{d}^3 N_\gamma(k,r)}{\mathrm{d}k\,\mathrm{d}^2 r} = \frac{Z^2\alpha x^2}{\pi^2 k r^2} K_1^2(x), \tag{1.13}$$

where k is the photon energy, Z is the charge of the ion, $x = kr/\gamma$, and K_1 represents the modified Bessel function. Natural units are assumed in all equations.

To ensure that no hadronic interaction accompanies the photonuclear collision, the probability of one or more hadronic interactions is computed as a function of the impact parameter. The nuclear density is modeled with a Woods-Saxon distribution for symmetric nuclei, denoted A, as follows:

$$\rho_A(s) = \frac{\rho_0}{1 + exp[(s - R_{WS})/d]}. \tag{1.14}$$

Here, s represents the distance from the center of the particle, R_{WS} is the radius of the particle, and d is the nuclear skin depth. The parameters R_{WS} and d are determined through fits to electron scattering data, while the parameter ρ^0 is fixed by normalization.

To determine the probability of hadronic interaction at a given impact parameter b, an overlap function is employed:

$$T_{AA}(|\vec{b}|) = \int \mathrm{d}^2\vec{r}, T_A(\vec{r}), T_A(\vec{r} - \vec{b}). \tag{1.15}$$

Here, $\vec{r}$ and $\vec{b}$ are 2D vectors perpendicular to the direction in which the nucleus is traveling, denoted as z. The function $T_A(\vec{r})$ represents the nuclear thickness and is defined as:

$$T_A(\vec{r}) = \int \mathrm{d}z, \rho_A(\sqrt{|\vec{r}|^2 + z^2}). \tag{1.16}$$

A Poisson distribution with a mean of $T_{AA}(b)\sigma_{NN}$ describes the number of nucleon-nucleon collisions. Here, σ_{NN} represents the total nucleon-nucleon interaction cross section. Using the above mentioned expressions, the probability of no hadronic interaction is given by:

$$P_{0H}(b) = \exp(-T_{AA}(b)\sigma_{NN}). \tag{1.17}$$

Finally, integrating Eq. 1.13 over r and combining it with the probability of no hadronic interaction from Eq. 1.17 gives the total photon flux.

$$\frac{\mathrm{d}N_\gamma(k)}{\mathrm{d}k} = \int_0^\infty 2\pi b\,\mathrm{d}b P_{0H}(b) \int_0^R \frac{r\,\mathrm{d}r}{\pi R_A^2} \int_0^{2\pi} \mathrm{d}\phi \;\; \frac{\mathrm{d}^3 N_\gamma(k, b + r\cos(\phi))}{\mathrm{d}k\,\mathrm{d}^2 r} \tag{1.18}$$

Both models also employ the same approach to determine the fractions of the total photon flux contributing to each EMD class. This approach relies on photoproduction data measured at lower energies and extrapolates them to LHC energies.

However, there are two notable differences between them. First, $\mathbf{n^{O}_{O}n}$ utilizes the giant-dipole resonance data from [48], while STARlight employs their Lorentz-line parameterization. Nevertheless, the difference between these two approaches is negligible. The second and more significant difference lies in the fact that STARlight uses data from photon-nucleon interactions [49, 50] in the nucleon resonance region [51], whereas $\mathbf{n^{O}_{O}n}$ relies on photonuclear Pb data in this region.

The resulting photon fluxes for the different EMD classes from both STARlight and $\mathbf{n^{O}_{O}n}$ are highly consistent, except for the most forward rapidity region. In this specific region, the models exhibit differences of up to 20% in the flux values. As the $\mathbf{n^{O}_{O}n}$ model relies on data from γPb collisions, which are the focus of this thesis, the flux values from this model have been utilized for the final results presented in Chap. 4.

1.8.2 Photonuclear cross section

There are many groups providing predictions for the values of σ_{PbPb}, see [21, 14, 52, 53, 54, 55, 56, 57]. However, only some of these groups provide their predictions in EMD classes.

Impulse approximation

First, it is essential to introduce the impulse approximation (IA) [38, 58]. In this approach, the many-body character of the photonuclear collision is treated as a superposition of independent photon-nucleon collisions. As discussed in Sec. 1.3, this treatment is not correct, but it serves a useful purpose since the ratio (S_{Pb}) between the photonuclear cross section predicted by the IA ($\sigma^{\mathrm{IA}}_{\gamma\mathrm{Pb}}$) and the measured cross section can be used to quantify the effect of nuclear shadowing. The square root in the formula for S_{Pb} is employed to account for the fact that the cross section depends on the square of the gluon PDF in Eq. 1.2.

$$S_{\mathrm{Pb}}(W_{\gamma\mathrm{Pb,n}}) = \sqrt{\frac{\sigma_{\gamma\mathrm{Pb}}}{\sigma^{\mathrm{IA}}_{\gamma\mathrm{Pb}}}} \tag{1.19}$$

STARlight model

The computation of the photonuclear cross section in the STARlight model by Klein and Nystrand [21] is based on existing $\gamma p \to V p$ cross section data and employs the

Glauber calculation to account for the transition to the nuclear case. In this context, the existing data can be parameterized as:

$$\left.\frac{\mathrm{d}\sigma(\gamma p \to V p)}{\mathrm{d}t}\right|_{t=0} = b_V (X W^{\varepsilon} + Y W^{-\eta}), \tag{1.20}$$

where W represents the center-of-mass energy, and the parameters b_V, X, Y, ε, and η are determined through fitting procedures with the available data. The first term (XW^{ε}) in Eq. 1.20 corresponds to Pomeron exchange, while the second term ($YW^{-\eta}$) represents meson exchange. Notably, for the case of J/ψ, the Pomeron exchange term dominates significantly.

To transition to the nuclear case, the optical theorem and an eikonalization technique are applied following the vector dominance model (VDM) [59]. The corresponding cross section at $t = 0$ is expressed as:

$$\left.\frac{\mathrm{d}\sigma(\gamma p \to V p)}{\mathrm{d}t}\right|_{t=0} = \frac{4\pi\alpha}{f_{\mathrm{V}}^2} \left.\frac{\mathrm{d}\sigma(V p \to V p)}{\mathrm{d}t}\right|_{t=0}. \tag{1.21}$$

Here, α represents the electromagnetic coupling constant, and f_{V} denotes the vector meson-photon coupling. The definition of f_{V} is given as:

$$\frac{f_{\mathrm{V}}^2}{4\pi} = \frac{M_{\mathrm{V}} \alpha^2}{3\Gamma_{V \to e^+e^-}}, \tag{1.22}$$

where M_{V} stands for the mass of the produced vector meson, and $\Gamma_{V \to e^+e^-}$ is the decay width to the e^+e^- decay channel. However, due to the observed discrepancy between the measured f_{V} values in photoproduction data and leptonic decay width data [60], a correction is introduced to account for the coupling through higher mass vector mesons, following the generalized vector dominance model (GVDM).

By employing the optical theorem, the total Vp scattering cross section can be expressed as

$$\sigma_{tot}^2(Vp) = 16\pi \left.\frac{\mathrm{d}\sigma(V p \to V p)}{\mathrm{d}t}\right|_{t=0}. \tag{1.23}$$

With the Glauber calculation, the photonuclear cross section $\sigma_{tot}(VA)$ is given by

$$\sigma_{tot}(VA) = \int \mathrm{d}^2\vec{r} \left(1 - e^{-\sigma_{tot}(Vp) T_{AA}(\vec{r})}\right). \tag{1.24}$$

Here, $T_{AA}(\vec{r})$ signifies the nuclear overlap function from Eq. 1.15. Combining the above equations yields

$$\left.\frac{\mathrm{d}\sigma(\gamma A \to VA)}{\mathrm{d}t}\right|_{t=0} = \frac{\alpha\sigma_{tot}^2(VA)}{4f_V^2}. \tag{1.25}$$

The size of the total cross section is contingent upon the shape of the $\mathrm{d}\sigma/\mathrm{d}t$ distribution. For nuclei, this shape is determined by the nuclear form factor, which is the Fourier transform of the nuclear density function. Since the Woods-Saxon distribution cannot be analytically Fourier transformed, an approximation is used, involving a hard sphere with a radius R_A convoluted with a Yukawa potential having a range of $r = 0.7$ fm. The Fourier transform of this approximation is the product of the two terms transformed separately.

$$F(q = \sqrt{|t|}) = \frac{4\pi\rho_0}{Aq^3}\left[\sin(qR_a) - qR_a\cos(qR_A)\right]\left[\frac{1}{1+a^2q^2}\right] \tag{1.26}$$

The agreement between this approximation and a numerical result for the Fourier transform of a Woods-Saxon distribution is highly satisfactory.

Using the form factor, the integrated photonuclear cross section is given by

$$\sigma(\gamma A \to VA) = \left.\frac{\mathrm{d}\sigma(\gamma A \to VA)}{\mathrm{d}t}\right|_{t=0}\int_{t_{min}}^{\infty}\mathrm{d}t|F(t)|^2, \tag{1.27}$$

where $t_{min} = (M_V^2/4k)^2$.

Finally, by considering the photon flux from Eq. 1.18 and integrating over the photon energies, the total UPC cross section can be expressed as

$$\begin{aligned}\sigma(AA \to AAV) &= \int \mathrm{d}k\frac{\mathrm{d}N_\gamma(k)}{\mathrm{d}k}\sigma(\gamma A \to VA)\\ &= \int_0^\infty \mathrm{d}k\frac{\mathrm{d}N_\gamma(k)}{\mathrm{d}k}\int_{t_{min}}^{\infty}\mathrm{d}t\left.\frac{\mathrm{d}\sigma(\gamma A \to VA)}{\mathrm{d}t}\right|_{t=0}|F(t)|^2.\end{aligned} \tag{1.28}$$

Leading logarithmic approximation of perturbative QCD

Starting from Eq. 1.2 and extending the work beyond what was presented in [13], Guzey, Kryshen, and Zhalov [14] calculate predictions for coherent J/ψ photoproduction within the framework of the leading logarithmic approximation of pQCD. For the normalization parameter $C_p(\mu^2)$ in Eq. 1.2, they derive [61, 62]

$$C_p(\mu^2) = F^2(\mu^2)\bar{R}_g^2(1+\eta^2)\pi^3\Gamma_{ee}M_{J/\psi}^3/(48\alpha_{\mathrm{e.m.}}\mu^8), \tag{1.29}$$

where $F^2(\mu^2)$ represents a correction factor accounting for the non-zero transverse momentum of the quarks in the J/ψ wave function, $\bar{R}_g$ is the skewness correction to

accommodate the off-forward kinematics of the $\gamma p \to J/\psi p$ process, and η denotes the ratio of the real and imaginary parts of the scattering amplitude.

The value of μ^2 for the predictions is determined through fits to HERA and LHCb data, and $C_p(\mu^2)$ is chosen to describe the experimental cross section at $W = 100$ GeV. Using this approach, a good description of the available data is achieved.

Transitioning from a proton target to a nuclear target and integrating over t, Eq. 1.2 can be reformulated as shown in Ref. [63].

$$\begin{aligned}\sigma_{\gamma A\to VA}(W_{\gamma p}) &= C_A(\mu^2)[\alpha_s(\mu^2)xg_A(x,\mu^2)]^2\Phi_A(t_{\min}) \\ &= \frac{C_A(\mu^2)}{C_p(\mu^2)}\frac{d\sigma_{\gamma p\to Vp}(W_{\gamma p},t=0)}{dt}\left[\frac{xg_A(x,\mu^2)}{Axg_p(x,\mu^2)}\right]^2\Phi_A(t_{\min})\end{aligned} \tag{1.30}$$

Here,

$$C_A(\mu^2)/C_p(\mu^2) = (1+\eta_A^2)\bar{R}_{g,A}^2/[(1+\eta^2)\bar{R}_g^2], \tag{1.31}$$

where η_A and $\bar{R}_{g,A}$ are, in analogy to the above expressions, the ratio of the real and imaginary parts of the scattering amplitude and the skewness correction for the $\gamma A \to VA$ process.

The function $g_A(x,\mu^2)$ represents the nuclear gluon PDF, A is the atomic number of the nucleus, and

$$\Phi_A(t_{\min}) = \int_{-\infty}^{t_{\min}} dt|F_A(t)|^2, \tag{1.32}$$

where $F_A(t)$ is the nuclear form factor, and $t_{\min} = -x^2m_N^2$, with m_N denoting the mass of a nucleon.

To derive the final predictions from Eq. 1.30, two methods are employed. The first method utilizes the EPS09-LO nuclear parton distribution functions (PDFs) [64] to calculate the value of $xg_A(x,\mu^2)/Axg_p(x,\mu^2)$, while the second method involves the application of the leading twist approximation (LTA) of nuclear shadowing [65] to obtain this ratio.

The photon flux values used in the computation of the UPC cross section are taken from the STARlight model.

Impact-parameter dependent Balitsky–Kovchegov equation

The next set of predictions has been provided by Bendova, Cepila, Contreras, and Matas [55]. Their computation is based on the color-dipole approach and utilizes the

impact-parameter dependent Balitsky–Kovchegov equation [66, 67]. The coherent J/ψ photoproduction cross section is calculated as follows

$$\left.\frac{d\sigma_{\gamma Pb}}{d|t|}\right|_{T,L} = \frac{\left(1+\beta^2\right)\left(R_g^{T,L}\right)^2}{16\pi}|\mathcal{A}_{T,L}|^2, \tag{1.33}$$

where t represents the square of the momentum transferred in the γPb interaction, T and L denote the contribution from transversely and longitudinally polarized photons, $(1+\beta^2)$ serves as a correction factor accounting for the contribution of the real part of the amplitude, and $(R_g^{T,L})^2$ is the skewness correction [68].

The scattering amplitude $\mathcal{A}_{T,L}(x,Q^2,\vec{\Delta})$ can be expressed as

$$\mathcal{A}_{T,L}(x,Q^2,\vec{\Delta}) = i\int d\vec{r}\int_0^1 \frac{dz}{4\pi}\int d\vec{b}|\Psi_V^*\Psi_{\gamma^*}|_{T,L}\exp\left[-i\left(\vec{b}-(1-z)\vec{r}\right)\vec{\Delta}\right]\frac{d\sigma^{q\bar{q}}}{d\vec{b}}, \tag{1.34}$$

where Q^2 represents the photon virtuality, $\vec{\Delta}^2 \equiv -t$, $\vec{r}$ denotes the size and orientation of the color dipole, $\vec{b}$ stands for the impact parameter between the dipole and the lead target. Ψ_{γ^*} represents the wave function of the virtual photon fluctuating into a color dipole, and Ψ_V represents the wave function of the dipole transforming into a vector meson. Finally, z denotes the fraction of the total quark-antiquark dipole energy carried by the quark. The dipole cross section $d\sigma^{q\bar{q}}/d\vec{b}$ is given by

$$\frac{d\sigma^{q\bar{q}}}{d\vec{b}} = 2N(\vec{r},\vec{b};x), \tag{1.35}$$

where $N(\vec{r},\vec{b};x)$ represents the dipole scattering amplitude, which is the outcome of the Balitsky-Kovchegov equation.

Two sets of dipole scattering amplitudes [67] are utilized for the predictions. The first one, denoted as b-BK-GG, employs proton data as the initial condition for the Balitsky-Kovchegov equation. To compare with the PbPb data, the Glauber-Gribov method [69, 70] is applied to the results.

The second approach, denoted as b-BK-A, directly employs lead nucleus initial conditions for the Balitsky-Kovchegov equation, eliminating the need for additional steps after the evolution. This prediction has been chosen for comparison with the analysis results presented in Chap. 4.

The techniques used to derive this prediction are valid only in the domain of small Bjorken-x. For this reason, the UPC cross section predictions from this model cannot be used for $|y|$ larger than approximately three, as in this kinematic region, the UPC cross section is dominated by the high Bjorken-x contribution from Eq. 1.6.

The photon fluxes used for the computation of the UPC cross section are taken from the $\mathbf{n}^{\mathbf{O}}_{\mathbf{O}}\mathbf{n}$ model.

Energy-dependent hot-spot model

The predictions by Cepila, Contreras, and Krelina [53] are also based on the color-dipole approach and utilizing the Good–Walker formalism [71, 72, 73]. In this formalism, the coherent photon-nucleus cross section is given by the square of the amplitude averaged over different geometrical configurations j of the nucleus inner structure. See [74] for a review of this approach.

$$\left.\frac{\mathrm{d}\sigma_{\gamma\mathrm{A}}}{\mathrm{d}t}\right|^{\mathrm{coh}}_{T,L} = \frac{(R_g^{T,L})^2}{16\pi}\left|\left\langle A^j(x,Q^2,\vec{\Delta})_{T,L}\right\rangle_j\right|^2 \tag{1.36}$$

Similarly to Eq. 1.33, t is the square of the momentum transferred, $R_g^{T,L}$ is the skewness correction [68], and T and L represent the contributions from transversely and longitudinally polarized photons. The amplitude $A^j(x,Q^2,\vec{\Delta})_{T,L}$ is given by the same formula as in Eq. 1.34.

Two approaches, discussed in [75], were used to compute the dipole-nucleus cross section from Eq. 1.34. The first one, denoted as GG, uses the Glauber-Gribov method [69, 70] to determine the dipole-nucleus cross section from the dipole-proton cross section.

$$\left(\frac{d\sigma_{\mathrm{dA}}}{d\vec{b}}\right)_j = 2\left[1-\exp\left(-\frac{1}{2}\sigma_{\mathrm{dp}}(x,r)T_{\mathrm{A}}^j(\vec{b})\right)\right], \tag{1.37}$$

Here, $T_{\mathrm{A}}(\vec{b})$ represents the nuclear profile, and the dipole-proton cross section is modeled using the Golec-Biernat and Wusthoff [76] model

$$\sigma_{\mathrm{dp}}(x,r) = \sigma_0\left[1-\exp\left(-r^2Q_s^2(x)/4\right)\right], \tag{1.38}$$

where $\sigma_0 = \pi R_{\mathrm{p}}^2$, with R_{p} being the proton radius, and $Q_s^2(x) = Q_0^2(x_0/x)^\lambda$ is the saturation scale with parameter values taken from [75].

The second approach factorizes the dependence on $\vec{b}$ and x as follows [75]

$$\left(\frac{d\sigma_{\mathrm{dA}}}{d\vec{b}}\right)_j = \sigma_0^{\mathrm{A}}\left[1-\exp\left(-r^2Q_{A,s}^2(x)/4\right)\right]T_{\mathrm{A}}^j(\vec{b}). \tag{1.39}$$

Here, $\sigma_0^{\mathrm{A}} = \pi R_{\mathrm{A}}^2$, with R_{A} being the nuclear radius from the Woods-Saxon distribution, and the nuclear saturation scale $Q_{s,\mathrm{A}}$ is given by the nucleon saturation scale Q_s with a geometric scaling prescription [77]

$$Q^2_{s,\mathrm{A}}(x) = Q^2_s(x) \left(\frac{\mathrm{A}\pi R^2_\mathrm{p}}{\pi R^2_\mathrm{A}} \right)^{\frac{1}{\delta}}, \tag{1.40}$$

where the parameter values are taken from [75, 77]. This model is denoted GS.

Two different approaches were also used to compute the nuclear profile function. The first one, labeled as n, assumes the nucleus to be composed of nucleons with a Gaussian profile and width B_p, placed at random positions within the nucleus $\{\vec{b}_i\}^j$, which are sampled from a Woods-Saxon distribution for each configuration j.

$$T^j_\mathrm{A}(\vec{b}) = \frac{1}{2\pi B_\mathrm{p}} \sum_{i=1}^{\mathrm{A}} \exp\left(-\frac{(\vec{b} - \vec{b}^j_i)^2}{2B_\mathrm{p}} \right) \tag{1.41}$$

The second method, labeled as hs, assumes hot spots as subnucleonic degrees of freedom. The number of hot spots for a given nucleon increases with decreasing x which goes beyond what has been done in previous publications [54, 78]. Also the hot spots have a Gaussian profile with width B_hs

$$T^j_\mathrm{A}(\vec{b}) = \frac{1}{2\pi B_\mathrm{hs}} \sum_{i=1}^{\mathrm{A}} \frac{1}{N_\mathrm{hs}} \sum_{k=1}^{N_\mathrm{hs}} \exp\left(-\frac{(\vec{b} - \vec{b}^j_i - \vec{b}^j_k)^2}{2B_\mathrm{hs}} \right). \tag{1.42}$$

Here, N_hs is a random number determined by a zero-truncated Poisson distribution with the mean value

$$\langle N_\mathrm{hs}(x) \rangle = p_0 x^{p_1} (1 + p_2 \sqrt{x}), \tag{1.43}$$

where the parameter values are taken from [75].

For a comparison with the results presented in Chap. 4, the model denoted as GG-HS, based on the Glauber-Gribov method with subnucleonic hot spots, was selected. The photon fluxes used to compute the UPC cross section are taken from the $\mathbf{n^O_O n}$ model.

Chapter 2

ALICE in Run 2

This chapter serves as an introduction to key components of the ALICE (A Large Ion Collider Experiment) detector during the LHC (Large Hadron Collider) Run 2 (2015-2018) that are integral to the analysis presented in Chap. 4, for more details see [79, 80].

ALICE is a general-purpose heavy-ion detector situated at the LHC facility at CERN. The construction and operation of the detector are overseen by the ALICE collaboration, a collective of 2000 members originating from 172 institutes spanning 46 countries.

The collaboration focuses on studying the strong interaction sector of the Standard Model. Its primary objective is to investigate the properties of strongly interacting matter and the quark-gluon plasma formed in high-energy and high-density nucleus-nucleus collisions. The detector allows for a comprehensive analysis of hadrons, electrons, muons, and photons produced in heavy-ion collisions with high multiplicities.

ALICE has a substantial size of $16 \times 16 \times 26$ m^3 and weighs approximately 10 000 t. Its design comprises a central barrel region and a forward muon spectrometer. The central part covers a wide range of polar angles from 45° to 135° and features various detector systems, including Inner Tracking System (ITS), Time-Projection Chamber (TPC), and particle identification arrays such as Time-of-Flight (TOF) detector. The forward muon arm covers angles from 2° to 9° and incorporates absorbers, a large dipole magnet, and tracking and triggering chambers. Other detectors, such as Zero-Degree Calorimeter (ZDC), AD, and V0, are strategically placed at small angles for event characterization and triggering purposes. The schema of the ALICE detector with all of its subdetectors is depicted in Fig. 2.1.

The detector's tracking system utilizes three-dimensional hit information and a moderate magnetic field of 0.5 T. It also incorporates multiple particle identification techniques, including specific ionization energy loss, time-of-flight, muon filters, and topological reconstruction. It utilizes selective triggers and a high-bandwidth Data

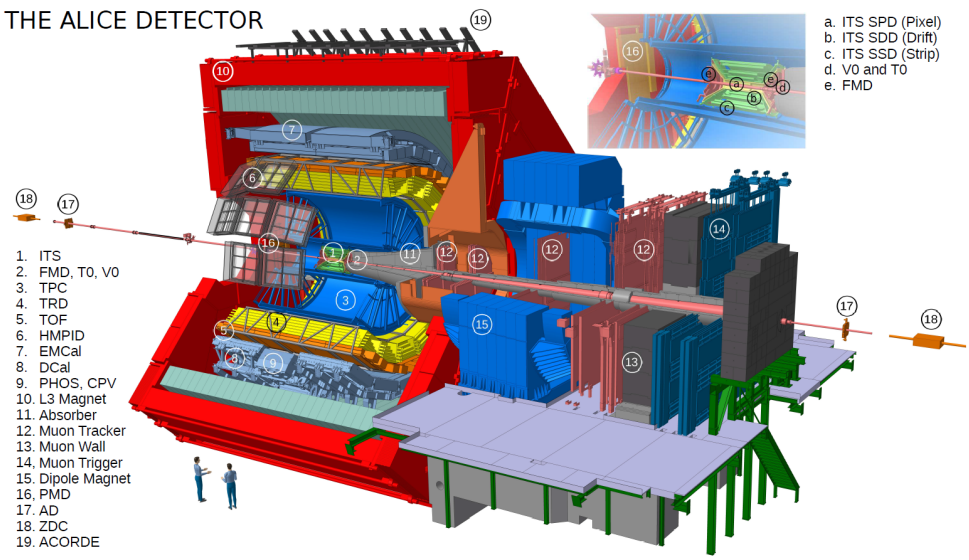

Figure 2.1: Schema of the ALICE detector during Run 2 with a description of its subdetectors. Taken from [81].

Acquisition (DAQ) system to capture rare signals and collect a significant number of events during LHC's ion operation periods.

2.1 ITS

The Inner Tracking System [82] has several key tasks within the ALICE experiment. These include precise localization of the primary vertex, reconstruction of secondary vertices from particle decays, tracking and identification of low-momentum particles, improved momentum and angle resolution for particles detected by the TPC, and reconstruction of particles passing through inactive regions of the TPC. The ITS consists of six cylindrical layers of silicon detectors surrounding the beam pipe, covering a rapidity range of $|\eta| < 0.9$. A schematic layout of the detector can be seen in Fig. 2.2 (top). The layer configuration was optimized to facilitate efficient track finding and high impact-parameter resolution. The innermost two layers utilize Silicon Pixel Detectors (SPD), which can be seen in Fig. 2.2 (bottom), followed by two layers with Silicon Drift Detectors (SDD), and the outermost layers employ double-sided Silicon micro-Strip Detectors (SSD). The outer layers also feature analogue readout for particle identification via ionization-loss measurement (dE/dx).

To achieve the required impact-parameter resolution and handle the expected particle density in heavy-ion collisions, the ITS detector was designed with minimum material thickness (effective thickness corresponding to 0.4% of radiation length (X_0)) and effective coverage of the solid angle. The cooling system for the outer layers ensures temperature stability and uniformity. The ITS demonstrates excellent momentum resolution, with better than 2% resolution achieved for pions in the transverse momentum range of 100 MeV/c to 3 GeV/c. The ITS detector

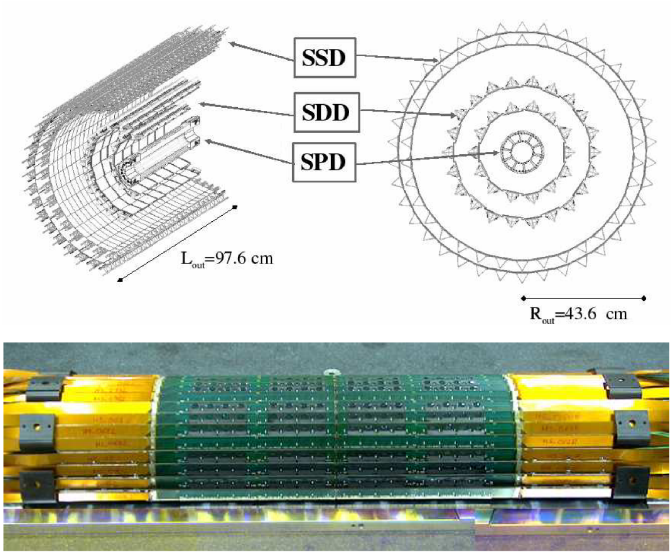

Figure 2.2: Schema of the ITS detectors (top) and a photo of the SPD half barrel (bottom). Taken from [79].

offers spatial resolutions on the order of tens of micrometers, enabling accurate impact-parameter measurements, particularly for heavy-flavored particle detection. Radiation hardness testing was conducted on all ITS components, ensuring resilience to expected radiation doses throughout the experiment's lifetime.

2.2 TPC

The Time-Projection Chamber [83] is the primary tracking detector in the central barrel, optimized for accurate momentum measurements, particle identification, and vertex determination. Its coverage extends up to $|\eta| = 0.9$ in pseudo-rapidity for tracks with full radial track length, and up to $|\eta| = 1.5$ for reduced track length. The TPC covers the full azimuthal range with a wide p_{T} range from 0.1 GeV/c to 100 GeV/c. The design of the TPC was driven by an assumed extreme charge particle multiplicity density of $\mathrm{d}N_{\mathrm{ch}}/\mathrm{d}\eta = 8000$, resulting in unprecedented track density. The TPC design was optimized to achieve maximum occupancies of approximately 40% at the innermost radius and 15% at the outermost radius.

The TPC's structure consists of a cylindrical field cage that is filled with 90 m^3 of $\mathrm{Ne/CO_2/N_2}$ gas. The detector has an inner radius of approximately 85 cm, an outer radius of around 250 cm, and a length of 500 cm along the beam direction. A schematic layout of the TPC detector is depicted in Fig. 2.3 (left), while a photograph of the fully assembled TPC above ground is shown in Fig. 2.3 (right). The transportation of primary electrons occurs over a maximum distance of 2.5 m on both sides from the central electrode, extending towards the end plates. At each end

plate, 18 trapezoidal sectors house multi-wire proportional chambers with cathode pad readout.

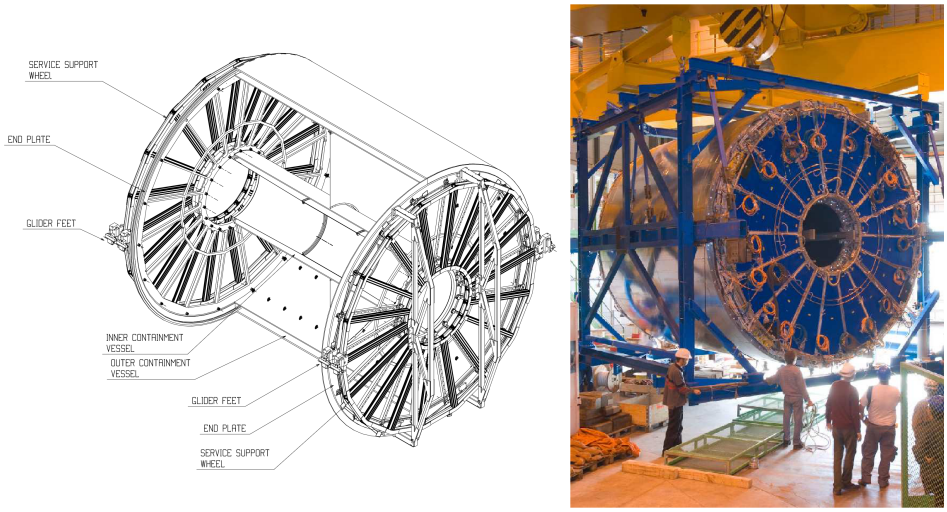

Figure 2.3: Schema (left) of the TPC field cage and service support wheels (without readout chambers). The support rods and Mylar strips are omitted in this visualization. Photo of TPC as assembled above ground (right). Taken from [79].

2.3 TOF

The Time-Of-Flight detector [84] covers $|\eta| < 0.9$ in the central pseudo-rapidity region and is primarily used for particle identification (PID) in the intermediate momentum range. The TOF detector is capable of identifying pions and kaons with momenta below approximately 2.5 GeV/c, and protons up to 4 GeV/c, achieving a separation better than 3σ for π/K and K/p pairs.

To meet the requirements of efficient operation and low occupancy, the TOF detector employs the Multi-gap Resistive-Plate Chamber (MRPC) technology (see Fig. 2.4 (right)). The MRPC chambers operate at atmospheric pressure and provide a high and uniform electric field throughout the detector's sensitive gaseous volume, enabling immediate gas avalanche generation upon ionization by charged particles. This eliminates the need for electron drift time and results in excellent intrinsic time resolution, typically better than 40 ps.

The TOF detector consists of 90 modules arranged in a cylindrical shell (internal radius of 370 cm and and external one of 399 cm) with 18 sectors in ϕ and 5 segments in z direction (see Fig. 2.4 (left)). Each module contains MRPC strips arranged in a tilted geometry to minimize the transversal path of incident particles. The angle of the strips progressively increases from 0° in the central part ($\theta = 90°$) to 45° in the extreme part of the external module ($\theta = 45°$), reducing the sharing effect of signals among adjacent pads. The strips are overlapped inside the modules, eliminating dead

zones and creating a full active area. The modules are enclosed in gas-tight boxes supported by an aluminum-honeycomb plate that provides mechanical stiffness.

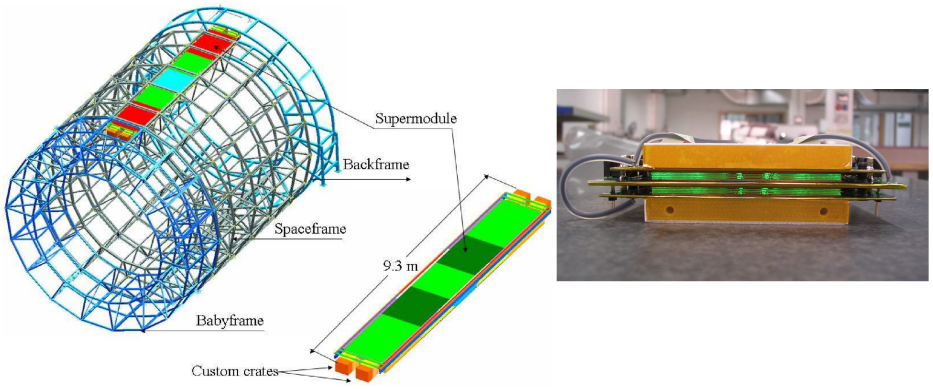

Figure 2.4: Schematic layout of a TOF supermodule within the ALICE spaceframe (left). The supermodule is composed of five individual modules. Photo of a 10-gap double-stack MRPC strip (right). Taken from [79].

2.4 Muon Spectrometer

The forward-rapidity Muon Spectrometer [85] of ALICE has a pseudorapidity acceptance of $-4.0 < \eta < -2.5$ and full coverage in azimuthal angle. It consists of absorbers, tracking chambers with a dipole magnet and triggering chambers. These components are depicted in the longitudinal layout of the detector which can be seen in Fig. 2.5.

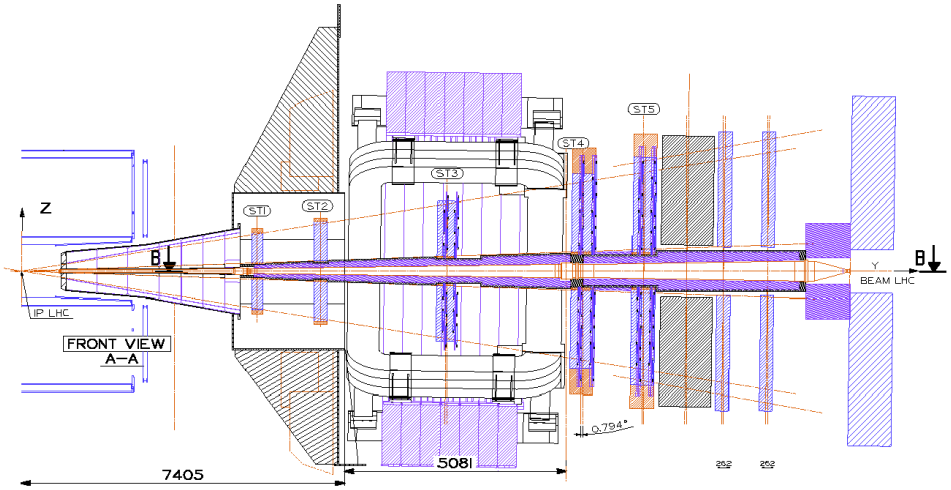

Figure 2.5: Schema of the longitudinal cross section of the forward muon spectrometer. Taken from [79].

2.4.1 Absorbers

To stop the charged particles produced in heavy ions collisions, except muons, before the tracking chambers, there is a carbon and concrete composite absorber located in front of the first tracking station. The absorber is 4.13 m long which corresponds to approximately 10 interactions lengths (λ_{int}) and approximately 60 radiation lengths (X_0).

To protect the spectrometer chambers from background coming from the beam interactions with residual gas in the beam line, there is a tubular absorber around the beam pipe. It has a conical geometry and it is made out of tungsten, lead and stainless steel.

Finally, before the trigger chambers there is an additional 1.2 m long muon filter made out of iron. This corresponds to approximately 7.2 λ_{int}. Together, the front absorber and the muon filter stop any muons with momentum smaller than 4 GeV/c from reaching the trigger chambers.

2.4.2 Tracking chambers

The muons which pass the front absorber are detected in five stations of cathode strip tracking chambers. The space resolution of the tracking chambers is 100 μm. Each chamber is composed of two planes of strips to provide two-dimensional hit information. To minimize the multiple scattering effects, the material of the chambers and its thickness were selected so that the radiation length is approximately 0.03 X_0.

The first two tracking stations adapt a quadrant structure with readout electronics located on the surface of the strips. The smallest of them, located on the first station, have the dimensions of 4.2×6.3 mm^2.

The rest of the tracking stations do not require such fine granularity so they have a slat architecture where the readout electronic is located on the sides of the strips. The largest of them have dimensions of 40×280 cm^2. The third tracking station is located inside a 0.67 T dipole magnet to enable momentum measurement with the Muon Spectrometer.

2.4.3 Trigger chambers

To suppress the background of low p_{T} muons coming from pion and kaon decays and trigger only events with high p_{T} muons coming from heavy quarkonia decays, there is a muon trigger capable of triggering on the muon track p_{T}. The p_{T} threshold for the trigger can be set in the range of 0.5 GeV/c to 2 GeV/c. This is achieved with a position-sensitive trigger detector.

The spatial resolution of the detector is less than 1 cm. It is composed of four planes of Resistive Plate Chambers (RPCs) grouped in two stations located behind

the muon filter. Each plane of the muon trigger consists of 18 RPCs modules with approximate size of 70×300 cm^2.

2.5 V0

At forward rapidity, close to the LHC beam pipe, there are located two sets of scintillator counters of the V0 detector [86] with stations on both sides from the interaction point. These stations are called V0C and V0A and their photos can be seen in Fig. 2.6.

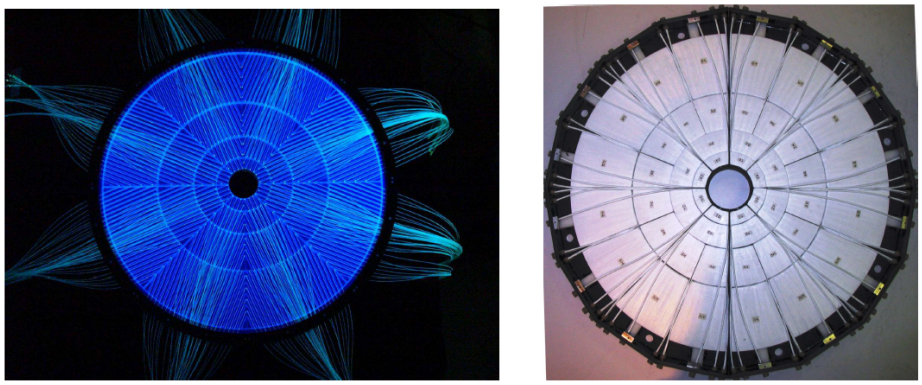

Figure 2.6: Photo of the V0A detector station (left) and photo of the V0C detector stations (right). Taken from [79].

The V0A detector is located 340 cm from the interaction point on the opposite side from the Muon Spectrometer. It covers $2.8 < \eta < 5.1$ in pseudorapidity. The scintillating material used to construct the detector is 2.5 cm thick and its transverse face is embedded with 1 mm radius Wavelength Shifting (WLS) fibers in 1 cm intervals. The detector consists of 32 scintillator counter elements organized in 4 concentric rings and 8 symmetric sectors. The signal from the WLS fibers is read out directly by photomultipliers (PMTs) which are arranged in groups of 4 on the V0A support structure.

The V0C detector is located 90 cm from the interaction point on the same side as the Muon Spectrometer. It covers $-3.7 < \eta < -1.7$ in pseudorapidity and it is mounted directly on the face of the front muon absorber. The scintillating material for the V0C station is 2.0 cm thick with the WLS fibers glued to the radial edges of its segments. The V0C is composed of 48 segments organized in 2 inner rings with 8 cells and 2 outer rings with 16 cells. The signal from the WLS fibers is transferred via 3.22 m long optical fibers to the PMTs which are mounted in groups of 8 on the sides of the front muon absorber.

The V0 detector serves as a trigger for minimum-bias events. It also serves as an estimator of centrality of the collisions via multiplicity measurement. In addition, it is used for luminosity measurement. In UPCs it serves as a trigger veto to ensure exclusivity of the measured events.

2.6 AD

The ALICE Diffractive detector [87] (see Fig. 2.7) consists of two stations constructed from scintillation plastic and installed in the forward region. The first station, located at a distance of 17 meters from the interaction point on the A side, covers the pseudo-rapidity range $4.7 < \eta < 6.3$. The second station, situated at 19.5 meters from the interaction point on the C side, covers the range $-6.9 < \eta < -4.9$. These detectors are designed to enhance ALICE's sensitivity to diffractive masses, enabling the detection of particles close to the diffraction threshold of 1.08 GeV/c, which corresponds to the sum of the proton and pion masses.

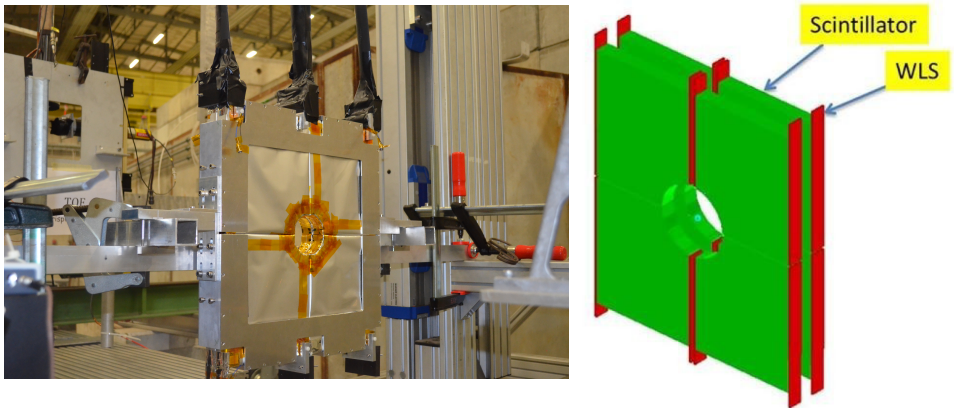

Figure 2.7: Schema (right) of the AD detector module. Photo of the assembled AD module (left). Taken from [88].

Each AD detector consists of eight scintillation plastic cells, measuring approximately 22×22 cm^2 and 2.5 cm in thickness. The cells are arranged in two layers around the beam pipe. The scintillation plastic, BC404, emits light when particles pass through it, and this light is collected by Wave Length Shifting (WLS) bars attached to two sides of each cell. The collected light is then transmitted to photomultiplier tubes (PMTs) via bundles of 96 transparent optical fibers per bar. Hamamatsu R5946 fine mesh PMTs are used to convert the light into electric pulses. The PMT signals are processed by an electronic card, which generates two signals. The first signal, amplified by a factor of 10 and clamped at approximately 300 mV, is used for timing measurement. The second signal, the direct signal, is utilized for charge integration. The electronics, including the PMTs and electronic card, are located several meters away from the detectors, near the Front End Readout electronics. The Front End Electronics, which is the same as the one used in the V0 detector, provides signals for the level 0 trigger of ALICE.

2.7 ZDC

The Zero-Degree Calorimeter [89, 90] is a quartz-fiber sampling calorimeter designed to measure particles along the beam direction. It consists of two stations located 112.5 m from the interaction point on opposite sides. Each station contains a neutron calorimeter (ZN) and a proton calorimeter (ZP). The ZN is located at 0 degrees with respect to the LHC beam axis while the ZP is located on the outside of the beam pipe with the beam outgoing from ALICE. The schema of the ZN and ZP detectors as they are located around the beam pipe together with a photo of their placement can be seen in Fig. 2.8.

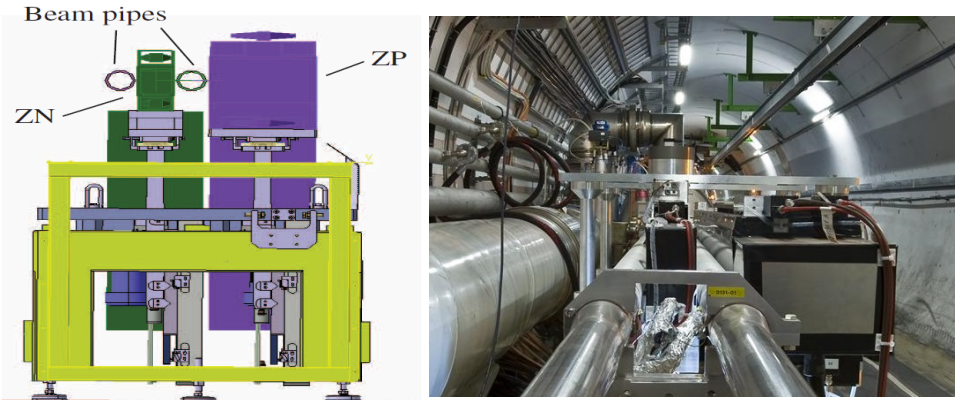

Figure 2.8: Schema of the ZN and ZP detectors as they are located around the LHC beam pipes (left) and a photo of the real detector placement (right). Taken from [79, 91].

Due to space constrains between the LHC beam pipes, the passive material used for the ZN detector is a dense tungsten alloy selected to contain most of the showers produced by the incoming particles. The dimensions of the ZN are 7.04 $\times$ 7.04 $\times$ 100 cm^3. The ZP is adjacent to the beam pipe outgoing from ALICE where the space constraints are not so stringent. The forward emitted protons are deflected in the direction of the ZN by a dipole magnet of the LHC. As the protons have a wider spacial distributions than the neutrons the ZN has dimensions of 12 $\times$ 22.4 $\times$ 150 cm^3 and it is made out of brass.

The tungsten alloy and the brass are machined into plates with grooves in the direction of the beam. The active quartz fibers are then placed inside these grooves. In total there are 1936 fibers for the ZN and 1690 fibers for the ZP. They are each divided into 4 quadrants which are read out separately by 4 PMTs. In addition, there is a fifth PMT which serves as a common readout for the entire station of the ZN or ZP detector. This provides redundancy in the readout for cross checks and allows the ZDC to access also spatial information.

Both the ZN and ZP detectors are located on moving platforms which enable to move them out of the beam plane when they are not being used. This improves their lifetime as they are operated in very hard radiation conditions.

The ZDC is used as a trigger and for luminosity measurement. However, in the analysis described in Chap. 4 the ZN plays a different role. As it allows to measure the neutrons emitted in an EMD, the signals from the ZN on the A and C side of ALICE are the selection criteria for categorizing the measured events into neutron emission classes.

The hadronic calorimeters are complemented by 2 electromagnetic calorimeters (ZEMs) which are placed 7.35 m from the interaction point on the side opposite from the Muon Spectrometer. The ZEM has a pseudorapidity coverage of $4.8 < \eta < 5.7$.

2.8 Trigger and DAQ

The ALICE Central Trigger Processor (CTP) is a crucial component responsible for event selection based on various physics requirements and the limitations imposed by the Data Acquisition system and High-Level Trigger (HLT). The main challenge of the ALICE trigger system is to effectively utilize the individual detectors, which have different busy periods following a valid trigger, and to optimize trigger selections for different running modes such as ion (Pb–Pb and lighter species), pA, and pp collisions, which exhibit counting rates varying by nearly two orders of magnitude. The trigger system operates in multiple levels, with Level 0 (L0) and Level 1 (L1) signals providing fast responses to the detectors at 1.2 μs and 6.5 μs, respectively. The trigger decisions are made within 100 ns, while the remaining latency arises from trigger input signal generation and cable delays. Additionally, the ALICE trigger incorporates "past-future protection" to ensure the exclusivity of events containing more than one central collision, with a Level 2 (L2) trigger verifying event eligibility after an 88 μs interval.

The ALICE trigger system consists of seven types of 6U VME boards housed in a single VME crate. These boards, together with the Local Trigger Unit (LTU), distribute trigger signals to the detectors and can also be decoupled from the CTP to emulate a signals for testing purposes. Given the number of trigger inputs and classes required for ALICE (24 L0 inputs, 24 L1 inputs, 12 L2 inputs, and 50 trigger classes), the trigger logic employs a three-state approach involving the states of inputs (asserted, negated, not relevant) connected via logical AND gates. Negated inputs are limited to six out of the fifty trigger classes, while the rest allow only the asserted and not relevant requirements. Specifically, the definition of an interaction, which forms the basis of the minimum bias trigger, necessitates an OR combination of different detector inputs due to lower trigger efficiencies in pp interactions. Four specific L0 inputs are selected for this purpose, enabling the application of arbitrary logic using a look-up table.

The ALICE experiment encompasses various physics observables and beam conditions, resulting in a wide range of trigger classes. Some triggers, such as central, semi-central, and minimum bias triggers, are frequent and heavily utilize the data acquisition system's bandwidth. In contrast, rare triggers like dimuon or dielectron events require less bandwidth but are limited by detector livetime and

luminosity. To ensure efficient data taking, the ALICE Trigger, DAQ, and HLT systems are designed to select interesting physics events, provide access for high-level trigger algorithms, and archive data for subsequent analysis. The systems aim to allocate trigger and DAQ resources equitably based on the DAQ bandwidth for frequent triggers and detector livetime for rare triggers. Because different detectors have significantly varying readout times, each trigger class definition includes the list of detectors required for the trigger decision. The signals from these detectors are then read out simultaneously, and this group is referred to as a trigger cluster. The goal is to strike a balance between recording large central collision events and acquiring the maximum fraction of rare events.

The Tier-0 of the LHC Computing Grid project provides ample bandwidth for data acquisition and reconstruction. The raw data are processed on the Grid and transformed into Event Summary Data (ESD) and Analysis Object Data (AOD), which are used for physics analysis.

Chapter 3

MFT and ALICE in Run 3

This chapter briefly describes the upgrades done during the Long Shutdown 2 (LS2) in preparation for LHC Run 3 (2022-2025), for more details see Ref. [2]. A special focus is given to the MFT project and the Quality Control (QC) software where the author made significant contributions during his studies.

After the LHC Run 2 finished at the end of October 2018, ALICE entered into the LS2 period. The LS2 was originally planed to last until spring of 2021. However, due to the complications brought by the COVID-19 pandemic, the LS2 was prolonged until spring of 2022. During the LS2 the ALICE experiment aimed to enhance its capabilities to study the quark-gluon plasma with heavy-flavor quarks and enable new measurements of thermal emission using dielectron pairs. Additionally, the upgrade intended to improve precision in various areas, such as jet quenching phenomena, light nuclei production, momentum correlations, and collective effects in proton collisions. To achieve these goals, a two-fold approach was adopted: enhancing pointing resolution and increasing the readout rate capabilities of the entire system to collect larger data samples. The layout of the ALICE detector after the upgrades of LS2 can be seen in Fig. 3.1, this upgraded state of the detector is referred to as ALICE 2 (while the state during Runs 1 and 2 is called ALICE 1).

In Runs 1 and 2 the full ITS had a limited readout rate of 1 kHz. In the LS2 upgrade, the ITS was replaced with a new detector called ITS2, see detector layout in Fig. 3.2. The ITS2 features seven layers of ALPIDE monolithic active pixel sensors (MAPS), which improves the pointing resolution by a factor of three in the transverse direction and by a factor of six in the longitudinal direction due to its reduced weight, distance to the interaction point, and better position resolution. It is also capable of handling the hit densities resulting from Pb–Pb collisions at a 50 kHz interaction rate.

The multi-wire proportional chambers, used in the TPC during Run 2, required active gating to suppress ion backflow into the drift region. However, this limited the readout rate to approximately 700 Hz for Pb–Pb collisions. In the upgraded TPC, readout chambers based on Gas Electron Multiplier (GEM) foils are employed, reducing the ion backflow and resulting space charge in the TPC. This improvement

allows for operation with Pb–Pb interaction rates up to 50 kHz. See photo of a stack of GEMs in Fig. 3.3.

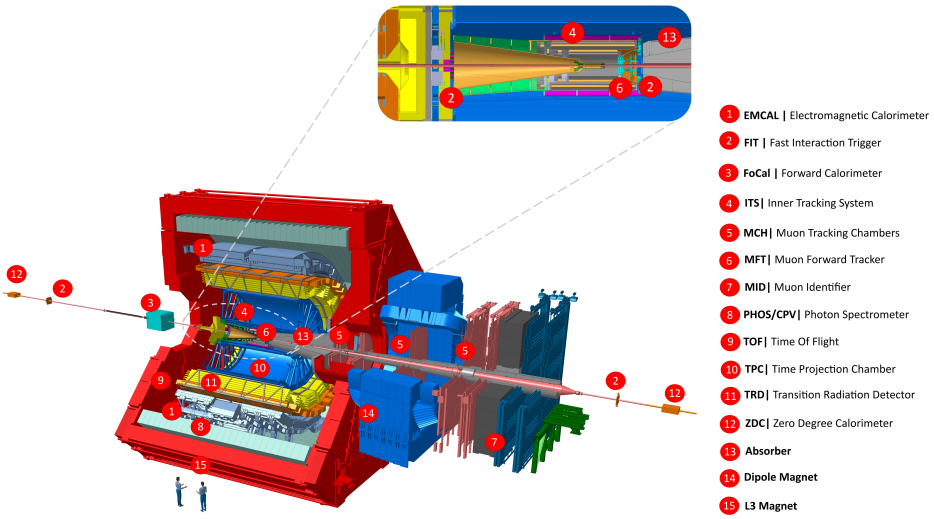

Figure 3.1: Schema of the ALICE detector during Run 3 with a description of its subdetectors. Taken from [81].

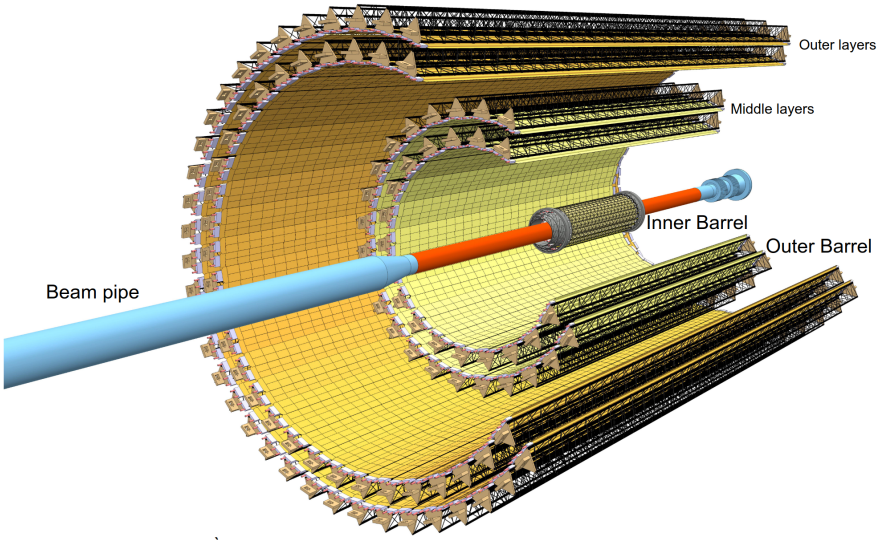

Figure 3.2: Schema of the ITS2 showing the arrangement of its components. The innermost trio of layers comprises the inner barrel, while the middle and outer layers constitute the outer barrel. Taken from [2].

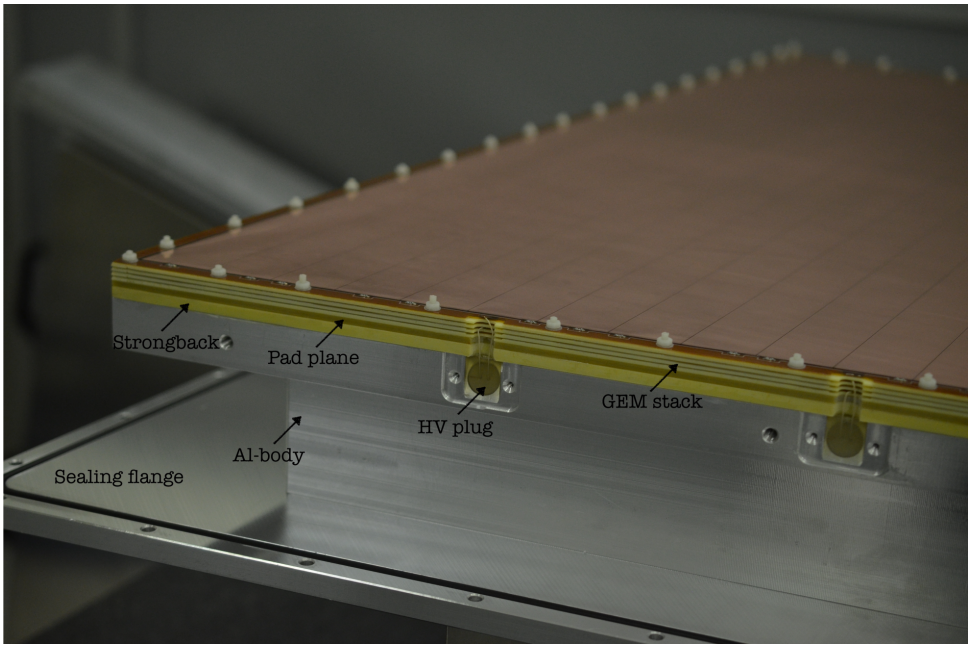

Figure 3.3: Photo showing an assembled stack of four GEMs mounted onto the chamber body, accompanied by HV wires soldered to the HV flaps of the foils. Taken from [92].

As part of the upgrade, the TOF detector underwent consolidation work on the front-end electronics, and the readout system was upgraded to handle the increased interaction rates.

The main muon detector stations employ multi-wire proportional chambers (muon tracking chambers, MCH) and resistive plate chambers (muon identifier, MID). These detectors have been equipped with new front-end electronics. A new addition to the muon detectors in ALICE 2 is the Muon Forward Tracker (MFT). The MFT consists of tracking stations with ALPIDE silicon pixel sensors installed in front of the muon absorber. The MFT improves mass resolution and pointing resolution for the detection of secondary charmonia and muons from B-meson decays.

The Fast Interaction Trigger (FIT) system (see Fig. 3.4), used for triggering, event selection, and collision time determination, consists of two arrays of fast Cherenkov radiators (FT0) and three sets of scintillator detectors. The interaction trigger is provided by the FT0 in conjunction with a large azimuthally segmented scintillator detector placed on the opposite side of the muon detectors. This scintillator detector is also used to determine the reaction-plane orientation in Pb–Pb collisions. Two additional scintillator detectors (FDD) are positioned on opposite sides of the interaction point at large distances to cover specific rapidity gaps for the selection of diffractive and ultra-peripheral collisions. The FIT detector replaces the T0, V0, and AD detectors present in the previous ALICE version, as they performed similar functions.

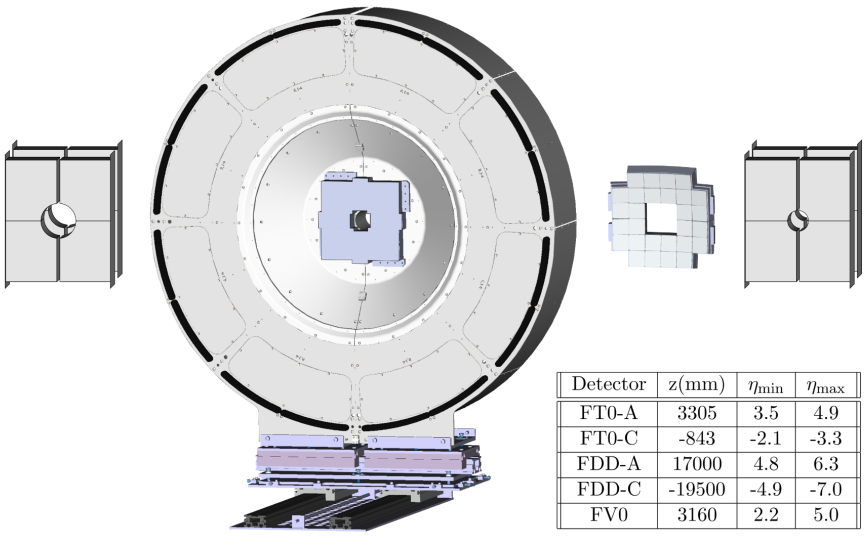

Detector	z(mm)	$\eta_{\min}$	$\eta_{\max}$
FT0-A	3305	3.5	4.9
FT0-C	-843	-2.1	-3.3
FDD-A	17000	4.8	6.3
FDD-C	-19500	-4.9	-7.0
FV0	3160	2.2	5.0

Figure 3.4: Schematic representation of the FIT detectors, highlighting the relative sizes of each component. Starting from the left side, the detectors shown are FDD-A, FT0-A, FV0, FT0-C, and FDD-C. It is worth noting that FT0-A and FV0 share a common mechanical support. In the image, FT0-A appears as a small quadrangular structure positioned at the center of the larger circular FV0 support. All detectors are planar, except for FT0-C, which exhibits a concave shape centered on the interaction point (IP). Additionally, the inset table provides information on the distance from the interaction point and the pseudorapidity coverage for each component. Taken from [2].

In the LS2 upgrade, the readout electronics of the ZDC were upgraded to match the readout rate of the rest of the system.

In order to minimize costs and data processing/storage requirements, the ALICE computing model for Runs 3 and 4 aimed to achieve maximum compression of the data volume read out from the detectors during data acquisition. The large data flow from the TPC was compressed through online track reconstruction. Furthermore, calibration data were extracted during online processing, eliminating the need for additional offline calibration passes over the entire data set.

The online data processing occurs in two steps on the ALICE online/offline facility (O^2), which consists of First Level Processors (FLPs) located in the Counting Room 1 (CR1) at the experiment access shaft receiving the raw data from the detectors via optical links and Event Processing Nodes (EPN) in dedicated computing containers located in the Counting Room 0 (CR0) on the ground level at the ALICE site. The facility provides network infrastructure for data distribution, a large disk storage capacity, and interfaces with the GRID computing network, as well as the permanent data storage at the Tier 0 computing center. An illustration of the O^2 components and the data flow among them is shown in Fig. 3.5.

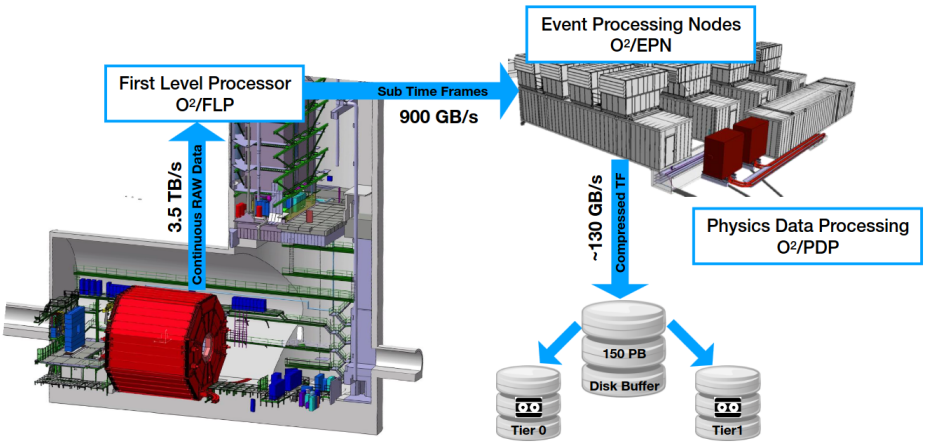

Figure 3.5: Illustration of the main components of the O^2 data readout and processing systems, as well as the primary routes through which data flow. Taken from [2].

The upgraded online system supports both continuous and triggered readout, with triggered readout used for legacy sub-systems that were not upgraded to continuous readout and for commissioning and calibration runs[1]. The data produced by the detectors are compressed, multiplexed, and transferred to the memory of the FLPs via Common Readout Units (CRU).

The ALICE data stream is divided into heartbeat frames (HBFs) with an approximate length of 88.92 μs, which is synchronized with the LHC clock and corresponds to the duration of an LHC orbit. A configurable number of HBFs form a Time Frame (TF), which serves as the data container for further processing and replaces the traditional event entity. The FLPs are responsible for the initial data compression using the zero suppression technique, achieving a compression rate of 900 GB/s. Additionally, the FLPs perform calibration tasks based on local information specific to the detectors they are connected to.

A Sub Time Frame (STF) comprises all HBFs that belong to a particular TF from a single FLP. Once all FLPs have constructed their respective STFs for an individual TF, an available EPN is selected to receive the STFs and assemble the full TF. Dedicated FLPs are assigned the tasks of collecting and processing data from the Detector Control System (DCS), as well as processing the trigger signals sent by the CTP to the detectors.

The EPN farm consists of 280 servers, each hosting 8 GPUs and 64 CPU cores, providing the necessary computational power for reconstruction, calibration extraction, and data compression. The compressed data are aggregated into compressed time frames (CTFs) and written to a disk buffer at an output rate of approximately 130 GB/s. Calibration data from EPNs are processed and stored in the condition

[1] So far, the LHC Runs (capitalized) have been discussed, referring to long periods of the LHC operation. Meanwhile, the ALICE runs (lowercase) discussed here refer to short periods of ALICE data taking under consistent experimental conditions.

and calibration database (CCDB), distributed back to the O^2 farm, and migrated to offline CCDB and GRID storage elements for ongoing reconstruction and later processing and simulation. The CTFs are transferred to the GRID for archiving.

After data acquisition and full detector calibration, multiple asynchronous reconstruction passes are performed on the GRID and EPN farm. The output of these passes are stored as Analysis Object Data (AOD), which serve as input for physics analysis. To reduce data size and facilitate specific physics analyses, events of interest can be filtered out, retaining only the minimum event information required. The processing of pp data follows a similar chain, with an additional step involving the selection of interesting collisions during asynchronous reconstruction and the retention of associated data. Reconstruction passes are followed by Monte Carlo production cycles that account for time-dependent detector conditions.

3.1 Quality Control

A crucial aspect of data processing is monitoring the quality of the generated data, which is accomplished through the Quality Control (QC) system of the O^2 framework. The QC system consists of several predefined classes with distinct roles, and they can be customized to suit the specific requirements of ALICE's subdetectors. Each detector team is responsible for developing their own QC module, which is stored in the QC GitHub repository.

The first class in the QC package is the QC Task. This class can subscribe to any available input from the detector readout chain and sample a specified percentage of the data based on given conditions. The actual transmission of data is managed by a data processor called the Dispatcher. The required data sampling conditions are specified in a configuration JSON file. If a task needs to sample the entire 100% of the data, the sampling can be omitted, and the task can connect directly to the device producing the monitored data. The QC task then performs necessary calculations or analyses to produce Monitoring Objects (MOs). These MOs are encapsulated histograms or other TObject types used to monitor the different signals from the detector. The MOs generated by the QC task are sent to the QC Database (QCDB) repository, which shares the same technology as the CCDB. In the QCDB, the MOs are stored and can be displayed using a web-based Graphical User Interface (GUI). The MOs are stored in a tree folder structure, see Fig. 3.6, but the GUI allows users to create layouts, modify the visual aspects of the TObjects, and filter the QCDB based on criteria such as the run number. Optionally, the MOs can be first passed through the QC checker.

The second class in the QC system is the QC Checker. The primary function of the QC Checker is to assess the quality of the Monitor Objects generated by the QC Task class. Checkers can receive multiple Monitor Objects from various tasks and execute the check() method to evaluate their quality. The check() function applies predefined criteria and algorithms to analyze the Monitor Objects, determining their reliability and adherence to expected standards. The checker produces a Quality

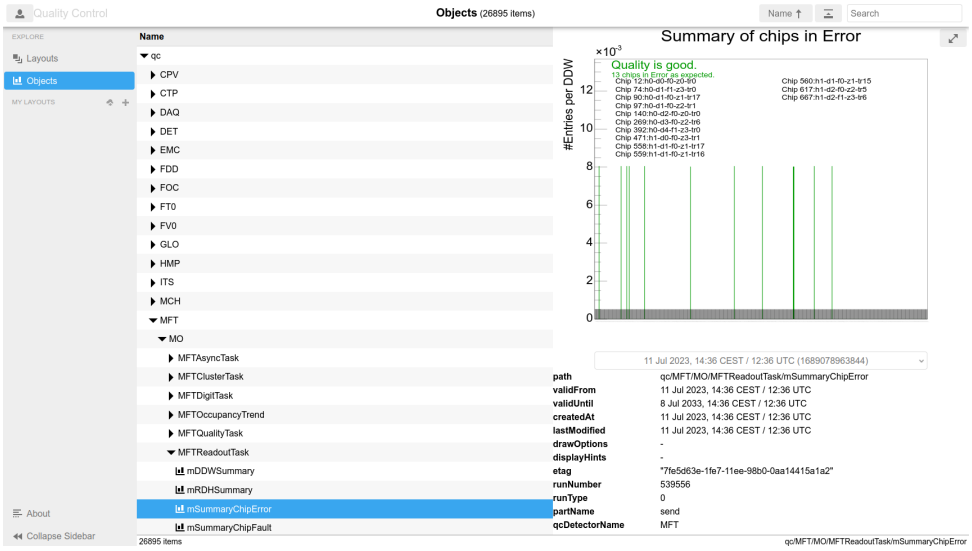

Figure 3.6: Screenshot of the QC web-based Graphical User Interface tree object structure.

Objects (QOs), which includes a decision flag: good, medium, or bad. Based on the quality flag, the QC checker can also invoke the beautify() method to modify the visual aspects of the MO. Additionally, it can display warning messages or provide additional information.

The QOs can be combined using the Aggregator class. By combining the QOs from different tasks and checks, the Aggregator class generates new QOs that provide valuable insights into the performance and behavior of the detector system as a whole. This process is particularly useful for evaluating the collective performance of multiple detectors or analyzing the data from a broader perspective. Finally, all the QOs from the checkers and aggregators are published in the QCDB.

The final class in the QC package is the Post-Processing Task. The Post-Processing Task has access to all information stored in the QCDB and can analyze the objects generated by QC tasks and checkers. It enables the correlation and trending of different properties of the detectors, providing valuable insights into their performance. Users can customize the post-processing tasks or utilize the convenience classes provided by the framework to meet specific requirements. These tasks run asynchronously to the data-taking process but can be triggered by selected events such as the start or end of a run, periodic intervals, or updates to objects in the QCDB or CCDB. Triggers and timestamps associated with events provide flexibility in accessing and processing data, enabling reruns for any run and reconstruction pass. The generated results are then stored back in the QCDB. Checks can be applied to the results of post-processing tasks to further evaluate the data. The framework's convenience classes include Trending Task, Slice Trending Task, and Quality Task, which offer pre-defined functionality for common post-processing use-cases.

In the Trending Task class, Monitor Objects from the QC database are trended over time using a TTree data structure. The class extracts characteristics of the

objects using Reductors, providing a flexible way to track and analyze data. The values are stored in the TTree, with each data source forming a separate branch. The TTree is periodically updated and stored back in the QC database, enabling continuous monitoring and analysis. See an illustration of the Trending Task class structure in Fig. 3.7.

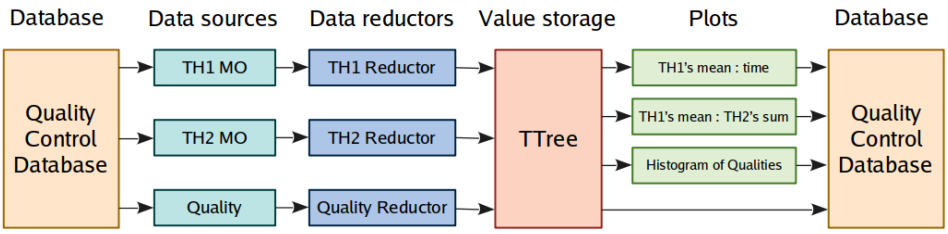

Figure 3.7: Schema of the Trending Task class architecture. Taken from [93].

The Slice Trending Task class complements the standard Trending Task and enables trending and slicing of canvas objects containing multiple histograms. It allows the division of histograms into subsections along one or two dimensions, which are trended in parallel. The class includes specific Reductors for TH1 and TH2 objects, facilitating the analysis of multi-dimensional data.

The Quality Task class focuses on trending Quality Objects stored in the QCDB, displaying their names, values, and associated messages on a canvas. It creates a 1-D distribution of quality values (Good/Medium/Bad/Null) for each Quality Object and provides an estimation of the fraction of good data for a given run. Quality Objects are fetched from the QCDB, and the canvas is updated with the current values during each trigger.

In order to execute the QC classes, a QC workflow must be created. This is achieved by utilizing configuration JSON files. These JSON files specify the QC tasks, checkers, and post-processing tasks to be included in the workflow. The configuration file also defines the inputs for each of these components, and in the case of post-processing tasks, it specifies the outputs as well. The Data Processing Layer (DPL) software framework, developed as part of the O^2 project, generates and executes the processing topology based on the user's code declarations using the JSON configuration file. The framework organizes the computational processes into units called Data Processors. These processors communicate with each other through messages. The DPL framework handles the serialization and deserialization of messages, ensuring that the data processors receive all the expected messages for a given timestamp.

QC workflows are not only utilized for the online (synchronous) monitoring of data but also play a crucial role in offline (asynchronous) data reconstruction and processing. Furthermore, QC workflows are used to monitor Monte Carlo reconstructions as well. For each of these domains separate workflows with their specifics are prepared, each having their dedicated configuration JSON files. The

design of the QC architecture, along with the physics data flow, is illustrated in Fig. 3.8.

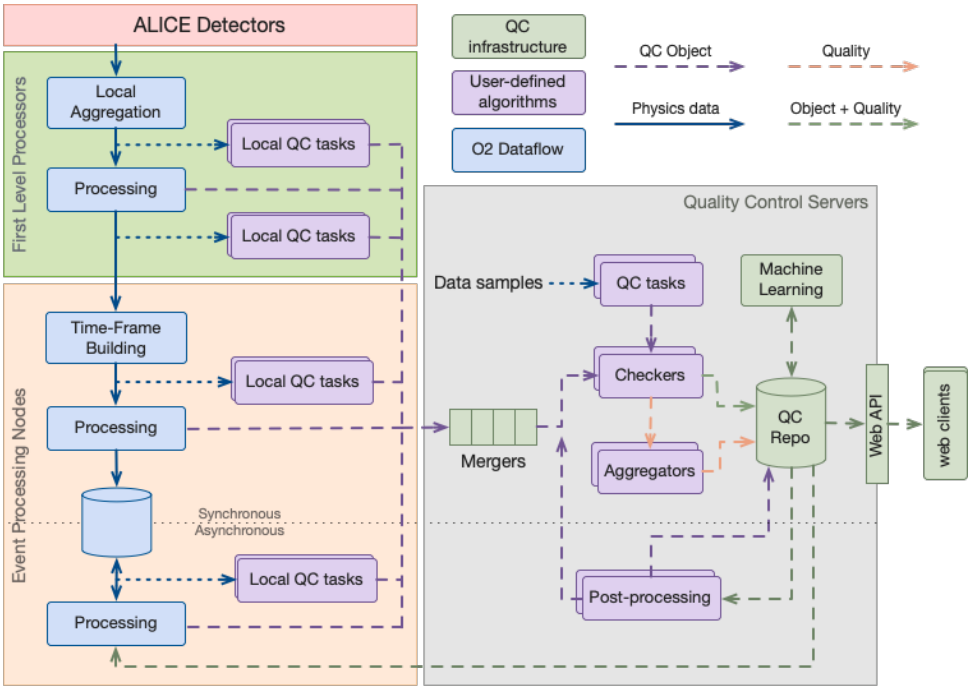

Figure 3.8: Schema of the QC workflow architecture together with the physics data flow. Taken from [93].

The detector readout electronics send data to the FLPs. These are responsible for aggregating the data from individual readout lanes into Sub Time Frames. The FLPs also have the capability for partial data processing and can be utilized to execute QC tasks. The FLP machines then transmit the data to the EPNs where the Time Frames are constructed, and additional QC tasks are performed on the data. The Monitoring Objects, obtained from either the FLPs or EPNs, are merged on the QC servers. The merged Monitoring Objects are processed by the QC checkers and stored in the QC database. The Quality Objects can be aggregated and then are stored in the QCDB as well. Additionally, the post-processing tasks run on the QC servers to further analyze the data.

3.2 MFT

The Muon Forward Tracker utilizes ALPIDE silicon pixel sensors to achieve a high spatial resolution, thereby enhancing the detection capabilities for secondary charmonia and muons originating from B-meson decays. Located in the inner barrel of the ITS and positioned ahead of the muon absorber, the MFT's precise tracking stations greatly enhance pointing resolution of the Muon Spectrometer. This enhancement enables accurate measurements of charged particle tracks within its acceptance range. For a detailed review see Ref. [94].

3.2.1 MFT Project Organization

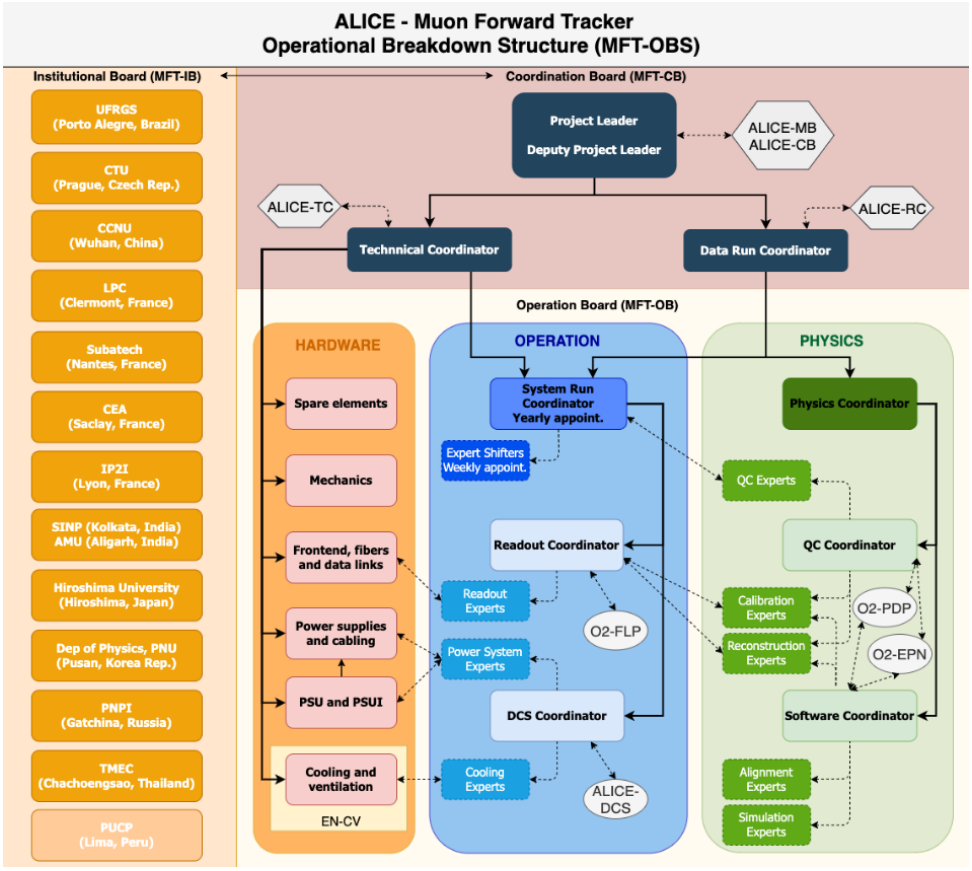

Figure 3.9: Schema of the MFT Operational Breakdown Structure. Taken from [95].

The MFT project is a collaborative effort involving 14 institutes [96] from 10 countries across Europe, Asia, and South America. These institutes constitute the MFT Institutional Board (MFT-IB), which plays a crucial role in making major decisions pertaining to the MFT project. However, the actual coordination of the project is carried out by the MFT Coordination Board (MFT-CB). The MFT-CB is led by the MFT Project Leader and the Deputy Project Leader, who represent the MFT project at the ALICE Management Board (ALICE-MB) meetings and the ALICE Collaboration Board (ALICE-CB) meetings. Additionally, the MFT-CB includes a Technical Coordinator responsible for overseeing the technical aspects of the detector and representing the project at the ALICE Technical Board (ALICE-TB) meetings. Lastly, the MFT-CB has a Data Run Coordinator who assumes the responsibility for data acquisition and analysis, acting as the main point of contact between the project and the ALICE Run Coordination (ALICE-RC). The Operational Breakdown Structure of the MFT Project is illustrated in Figure Fig. 3.9.

It is the responsibility of the MFT System Run Coordinator (MFT-SRC) to ensure the smooth operation and data acquisition of the MFT detector. The MFT-SRC oversees the training and supervision of expert MFT shifters who work on a weekly

rotation and are available 24/7 to address any issues with the MFT detector that fall outside the scope of the central ALICE shifter team. In cases where the MFT expert shifter is unable to resolve the issue independently or when the issue is severe, they contact the MFT-SRC. Therefore, the MFT-SRC must also be available round-the-clock to handle emergencies. The MFT-SRC maintains communication with the MFT-CB and collaborates with the MFT Readout, DCS, QC, and Software Coordinators. This collaboration becomes crucial when dedicated actions are required for a detector subsystem that affects the overall detector operation, such as software upgrades, hardware replacements, or bug fixes. The MFT-SRC actively participates in the ALICE Run Coordination Weekly meetings, providing updates on the detector's status when requested, and coordinating with other detector SRCs and the ALICE Run Coordination team regarding the ALICE operation program. Additionally, the MFT-SRC and the expert MFT shifters take part in the ALICE Run Coordination Daily meetings, where daily updates on ALICE operations are discussed.

The MFT Physics Coordinator assumes responsibility for the data analysis of the MFT detector and collaborates closely with the QC Coordinator and the Software Coordinator to ensure accurate data quality, calibration, reconstruction, alignment, and simulation. Furthermore, the Physics Coordinator serves as a liaison between the MFT project and the Physics Working Groups (PWGs) or Physics Analysis Groups (PAGs) within ALICE who utilize the MFT data.

Every week, the MFT Coordinators, along with the members of the MFT-CB, convene for the MFT Operation Board (MFT-OB) meeting. During this meeting, each system provides a report, updates on MFT operations are discussed, the ALICE program is presented, and the MFT planning for the upcoming week is established. In addition to the MFT-OB meeting, there are three dedicated expert meetings held weekly. The first meeting focuses on the Readout and DCS systems, the second meeting centers around Software and Physics matters, and the third meeting is dedicated to the MFT Quality Control system.

3.2.2 MFT Detector Structure

The Muon Forward Tracker (MFT) is a silicon pixel detector equipped with ALPIDE (ALice PIxel DEtector) chips [97], which are based on Monolithic Active Pixels Sensors (MAPS) [98] and implemented using a 180 nm CMOS TowerJazz [99] technology for imaging sensors. The ALPIDE chips have dimensions of 30×15 mm^2 and a thickness of 50 μm. They are composed of 512×1024 pixels, with a pixel size of 29.24×26.88 μm. The ALPIDE sensors achieve a spatial resolution of 5 μm, with a charge integration time of 30 μs. The MFT is divided into two half-cones, namely H0 (the bottom half) and H1 (the top half). Each half-cone consists of five half-disks, denoted as D0, D1, D2, D3, and D4, in order moving away from the interaction point (IP). Each half-disk has two faces: F0, which faces towards the IP, and F1, which faces away from the IP. The distances of the disks from the interaction point

are 460 mm, 493 mm, 531 mm, 687 mm, and 768 mm. A schematic representation of the MFT detector can be seen in Fig. 3.10.

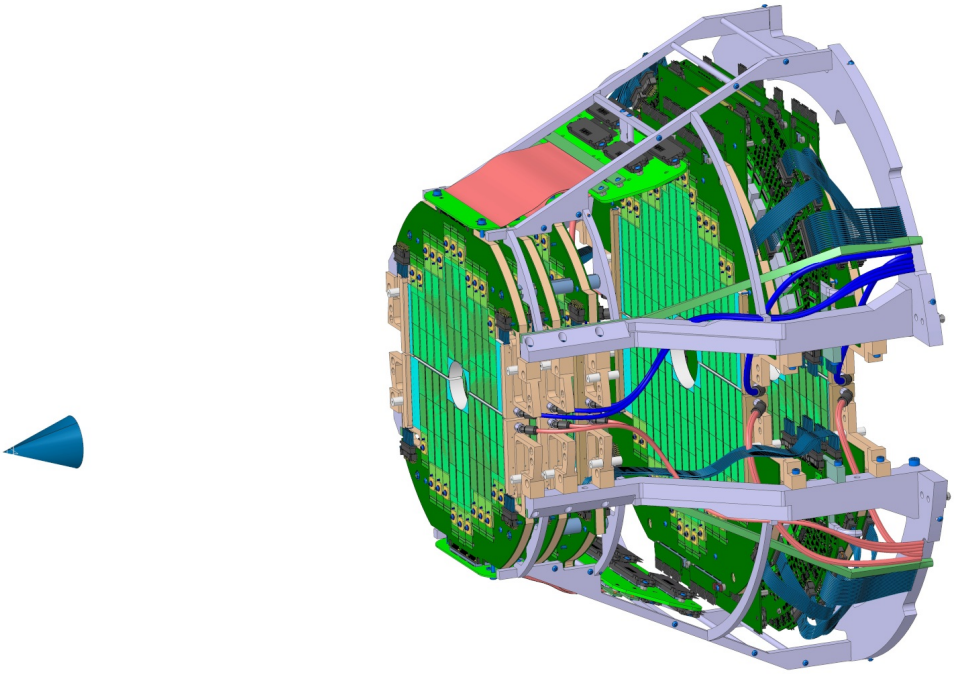

Figure 3.10: Schema of the Muon Forward Tracker showing the five disks together with the MFT support structure and cabling. Taken from [100].

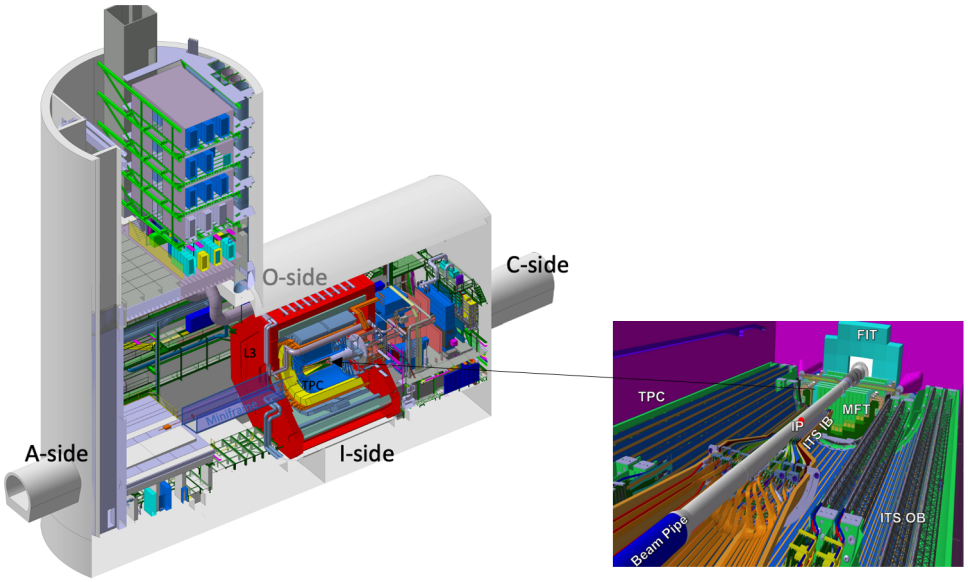

Figure 3.11: Schematic diagram of the ALICE cavern (UX25), highlighting a magnified view of the MFT's specific location. Taken from [100].

The MFT is installed within a barrel alongside the FIT FT0-C detector. This MFT barrel is positioned within the ITS Outer Barrel (ITS OB), situated between the Muon

Spectrometer absorber and the ITS Inner Barrel (ITS IB). The barrel is securely mounted to a cage that also supports the ITS detector. This cage is situated inside the TPC and is thermally shielded to maintain a stable temperature for the TPC gas filling. A schematic diagram depicting the MFT's location within the ALICE cavern is presented in Fig. 3.11. The figure also includes the ALICE reference system of directions: A-side (LHC anti-clockwise direction when viewed from above), C-side (LHC clockwise direction when viewed from above), I-side (LHC inner side), and O-side (LHC outer side).

H0	**Zone 0**		**Zone 1**		**Zone 2**		**Zone 3**	
	#lad.	#chips	#lad.	#chips	#lad.	#chips	#lad.	#chips
D0	3	8	3	9	3	9	3	7
D1	3	8	3	9	3	9	3	7
D2	3	8	3	11	3	10	4	12
D3	4	14	4	16	4	16	4	13
D4	5	19	4	17	4	18	4	14

Table 3.1: Table with the number of ladders and chips for the MFT H0 per zone. The H1 is a mirror copy of the H0 and F0 are identical to F1.

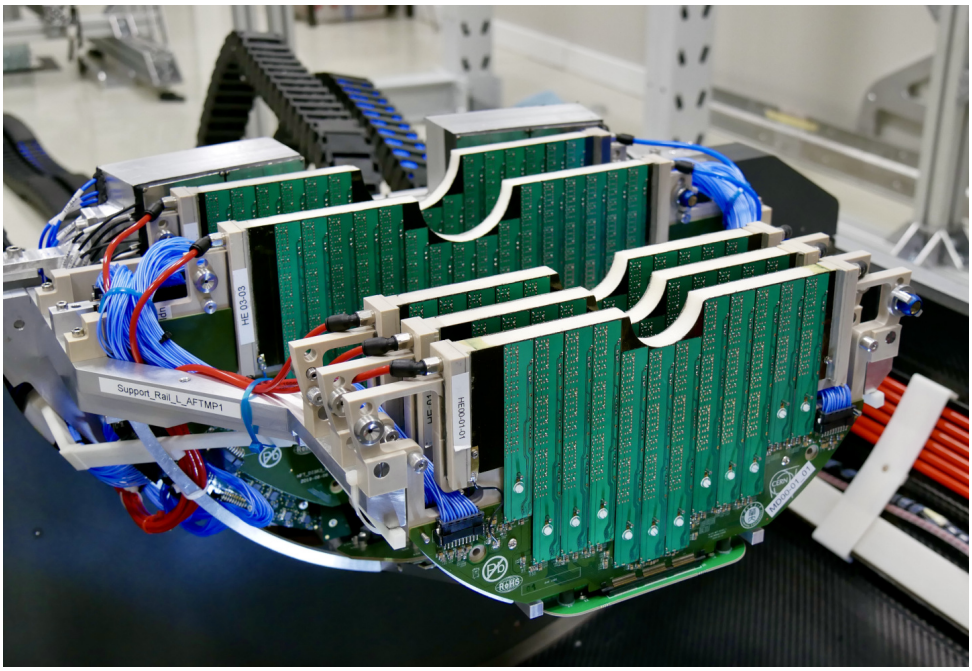

Figure 3.12: Photo of the bottom half-cone of the MFT showing the five half-disks together with the MFT support structure and cabling. Taken from [101].

The MFT has a pseudorapidity acceptance range of $-3.6 < \eta < -2.45$. The first two half-disks are identical, while the remaining three increase in size as they move farther from the interaction point. The ALPIDE chips are mounted on the half-disks in a ladder configuration. These ladders consist of flexible printed circuits (FPCs) with aluminum tracks, with the ALPIDE chips attached and wire-bonded to them. The FPCs are produced in four different sizes, ranging from 100 to 190 mm in

length, depending on the number of chips they accommodate (two to five chips per ladder). Each half-disk contains 24, 24, 26, 32, and 34 ladders, from the smallest to the largest half-disk, respectively. On each face of every half-disk, the ladders are divided into four readout zones (Z0, Z1, Z2, Z3). The distribution of chips and ladders per zone is summarized in Table Tab. 3.1. Across the entire MFT, there are a total of 280 ladders, with 936 sensors mounted on them, covering an approximate area of 0.4 m^2. The number of sensors per half-disk, from the front of the MFT, are 66, 66, 82, 118, and 136, respectively. To cool the ALPIDE sensors, a water cooling system is employed. The choice of materials for constructing the MFT was based on achieving radiation length losses of less than 0.6% per disk. A photograph of the assembled bottom half-cone of the MFT, prior to installation in the ALICE cavern, is presented in Figure Fig. 3.12.

3.2.3 MFT Detector Powering

The power supply of the MFT is ensured by CAEN crates, which are controlled via WinCC OA. A diagram illustrating the power supply architecture can be seen in Fig. 3.13. The CAEN SY4527 Universal Multichannel Power Supply System was selected for the MFT Main Frame (MF). Three Branch Controllers (BCs) A1776A are connected to the MF. One BC is used to control the power for the detector (DET), another is used to control the power for the readout units (RUs), and the third is kept as a spare.The BCs are equipped with two lines: the first line provides 48 V service power (SP), while the second line serves as the control bus (CTRL). These lines are connected to the A3486 Power Generators (PGs). The MFT, BCs, and PGs are located in Counting Room four (CR4) within the ALICE access shaft. They are connected to the CAEN Easy 3000 crates in the ALICE cavern via cables that are 90 m long for the RUs power supply and 110 m long for the detector power supply. The PGs convert three-phase AC to 48 V DC and supply the Easy crates. The Easy crates house 14 power supply boards, 12 of the A3009 type and 2 of the A3006 type. These boards provide power to the RUs and the detector Power Supply Unit (PSU).

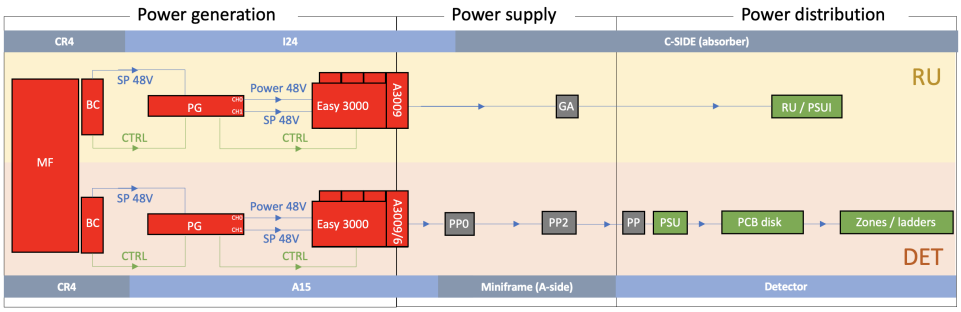

Figure 3.13: Diagram illustrating the power distribution to the detector (DET) and the readout units (RU) of the MFT system. Taken from [100].

For the RU side, there are 80 channels responsible for delivering power to the individual readout units, with one channel dedicated to each of the MFT zones. Additionally, there are 4 channels specifically designated for delivering power to the

Power Supply Unit Interface (PSUI). These cables originate from the Easy crates and reach the C-side of ALICE. At this point, a gauge adaptation (GA) of the cables is performed to reduce their size, after which they are directly connected to both the RUs and the PSUI.

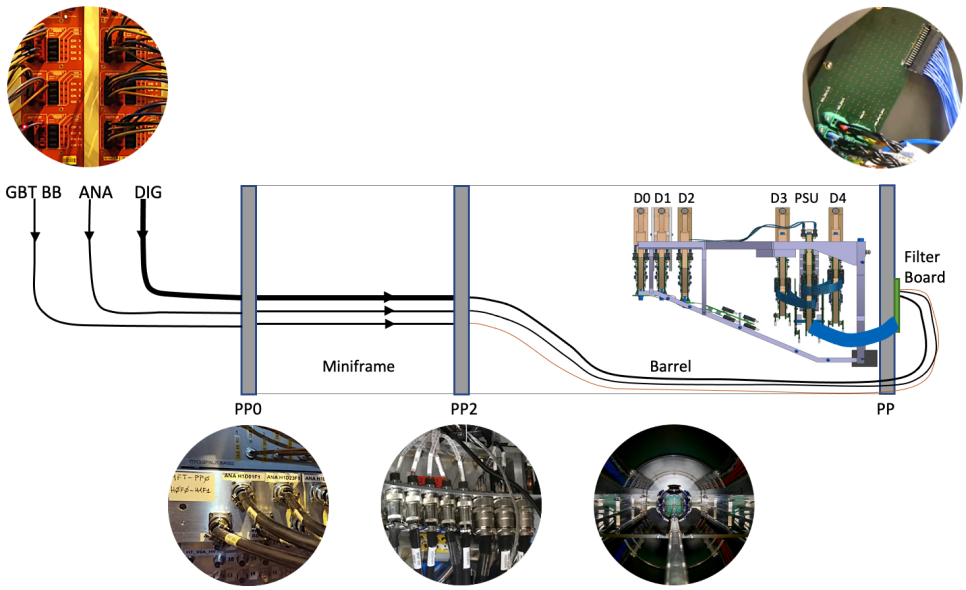

Figure 3.14: Diagram and accompanying photos depicting the power distribution going through the central barrel to the MFT. Taken from [100].

For the detector side, there are 20 channels dedicated to delivering analog power and 20 channels for delivering digital power. Each MFT disk-half-face is assigned one channel for analog power and one channel for digital power. Additionally, there are 4 channels designated for providing power to the Giga-Bit Transceiver Slow Control Adapter (GBT-SCA) [102], 4 channels for the chip Back Bias (BB) negative power, and 4 channels for the BB positive power (ground is used as the positive BB). Each MFT half-face has one channel for the GBT-SCA power, one channel for the negative BB power, and one channel for the positive BB power. This sums up to a total of 52 channels. The cables carrying these 52 channels extend from the Easy crates to the ALICE A-side. There, they are connected to the Patch Panel 0 (PP0) located within the ALICE Miniframe. From PP0, the cables traverse the Miniframe until they reach Patch Panel 2 (PP2), which is situated in front of the ALICE central detector region. At PP2, the gauge of the cables is reduced. Subsequently, the cables continue along the central barrel until they reach the MFT Patch Panel (PP). At the PP, the cables are plugged into a filter board that facilitates the reduction of multiple single cables into a few multi-threaded cables. This simplifies the cable management process and allows for the final connection to the MFT Power Supply Unit (PSU). A diagram illustrating the aforementioned connections can be found in Fig. 3.14.

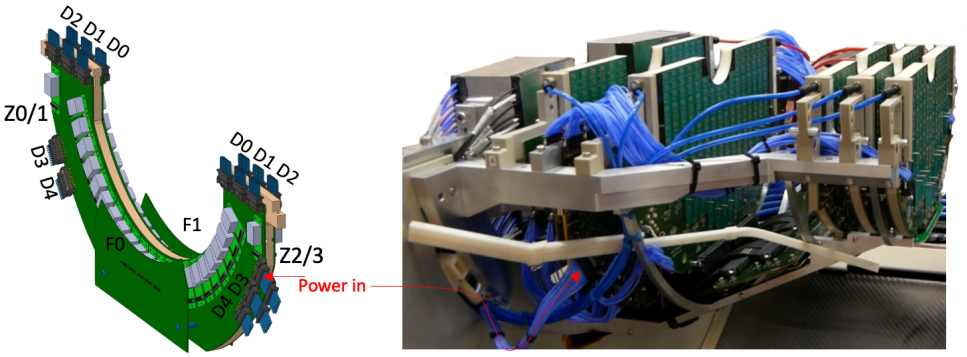

Figure 3.15: Mapping of the PSU (left) and a corresponding photo of the MFT with visible blue power cables (right). Blue cooling pipes can also be observed on top of the half-disk. Taken from [100].

Four Power Supply Units are installed inside the MFT detector, positioned between disks three and four. Each PSU has the responsibility of providing analog, digital, and back bias power to 20 zones, utilizing 24 DC-DC converters. As a protective measure for the detector, latch-up protection is implemented on all PSU outputs, enabling the power to be stopped if the current in a particular line exceeds a predefined threshold. Furthermore, a regular check is performed every 20 ms to ensure communication with the GBT-SCAs is functional. If the communication is lost for more than 5 s, all power outputs from the PSU are automatically shut down. Voltages, currents, and temperatures on the PSU are continuously monitored using a set of GBT-SCAs. Another set of GBT-SCAs is utilized for controlling the back bias voltage and the latch-up current threshold. The PSUs are affixed to a water-cooled plate to regulate their temperature. Each main PSU board is connected to a small PSU mezzanine via a 300-pin connector. The mezzanine contains five additional DC-DC converters and five GBT-SCAs for monitoring ambient temperature and humidity. A single PSU possesses one power input and 10 outputs dedicated to a specific half and face of the detector. One side of the PSU provides outputs for zones zero and one of all disks, while the other side is responsible for zones three and four. A visual representation of this arrangement can be seen in Fig. 3.15.

The ALPIDE chips within the MFT are powered by two 1.2 V lines, which respectively provide power to the analog and digital circuits of the chip. Additionally, a reverse bias voltage of up to -3 V can be applied to the chip to enhance its efficiency. This is done to cope with the efficiency degradation over the lifetime of the detector due to radiation damage. Each ladder accommodates two to five ALPIDE chips. The FPCs of the ladders serve as the common circuit to supply the chips with the required power. To minimize voltage drop across the ladder, the FPCs are constructed from aluminum, which has low electrical resistance. The number of ladders connected to a face of the MFT half-disk varies depending on the specific disk, ranging from 12 to 17 ladders. These ladders are connected to the half-disk base using a Hirose connector. A diagram illustrating this configuration can be seen in Fig. 3.16.

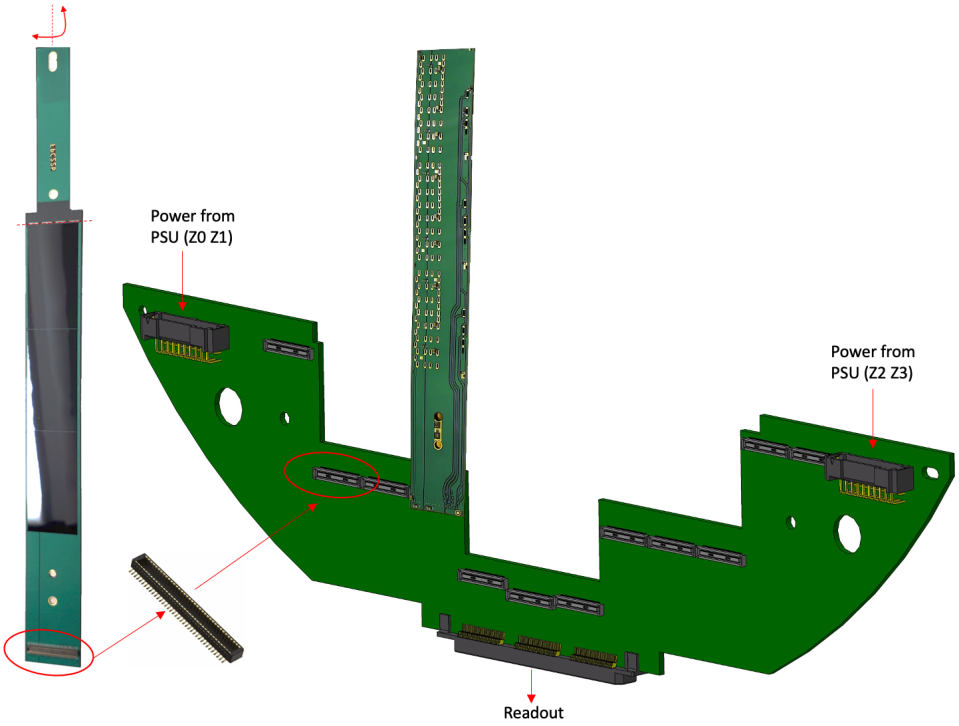

Figure 3.16: Diagram illustrating the connection of a ladder to the disk Printed Circuit Board (PCB) via the Hirose connector. The figure highlights the power input connections and readout connections on the disk Printed Circuit Board (PCB). Taken from [100].

3.2.4 MFT Detector Readout

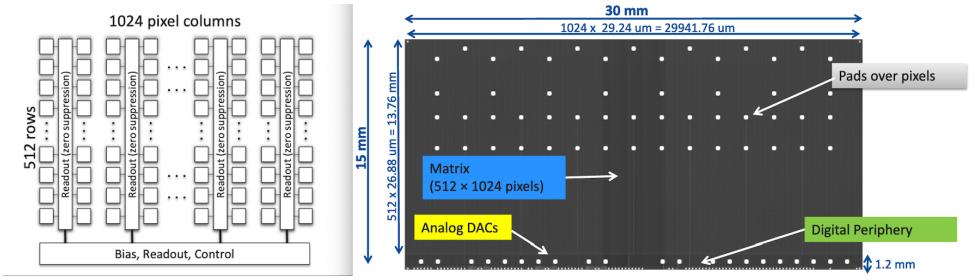

Figure 3.17: Diagram illustrating the size and architecture of the ALPIDE chip. Taken from [100].

The back bias, control, and readout components of the ALPIDE chips are situated at the chip's edge within a 1.2×30 mm^2 region. Metallic pads on the top face of the chip serve as connections. See Fig. 3.17 for a diagram illustrating the chip's architecture and size. Each pixel consists of a sensing diode, a front-end amplifying and shaping stage connected to a discriminator, and a digital section. The signal originates from the collection diode or an injection capacitor for test charge injection. Following amplification by the shaping amplifier, the signal passes through a discriminator, which applies a common threshold level to all chip pixels. The peaking time of the amplified signal is approximately 2 μs, while the duration of the discriminator

pulse ranges from 5 μs to 10 μs. The signal is then directed to a storage register within the digital section. The digital section contains a Multi Event Buffer housing three in-pixel memory cells. The latching of the discriminator signal into the memory cells is controlled by global strobe signals generated at the chip's periphery. The length of the strobe signal can be programmed, and its generation can be triggered externally or initiated by an internal sequencer. In addition to test charge injection at the input stage, a digital-only pulsing mode is available, enabling the forced writing of a logic signal to the pixel memory cell. This mode also facilitates pixel masking during data acquisition, effectively suppressing signal generation.

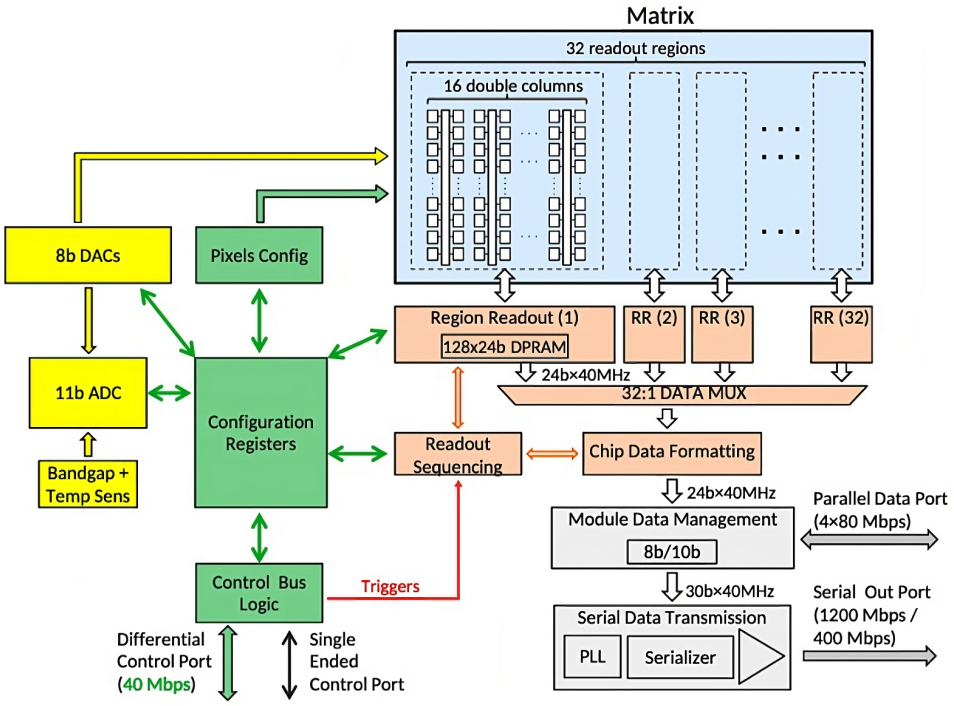

Figure 3.18: Block diagram illustrating the readout system of the ALPIDE chip. Taken from [100].

The ALPIDE readout is organized into 32 regions, each consisting of 512×32 pixels. Within each region, 16 double columns are processed by 16 Priority Encoder circuits. The chip's periphery houses 32 readout modules referred to as Region Readout Units, which oversee the readout process for a submatrix. Sequential readout takes place for the 16 Double Columns within each region, while the 32 submatrices are concurrently read out in parallel. The data from each Region Readout Unit is transferred at a rate of 40 MHz via a 128x24b Dual-Port Random Access Memory (DPRAM) and it undergoes formatting and multiplexing. The Data Transmission Unit transmits the formatted data from the chip via a 1200 Mbps serial output port. The chip's registers and pixel configuration are controlled through a 40 Mbps differential control port. A block diagram of the ALPIDE chip readout can be seen in Fig. 3.18. The ALPIDE chips can be operated in two modes: Master mode and Slave mode. In the Master mode, each chip is controlled and read out individually, while in the Slave mode, the slave chip is controlled and read out via

a daisy-chain connection to a master chip. The Slave mode is employed for the ITS2 Outer Barrel, whereas the MFT and the ITS2 Inner Barrel utilize the Master mode.

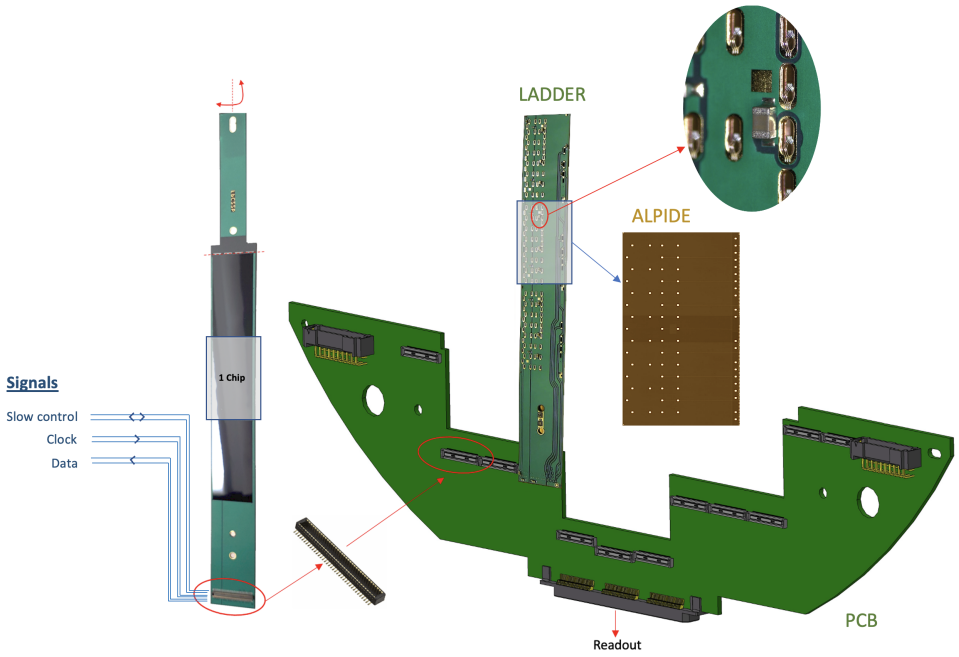

Figure 3.19: Diagram depicting the connection between the ALPIDE chip and the ladder Flexible Printed Circuit (FPC), as well as the connection of a single ladder on a disk Printed Circuit Board (PCB). Taken from [100].

The ALPIDE chips are connected to the FPC of a ladder using an ultrasonic micro-wire bonding technique. Each bond consists of three 25μm wires that are connected to a metallized pad on the FPC. For a single ALPIDE chip, there are a total of 74 pad connections on the FPC. As depicted in Fig. 3.19, the ladder facilitates the transfer of signals from the chips to the disk Printed Circuit Board (PCB) via a 70-pin connector, achieving a transmission speed of 1200 Mbps.

The connections between the PCBs of Disks 3 and 4 are directly linked to the readout units (RUs). On the other hand, Disks 0, 1, and 2 are connected to Mother Boards (MBs) through flexible SAMTEC cables. Specifically, Disk 0 is connected to MB0, Disk 1 is connected to MB1, and Disk 2 is connected to MB2. Additionally, MB0 and MB1 are connected to MB2, which further connects to the RUs. Refer to Fig. 3.20 for a photo displaying the MBs and their connections. To transmit the data recorded by the GBT-SCAs from the PSU monitoring, two connectors on the PSU mezzanine facilitate the transfer from the detector cone. The SAMTEC cables from MB2 (containing data from Disks 0, 1, and 2), Disk 3, Disk 4, and the PSU mezzanine are directed to the MFT PP. At the MFT PP, these cables are then connected to a set of 6.5 m long SAMTEC cables, which transport the data along the muon absorber. Finally, the data reaches the C-side at the end of the solenoid magnet, where the MFT RU crates are positioned, see Fig. 3.21 for a diagram of the connections.

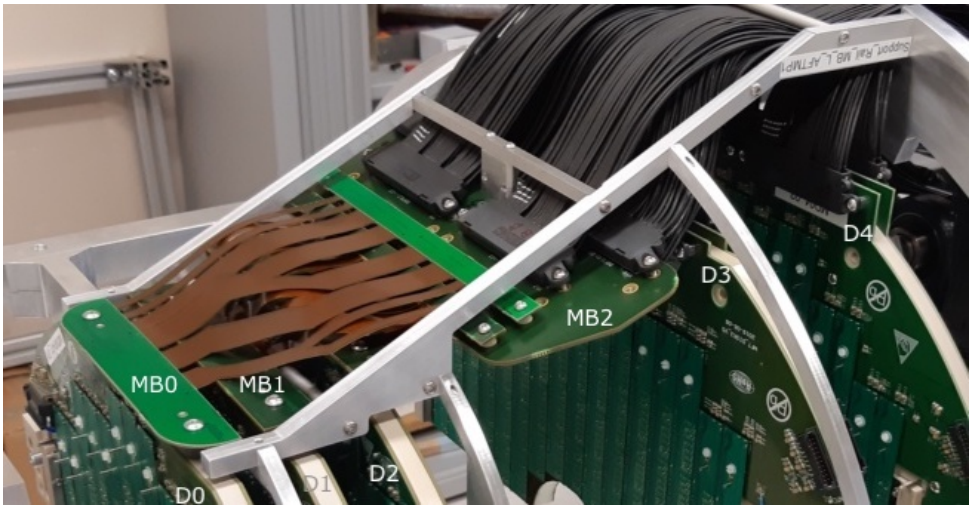

Figure 3.20: Photograph depicting the connection of the Mother Boards (MB) to the Printed Circuit Boards (PCB) of Disks 0, 1, and 2. Taken from [100].

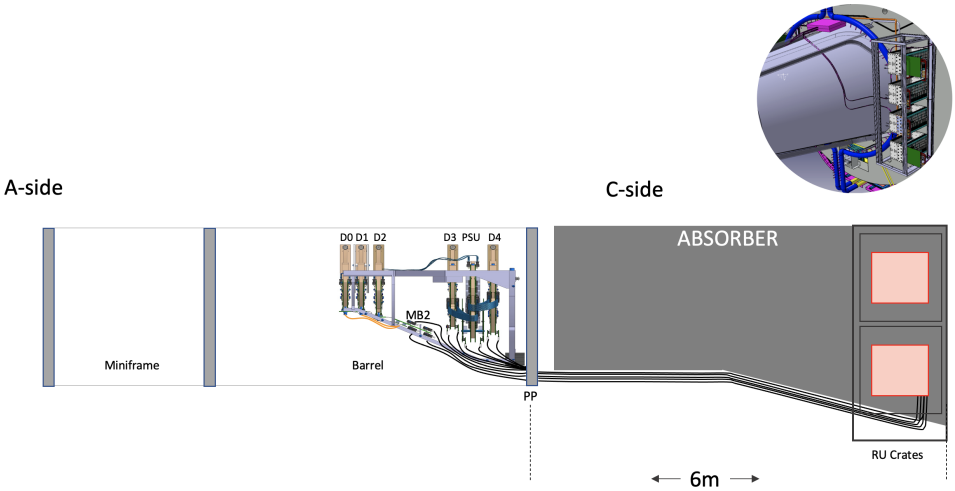

Figure 3.21: Diagram illustrating the cable routing along the absorber, connecting the detector to the readout crates located at the C-side. Taken from [100].

There are four RU crates allocated for the MFT, with each crate serving a specific quarter of the detector. On the I-side, adjacent to the absorber, there are crates for H0F0 and H1F1, while on the O-side, there are crates for H0F1 and H1F0. Each RU crate comprises 1 PSU interface, 4 dispatching boards, 20 readout units, and 2 optical splitters. The cables from the Disks are connected to the rear side of the dispatching boards. These boards effectively dispatch the signals in a manner that one connector on the front side carries signals from two ladders. A SAMTEC hydra cable, branching out from the front port, further splits the signal into two cables, each corresponding to one ladder, and they are then connected to the transceiver board of the readout unit. Consequently, each RU is responsible for receiving data from one full zone.

FLP	CRU 1	CRU 2
182	H0D0	H1D4
183	H0D1	H1D3
184	H0D2	H1D2
185	H0D3	H1D1
186	H0D4	H1D0

Table 3.2: Table showing the mapping of the half disk data readout to the different CRUs in the five FLPs of MFT.

The RU crates are connected to the detector's data readout, control, and clock lines, while also receiving trigger and control information from the ALICE CTP. The main logical chip of the RU is the Static Random-Access Memory (SRAM) Field-Programmable Gate Array (FPGA), which runs the firmware responsible for managing the data stream and readout process. Additionally, there is a secondary flash-based FPGA from the ProASIC 3 series. The simultaneous transfer of detector, timing, and trigger signals, as well as slow control and monitoring data, is efficiently handled by the radiation-tolerant GBT chip set. Within this chip set, the GBT-SCA ASIC (Application-Specific Integrated Circuit) plays a crucial role in handling the control and monitoring signals to the detector front-end electronics. For connecting to the RUs the GBT chip set employs versatile transceivers. These transceivers are radiation-resistant, magnetic field tolerant, low-power, and low-mass bidirectional digital-optical data links. Operating in either multi-mode or single-mode regimes, they use wavelengths of 850 nm and 1310 nm respectively, at rates up to 4.8 Gbit/s. Each RU contains three versatile transceivers: one versatile transceiver (VTRx) in multi-mode regime for data and slow control, one versatile twin transceiver (VTTx) for data, and one VTRx in single-mode regime for trigger signals. The control and data signals travel from the RUs via 4m long optical fibers to a terminal plate fixed on top of the muon absorber. From the terminal plate, the signals are then transmitted via 114m long optical cables to CR1, where a crate housing the five FLPs dedicated to MFT is located. Each FLP hosts two CRUs, with the mapping of the CRUs done according to Tab. 3.2 in order to balance the data load coming from different half disks of the detector. In each CRU, there are two endpoints, each receiving data from a single face of the half disk. A sixth FLP (number 202) is connected to the PSU outputs. In addition to managing the readout, the FLPs also host the ALF server, which communicates with the FRED[103] server of the DCS.

The trigger clock travels via fibers from the 10 data CRUs and 1 PSU CRU to the Passive Optical Splitter (PON). From the PON, located in CR1, the trigger signal travels through a single 145 m long fiber to the cavern under the muon spectrometer. Here, it is connected to the MFT Local Trigger Unit (LTU), which is an integral part of the CTP. From the MFT LTU 8 fibers lead to a splitter module from which a single 40 m cable with 24 fibers (only 8 are utilized) goes to the terminal plate on top of the muon absorber. At this point, another splitter module separates the signal back to 8 individual cables. Each of these fibers is then connected to an optical splitter, which further distributes the signal to the 80 RUs of MFT. A diagram illustrating the

global scheme of the data readout, slow control, and clock signal transmission can be seen in Fig. 3.22.

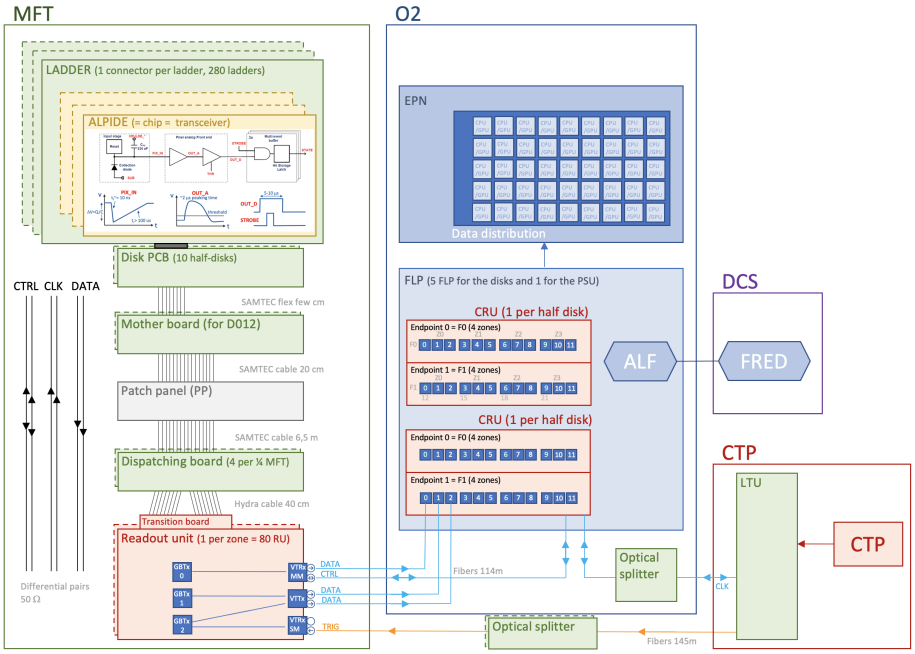

Figure 3.22: Diagram illustrating the global scheme of the MFT data readout, slow control, and clock signal transmission. Taken from [100].

3.2.5 MFT Detector Cooling

The MFT cooling operates as a leakless system, utilizing a negative differential pressure. Its primary objective is to maintain working temperatures between 17°C and 19°C by efficiently evacuating the heat produced by both the detector (382 W) and the RU crates (2500 W). The total water flow of the cooling system is approximately 3900 l/h. The system is composed of a cooling plant, 12 detector cooling loops, and 4 cooling loops dedicated to the readout crates.

The cooling plant is located on the ground floor of the ALICE cavern, see Fig. 3.23. It comprises a 340 l water reservoir, two redundant pumps, a heat exchanger, an electrical heater, a water deionizing system, and a system of sensors to monitor water flow, temperature, and pressure. From the cooling plant, there are 12 cooling loops extending to the detector, with 10 of them responsible for cooling the MFT half disks and 2 designated to cool the PSUs. Additionally, there are 4 cooling loops dedicated to cooling the RUs, with each loop connected to one readout crate. Each cooling loop consists of a pneumatic input valve, a pneumatic controlled valve (automatically adjusted to regulate the input pressure to a given set point), an input pressure sensor, an output pressure sensor, and a pneumatic output valve. However, the readout crate cooling loops lack the output pressure sensor, relying solely on

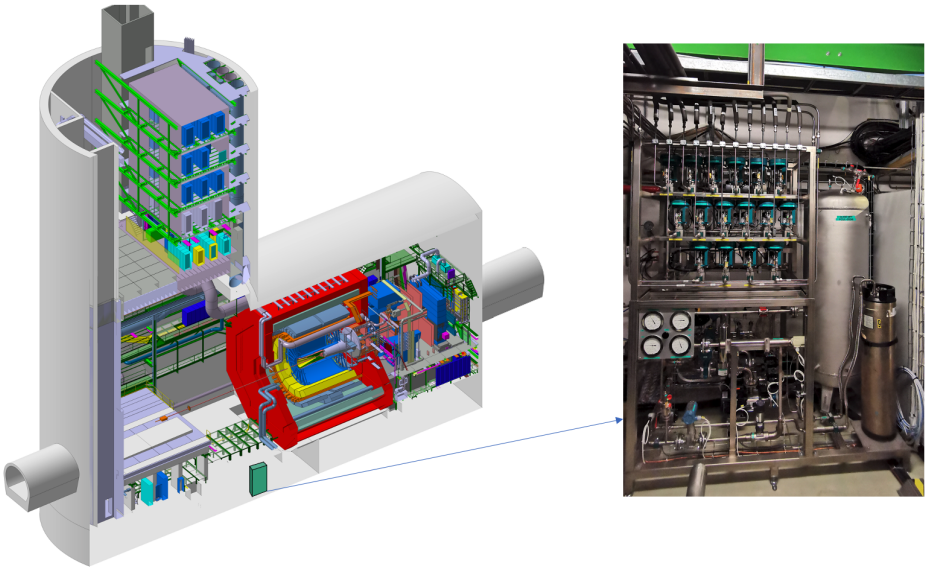

Figure 3.23: Diagram displaying the MFT cooling plant's location in the ALICE cavern along with a photograph of the cooling plant. Taken from [100].

the control of the input pressure via the pneumatic controlled valve. A simplified diagram of the cooling system is presented in Fig. 3.24.

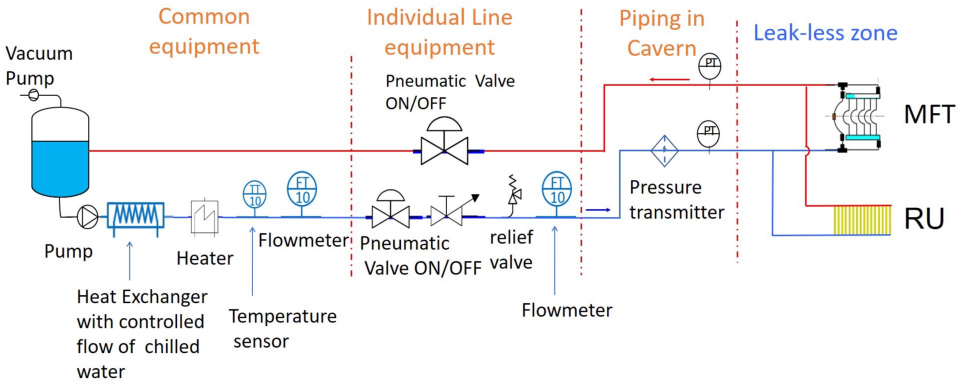

Figure 3.24: Diagram of the MFT cooling system architecture. Taken from [100].

Each cooling loop can be in one of three states:

1. **ON**: This state represents the standard operational condition, where both the input and output valves are open, and the pneumatic control valve regulates the flow of coolant.

2. **OFF**: In this state, the input valve is closed, while the output valve remains open, effectively halting the flow of coolant. However, the loop is still pumped out.

3. **LOCKED**: In the LOCKED state, both the input and output valves are closed, completely isolating the loop and ensuring a constant pressure difference.

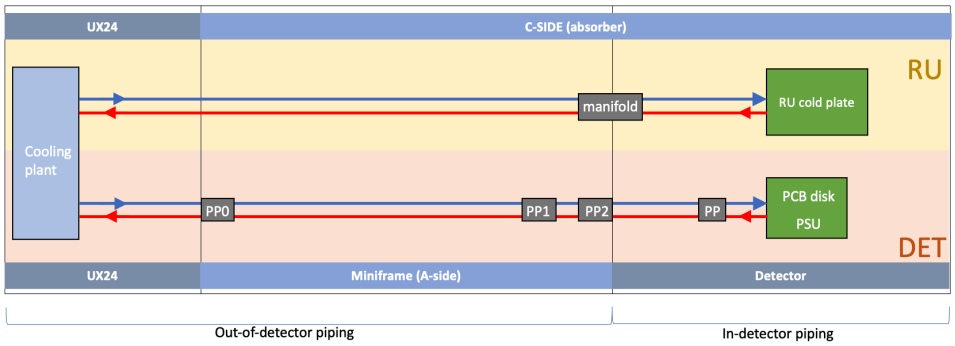

Figure 3.25: Diagram illustrating the piping scheme from the cooling plant to the detector and the readout crate loops. Taken from [100].

The piping used for the detector loops from the cooling plant is constructed using stainless steel pipes, which are further surrounded by thermal insulating foam. The piping goes through PP0 to PP1. Subsequently, the water is conveyed via flexible plastic pipes to PP2 and further directed through the central ALICE barrel to the MFT PP and the detector itself. As for the readout crate loops, stainless steel pipes are used for the piping until they reach the top of the readout crates. At this point, they are connected to flexible plastic pipes, which, in turn, link to the readout crate input manifolds. A diagram illustrating the piping scheme of the loops can be found in Fig. 3.25.

Each MFT half disk features a heat exchanger composed of a sandwich of two carbon composite cold plates with embedded polyamide pipes of 1 mm diameter, along with a Rohacell foam. Disks 0, 1, and 2 are equipped with three pipes for each face, whereas Disks 3 and 4 have four pipes for each face. Manifolds are placed at the input and output of these pipes to ensure even water distribution throughout the cooling system. For each PSU, a single stainless steel pipe with a 4 mm diameter is routed between the two faces of the PSU, positioned just below the DCDC converters on the PSU main board. Each readout crate is equipped with a manifold that distributes water to the 20 RUs at the input of their cooling plates, which are extended under the VTRx by an additional copper plate.

3.2.6 Detector operation for the MFT

The Detector Control System (DCS) provides complete control over the ALICE subdetectors. Each detector group is responsible for developing and maintaining its own DCS project, which is part of the central ALICE DCS. The MFT DCS is a distributed project that controls the CAEN power supply system, the MFT PSU, the configuration and control of the RUs and chips, and monitors the cooling plant and signals from the GBT-SCA in the detector. The DCS can be accessed only from

the CERN network by a remote connection to the DCS gateway server. From the DCS gateway, it is possible to connect to the MFT operator node remote server, where the DCS GUI can be launched. A screenshot from the main panel of the MFT DCS can be seen in Fig. 3.26.

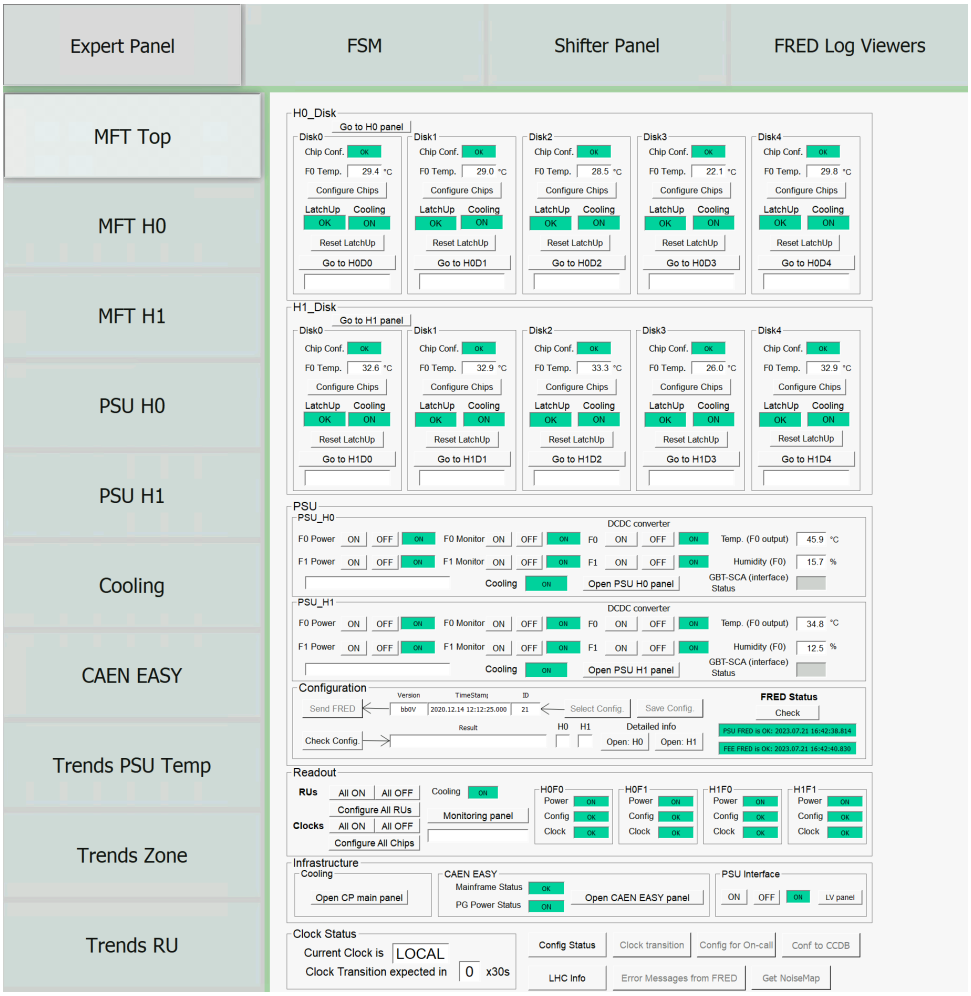

Figure 3.26: Screenshot of the MFT Top control panel from the MFT DCS GUI.

The MFT Top panel displays the status of configuration, cooling, and latch-up for each MFT half disk. The displayed status can have the values: ON, where all chips are on; OFF, where all chips are off; ERROR, when at least one chip is in error; and MIXED, where some chips are on and some chips are off. The panel also allows resetting the latch-up, configuring the chips, as well as showing the disk temperature. Additionally, the Top panel provides control and status information on the power, monitoring, and DCDC converters. It also shows the temperature, humidity, and cooling status. The configuration file with parameters for the chips can also be checked and selected via the panel. Furthermore, there is a status indication for the connection to the two FRED servers used by MFT, along with a dedicated section for the RU and chip clock configuration. The global ALICE clock status and transitions are also monitored. Moreover, for each part of the detector, there are more detailed

panels that allow further control. There are also dedicated trending panels which show the time evolution of the variables monitored in the DCS. The commands from the MFT DCS GUI are executed on three MFT DCS worker node remote servers, each hosting part of the MFT DCS project. The CAEN power supply system is hosted on the first MFT worker node, the chip and RU powering, monitoring, and configuration are handled by the second MFT worker node, and the PSU control and the main MFT DCS project are hosted on the third MFT worker node. Access to the advanced DCS panels of MFT is restricted to MFT experts, the central ALICE DCS shifter has access only to the simplified MFT Shifter Panel. However, the DCS panels are used (by the central DCS shifter or the MFT expert) only in case of emergencies or for special operations. In normal operating conditions, all actions are performed via the Finite State Machine (FSM).

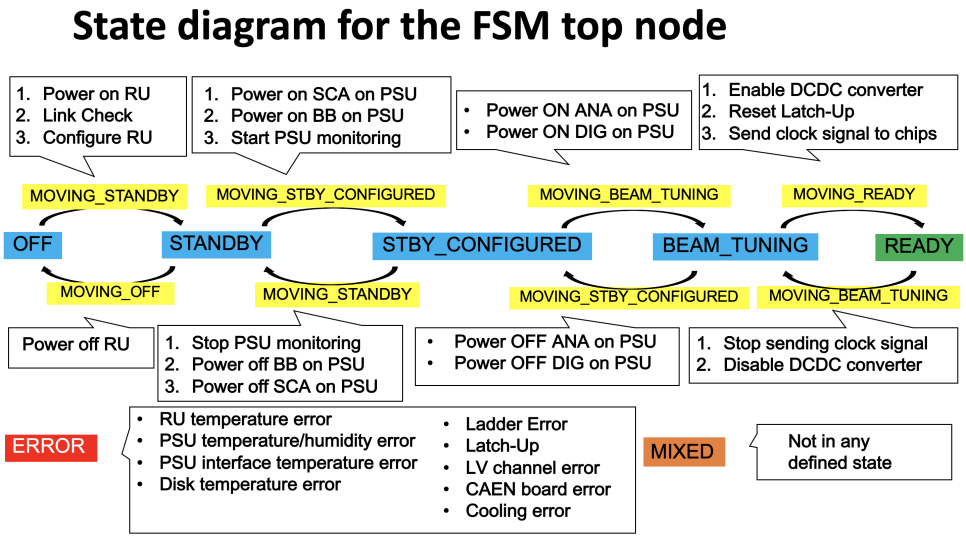

Figure 3.27: Diagram illustrating the states of the MFT FSM top node and the necessary steps for transitions between them. Taken from [100].

The FSM is an integral component of the DCS project, featuring a hierarchical tree structure composed of nodes based on the architecture of the specific detector. Within the FSM, transitions from one detector state to another are defined as a sequence of given operations for each detector node. To prevent concurrent command submissions by multiple operators, a system of locks has been implemented. This design ensures that only the individual currently in possession of the lock associated with a specific subdetector has the authorization to transmit commands to it. In the case of the MFT, there are five achievable states for the FSM top node: Off, Standby, Standby Configured, Beam Tuning, and Ready. The actions required for transitioning between these top node states can be seen in Fig. 3.27. In the FSM tree structure, it is possible to exclude a node, resulting in the omission of the node's status in the computation of the top node status, and this excluded node will not execute any commands received from the top node. The smallest part of the MFT that can be excluded as a node is one zone, corresponding to one RU.

Operation	MFT Safety Status	MFT FSM Status
LHC beam injection	Safe	Beam Tuning
LHC beam test	Super Safe	Off
ALICE magnet transition	Magnet Safe	Off

Table 3.3: Table displaying the ALICE safe states alongside the corresponding MFT FSM top node states for the respective operations.

To ensure the safety of the ALICE subdetectors, safety states are defined for regular LHC and ALICE operations to mitigate potential damage to certain detector components. During LHC beam injections, various instabilities may arise, leading to radiation damage to the detectors. Consequently, the ALICE subdetectors must transition to the Safe state to prepare for beam injection. In the case of MFT, the Safe state corresponds to the Beam Tuning FSM top node state. During machine development days, the LHC team may circulate the beam in non-standard conditions, resulting in higher probability of events known as splashes, where a portion of the beam collides with material in the beam pipe, causing particles flooding the detectors. Given the increased potential for radiation damage to the detectors, ALICE must be in the Super Safe state during such conditions. For MFT, the Super Safe states correspond to the FSM Off state. Additionally, transitions in the ALICE solenoid or dipole magnet can induce currents in the detector systems, posing a serious risk of damage. To address this concern, ALICE must be in the Magnet Safe state, equivalent to the FSM Off state in MFT. A summary of the MFT safe states can be seen in Tab. 3.3.

In addition to the control panels and the FSM interface, the DCS GUI also includes the alarms panel. This panel collects monitoring information from the DCS, allowing detector groups to define alarms based on specific monitoring outputs. The alarms are categorized as follows:

1. **Warning**: This alarm is triggered when an observed variable slightly diverges from its usual value.
2. **Error**: The Error alarm is activated when an observed variable significantly deviates from the expected value.
3. **Fatal**: In cases where the observed values pose a danger to the detector, triggering a Fatal alarm necessitates immediate action.

For the Warning and Error alarms, detailed explanations and instructions are provided to the central DCS shifter within the panel. These instructions typically involve simple actions for the shifter to perform or commands to contact the detector on-call expert. For Fatal alarms, an immediate response is ensured by initiating software FSM interlocks, which promptly switch off the problematic detector segment. Consequently, the detector FSM state transitions to Error.

As for the MFT system, the currently implemented alarms include monitoring the following parameters:

- The pressure difference between the detectors' loop inlet and outlet.
- The status of cooling loop valves.
- RU current values.
- RU voltage values.

The final level of protection in case of major accidents is the Detector Safety System (DSS). Unlike other safety systems, the DSS operates independently of any software logic as it is directly wire-connected to the central DSS relay station in CR4. Here, it triggers a hardware interlock on the endangered detector power supply system. For the MFT, the DSS is implemented to monitor the cooling loops. Whenever a cooling loop is off, locked, or encounters an error, a DSS signal is generated, initiating a pre-alarm. This pre-alarm is immediately visible at the central DSS workstation in the ALICE Run Control Center (ARC), where the shifter crew, responsible for operating the ALICE detector, can take prompt action. After two minutes from the pre-alarm start, a DSS interlock is triggered for the affected MFT CAEN power supply module. As each CAEN module supplies power to a quarter of the detector, the corresponding part of MFT is turned off, and the associated alarms are displayed on the DSS and DCS alarm panels. In addition to the pre-alarm, when the DSS signal is generated, an e-mail notification is sent to the MFT cooling experts, informing them of the issue. This ensures that the appropriate personnel are promptly aware of the situation. For the purposes of the MFT cooling plant operation tests, there is an additional DSS input that can be controlled via DCS. This input causes an inhibition of the interlock on the CAEN power supply modules. However, this functionality is restricted to selected MFT experts and must be treated with extreme care, as it involves disabling a vital safety system.

The Experiment Control System (ECS) enables the initiation and termination of data acquisition. The ECS interface equips shifters with preset configurations for standard operational conditions. However, within the advanced settings, the interface allows for customization of factors such as software version, hardware resource allocation, software components in the workflow, configurable parameter values, and more. Much like the DCS, a locking mechanism is implemented to ensure that only a single operator can initiate a run with a specific detector.

A schematic depiction of the integration of MFT detector operations within the central ALICE systems is presented in Fig. 3.28. In addition to the previously discussed DCS, ECS, and QC systems, this illustration also includes Grafana and Infologger displays. Grafana functions as a monitoring system, offering insights into processes executed on specific hardware components. This presentation encompasses details like run numbers, unique workflow IDs, active DPLs within the workflow, data rates across different segments of the workflow, as well as memory and CPU utilization of individual DPLs. Furthermore, it highlights the processing status of the TF and various other parameters, charting their evolution over time through graphical representations. Conversely, the Infologger serves as a text-based monitoring system that provides an interface for displaying messages generated by

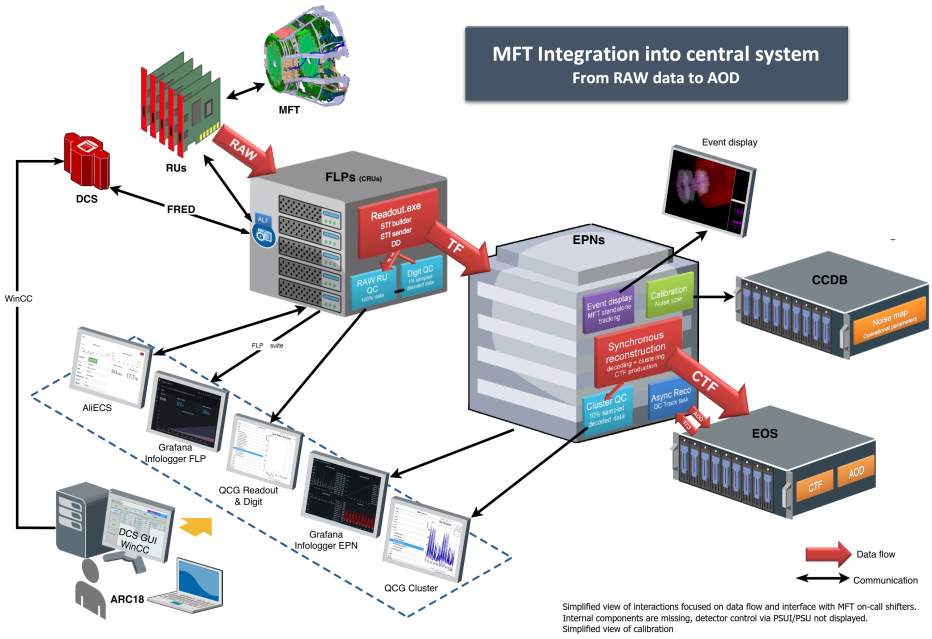

Figure 3.28: Schematic representation of the integration of MFT detector operations into the central ALICE systems, as observed from the perspective of the MFT on-call shifter. Taken from [100].

running workflows. These messages can encompass user-defined content, along with pertinent information such as message production time, the originating device and process, process ID, run number, detector details, and more. Additionally, the Infologger messages are categorized into five levels based on their severity: Debug, Info, Warning, Error, and Fatal.

3.2.7 Quality Control for the MFT

Quality Control for readout

The first task of the MFT QC involves overseeing the readout process of the detector. The Readout Task operates across the five MFT FLPs, monitoring the Readout Data Headers (RDH) of the raw data at a comprehensive rate of 100%. Embedded within this raw data is a Data Diagnostic Word (DDW), housing information regarding the status of the respective chip. This information is encoded into two bits, affording four distinct potential states: 'Ok,' 'Warning,' 'Error,' and 'Fault.' With increasing severity, these states correspond to anomalies within the data readout chain. For each of these states, the QC task generates a TH1F histogram that delineates the frequency of these states, normalized in relation to the count of DDW instances. Each histogram consists of 936 bins, aligning with the number of MFT chips. A dedicated Readout Checker observes the count of chips in 'Warning,' 'Error,' or 'Fault' conditions. This count is then displayed at the top of the histogram, accompanied

by a color-coded message intended for the shifter, instructing appropriate actions as required. These instructions are categorized into three levels based on the quality of MO. The thresholds for 'good,' 'medium,' and 'bad' quality can be adjusted as parameters within the configuration JSON files of the checker. Furthermore, a list of potentially up to 20 chips encountering the given issue is displayed, along with their corresponding software IDs and hardware locations. An illustrative instance of the histogram, spotlighting the count of chips in 'Error' state during an episode marked by a substantial volume of errors, is provided in Fig. 3.29.

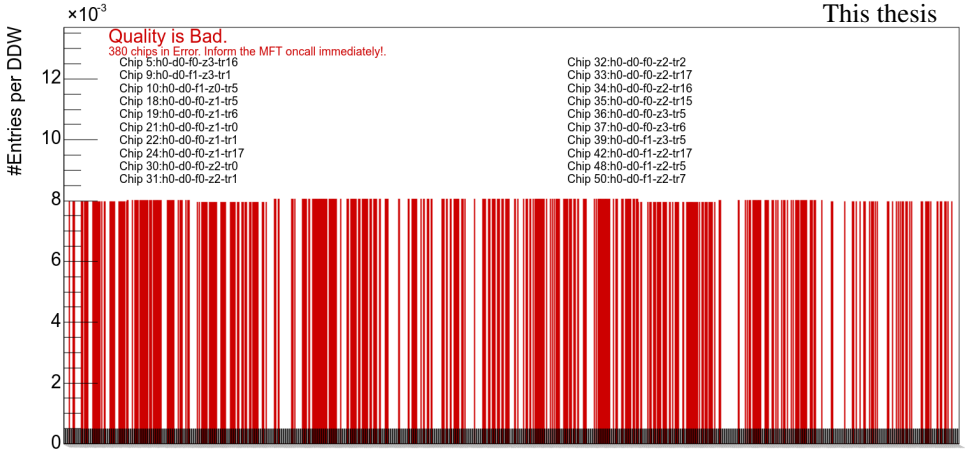

Figure 3.29: Histogram illustrating the frequency of chips in 'Error'. The 'Error' counts are normalized with respect to the corresponding number of DDW for each chip. A compilation of a maximum of 20 chips with 'Error' is presented, accompanied by their respective software IDs and hardware locations. Additionally, a color-coded instructional message intended for the shifter is provided.

An alternative and more compact representation of the identical data is offered through TH2F histograms. These histograms feature 10x8 bins, aligning with the chip rates categorized as 'Warning,' 'Error,' or 'Fault' within a specified MFT readout zone.

Additionally, apart from the Readout Task and Checker, a Readout Trending Task is also present. This post-processing task observes the temporal progression of the count of chips categorized as being in a 'Warning,' 'Error,' or 'Fault' state. Starting from the summer of 2023, a new functionality has been integrated into the MFT DCS, enabling the reconfiguration of a chip while data acquisition is ongoing. This capability can be initiated either manually by the shifter or automatically once a predefined threshold of problematic chips is reached. This feature significantly enhances the efficiency of MFT data acquisition. An illustrative instance of this functionality is evident in the trend showcased in Fig. 3.30.

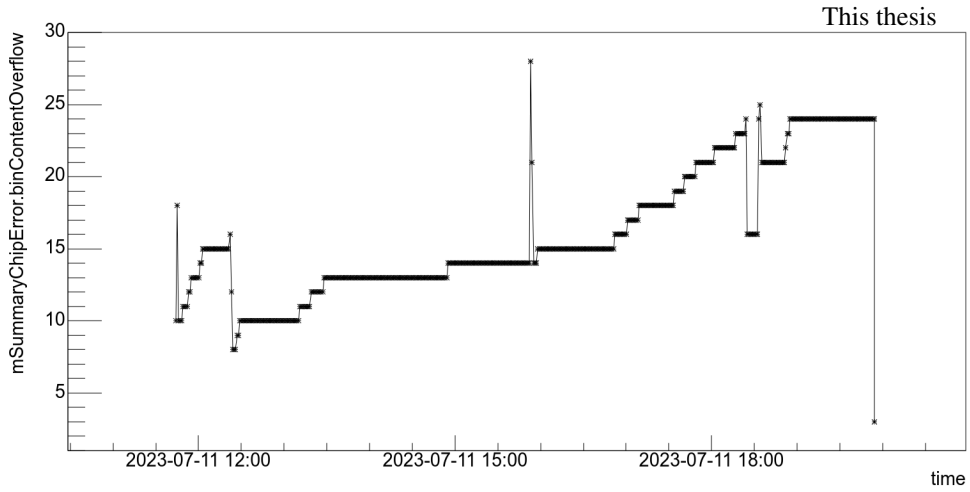

Figure 3.30: Histogram illustrating the time evolution of the number of chips reporting 'Error'.

Quality Control for digits

The next QC task is centered around the monitoring of digits. Digits represent a data structure that encompasses information about a single MFT pixel. This information comprises the chip ID, the specific pixel's row and column on the chip, as well as the pixel's signal value. The Digit Task is operated on each of the five MFT FLPs. Considering that, within the general data stream of ALICE, digits are reconstructed from raw data solely at the EPN level, a specialized MFT digit decoder must be executed on the MFT FLPs for the purpose of QC. A data sampler provides the decoder with a designated percentage of raw data. However, this percentage significantly varies depending on the type and frequency of LHC collisions. All data that the decoder reconstructs are subsequently transmitted to the Digit QC Task, which undertakes the responsibility of their monitoring.

The fundamental MO of the Digit Task is a digit chip occupancy TH1F histogram. This histogram illustrates the count of digits per chip, normalized relative to the number of Readout Frames (ROF), for each of the 936 chips. Refer to Fig. 3.31 for visualization. The normalization process with respect to the number of ROFs is executed by the Digit Checker.

For a more comprehensive analysis, a series of 20 TH2F histograms are generated, portraying the digit chip occupancy. These histograms are structured to mimic the genuine geometry of the detector setup. This layout is presented in Fig. 3.32. For these particular histograms, the Digit Checker accesses information regarding disabled or faulty chips from the CCDB and superimposes a skull symbol at the corresponding chip's location. This aids the MFT on-call shifter in recognizing chips that are not generating data due to known issues.

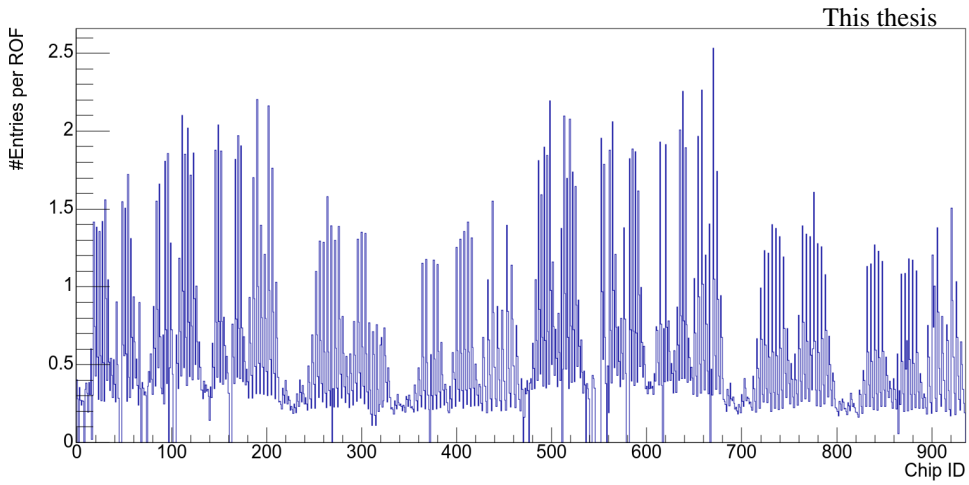

Figure 3.31: Histogram illustrating the normalized digit chip occupancy relative to the number of Readout Frames (ROFs).

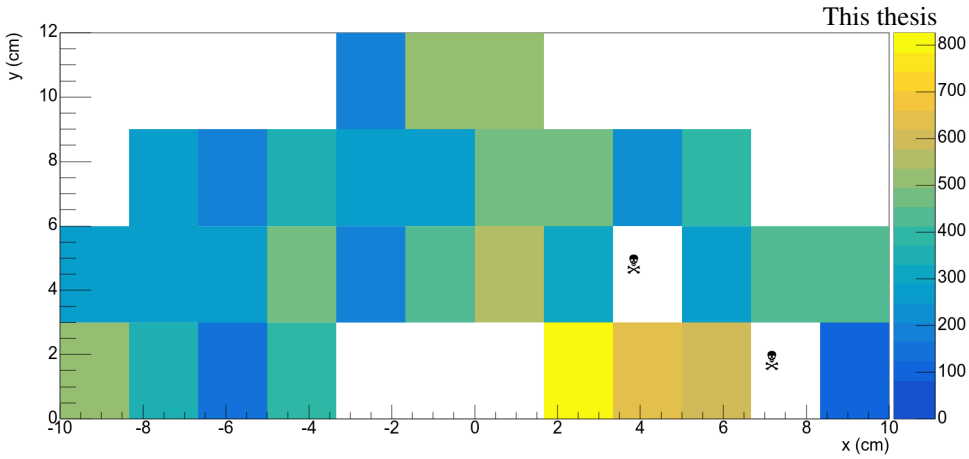

Figure 3.32: Histogram depicting the digit occupancy within a layout that corresponds to the authentic geometry of the detector. This specific histogram shows the H1-D0-F1 of the detector.

In the case of central shifters, a more condensed histogram is utilized. Specifically, a TH2F plot is employed to provide a concise overview of the digit occupancy per MFT zone. This summary is visualized in Fig. 3.33. The Digit Checker constantly monitors the quantity of vacant zones in this MO. If the count surpasses the predefined threshold, an error message is triggered, accompanied by instructions directed to the central shifter.

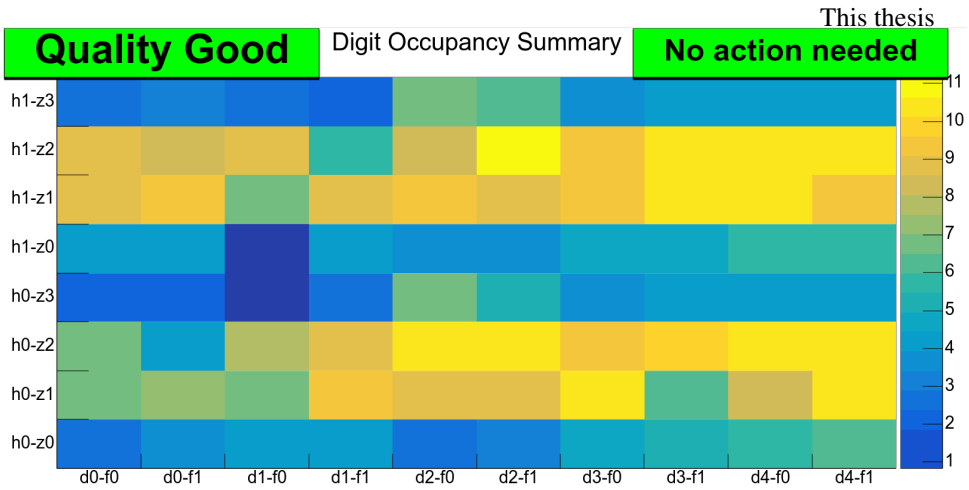

Figure 3.33: Histogram summarizing the digit occupancy per MFT zone.

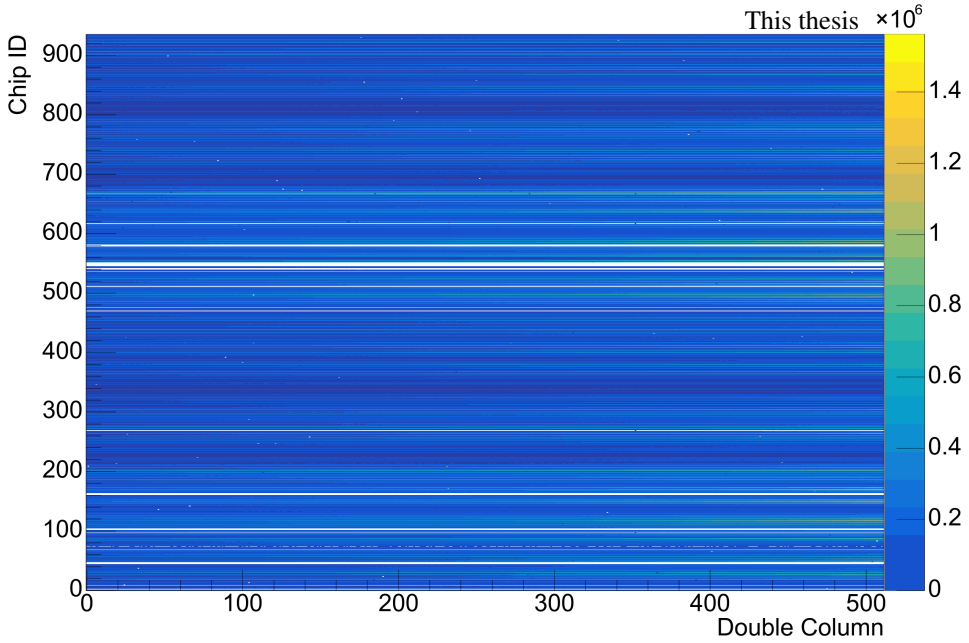

Figure 3.34: Histogram illustrating the digit occupancy per double column for all 936 MFT chips.

For an expert conducting an in-depth investigation into potential issues, the most comprehensive information accessible during the acquisition of physics data is contained within the TH2F histogram, which tracks the digit occupancy of 936 chips across their 512 double columns, as depicted in Fig. 3.34. This presentation entails a reduction by a factor of 1024, achieved by aggregating data along the rows, and an additional reduction by a factor of 2 due to the representation of double columns instead of individual columns. These reductions are essential due to the limitations of the QC system, which cannot accommodate the real-time processing of data at the granularity of individual pixels, particularly given the high data rates of the LHC.

However, the constraint imposed by the high data rate does not hold true during specialized calibration runs known as noise scans. During these runs, collisions are absent, and solely the inherent background originating from cosmic rays and other sources is observed. In the context of these relatively brief ($\approx$ 3 minutes) calibration runs, 936 comprehensive TH2F plots that encompass information from every pixel within the chip are generated. An exemplar of such a plot can be observed in Fig. 3.35.

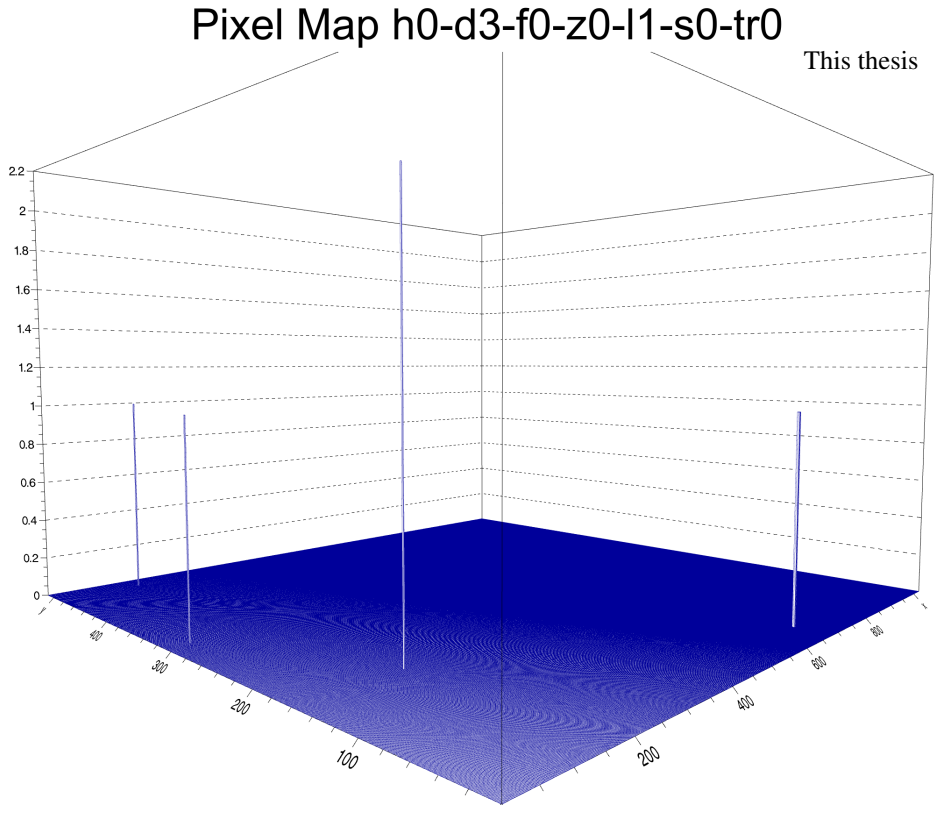

Figure 3.35: Comprehensive histogram displaying the quantity of digits across all 512x1024 pixels of an MFT chip.

To assess the accurate time synchronization between the detector and the LHC clock, a histogram depicting the quantity of digits generated within a particular BC is generated, as demonstrated in Fig. 3.36. Notably, the BCs exhibiting the highest digit counts should align with the identifiers of the colliding BCs according to the LHC's filling scheme. The Digit Task also generates a histogram that portrays the distribution of the digit count per ROF. This distribution is notably influenced by the specific collision type and tends to produce a wider distribution for Pb–Pb collision with respect to pp collisions.

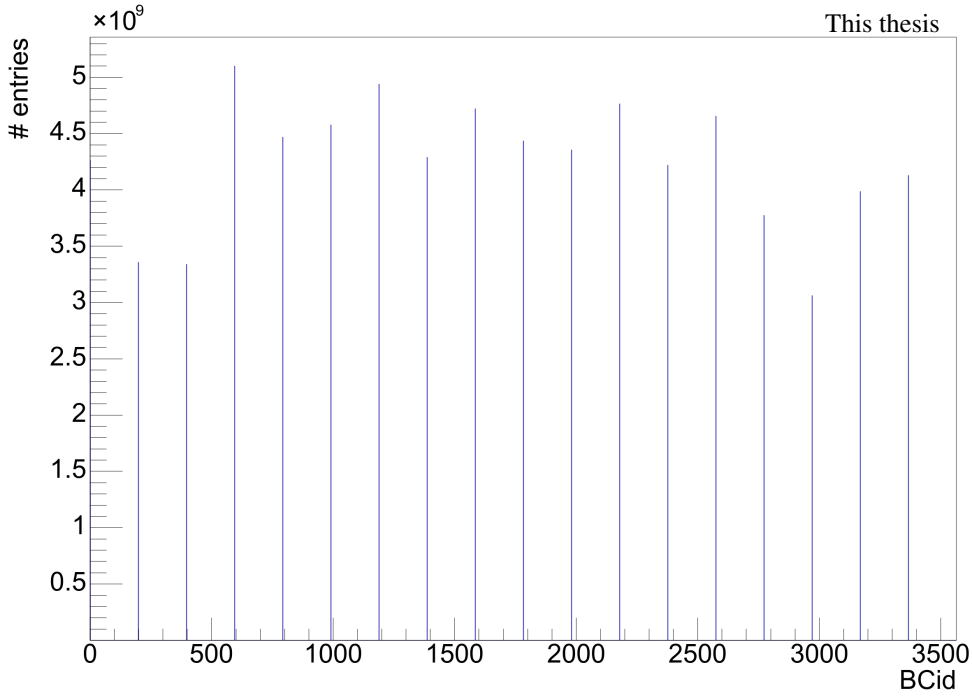

Figure 3.36: Histogram depicting the count of digits generated within a specific BC.

Lastly, the Digit Trending Task graphs the progression of the count of chips without any digits. Concurrently, a Digit Slice Trending Task is engaged in tracking the average digit occupancy across the top and bottom halves of the MFT detector, see Fig. 3.37.

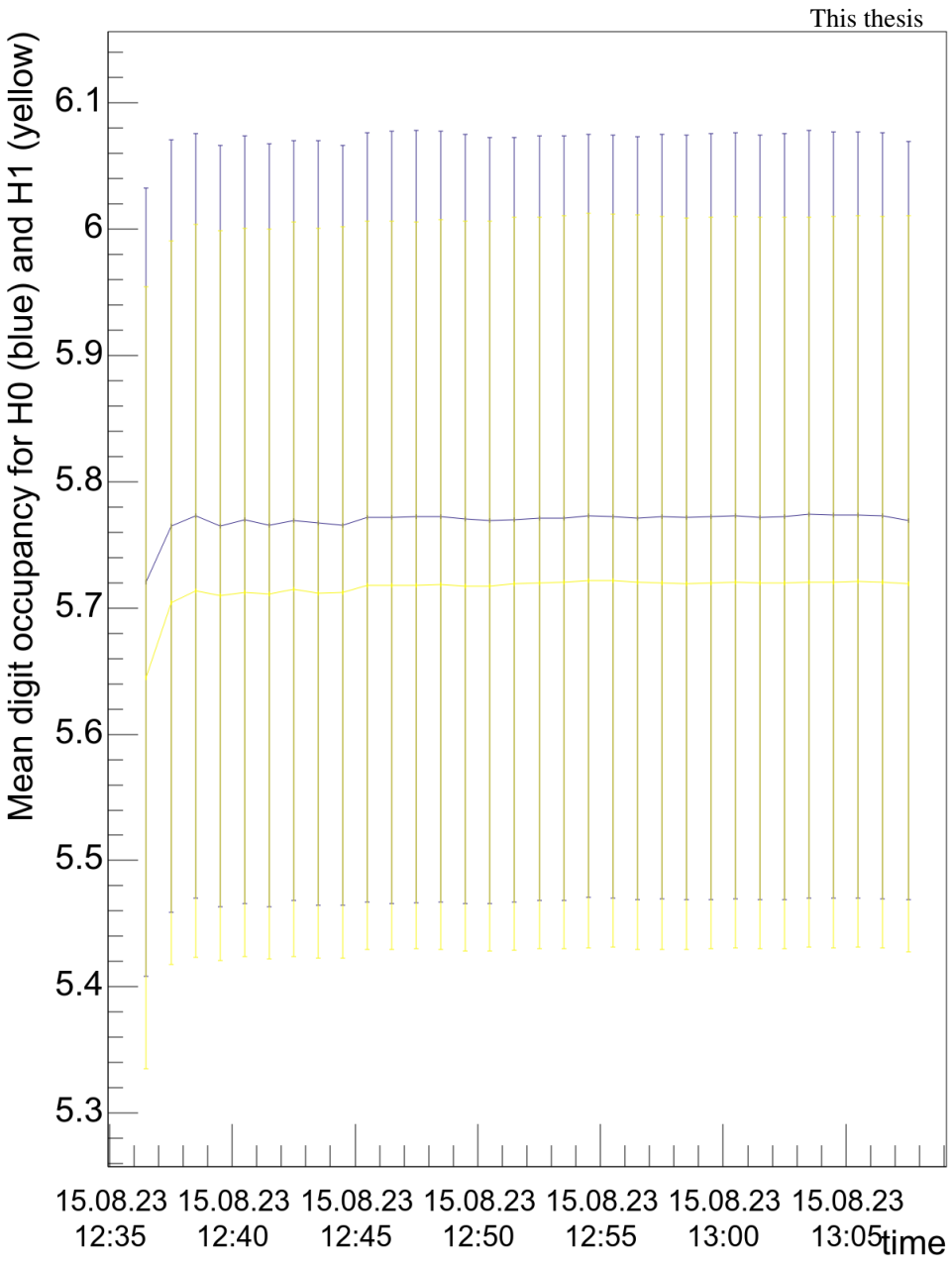

Figure 3.37: Histogram showing the trending behavior of the average digit occupancy for each half of the MFT.

Quality Control for clusters

The Cluster QC Task is the first QC task which is executed on the EPN farm. It is executed after the clusters are reconstructed from the data. Clusters denote specific arrangements of digits situated within a predetermined spatial domain. Each distinct cluster topology is associated with a designated ID number. The sequential assignment of these ID numbers is determined by referencing a cluster dictionary, wherein values ascend in numerical order. This ascending order is structured to progress from the most frequently encountered cluster topologies to those less commonly observed. This progression is intrinsically linked to the data sample utilized for the creation of the cluster dictionary. Consequently, any modifications made to this dictionary can induce alterations in the pattern ID. The pattern ID assigned to a cluster configuration serves as a pivotal parameter subject to continuous monitoring through the QC. A visual representation in the form of a histogram illustrates the frequency distribution of clusters possessing a specific pattern ID. This distribution is normalized in relation to the total number of TFs, thereby facilitating enhanced comparability in analyses. An illustrative depiction of this histogram is presented in Fig. 3.38.

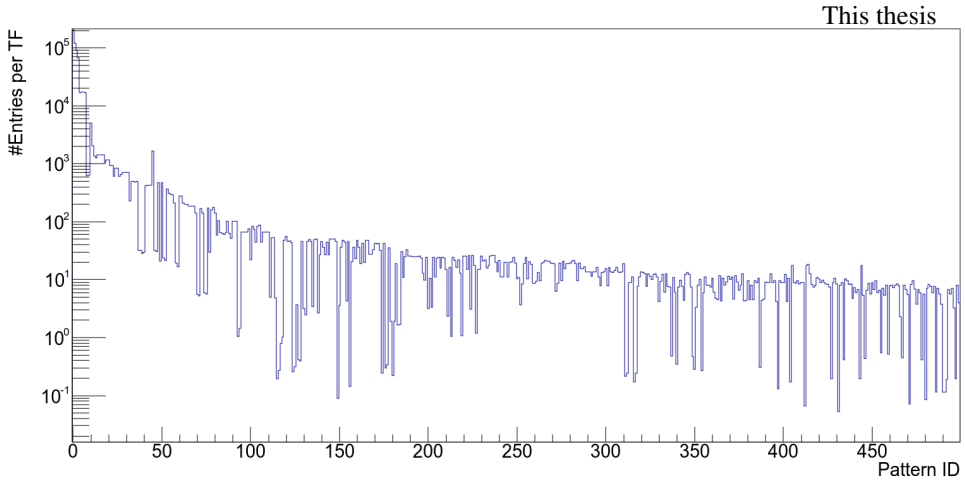

Figure 3.38: Histogram depicting the count of clusters with a specific pattern ID normalized by the number of TFs.

The preceding histogram predominantly serves the purpose of initial-level monitoring. However, for a more comprehensive analysis, a more differential iteration of this histogram is generated. Specifically, this takes the form of a TH2F histogram, which tracks the pattern ID of each cluster on an individual basis across all 936 MFT chips. See Fig. 3.39 for a visual representation of this histogram.

As previously mentioned, the cluster pattern ID pertains to a specific cluster topology. However, another noteworthy variable deserving of observation is the effective size of the clusters, quantified in terms of the number of active pixels they encompass. A histogram depicting the distribution of this parameter is presented in Fig. 3.40. Notably, this histogram exclusively represents clusters that exhibit

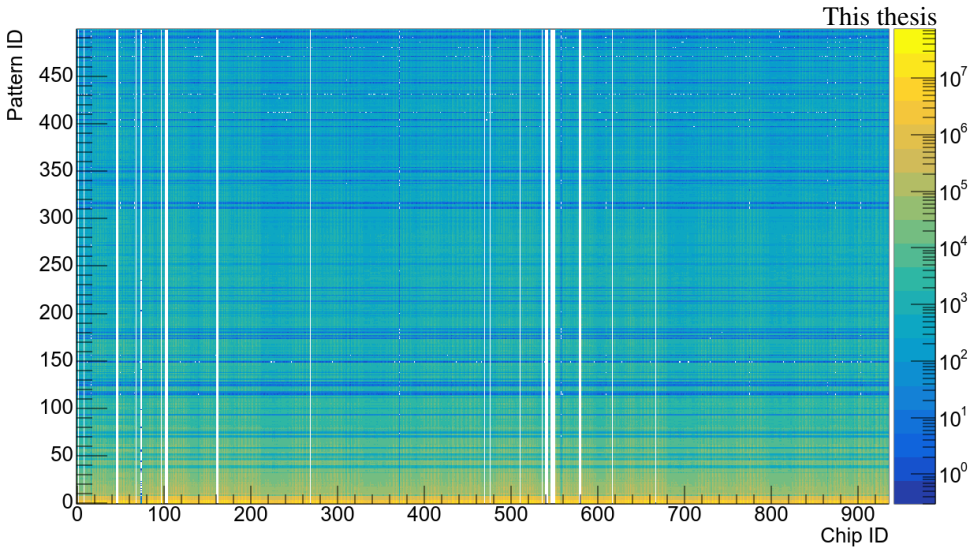

Figure 3.39: Histogram illustrating the count of clusters with a particular pattern ID registered by a chip with a given ID.

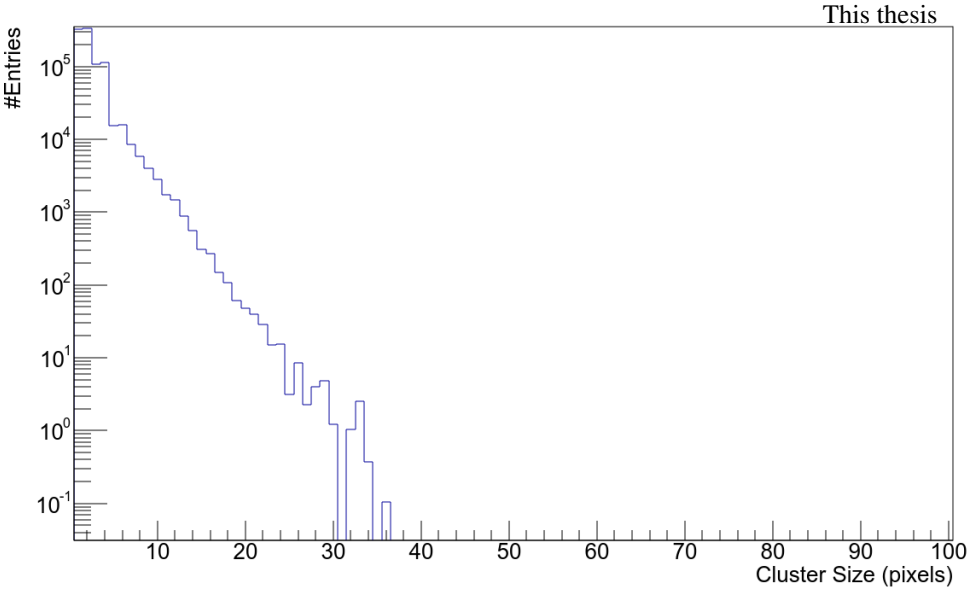

Figure 3.40: Histogram displaying the cluster sizes in terms of the number of active pixels.

a continuous topology. Beyond a certain threshold size, clusters cease to be evaluated as continuous topologies. Instead, they are circumscribed by a bounding box encompassing an area that may accommodate arrangements of active pixels lacking continuity. These clusters are termed "grouped clusters" and a distinct histogram is employed to illustrate their size in terms of active pixels.

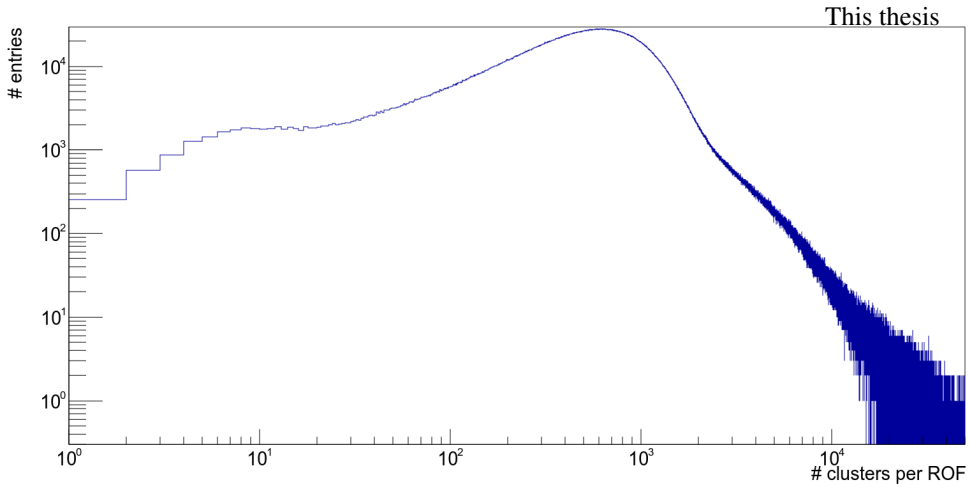

Figure 3.41: Histogram depicting the size of ROFs in terms of the number of clusters they contain.

In a manner akin to the Digit Task, an analogous histogram that delineates the dimensions of ROFs, quantified in relation to the number of clusters they encompass, is likewise featured within the Cluster Task. This representation can be observed in Fig. 3.41. Furthermore, in alignment with this shared histogram, there exists a collection of analogous histograms that correspond to their digit-based counterparts deliberated upon in the earlier section:

- `TH1F` histogram illustrating normalized cluster chip occupancy relative to the number of TFs.
- `TH2F` histogram summarizing the cluster occupancy for each MFT zone.
- Set of `TH2F` histograms depicting cluster occupancy within a layout corresponding to the authentic detector geometry (total of 20 histograms).
- `TH1F` histogram representing the count of clusters within a specific BC.

The Cluster Checker performs identical checks as those carried out for the equivalent digit MOs. It also assumes the responsibility of normalization. However, for the clusters, normalization is executed with respect to the number of ROFs. The monitoring of the number of clusters within a singular face of a designated MFT disk is facilitated by two histograms, which lack a corresponding counterpart in the Digit Task. This analysis is conducted individually for H0 and H1 of the detector.

The final aspect of cluster monitoring is concerned with the detailed positioning of the clusters. Each MFT disk and face is accompanied by a dedicated TH2F histogram, illustrating the (x,y) coordinates of the clusters. For an example of this depiction, please refer to Fig. 3.42. Moreover, an additional series of TH1F histograms illustrates the radial distribution of clusters relative to the beam axis

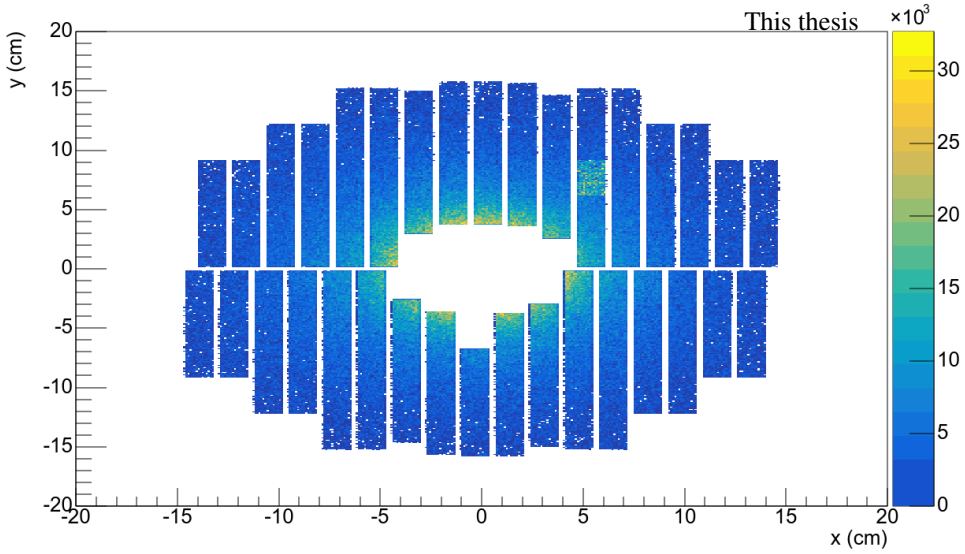

Figure 3.42: Histogram displaying the x and y coordinates of clusters in D4-F0.

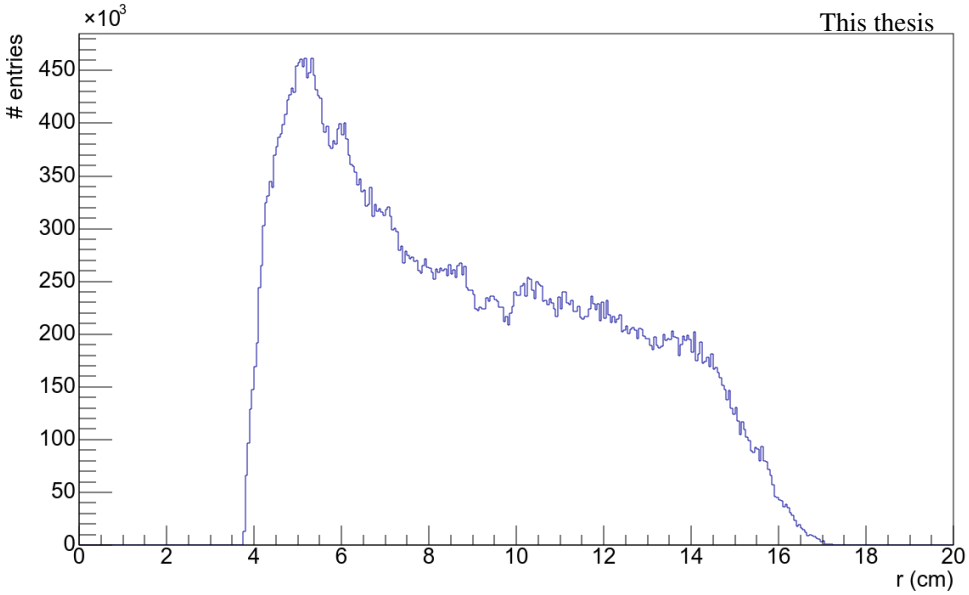

Figure 3.43: Histogram showing the radial position of clusters from the LHC beam axis for D4-F1.

for each face and disk. Illustration of this visualization is present in Fig. 3.43. Concurrently, a single histogram is employed for the monitoring of the distribution of clusters along the beam axis, as presented in Fig. 3.44. This histogram distinctly showcases the positions of the MFT faces and disks along the the beam axis.

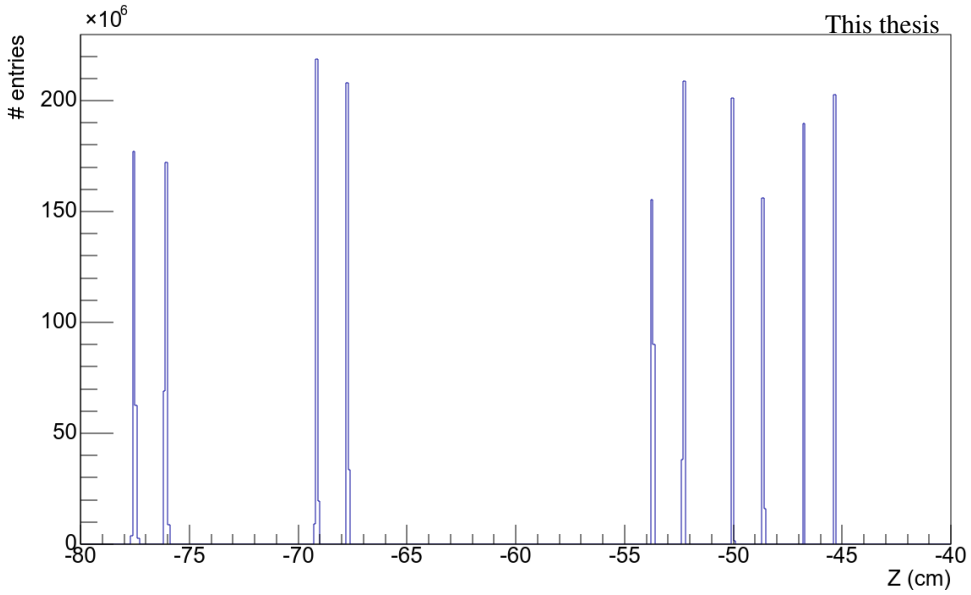

Figure 3.44: Histogram illustrating the positions of clusters along the beam axis of the LHC (denoted as Z).

Quality Control for tracks

The last QC task is dedicated to the monitoring of MFT tracks. Following the reconstruction of a subset of MFT tracks, the Track QC Task is executed on the EPN farm. This reconstruction process involves the connection of clusters and can be divided into two steps. The first step is track finding, which discerns two types of MFT tracks: firstly, straight tracks reconstructed through the utilization of the Linear Tracking Finder (LTF) algorithm [94], involving fitting clusters with linear trajectories; secondly, curved tracks reconstructed by employing the Cellular Automaton (CA) algorithm [104] to identify track candidates. Both the LTF and CA track candidates are then fitted using the Kalman filter [94, 105] to obtain the final track parameters. The QC task processes the entirety of the reconstructed tracks, and a subset of these tracks is also employed in the ALICE event display. A threshold can be imposed on the tracking software to exclusively accept tracks that possess a specified minimum number of clusters. The presently employed value for this threshold is five clusters.

The initial aspect of track properties monitored by the Track Task pertains to their angular distribution. A TH2F histogram that portrays the distribution of MFT tracks in the (η, φ) plane is presented in Fig. 3.45. Additionally, single-dimensional angle distributions can also be accessed through TH1F histograms for the track angles η, φ, and $\tan\lambda$. These are illustrated in Fig. 3.46, Fig. 3.47, and Fig. 3.48, respectively.

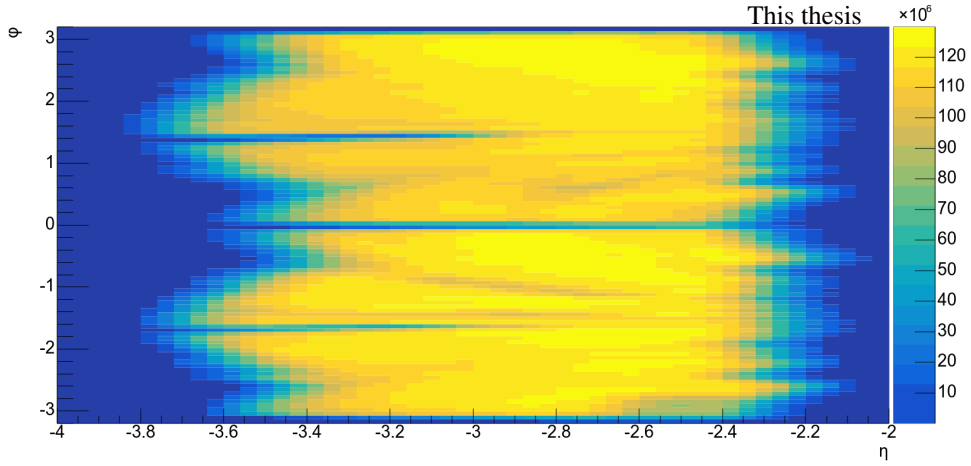

Figure 3.45: Histogram illustrating the distribution of MFT tracks in the (η, φ) plane.

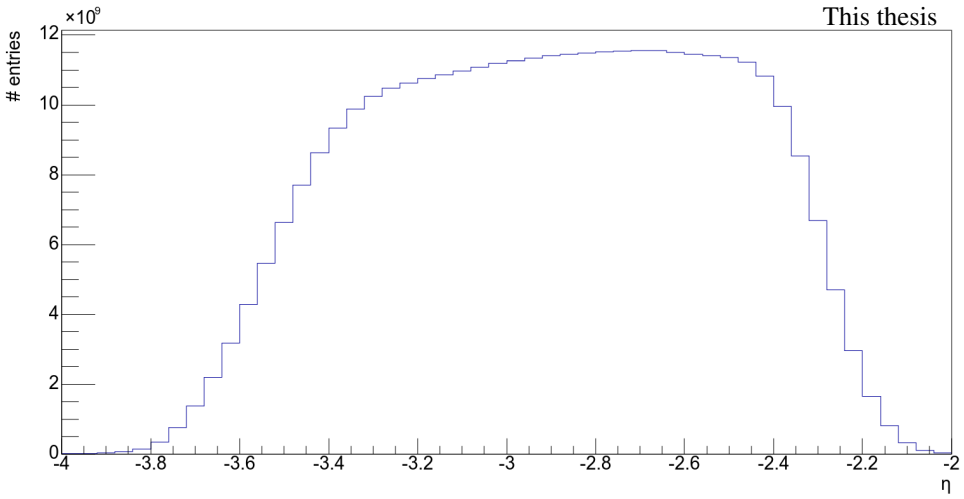

Figure 3.46: Histogram depicting the distribution of MFT tracks in terms of η.

The λ angle is the complementary polar angle used in the MFT tracking algorithm for convenience. The η distribution is separately available for LTF and CA tracks, while the φ distribution is accessible for both positive and negative tracks individually. Furthermore, the (η, φ), η, and φ track angle distributions are separately monitored based on the number of clusters contained, ranging from four to ten. Another track parameter being monitored is the track charge q over the track transverse momenta p_{T}, see Fig. 3.49.

Similarly to the clusters, the track coordinates in the (x, y) plane are represented using a TH2F histogram, as demonstrated in Fig. 3.50. The plot exhibits a small fraction of tracks extending beyond the detector's acceptance. This constitutes a recognized concern inherent to the tracking algorithm, and ongoing endeavors are dedicated to refining this behavior. This histogram is generated individually for tracks with varying minimum numbers of clusters, ranging from four to ten.

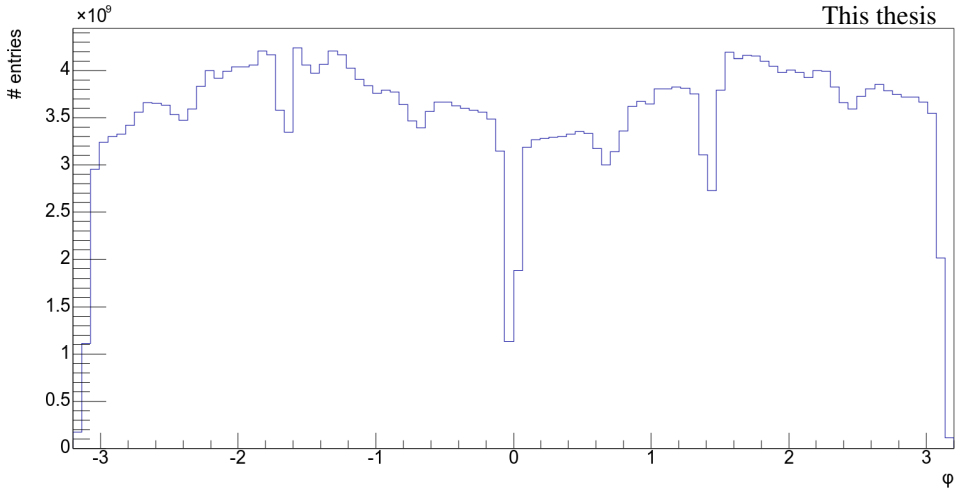

Figure 3.47: Histogram illustrating the distribution of MFT tracks in terms of φ.

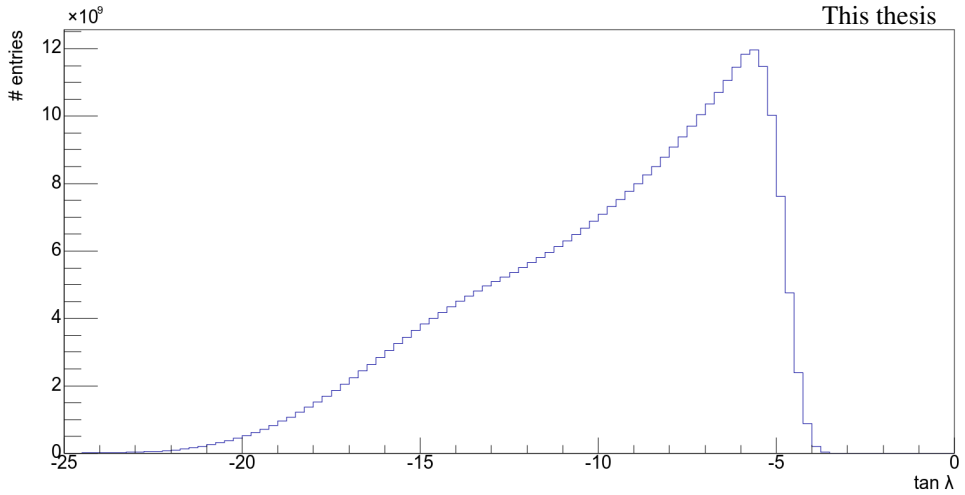

Figure 3.48: Histogram depicting the distribution of MFT tracks in terms of $\tan\lambda$.

Additional histograms, which share an equivalent counterpart in the Cluster Task, include:

- `TH1F` histogram with the size of ROFs in terms of the number of tracks they contain.
- `TH1F` histogram with the count of tracks generated within a specific BC.

Moreover, there are also MOs unique to the Track Task:

- `TH1F` histogram with the ratio of the number of clusters associated to tracks to the number of all clusters.

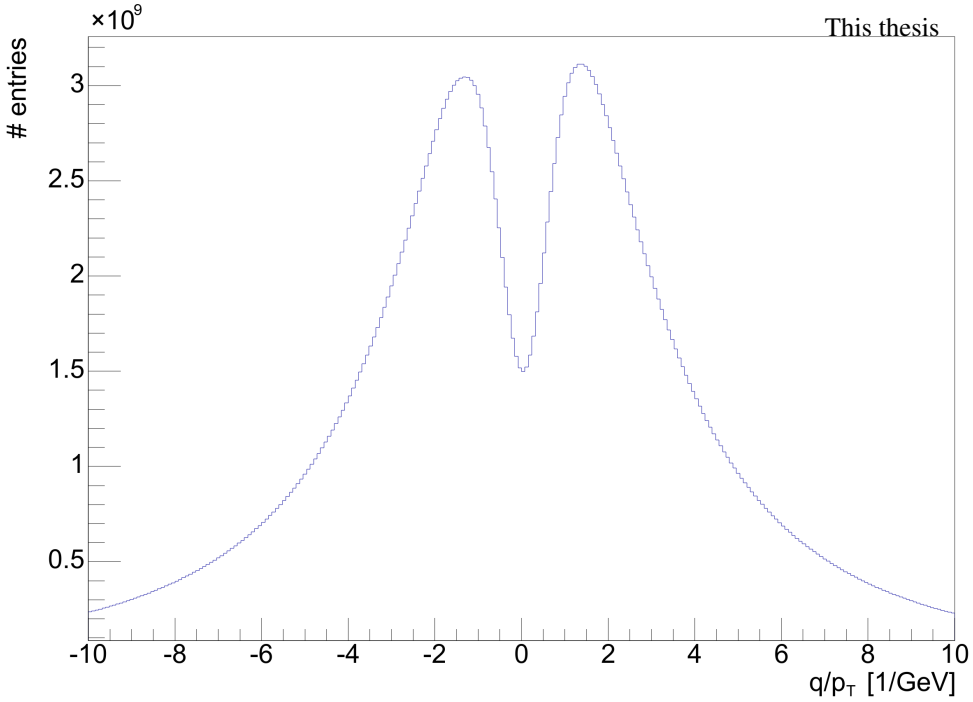

Figure 3.49: Histogram illustrating the distribution of track charge over the track transverse momenta.

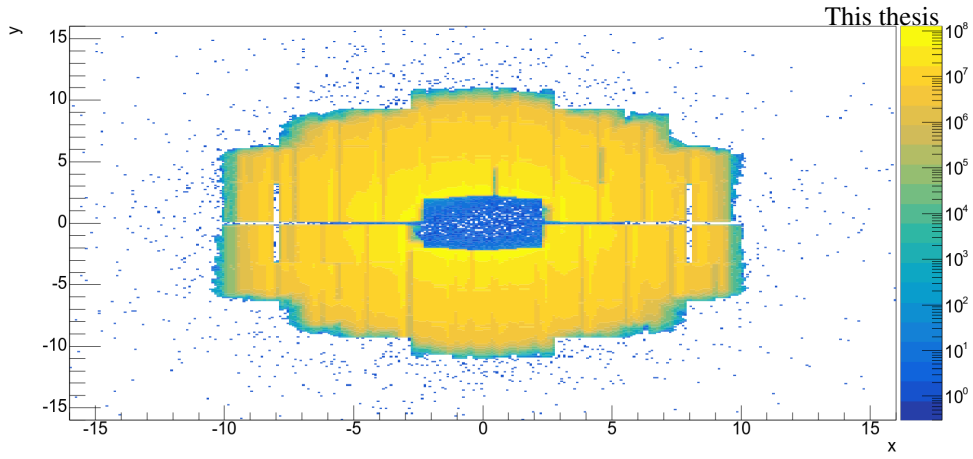

Figure 3.50: Histogram illustrating the distribution of MFT tracks in the (x, y) plane, considering exclusively the tracks comprising a minimum of five clusters.

- `TH1F` histogram with the number of clusters per track (also monitored separately for LTF and CA tracks).
- `TH1F` histogram with the track charge.
- `TH1F` histogram with the track χ^2/NDF.

Finally, by combining the information regarding the ratio of the number of clusters associated with tracks to the total number of clusters and the count of tracks generated within a specific BC, a TH2F histogram illustrating this combined distribution is generated and presented in Fig. 3.51.

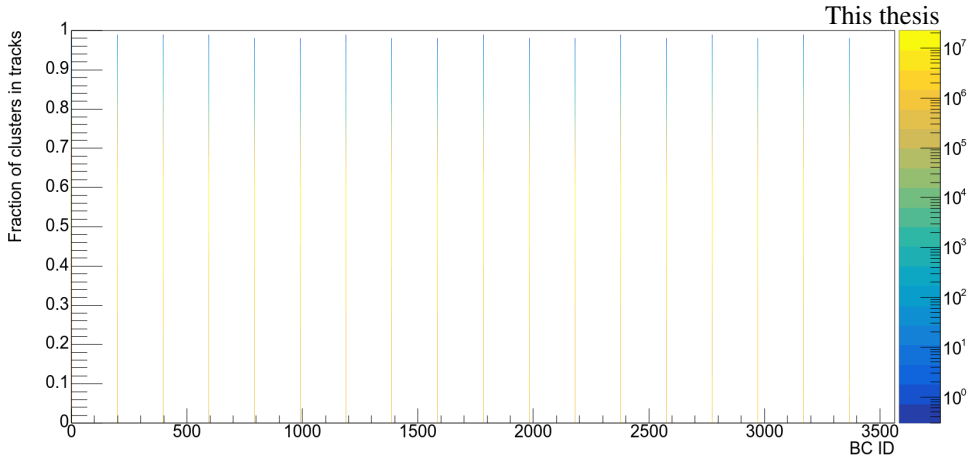

Figure 3.51: Histogram depicting the number of ROFs with a given ratio of the number of clusters associated with tracks to the total number of clusters as a function of the BC ID.

Global MFT quality

To facilitate a swift assessment of the global MFT quality by the central shifters, a post-processing task tracks the QOs generated by each individual MFT check. These outputs are then aggregated to compute the global MFT quality, represented as a logical AND operation across all inputs. An illustration of the MFT quality is presented in Fig. 3.52. Both this global quality and the individual qualities are additionally archived in trending histograms, as depicted in Fig. 3.53.

Figure 3.52: Display depicting the global quality status of the MFT, featuring the quality values associated with each of the MFT checkers.

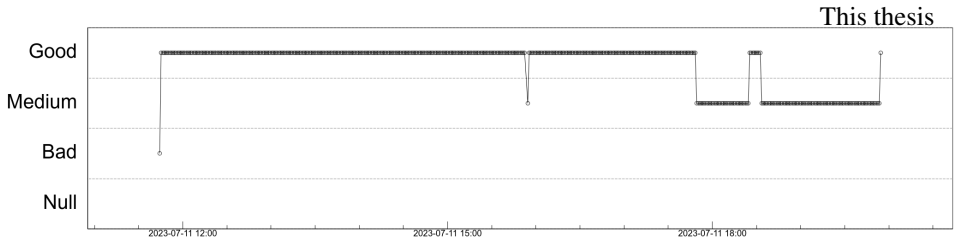

Figure 3.53: Time evolution trend depicting the global quality of the MFT over the course of a run.

Chapter 4

Analysis of coherent J/ψ photoproduction cross section using neutron emission classes

The analysis described in this chapter utilizes the measurement of the coherent J/ψ photoproduction cross section in Pb–Pb UPC events, accompanied by EMD, at a center-of-mass energy per nucleon pair of $\sqrt{s_{NN}} = 5.02$ TeV. This measurement allows for the extraction of the energy dependence of the photonuclear cross section, as discussed in Sec. 1.6. The results presented below represent the highest energy measurement of the γPb cross section available to date and were published in [1].

The analysis can be broadly divided into three parts. The first part consists of the EMD differential J/ψ photoproduction cross section analysis of the forward ALICE data set, the second part does the same but with the central ALICE data set, and the last part combines the results from the two data sets to extract the energy dependence of the γPb photonuclear cross section over the full ALICE rapidity coverage. The main focus will be given to the analysis of the forward data set and the final extraction of the photonuclear cross section. The analysis of the central data set was originally published in [34] and it was performed again with the modifications and additions needed for the EMD differential measurement by my supervisor. Therefore, only key information about the analysis at central rapidity will be discussed, highlighting noteworthy differences in comparison to the forward data analysis.

The analysis was performed using a C++ code based on ROOT scripts, utilizing the ALICE Analysis Task library (developed by the ALICE collaboration), the AliEn environment, and the ALICE Lego Train framework for efficient multi-user processing of large data samples. The necessary computing resources for the analysis were provided by the ALICE computing GRID.

The offline data processing, which included data distribution fits, computation of correction factors, photonuclear cross section extraction, and plotting, was performed using ROOT, RooFit, and Python scripts.

4.1 Data set and trigger selection

The analyzed data sample is from Run 2 of the LHC and it consists of two LHC periods (LHC 18q and LHC 18r which have opposite polarity of the ALICE magnets) of Pb–Pb data taking recorded in 2018 with ALICE. The collision center-of-mass energy per nucleon pair is $\sqrt{s_{\mathrm{NN}}} = 5.02$ TeV. The specific runs used in the analysis were selected based on recommendations provided by the Data Preparation Group (DPG) of ALICE, which is responsible for ensuring data quality (individual detector status, reconstruction status, etc.) for physics analysis. The detailed list of the 225 selected runs for the forward rapidity data sample can be found in Appendix B, while the list of the 219 runs selected for the central rapidity analysis can be found in Appendix C.

In addition, a Monte Carlo data set generated with the STARlight [46] generator (version r299) for ultra-peripheral collisions was used. The generated Pb–Pb collisions were anchored to the analyzed runs, thus following the time evolution of the detector conditions. They were then folded with the ALICE detector response using GEANT 3.21 [106] and subjected to the same reconstruction criteria as the real data. Monte Carlo data productions with the following processes were used in the analysis:

- Coherent J/ψ photoproduction;
- Incoherent J/ψ photoproduction;
- Coherent $\psi' \to$ J/ψ feed-down production;
- Incoherent $\psi' \to$ J/ψ feed-down production;
- $\gamma\gamma \to l^+l^-$ continuum.

The online trigger used for recording the relevant events with potential signal from the decay of the J/ψ vector meson in the forward data sample is defined as:

- `CMUP6-B-NOPF-MUFAST = 0MUL & !0VBA,`

where

- `0MUL`: unlike-sign dimuon trigger over low-p_{T} threshold;
- `0VBA`: at least one cell fired in V0A with beam-beam timing.

The low-p_{T} trigger threshold was set to 1 GeV/c and the exclamation mark is used to denote negation. The V0A decision contained in the trigger is computed online

during data taking. However, in the offline analysis, the detector decisions are also available. In ideal conditions, the offline and online information should be identical. But due to stringent constraints on the speed of the online trigger decisions, there are differences in how the detector decision is determined online and offline. These differences can then result in a different decision flag present in the online detector information than in the offline detector information. Both the online and the offline decision flags are available in the offline data analysis.

In comparison to the previously published ALICE results in [36], the trigger used for this analysis was chosen slightly differently. In an UPC with a vector meson photoproduction and an EMD, charged particles can be emitted at forward rapidity, as has been discussed in Sec. 1.6, which triggers the veto condition. For the neutron emission class differential analysis, it is necessary to compute a correction for this effect, see Sec. 4.8. For this reason, the 2015 Pb–Pb data set had to be excluded from this analysis because there was no control trigger present for this effect at the time. This results in approximately 1/3 lower size of the analyzed data sample when compared to the results published in [36, 34].

The online trigger used for recording the relevant events in the central data sample is defined as:

- `CCUP31-B-NOPF-CENTNOTRD = 0STG & 0OMU & !0VBA & !0VBC & !0UBA & !0UBC,`

where

- `0STG`: at least two pairs of fired chips in the inner and outer SPD layers with back-to-back topology;
- `0OMU`: between 2 and 6 fired TOF pads with at least two of them with difference in azimuth $150 < \Delta\varphi < 180$;
- `0VBA`: at least one cell fired in V0A with beam-beam timing;
- `0VBC`: at least one cell fired in V0C with beam-beam timing;
- `0UBA`: at least one quarter in ADA with beam-beam timing;
- `0UBC`: at least one quarter in ADC with beam-beam timing.

The integrated luminosity of the analyzed data set has been computed run by run using reference cross sections measured in van der Meer scans [107]. The total integrated luminosity of the forward data set summed for both periods amounts to $533 \pm 13\ \mu\text{b}^{-1}$, see Fig. 4.1 and Fig. 4.2. The integrated luminosity of the central data set is $233 \pm 7\ \mu\text{b}^{-1}$.

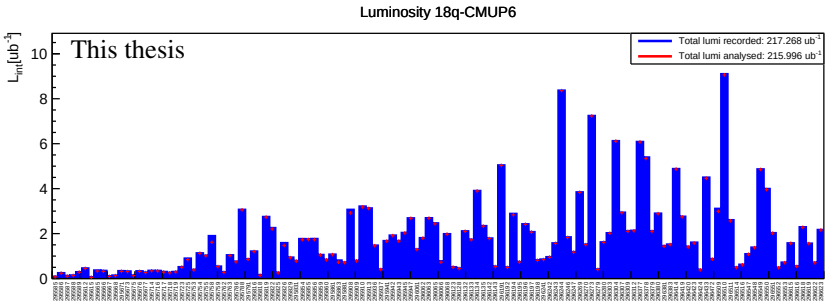

Figure 4.1: Luminosity computed for the analyzed data set of the LHC period 18q.

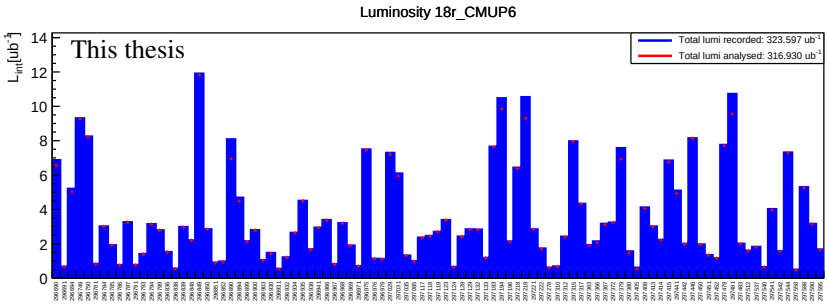

Figure 4.2: Luminosity computed for the analyzed data set of the LHC period 18r.

4.2 Event and track selection

In accordance with the selection of a different trigger for the forward data set when compared to the analysis presented in Ref. [36], as discussed in the previous section, the offline selection criteria were also slightly modified with respect to Ref. [36]. Specifically, the veto on a signal from the ADA and ADC detectors was not required. The global criteria applied to the candidate events in the forward data set, selected by the CMUP6 trigger, were the following:

- Exactly two unlike-sign tracks detected in the muon spectrometer.
- Offline decisions for the V0A detector to be empty to ensure the exclusivity of the collision.
- Offline decisions for the V0C detector to be either empty or with timing corresponding to beam-beam collisions. If there is a signal in the V0C, it must consist of a maximum of two hits in the V0C cells, as there should only be two muons coming from the J/ψ decay. The reason for the maximum is that the rapidity range of the muon spectrometer is slightly wider than that of the V0C, allowing muons to miss the V0C but still be detected in the muon spectrometer.

Additional requirements were also applied for the individual muon tracks:

- The pseudorapidity of each muon track is required to be within the range $-4.0 < \eta_\mu < -2.5$.
- The radial position of each muon track at the end of the front muon absorber, R_{abs}, must lie within the range 17.5 cm $< R_{\text{abs}} <$ 89.5 cm to ensure that they pass through the homogeneous region of the absorber.
- Each muon detected in the muon tracking chamber must be matched to a muon detected in the muon trigger chamber, passing the 1 GeV/c p_{T} threshold cut.
- The momentum-dependent DCA cut (distance of closest approach to the interaction point times momentum of the track) is set to $(p \times \text{DCA}) < 6\sigma$ for each track to remove beam-induced background.

Finally, conditions required for the candidate unlike-sign dimuons were the following:

- The rapidity of the dimuon should be in the range $-4.0 < y_{\mu\mu} < -2.5$.
- For the signal extraction in the invariant mass fit, the dimuon should have a transverse momentum of $p_{\text{T}}^{\mu\mu} < 250$ MeV/c to enrich the data sample with coherent events.
- For the transverse momentum fit, the invariant mass of the dimuon should be in the range $2.85 < M_{\mu\mu} < 3.35$ GeV/c^2, where the J/ψ count outweighs that of the background. This range is also used to extract the J/ψ yield.

The selection criteria applied to the candidate events in the central data set, selected by the `CCUP31` trigger, are the same as in Ref. [34]:

- A primary vertex reconstructed using at least two tracks and its position has to be within 15 cm from the nominal IP in the beam direction.
- Exactly two unlike-sign tracks in the central barrel.
- Offline decisions for the V0 and AD detectors to be empty to ensure the exclusivity of the collision.

Only lepton tracks passing the following quality criteria were considered:

- Each track is required to cross both SPD layers and at least 70 (out of 159) TPC pad rows.
- The DCA cut is set to DCA $<$ 2cm in the beam direction for each track.

For the selected track pairs:

- The dilepton should have a transverse momentum of $p_{\mathrm{T}} < 200$ MeV/c to enrich the data sample with coherent events for the signal extraction in the invariant mass fit.
- The dilepton invariant mass should be in the range $2.9 < M_{\mathrm{l^+l^-}} < 3.2$ GeV/c^2, where the J/ψ count outweighs that of the background, for the transverse momentum fit. This range is also used to extract the J/ψ yield.

To determine if a track should be identified as an electron or a muon the TPC energy loss PID capabilities are utilized.

To categorize the analyzed events into the four neutron emission classes (0n0n, 0nXn, Xn0n, XnXn) defined in Sec. 1.6, information from the ZDC detector is utilized. The decision flag for activity in the ZDC is constrained by a time selection. Only ZDC activity within a 2 ns window around the beam-beam collision time is taken into account in order to suppress background.

4.3 Models for yield extraction

The model used to describe the invariant mass distributions of the candidate events is composed of three functions. To account for the two charmonia resonances, the J/ψ and the ψ′, two Crystal Ball (CB) functions [108] were used

$$\begin{aligned} f(m;\alpha,n,m_0,\sigma) &= \exp\left(-\frac{1}{2}\bar{m}^2\right) \quad \text{for } \bar{m} > -\alpha, \\ &= A\,(B-\bar{m})^{-n} \quad \text{for } \bar{m} \leq -\alpha, \end{aligned} \tag{4.1}$$

where

$$\begin{aligned} \bar{m} &= \frac{m-m_0}{\sigma}, \\ A &= \left(\frac{n}{|\alpha|}\right)^n \exp\left(-\frac{|\alpha|^2}{2}\right), \\ B &= \frac{n}{|\alpha|} - |\alpha|. \end{aligned} \tag{4.2}$$

The function is composed of a Gaussian (with m_0 as the mean and σ as the width) and an exponential times a power-law tail (described by the parameters α and n). The tail corrects for the radiation losses of the particles within the detector. Additionally, the parameter α serves as the number of widths below the resonance peak where the function transitions between the two forms.

For fitting the J/ψ and ψ′ peaks in the data, the α and n parameters were fixed to values obtained from the reconstructed Monte Carlo data sets. The m_0 parameter

for the J/ψ was left free in the fit to the data. Since the width of the J/ψ was larger in the data than in the reconstructed Monte Carlo, the parameter σ was also left free for the J/ψ. For the ψ' peak, the σ parameter was fixed to the value of the σ parameter of the J/ψ multiplied by the ratio of the widths of the ψ' to the J/ψ in Monte Carlo (approximately 1.09). The m_0 parameter for the ψ' was fixed to that of the J/ψ and shifted by the corresponding mass values taken from PDG [109]. This adjustment was made because the ψ' peak in the data is not significant enough to reliably determine this parameter. In the end, the only free parameters left for the fit were the J/ψ mass, width, and normalizations of the J/ψ and ψ' peaks.

So far, the fitting procedure described here is identical between the central and forward data sets. However, the last part of the fitting model is dedicated to describing the background, primarily originating from the $\gamma\gamma \to l^+l^-$ process. The invariant mass distribution for this process follows an exponential shape, and in the central data set, it is modeled with a simple exponential, where the exponential slope and normalization are treated as free parameters. For the forward data set the situation is more complex. At high invariant masses, the background follows the expected exponential shape. However, below the J/ψ peak, it deviates from this shape due to the influence of the ALICE detector efficiency in this rapidity space. To account for this effect, the background distribution was fitted using a fourth-order polynomial, smoothly transitioning to an exponential tail from 4 GeV/c^2 onward:

$$\begin{aligned} f(m;\lambda,m_t,a_2,a_3,a_4) &= e^{\lambda m} && \text{for } m > m_t, \\ &= e^{\lambda m}[1 + a_2\bar{m}^2 + a_3\bar{m}^3 + a_4\bar{m}^4] && \text{for } m \leq m_t, \end{aligned} \tag{4.3}$$

where

$$\bar{m} = m - m_t, \tag{4.4}$$

with $m_t = 4$ GeV/c^2. The coefficients a_i of the polynomial were obtained by fitting the reconstructed Monte Carlo data. These coefficients were then kept fixed in the fit to the experimental data. Only the slope λ of the exponential term and the overall normalization of this contribution were left free, and the fitted slope is found to be very close in value to that obtained from Monte Carlo.

4.4 Invariant mass fit and yield extraction

All invariant mass fits were performed using the extended maximum likelihood method on unbinned data sets. The invariant mass fits used for yield extraction in forward data set are divided into three rapidity bins. The three rapidity bins are $-4.0 < y < -3.5$, $-3.5 < y < -3.0$, and $-3.0 < y < -2.5$. There is also a fit showing the distribution integrated in rapidity. The mass spectra are constrained by

the $p_{\mathrm{T}} < 0.25$ GeV/c cut to enrich the sample with coherent events. The invariant mass fits for the forward data set in the neutron emission integrated case are shown in Fig. 4.3, for the 0n0n class in Fig. 4.4, for the 0nXn class in Fig. 4.5, for the Xn0n class in Fig. 4.6, and for the XnXn class in Fig. 4.7.

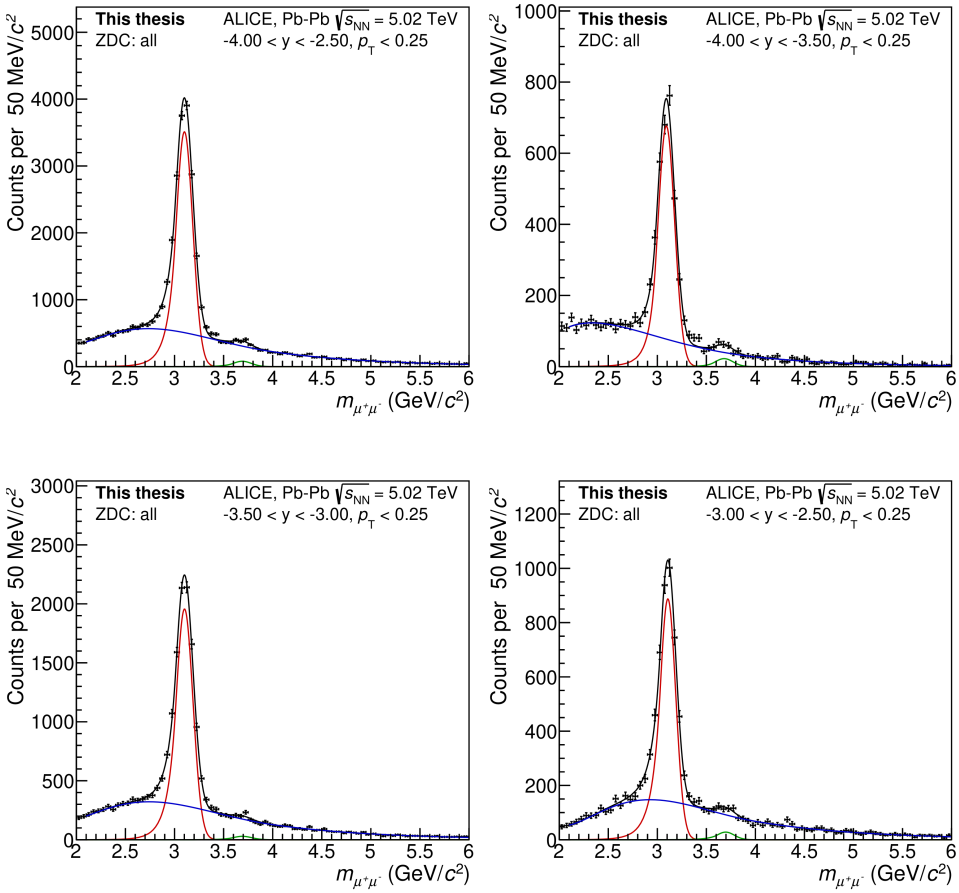

Figure 4.3: The fit of the invariant mass distribution for the selected dimuon events in the forward data set, as discussed in Sec. 4.1 and 4.2, integrated in neutron emission classes and divided into three rapidity bins ($-4.0 < y < -3.5$, $-3.5 < y < -3.0$, and $-3.0 < y < -2.5$). Additionally, a plot integrated in rapidity is also shown. The details of the fit model can be found in Sec. 4.3.

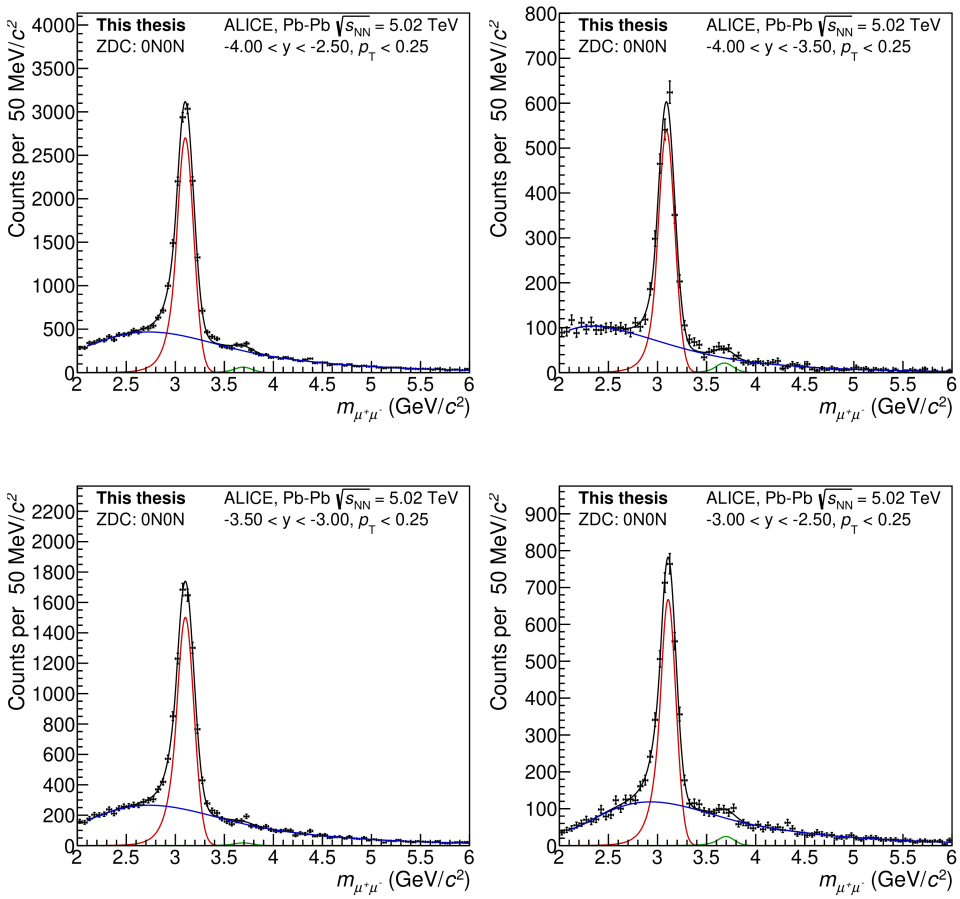

Figure 4.4: The fit of the invariant mass distribution for the selected dimuon events in the forward data set, as discussed in Sec. 4.1 and 4.2, in the 0n0n neutron emission class and divided into three rapidity bins ($-4.0 < y < -3.5$, $-3.5 < y < -3.0$, and $-3.0 < y < -2.5$). Additionally, a plot integrated in rapidity is also shown. The details of the fit model can be found in Sec. 4.3.

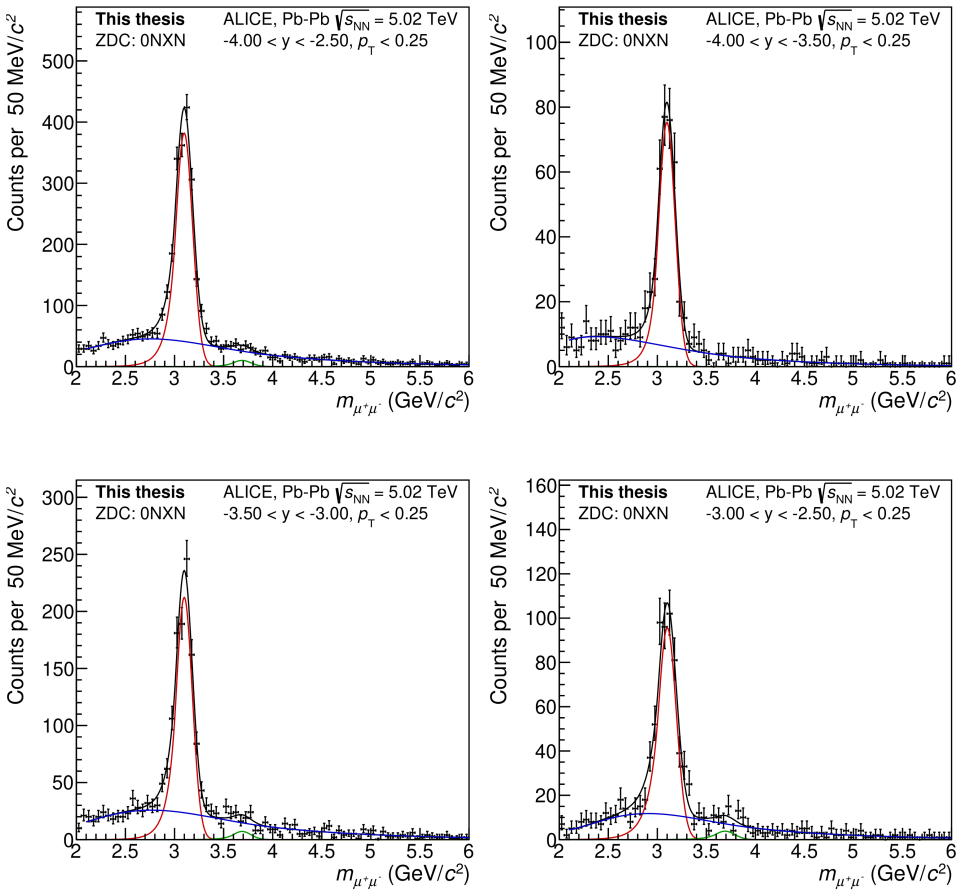

Figure 4.5: The fit of the invariant mass distribution for the selected dimuon events in the forward data set, as discussed in Sec. 4.1 and 4.2, in the 0nXn neutron emission class and divided into three rapidity bins ($-4.0 < y < -3.5$, $-3.5 < y < -3.0$, and $-3.0 < y < -2.5$). Additionally, a plot integrated in rapidity is also shown. The details of the fit model can be found in Sec. 4.3.

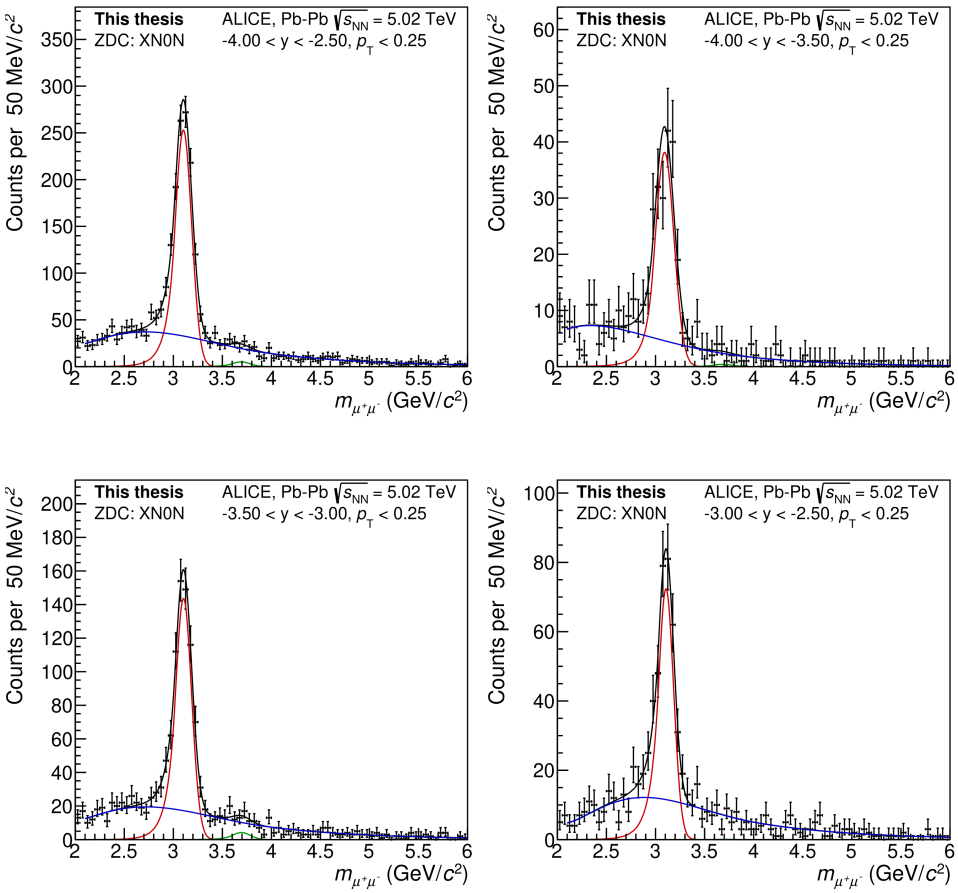

Figure 4.6: The fit of the invariant mass distribution for the selected dimuon events in the forward data set, as discussed in Sec. 4.1 and 4.2, in the Xn0n neutron emission class and divided into three rapidity bins ($-4.0 < y < -3.5$, $-3.5 < y < -3.0$, and $-3.0 < y < -2.5$). Additionally, a plot integrated in rapidity is also shown. The details of the fit model can be found in Sec. 4.3.

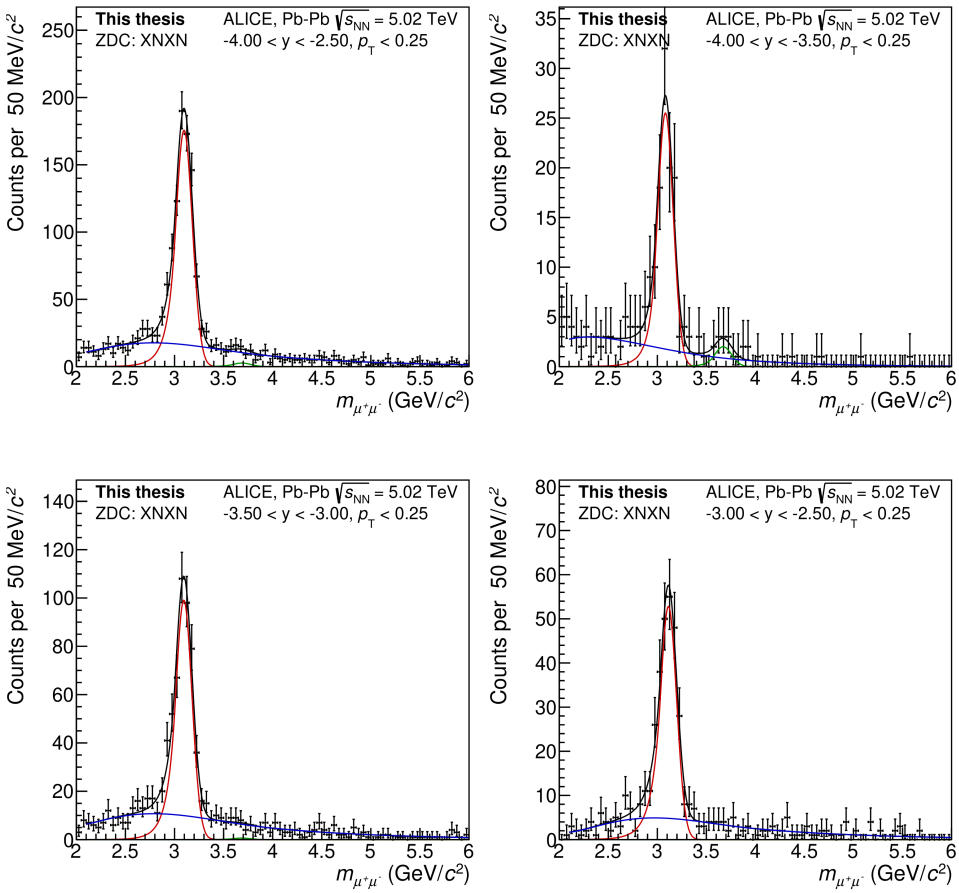

Figure 4.7: The fit of the invariant mass distribution for the selected dimuon events in the forward data set, as discussed in Sec. 4.1 and 4.2, in the XnXn neutron emission class and divided into three rapidity bins ($-4.0 < y < -3.5$, $-3.5 < y < -3.0$, and $-3.0 < y < -2.5$). Additionally, a plot integrated in rapidity is also shown. The details of the fit model can be found in Sec. 4.3.

As the analysis is differential in neutron emission classes, it results in having a smaller data set for each class. Especially, the XnXn class suffers from this effect. Therefore, in the central rapidity data set, the $J/\psi \to e^+e^-$ and $J/\psi \to \mu^+\mu^-$ decay channel measurements were joined into a single data set to include as many events as possible. In previous publications [34], it has been demonstrated that the cross sections measured in these decay channels are consistent, thus justifying this approach.

Due to the symmetrical nature of the measurement at central rapidity, the 0nXn and Xn0n EMD classes exhibit exactly the same behavior. For this reason, they were merged and treated as one data set in the analysis.

The invariant mass fit in the central data set is done similarly to the forward case; the differences are discussed in Sec. 4.1, Sec. 4.2, and Sec. 4.3. The yields are extracted in two rapidity bins, $|y| < 0.2$ and $0.2 < |y| < 0.8$.

The obtained J/ψ yields from the forward data set can be seen in Tab. 4.1 and from the central data set in Tab. 4.2.

EMD class	Rapidity	J/ψ yield
0n0n	$-4.0 < y < -2.5$	12490 ± 171
	$-4.0 < y < -3.5$	2939 ± 84
	$-3.5 < y < -3.0$	7102 ± 102
	$-3.0 < y < -2.5$	2403 ± 74
0nXn	$-4.0 < y < -2.5$	1773 ± 62
	$-4.0 < y < -3.5$	475 ± 26
	$-3.5 < y < -3.0$	952 ± 46
	$-3.0 < y < -2.5$	332 ± 27
Xn0n	$-4.0 < y < -2.5$	1149 ± 51
	$-4.0 < y < -3.5$	318 ± 28
	$-3.5 < y < -3.0$	638 ± 37
	$-3.0 < y < -2.5$	189 ± 16
XnXn	$-4.0 < y < -2.5$	811 ± 42
	$-4.0 < y < -3.5$	247 ± 23
	$-3.5 < y < -3.0$	450 ± 32
	$-3.0 < y < -2.5$	111 ± 16

Table 4.1: The values of the extracted J/ψ yields and their statistical uncertainty obtained from the fits to the forward rapidity data set for each of the EMD classes and rapidity intervals.

EMD class	Rapidity	J/ψ yield
0n0n	$\lvert y \rvert < 0.2$	1744 ± 49
	$0.2 < \lvert y \rvert < 0.8$	2179 ± 54
0nXn+Xn0n	$\lvert y \rvert < 0.2$	412 ± 23
	$0.2 < \lvert y \rvert < 0.8$	597 ± 28
XnXn	$\lvert y \rvert < 0.2$	84 ± 11
	$0.2 < \lvert y \rvert < 0.8$	134 ± 13

Table 4.2: The values of the extracted J/ψ yields and their statistical uncertainty obtained from the fits to the central rapidity data set for each of the EMD classes and rapidity intervals.

4.5 Acceptance times efficiency

The detector acceptance-times-efficiency values ($A \times \varepsilon$) were computed using the Monte Carlo simulation. This was done by taking the ratio between the number of reconstructed events in a given rapidity range, which passed the same selection criteria as applied in real data analysis, and the number of generated events in the corresponding rapidity range. The computed values are rapidity-dependent but do not change with neutron emission class. They can be found in Tab. 4.3.

Rapidity	$(A \times \varepsilon)$
$\lvert y \rvert < 0.2$	5.3%
$0.2 < \lvert y \rvert < 0.8$	2.4%
$2.5 < \lvert y \rvert < 3.0$	6.9%
$3.0 < \lvert y \rvert < 3.5$	19.4%
$3.5 < \lvert y \rvert < 4.0$	9.7%

Table 4.3: The detector acceptance-times-efficiency values computed using MC data sets with the same selection criteria as applied for the J/ψ yield extraction.

The MC simulation was performed assuming a transverse polarization of the photons, as was recently reported by the ALICE collaboration [110]. For the central rapidity measurement, the interference effect [45] can lead to an azimuthal anisotropy in the final state [111, 112]. This effect is most pronounced at low transverse momentum and low impact parameter. However, since the presented measurement is integrated in p_T, and the XnXn EMD class, which has the lowest impact parameter, has the highest statistical uncertainty, the interference effect is not visible in the analyzed data.

The $(A \times \varepsilon)$ is computed two times, once with the p_T cut (see Sec. 4.2) applied to the reconstructed events, and once without the p_T cut applied but within the restricted mass range of $2.85 < M_{\mu\mu} < 3.35$ GeV/c^2. This is because the first value is needed to compute the cross section, while the second is used in the transverse momentum fit to constrain the function corresponding to the feed-down contribution, see details in Sec. 4.7.

The number of analyzed Monte Carlo events is scaled proportionally to the run-by-run analyzed luminosity to ensure correct weighting of $(A \times \varepsilon)$ coming from individual runs, while attempting to utilize the maximum number of events available in the Monte Carlo production.

4.6 Feed-down fraction

To correct the extracted yields for the J/ψ particles originating from the decay of $\psi' \to J/\psi$+X, where the decay products X were not detected, it is necessary to determine a feed-down correction (f_D). This correction can be computed by utilizing the measured data and Monte Carlo simulations. First, it is necessary to determine the ψ' to J/ψ yield ratio (R_N) in the recorded data sample:

$$R_N = \frac{N_{\psi'}}{N_{J/\psi}}, \tag{4.5}$$

where N denotes the extracted yield. R_N can be also written out as a ratio of the number of primary ψ' and a sum of the primary and feed-down J/ψ. When the yields are expressed using cross sections (σ - which are unknown), branching ratios

(*BR* - which are taken from PDG [109]), and $(A \times \varepsilon)$ (which are determined from Monte Carlo), the formula takes the following form (for the dimuon decay channel):

$$R_N = \frac{N(\psi' \to \mu\mu)}{N(J/\psi \to \mu\mu) + N(\psi' \to J/\psi \to \mu\mu)} =$$

$$= \frac{\sigma_{\psi'} BR_{\psi' \to \mu\mu} (A \times \varepsilon)_{\psi'}}{\sigma_{J/\psi} BR_{J/\psi \to \mu\mu} (A \times \varepsilon)_{J/\psi} + \sigma_{\psi'} BR_{\psi' \to J/\psi} (A \times \varepsilon)_{\psi' \to J/\psi} BR_{J/\psi \to \mu\mu}}. \quad (4.6)$$

By algebraic manipulations, it is possible to express the unknown ratio of the ψ' to J/ψ cross sections from Eq. 4.6, leaving only the ratio R_N, known from our data set, and the *BR* and $(A \times \varepsilon)$ values, which are also known. All other relevant factor cancel out in the ratio

$$\frac{\sigma(\psi')}{\sigma(J/\psi)} = \frac{R_N BR(J/\psi \to \mu\mu)\varepsilon(J/\psi)}{BR(\psi' \to \mu\mu)\varepsilon(\psi') - R_N BR(\psi' \to J/\psi)\varepsilon(\psi' \to J/\psi) BR(J/\psi \to \mu\mu)}. \quad (4.7)$$

With this, it is possible to finally express the feed-down correction factor by substituting Eq. 4.7 into Eq. 4.8 without the explicit knowledge of the respective J/ψ and ψ' cross sections.

$$f_D = \frac{N(\text{feed-down } J/\psi)}{N(\text{primary } J/\psi)} = \frac{\sigma(\psi')}{\sigma(J/\psi)} \frac{\varepsilon(\psi' \to J/\psi) BR(\psi' \to J/\psi)}{\varepsilon(J/\psi)}. \quad (4.8)$$

The feed-down correction is fixed across all rapidity bins and neutron emission classes, taking the values $f_D = 0.039 \pm 0.006$ and $f_D = 0.055 \pm 0.010$ for the central and forward rapidity data sets, respectively.

4.7 Transverse momentum fit and correction for incoherent contamination

Another correction that has to be applied to the J/ψ yields extracted from the invariant mass fits is the correction for the contribution originating from the incoherent J/ψ photoproduction. To determine the fraction of coherent to incoherent events (f_I) in the kinematic region used to extract the J/ψ yield, a fit to the transverse momentum distribution is performed. Only events under the J/ψ peak are considered: $2.85 < M_{\mu\mu} < 3.35$ GeV/c^2 for the forward data set and $2.9 < M_{l^+l^-} < 3.2$ GeV/c^2 for the central data set.

The p_T fits, like the invariant mass fits, utilize the extended maximum likelihood method on unbinned data sets. They are performed using RooFit PDF templates created from the reconstructed STARlight MC events. The fit model is constructed as a sum of the PDF templates.

The RooFit PDF templates are available for coherent J/ψ photoproduction, incoherent J/ψ photoproduction, coherent and incoherent feed-down contributions from ψ', and the $\gamma\gamma \to l^+l^-$ background continuum.

The normalization of the $\gamma\gamma$ background in the transverse momentum fit model was fixed to the background yield under the corresponding J/ψ peak region in the invariant mass fit. The normalization for the feed-down templates was fixed to that of their primary photoproduction counterparts and scaled down by the f_D correction factor (computed without the p_T cut present during the yield extraction).

In the transverse momentum spectra of the measured data there is a high p_T tail which comes from an incoherent J/ψ photoproduction with nucleon dissociation. For this process there is no Monte Carlo simulation describing its shape properly. To incorporate this contribution into the fit model a dependence used by the H1 collaboration in [113] is used.

$$\frac{dN}{dp_T} \sim p_T(1 + \frac{b_{pd}}{n_{pd}} p_T^2)^{-n_{pd}} \tag{4.9}$$

For the central rapidity data set, the parameter values used for the fit were taken from the high-energy data set (40 GeV $< W_{\gamma p} <$ 110 GeV) in [113]: $b_{pd} = 1.79$ (GeV^{-2}) and $n_{pd} = 3.58$.

In the forward rapidity data set, J/ψ photoproduction with nucleon dissociation contributes more significantly than in the central data set. Directly adopting the parameter values from [113] does not yield a satisfactory description of the distribution. Therefore, following the procedure used in [113] where a fit was unable to constrain both n_{pd} and b_{pd} simultaneously, the fit parameter n_{pd} is fixed to the value obtained in [113] ($n_{pd} = 3.58$). The b_{pd} parameter was estimated by fitting the 0nXn data sample enriched with dissociative events by requiring a signal in the AD detector.

The only remaining free parameters in the p_T fits are the normalization parameters for the different RooFit PDF templates and the normalization parameter for the model describing the dissociative tail.

The transverse momentum fits of the forward data set for the neutron emission integrated case are shown in Fig. 4.8, for the 0n0n EMD class in Fig. 4.9, for the 0nXn EMD class in Fig. 4.10, for the Xn0n EMD class in Fig. 4.11, and for the XnXn EMD class in Fig. 4.12. For each EMD class, the fits in the three rapidity bins used for yield extraction are shown, as well as a plot integrated in rapidity.

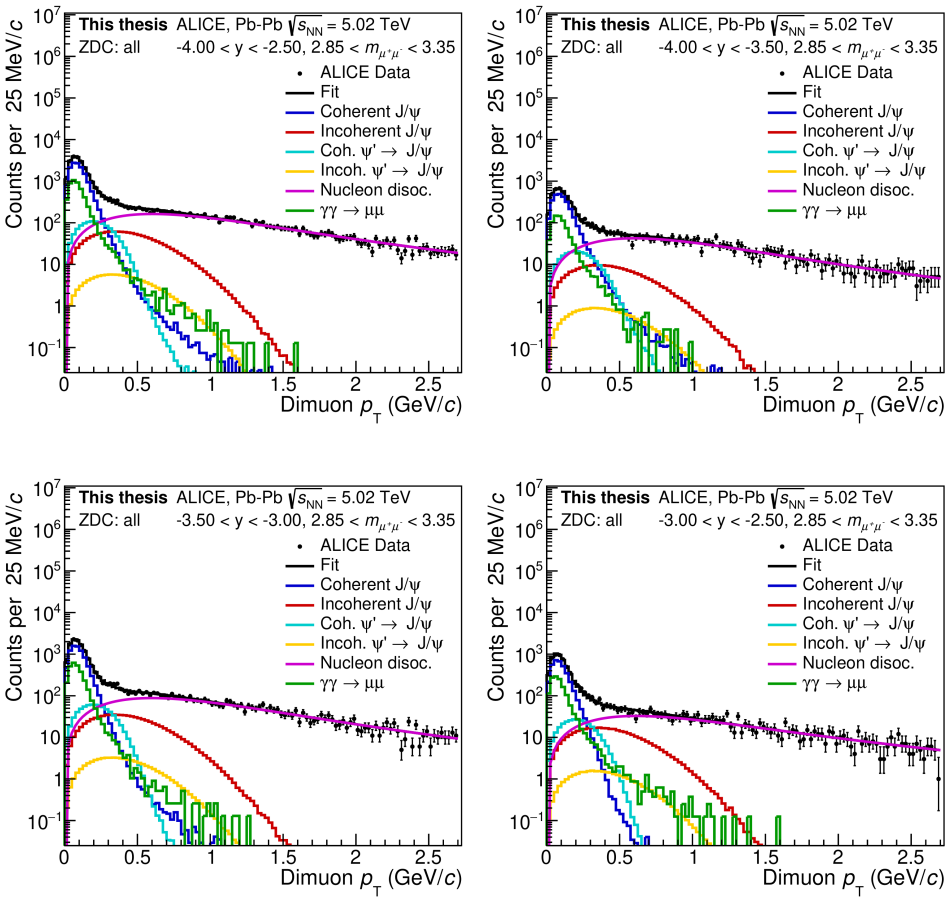

Figure 4.8: Fit of the transverse momentum distribution for the forward data set, integrated in neutron emission classes and divided into three rapidity bins (an integrated plot is also shown). The fit model consists of RooFit PDF templates for coherent J/ψ, incoherent J/ψ, coherent and incoherent feed down from ψ', and the $\gamma\gamma \to \mu\mu$ background, along with an H1 function used to describe the dissociative tail.

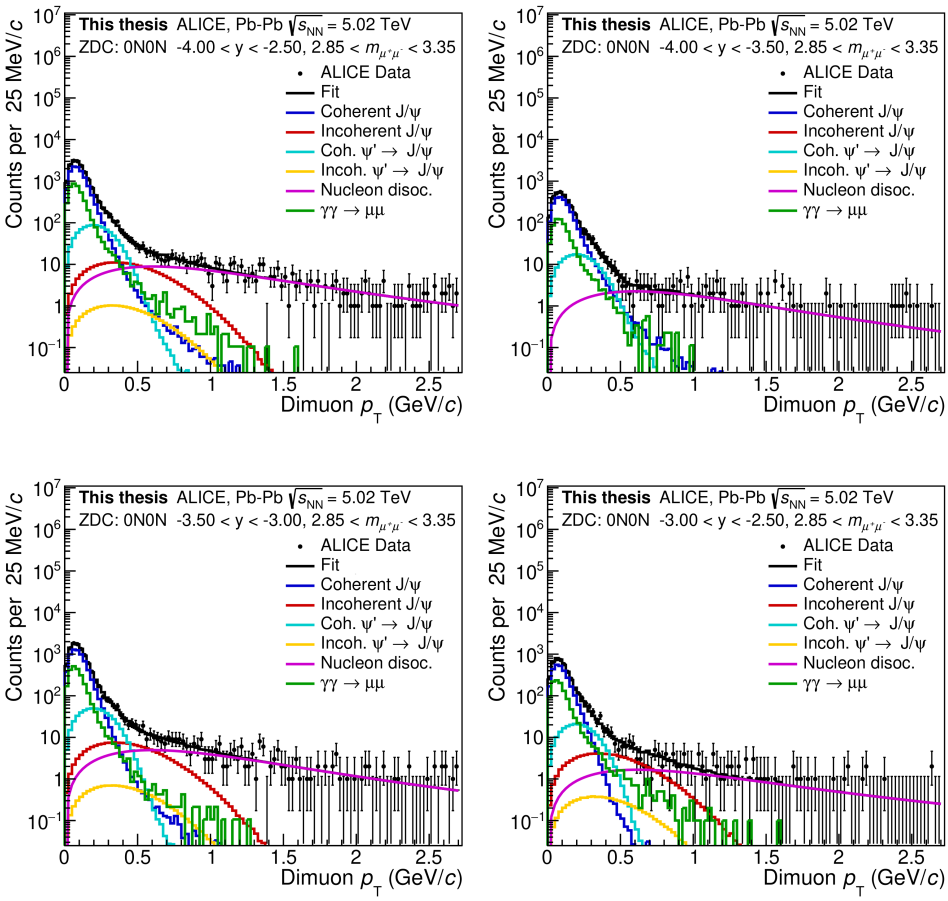

Figure 4.9: Fit of the transverse momentum distribution for the forward data set, within the 0n0n neutron emission class and divided into three rapidity bins (an integrated plot is also shown). The fit model consists of RooFit PDF templates for coherent J/ψ, incoherent J/ψ, coherent and incoherent feed down from ψ', and the $\gamma\gamma \to \mu\mu$ background, along with an H1 function used to describe the dissociative tail.

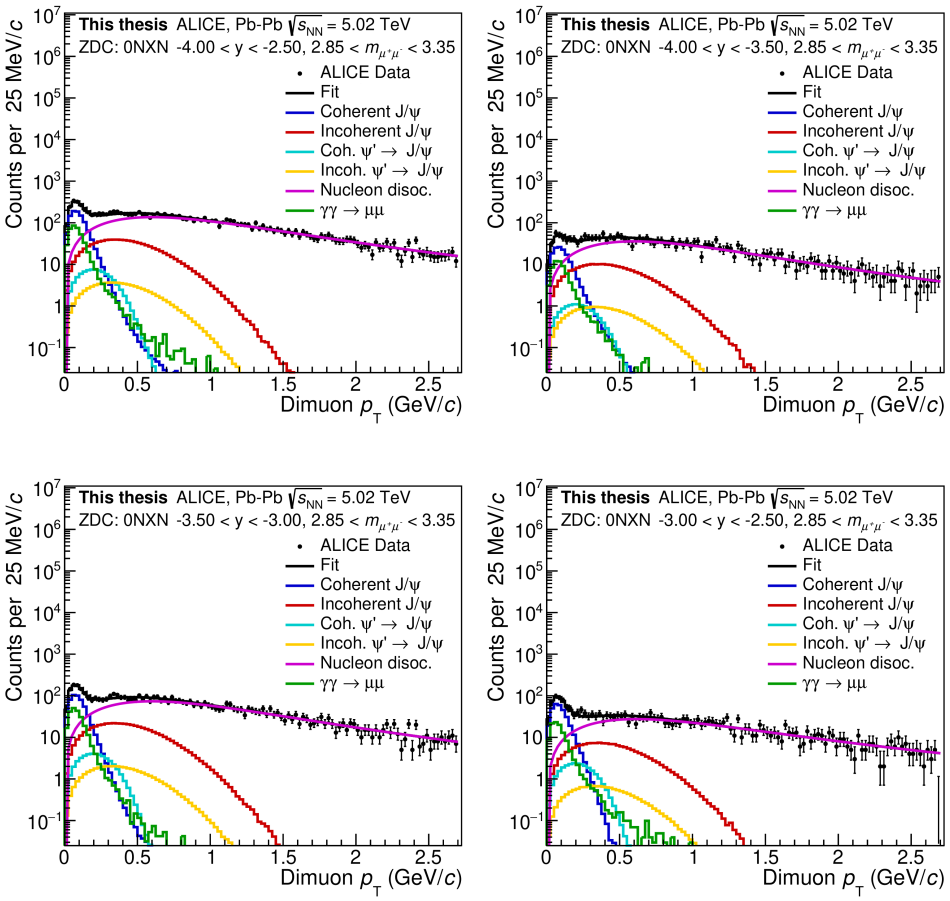

Figure 4.10: Fit of the transverse momentum distribution for the forward data set, within the 0nXn neutron emission class and divided into three rapidity bins (an integrated plot is also shown). The fit model consists of RooFit PDF templates for coherent J/ψ, incoherent J/ψ, coherent and incoherent feed down from ψ', and the $\gamma\gamma \to \mu\mu$ background, along with an H1 function used to describe the dissociative tail.

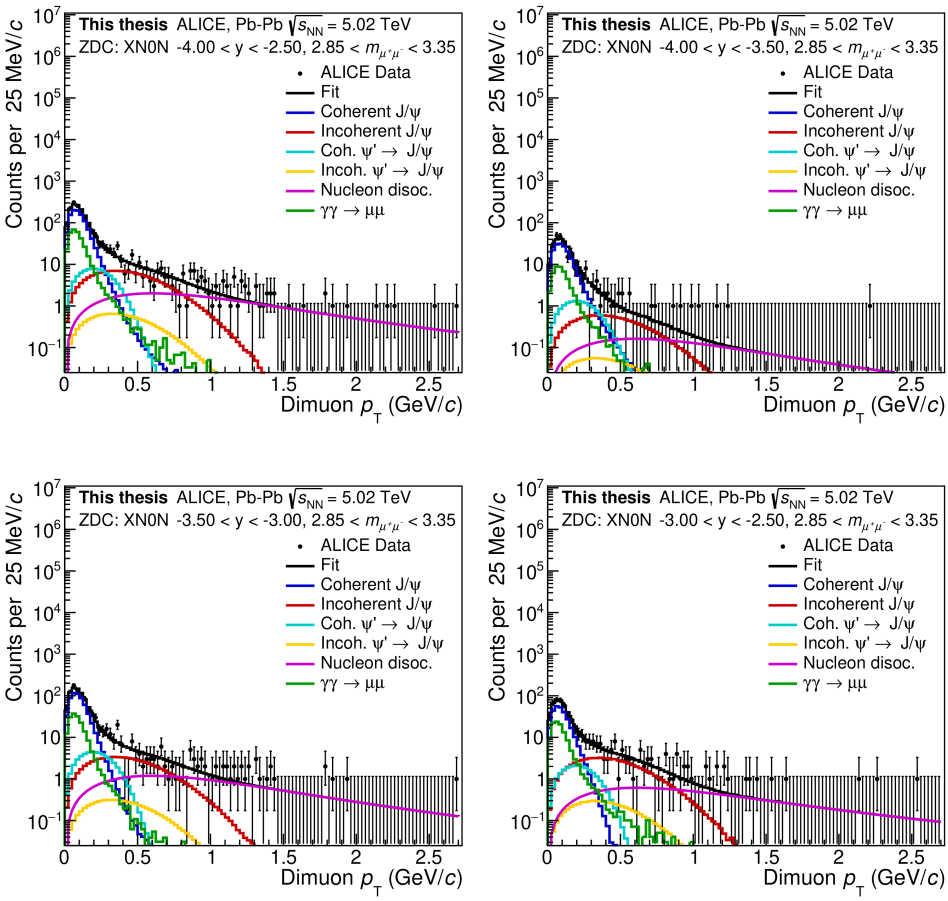

Figure 4.11: Fit of the transverse momentum distribution for the forward data set, within the Xn0n neutron emission class and divided into three rapidity bins (an integrated plot is also shown). The fit model consists of RooFit PDF templates for coherent J/ψ, incoherent J/ψ, coherent and incoherent feed down from ψ', and the $\gamma\gamma \to \mu\mu$ background, along with an H1 function used to describe the dissociative tail.

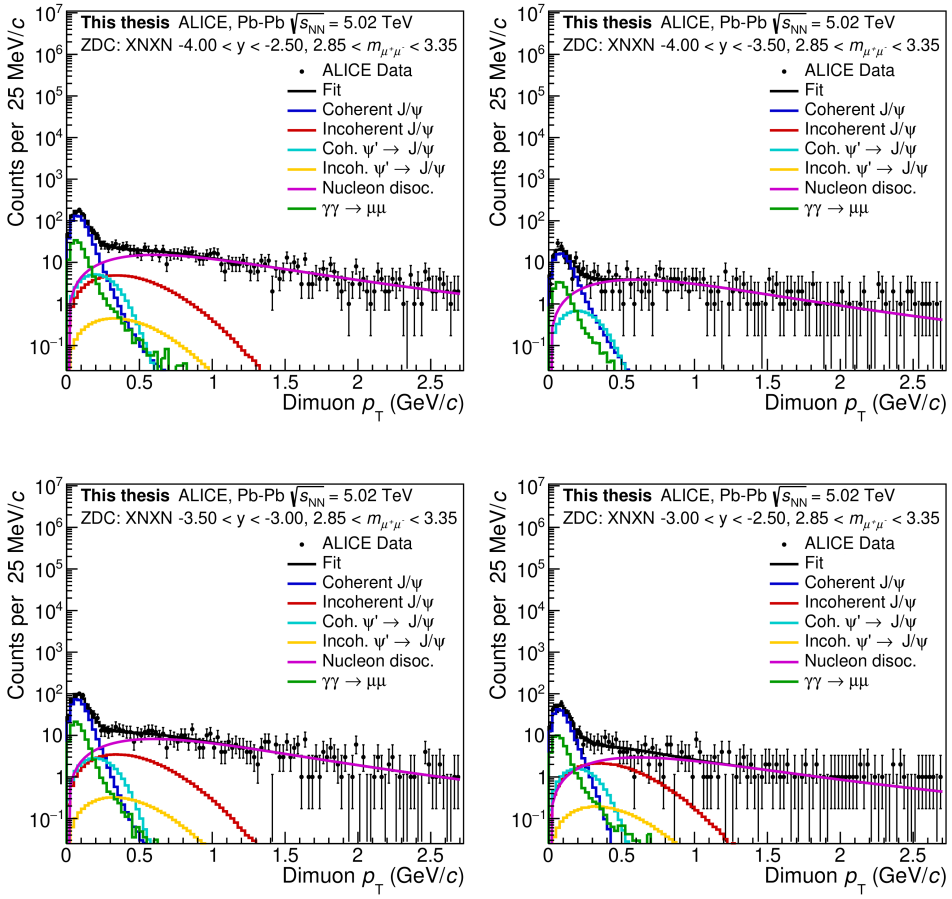

Figure 4.12: Fit of the transverse momentum distribution for the forward data set, within the XnXn neutron emission class and divided into three rapidity bins (an integrated plot is also shown). The fit model consists of RooFit PDF templates for coherent J/ψ, incoherent J/ψ, coherent and incoherent feed down from ψ', and the $\gamma\gamma \to \mu\mu$ background, along with an H1 function used to describe the dissociative tail.

The values for the incoherent fraction contamination (f_I) are computed as the ratio of the number of incoherent to coherent processes (N_{process}) contained in the p_T fit model. The yields are computed from the p_T fits while applying the p_T cut as it is applied in the invariant mass fits used to extract the number of J/ψ candidates. The formula to compute the f_I is

$$f_I = \frac{N_{\text{Incoh. J}/\psi} + N_{\text{Nucleon disoc.}}}{N_{\text{Coh. J}/\psi}}. \tag{4.10}$$

The values of f_I for the forward data set are provided in Tab. 4.4, and for the central data set, they are presented in Tab. 4.5.

EMD class	Rapidity	f_I
0n0n	$-4.0 < y < -2.5$	1.20%
	$-4.0 < y < -3.5$	0.70%
	$-3.5 < y < -3.0$	1.30%
	$-3.0 < y < -2.5$	1.40%
0nXn	$-4.0 < y < -2.5$	88.30%
	$-4.0 < y < -3.5$	171.00%
	$-3.5 < y < -3.0$	91.10%
	$-3.0 < y < -2.5$	50.90%
Xn0n	$-4.0 < y < -2.5$	5.20%
	$-4.0 < y < -3.5$	2.70%
	$-3.5 < y < -3.0$	4.80%
	$-3.0 < y < -2.5$	7.70%
XnXn	$-4.0 < y < -2.5$	14.50%
	$-4.0 < y < -3.5$	16.50%
	$-3.5 < y < -3.0$	15.90%
	$-3.0 < y < -2.5$	11.80%

Table 4.4: Table displaying incoherent fractions for the forward rapidity data sample, obtained from transverse momentum fits.

EMD class	Rapidity	f_I
0n0n	$\|y\| < 0.2$	1.4%
	$0.2 < \|y\| < 0.8$	1.4%
0nXn+Xn0n	$\|y\| < 0.2$	17.9%
	$0.2 < \|y\| < 0.8$	17.9%
XnXn	$\|y\| < 0.2$	14.4%
	$0.2 < \|y\| < 0.8$	14.4%

Table 4.5: Table displaying incoherent fractions for the central rapidity data sample, obtained from transverse momentum fits.

As shown in Tab. 4.4, the 0nXn EMD class exhibits a very high contribution from incoherent events in the forward data set, with incoherent events even dominating over the coherent ones in some rapidity regions. For this reason, the 0nXn neutron emission class was excluded from the final analysis results.

4.8 EMD corrections

As mentioned in Sec. 1.6, other particles besides neutrons can be produced in an EMD event. For sufficiently energetic photons, pion or proton production is possible [114], and this can lead to the event being vetoed by the forward detectors used to ensure the exclusivity of the recorded events.

In addition, the classification of events into EMD classes can be biased due to the pile-up of EMD events or efficiency losses in the ZDC, necessitating a correction for these effects. Since all of these corrections are connected to the EMD process, they have been grouped into this section and are discussed below.

4.8.1 Correction for events lost due to detector veto

As described in Sec. 4.1, the trigger `CMUP6` (`CCUP31`) used for event selection in the forward (central) rapidity region includes a veto for activity in the V0A (V0 and AD) detector(s). Additionally, an offline requirement for the detector decision being empty is applied. Under these conditions, some events are lost due to pileup from EMD processes, resulting in inefficiency in the application of the trigger veto requirements. There are two types of EMD losses:

- EMD pileup: Charged particles can be produced by an EMD in a collision of a different pair of ions, in the same bunch crossing, than those which produced the vector meson.
- EMD veto: Charged particles can be produced by an EMD in a collision of the same pair of ions that produced the vector meson under study.

Correction for EMD pileup

Correction for the pileup coming from a different pair of ions than the one producing the vector meson is computed using the `CTRUE-B` trigger. This is a special control trigger that aims to be as unbiased as possible by triggering only on beam-beam collision timing, rather than any detector signal:

- `CTRUE-B` $\equiv$ trigger on the bunch crossing time window.

For any veto requirements, the inefficiency originating from the decision is estimated by computing the probability of observing the studied detector signal in an otherwise empty detector. Specifically, for the forward analysis, this involves the V0A signal in beam-beam timing with no other signals present in the entire ALICE detector. This probability is a function of the average number of inelastic hadronic collisions per bunch-crossing (μ).

The study is conducted run by run, and to compute the average value, the probabilities are weighted using the run-by-run analyzed integrated luminosity for the corresponding trigger. This weighting is achieved by utilizing the Poisson probability distribution. The dependence of the V0A veto, along with a first-order polynomial fit demonstrating a linear dependence on the μ value, is plotted in Fig. 4.13. The average V0A veto efficiency, inclusive of both the online and offline trigger decisions, is displayed along with its statistical error.

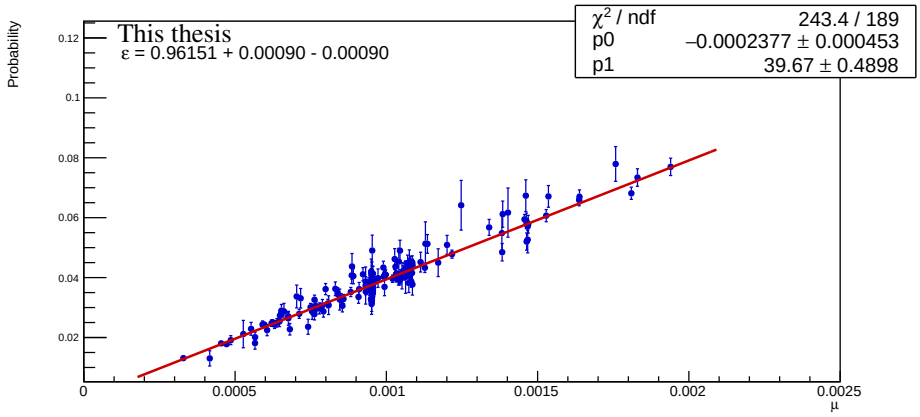

Figure 4.13: The probability of having the V0A (online + offline) decision fired in an otherwise empty detector as a function of μ. The data points are fitted using a first-order polynomial function. The average efficiency (ε) is computed with a Poisson distribution and weighted with the analyzed integrated luminosity run by run.

The probability of having a signal in the V0A (online + offline) in an otherwise empty detector is $\varepsilon_{\text{pileup}}^{\text{V0A}} = 3.85\% \pm 0.15\%$, with statistical and systematic uncertainties summed in quadrature. The systematic uncertainty was determined by making slight modifications to the definitions of the detector decision flags. The correction which is applied to the J/ψ yield is given as $\varepsilon_{\text{pu}} = (1 - \varepsilon_{\text{pileup}}^{\text{V0A}}) = 0.962 \pm 0.001$.

The value of $\varepsilon_{\text{pileup}}^{\text{V0A}}$ remains consistent across all neutron emission classes. When the CTRUE data sample is divided into neutron emission classes, and $\varepsilon_{\text{pileup}}^{\text{V0A}}$ is computed separately for each class, the results show consistency within uncertainty across all emission classes.

The procedure for the central data set follows the same approach, but the additional veto conditions result in a larger correction compared to the forward case, with $\varepsilon_{\text{pu}} = 0.920 \pm 0.002$.

Correction for EMD veto

In the forward data set, this correction is required only for the Xn0n and XnXn neutron emission classes. In the central data set, it is computed for the 0nXn+Xn0n and XnXn classes. This is because only in these classes does the EMD process produce particles in the direction of the detectors used as input for the veto.

In the forward data, to calculate the correction factor for the EMD pileup originating from the same pair of ions that produce the vector meson, it is first necessary to compute the inefficiency of the online veto of the V0A trigger. This inefficiency is estimated using the `C1ZED` trigger, which, like `CTRUE-B`, is triggered based on the beam-beam collision timing but also requires a signal in at least one of the ZDCs:

- C1ZED ≡ trigger on bunch crossing time window and require signal in at least one of the neutron ZDCs.

This online trigger inefficiency is computed as the ratio of the number of events satisfying the criteria expressed in the following expression:

$$\frac{\text{V0A offline \& !(V0A online) \& empty rest of the detector}}{\text{V0A offline \& empty rest of the detector}}. \tag{4.11}$$

If the online trigger veto was 100% efficient, this ratio would be zero. However, due to time constraints imposed on the trigger, the signal integration time is shorter in the online decision compared to the offline detector decision. Consequently, there are events that pass the online veto but are excluded by the offline veto. This is crucial because this fact allows for the correction of EMD losses caused by the online V0A veto within the CMUP6 trigger, even though there is no control trigger to monitor this effect in the forward data sample.

Note that the definition of an empty detector changes between the two neutron emission classes. In the Xn0n class, the criteria for emptiness include detectors on the C side and in the midrapidity region. Conversely, for the XnXn class, only the central region is required to be empty.

The events are studied as a function of μ and fitted with a first-order polynomial. The average online V0A veto efficiency is computed using a Poisson distribution, with the run-by-run analyzed luminosity of CMUP6 as weights. All of this can be observed in Fig. 4.14 and Fig. 4.15 for the Xn0n and XnXn neutron emission classes, respectively.

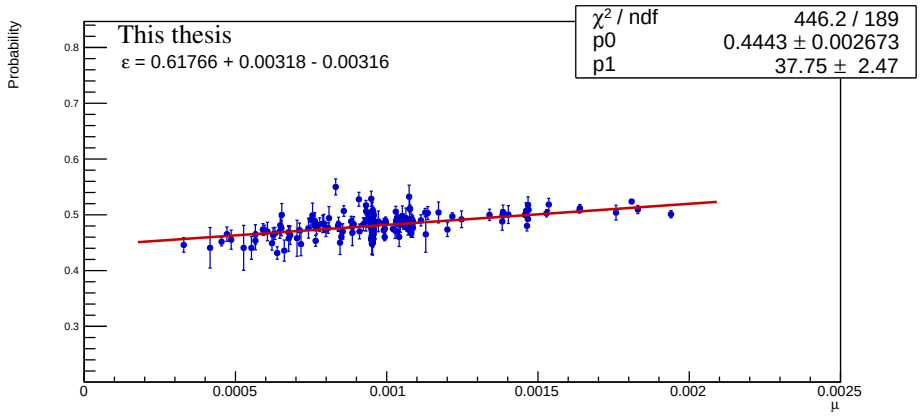

Figure 4.14: The probability of the V0A online decision not being triggered in a data set where the V0A offline decision is triggered and the rest of the detector is empty is examined as a function of μ for the Xn0n neutron emission class. The average efficiency (ε) is calculated using a Poisson distribution and weighted with the analyzed integrated luminosity on a run-by-run basis.

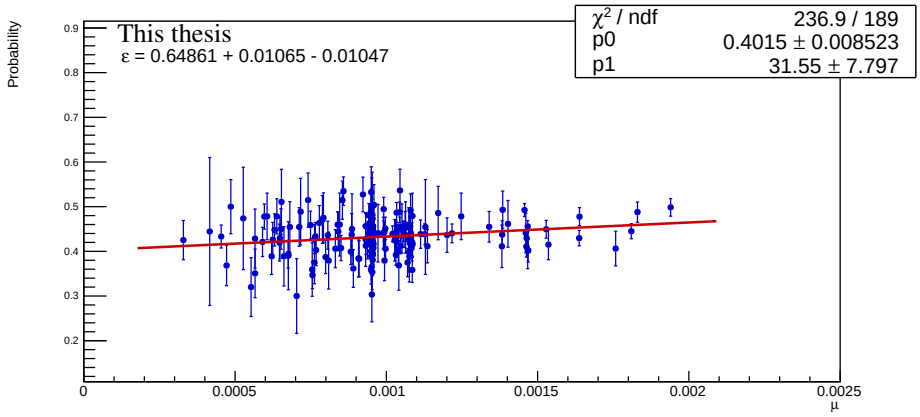

Figure 4.15: The probability of the V0A online decision not being triggered in a data set where the V0A offline decision is triggered and the rest of the detector is empty is examined as a function of μ for the XnXn neutron emission class. The average efficiency (ε) is calculated using a Poisson distribution and weighted with the analyzed integrated luminosity on a run-by-run basis.

The probability of the V0A online decision not being triggered in a data set with the V0A offline decision triggered and the rest of the detector empty (note that the definition of empty depends on the neutron emission class) is $\varepsilon_{\text{veto}}^{\text{V0A}} = 38\% \pm 3\%$ for the Xn0n neutron emission class and $\varepsilon_{\text{veto}}^{\text{V0A}} = 35\% \pm 5\%$ for the XnXn neutron emission class, with statistical and systematic uncertainties summed in quadrature. The systematic uncertainties were obtained by slightly modifying the definitions of the detector decision flags.

The correction factor, corresponding to a given neutron emission class, for the events lost due to an EMD coming from the same pair of ions that produced the vector meson can be defined as

$$\varepsilon_{\text{emd}} = \frac{N_{J/\psi(\text{seen})}}{N_{J/\psi(\text{true})}}, \tag{4.12}$$

where $N_{J/\psi(\text{seen})}$ represents the number of events observed in the analyzed data set and $N_{J/\psi(\text{true})}$ is the number of events actually produced in the collisions. When accounting for the events already corrected for losses due to pileup from a different ion pair, as described in Sec. 4.8.1, the number of observed events can be expressed as

$$N_{J/\psi(\text{seen})} = N_{J/\psi\ \&\ !\text{V0A}} + N^{\text{PU}}_{J/\psi\ \&\ !\text{V0A}}, \tag{4.13}$$

where $N_{J/\psi\ \&\ !\text{V0A}}$ is the J/ψ yield extracted in the invariant mass fit from the CMUP6 selected events with the V0A offline decision not triggered (as per the criteria used in the analysis described in Sec. 4.1). Additionally, $N^{\text{PU}}_{J/\psi\ \&\ !\text{V0A}}$ represents the

number of events lost due to EMD pileup from a different ion pair and it is computed as

$$N^{\mathrm{PU}}_{\mathrm{J}/\psi\ \&\ \mathrm{!V0A}} = \frac{N_{\mathrm{J}/\psi\ \&\ \mathrm{!V0A}}}{1-\varepsilon^{\mathrm{V0A}}_{\mathrm{pileup}}} - N_{\mathrm{J}/\psi\ \&\ \mathrm{!V0A}}. \tag{4.14}$$

Here, $\varepsilon^{\mathrm{V0A}}_{\mathrm{pileup}}$ is the correction factor computed in the previous section. The number of truly produced events can be expressed as

$$N_{\mathrm{J}/\psi(\mathrm{true})} = N^{\mathrm{VETO}}_{\mathrm{J}/\psi} + N_{\mathrm{J}/\psi\ \mathrm{and\ !V0A}} + N^{\mathrm{PU}}_{\mathrm{J}/\psi\ \mathrm{and\ !V0A}}, \tag{4.15}$$

where the second and third terms ($N_{\mathrm{J}/\psi\ \&\ \mathrm{!V0A}} + N^{\mathrm{PU}}_{\mathrm{J}/\psi\ \&\ \mathrm{!V0A}}$) are the same as in $N_{\mathrm{J}/\psi(\mathrm{seen})}$. In addition to them, the first term $N^{\mathrm{VETO}}_{\mathrm{J}/\psi}$ accounts for events lost due to EMD pileup from the same pair of ions that produced the vector meson. These events were excluded from the analyzed data set by the online V0A veto contained in the `CMUP6` trigger. The value of $N^{\mathrm{VETO}}_{\mathrm{J}/\psi}$ can be computed as

$$N^{\mathrm{VETO}}_{\mathrm{J}/\psi} = \frac{N_{\mathrm{J}/\psi\ \mathrm{and\ V0A}} - N^{\mathrm{PU}}_{\mathrm{J}/\psi\ \mathrm{and\ V0A}}}{1-\varepsilon^{\mathrm{V0A}}_{\mathrm{veto}}}. \tag{4.16}$$

$N_{\mathrm{J}/\psi\ \mathrm{and\ V0A}}$ is the J/ψ yield extracted in the invariant mass fit from the `CMUP6` selected events with the V0A offline decision triggered (opposite to the criteria used in the analysis). This yield needs correction for events where the V0A was triggered by EMD pileup from a different pair of ions than the ones that produced the vector meson. This correction is achieved by subtracting $N^{\mathrm{PU}}_{\mathrm{J}/\psi\ \mathrm{and\ V0A}}$, which is computed as

$$N^{\mathrm{PU}}_{\mathrm{J}/\psi\ \mathrm{and\ V0A}} = N_{\mathrm{J}/\psi\ \mathrm{and\ V0A}} - \frac{N_{\mathrm{J}/\psi\ \mathrm{and\ V0A}}}{1+\varepsilon^{\mathrm{V0A}}_{\mathrm{pileup}}}. \tag{4.17}$$

The corrected number of events (numerator in Eq. 4.16) undergoes the application of the correction factor (1-$\varepsilon^{\mathrm{V0A}}_{\mathrm{veto}}$), computed in this section. This correction accounts for the probability of the V0A online decision not being triggered in a data set with the V0A offline decision triggered and the rest of the detector empty. Consequently, through the (1-$\varepsilon^{\mathrm{V0A}}_{\mathrm{veto}}$) correction and using the count $N_{\mathrm{J}/\psi\ \mathrm{and\ V0A}}$ (J/ψ yield from `CMUP6` events with the V0A offline decision triggered), it becomes possible to determine the number of events that would have been observed by a trigger without the V0A trigger veto.

When all the equations above are combined, the final correction factor for a given neutron emission class is computed as

$$\varepsilon_{\text{emd}} = \frac{N_{\text{J}/\psi \text{ and !V0A}} + N^{\text{PU}}_{\text{J}/\psi \text{ and !V0A}}}{\frac{N_{\text{J}/\psi \text{ and V0A}} - N^{\text{PU}}_{\text{J}/\psi \text{ and V0A}}}{1-\varepsilon^{\text{V0A}}_{\text{veto}}} + N_{\text{J}/\psi \text{ and !V0A}} + N^{\text{PU}}_{\text{J}/\psi \text{ and !V0A}}}. \tag{4.18}$$

For the forward data set the correction factors are determined as $\varepsilon^{\text{Xn0n}}_{\text{emd}} = 0.88 \pm 0.01$ and $\varepsilon^{\text{XnXn}}_{\text{emd}} = 0.84 \pm 0.05$ for the Xn0n and XnXn neutron emission classes, respectively. For the 0n0n neutron class, the correction factor is equal to $\varepsilon^{\text{0n0n}}_{\text{emd}} = 1$.

The trigger used for the measurement of the central data set includes additional vetoes, as discussed in Sec. 4.1. The approach employed to compute the correction for the effects of the V0A and V0C vetoes follows the method described above. The computation of the correction for the ADA and ADC vetoes is simplified by the presence of a dedicated control trigger that does not contain the AD vetoes. The correction factors for the central data set are determined as $\varepsilon^{\text{0nXn+Xn0n}}_{\text{emd}} = 0.74 \pm 0.04$ and $\varepsilon^{\text{XnXn}}_{\text{emd}} = 0.57 \pm 0.05$ for the 0nXn+Xn0n and XnXn neutron emission classes, respectively.

4.8.2 Neutron emission class migration correction

The number of events in each of the neutron emission classes also needs correction for misclassification due to the combined effect of pileup and efficiency losses in the ZDC. Let N be the number of events (or cross section) before the correction for migrations of events between the EMD classes, and M be the corresponding number after the corrections have been applied. Let ε_{A} (ε_{C}) be the efficiency of the neutron ZDC on the A (C) side, and p_{A} (p_{C}) be the pileup probability for the neutron ZDC on the A (C) side. Then, the first equation describing the migrations for the 0n0n neutron emission class can be written as

$$\begin{aligned} N_{\text{0n0n}} \;=\; & M_{\text{0n0n}} \\ & -M_{\text{0n0n}} p_{\text{A}}(1-p_{\text{C}}) \\ & -M_{\text{0n0n}} p_{\text{C}}(1-p_{\text{A}}) \\ & -M_{\text{0n0n}} p_{\text{A}} p_{\text{C}} \\ & +M_{\text{0nXn}}(1-\varepsilon_{\text{C}})(1-p_{\text{A}})(1-p_{\text{C}}) \\ & +M_{\text{Xn0n}}(1-\varepsilon_{\text{A}})(1-p_{\text{A}})(1-p_{\text{C}}) \\ & +M_{\text{XnXn}}(1-\varepsilon_{\text{A}})(1-\varepsilon_{\text{C}})(1-p_{\text{A}})(1-p_{\text{C}}). \end{aligned} \tag{4.19}$$

The first line of Eq. 4.19 represents the ideal case without any corrections. The following three lines describe the corrections for losses from the 0n0n neutron emission class to the other classes due to pileup in either the ZNA, ZNC, or both of them. The next three lines then take into account the number of events that migrate

into this class due to inefficiency of the ZNC, ZNA, or both of them. Equation 4.19 can be simplified to the form of Eq. 4.20

$$\begin{aligned} N_{\mathrm{0n0n}} &= M_{\mathrm{0n0n}}(1-p_{\mathrm{A}})(1-p_{\mathrm{C}}) \\ &\quad +M_{\mathrm{0nXn}}(1-\varepsilon_{\mathrm{C}})(1-p_{\mathrm{A}})(1-p_{\mathrm{C}}) \\ &\quad +M_{\mathrm{Xn0n}}(1-\varepsilon_{\mathrm{A}})(1-p_{\mathrm{A}})(1-p_{\mathrm{C}}) \\ &\quad +M_{\mathrm{XnXn}}(1-\varepsilon_{\mathrm{A}})(1-\varepsilon_{\mathrm{C}})(1-p_{\mathrm{A}})(1-p_{\mathrm{C}}). \end{aligned} \tag{4.20}$$

Similarly, the migrations in and out of the neutron emission classes can be described by Eq. 4.21, Eq. 4.22, and Eq. 4.23 for the 0nXn, Xn0n, and XnXn classes, respectively.

$$\begin{aligned} N_{\mathrm{0nXn}} &= M_{\mathrm{0nXn}} \\ &\quad +M_{\mathrm{0n0n}}p_{\mathrm{C}}(1-p_{\mathrm{A}}) \\ &\quad -M_{\mathrm{0nXn}}\big[(1-\varepsilon_{\mathrm{C}})(1-p_{\mathrm{A}})(1-p_{\mathrm{C}})+\varepsilon_{\mathrm{C}}p_{\mathrm{A}}+(1-\varepsilon_{\mathrm{C}})p_{\mathrm{A}}p_{\mathrm{C}}\big] \\ &\quad +M_{\mathrm{Xn0n}}\big[(1-\varepsilon_{\mathrm{A}})p_{\mathrm{C}}\varepsilon_{\mathrm{C}}\big] \\ &\quad +M_{\mathrm{XnXn}}(1-\varepsilon_{\mathrm{A}})(1-p_{\mathrm{A}})[\varepsilon_{\mathrm{C}}+(1-\varepsilon_{\mathrm{C}})p_{\mathrm{C}}] \end{aligned} \tag{4.21}$$

$$\begin{aligned} N_{\mathrm{Xn0n}} &= M_{\mathrm{Xn0n}} \\ &\quad +M_{\mathrm{0n0n}}p_{\mathrm{A}}(1-p_{\mathrm{C}}) \\ &\quad +M_{\mathrm{0nXn}}\big[(1-\varepsilon_{\mathrm{C}})p_{\mathrm{A}}\varepsilon_{\mathrm{A}}\big] \\ &\quad -M_{\mathrm{Xn0n}}\big[(1-\varepsilon_{\mathrm{A}})(1-p_{\mathrm{A}})(1-p_{\mathrm{C}})+\varepsilon_{\mathrm{A}}p_{\mathrm{C}}+(1-\varepsilon_{\mathrm{A}})p_{\mathrm{A}}p_{\mathrm{C}}\big] \\ &\quad +M_{\mathrm{XnXn}}(1-\varepsilon_{\mathrm{C}})(1-p_{\mathrm{C}})[\varepsilon_{\mathrm{A}}+(1-\varepsilon_{\mathrm{A}})p_{\mathrm{A}}] \end{aligned} \tag{4.22}$$

$$\begin{aligned} N_{\mathrm{XnXn}} &= M_{\mathrm{XnXn}} \\ &\quad +M_{\mathrm{0n0n}}(p_{\mathrm{A}}p_{\mathrm{C}}) \\ &\quad +M_{\mathrm{0nXn}}\big[\varepsilon_{\mathrm{C}}p_{\mathrm{A}}+(1-\varepsilon_{\mathrm{C}})p_{\mathrm{A}}p_{\mathrm{C}}\big] \\ &\quad +M_{\mathrm{Xn0n}}\big[\varepsilon_{\mathrm{A}}p_{\mathrm{C}}+(1-\varepsilon_{\mathrm{A}})p_{\mathrm{A}}p_{\mathrm{C}}\big] \\ &\quad -M_{\mathrm{XnXn}}(1-\varepsilon_{\mathrm{A}})(1-p_{\mathrm{A}})(\varepsilon_{\mathrm{C}}+(1-\varepsilon_{\mathrm{C}})p_{\mathrm{C}}) \\ &\quad -M_{\mathrm{XnXn}}(1-\varepsilon_{\mathrm{C}})(1-p_{\mathrm{C}})(\varepsilon_{\mathrm{A}}+(1-\varepsilon_{\mathrm{A}})p_{\mathrm{A}}) \\ &\quad -M_{\mathrm{XnXn}}(1-\varepsilon_{\mathrm{A}})(1-\varepsilon_{\mathrm{C}})(1-p_{\mathrm{A}})(1-p_{\mathrm{C}}) \end{aligned} \tag{4.23}$$

This set of equations can be expressed in matrix form as

$$\begin{bmatrix} N_{0n0n} \\ N_{0nXn} \\ N_{Xn0n} \\ N_{XnXn} \end{bmatrix} = c_{ij} \cdot \begin{bmatrix} M_{0n0n} \\ M_{0nXn} \\ M_{Xn0n} \\ M_{XnXn} \end{bmatrix} , \tag{4.24}$$

where c_{ij} is the matrix composed from the equations above. To obtain the corrected M values, the matrix can be inverted

$$\begin{bmatrix} M_{0n0n} \\ M_{0nXn} \\ M_{Xn0n} \\ M_{XnXn} \end{bmatrix} = c_{ij}^{-1} \cdot \begin{bmatrix} N_{0n0n} \\ N_{0nXn} \\ N_{Xn0n} \\ N_{XnXn} \end{bmatrix} . \tag{4.25}$$

The pileup values (p_A, p_C) needed for the computation of the matrix are obtained in the same way as described in Sec. 4.8.1 for the EMD pileup coming from a different ion pair than the one producing the vector meson. Utilizing the `CTRUE-B` trigger, the number of events with ZNA or ZNC activity in an otherwise empty detector is studied as a function of μ. The data points are fitted with a first-order polynomial, and the average probability value is computed using the Poisson distribution and the analyzed luminosity in the `CMUP6` trigger as weights for the individual runs. The resulting plots can be seen in Fig. 4.16 for p_A and in Fig. 4.17 for p_C.

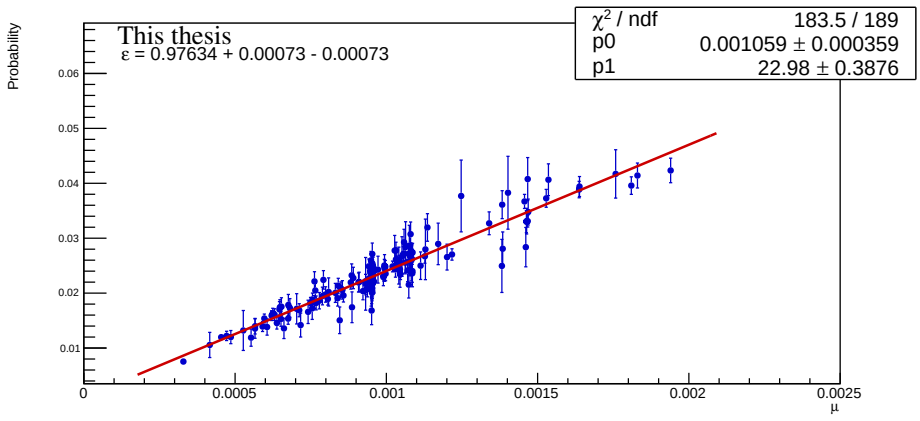

Figure 4.16: The probability of the ZNA offline decision being triggered in an otherwise empty detector as a function of μ. The data points are fitted using a first-order polynomial function. The average efficiency (ε) is calculated using a Poisson distribution and weighted with the analyzed integrated luminosity run by run.

The probability values computed for having a pileup event in the ZDC are $p_A = 2.37\% \pm 0.05\%$ for the ZNA and $p_C = 2.38\% \pm 0.06\%$ for the ZNC.

The efficiency values $(\varepsilon_A, \varepsilon_C)$ for the ZNA and ZNC were estimated using various methods in Ref. [115], with values reported as $\varepsilon_A = 93.3\% \pm 1.7\%$ and $\varepsilon_C = 93.1\% \pm 1.7\%$

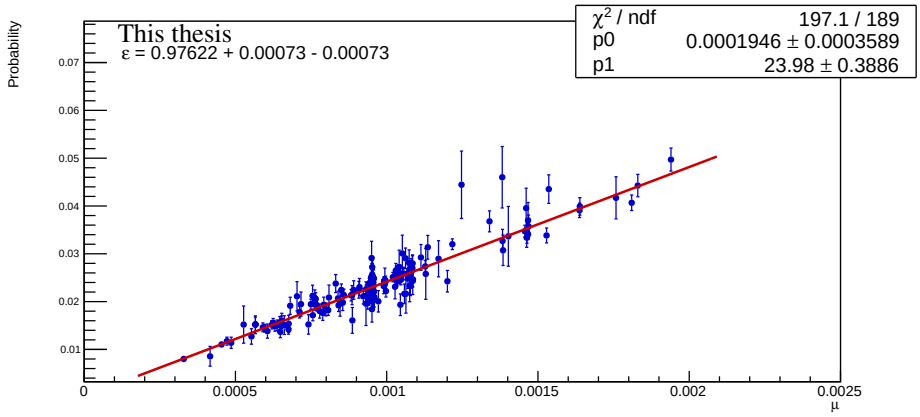

Figure 4.17: The probability of the ZNC offline decision being triggered in an otherwise empty detector as a function of μ. The data points are fitted using a first-order polynomial function. The average efficiency (ε) is calculated using a Poisson distribution and weighted with the analyzed integrated luminosity run by run.

Taking the values of ε_{A}, ε_{C}, p_{A}, and p_{C} and plugging them into Eq. 4.25, the J/ψ yields in both the central and forward data sets have been corrected. Note that by applying this correction, the total number of entries does not change; they only move to a different EMD class. As such, the uncertainties originating from this correction are inversely correlated.

4.9 Systematic uncertainties

The systematic uncertainty in the extraction of the J/ψ yield from the invariant mass fits in the forward rapidity data set was assessed by varying the Crystal Ball parameters obtained from the fit to the MC data set with a pure J/ψ signal. The variation was performed within the range of uncertainties provided by the fit.

For the central rapidity data set, the uncertainty was determined by comparing the yield obtained from the fit with values resulting from bin counting the entries in the J/ψ mass peak region after subtracting the $\gamma\gamma$ background continuum. This subtraction was achieved by removing events under the exponential function from the fit model. Another contributing factor arises from the non-ideal exponential behavior of the $\gamma\gamma$ continuum. The magnitude of this effect was estimated by slightly adjusting the fit range and observing the resulting change in the J/ψ yield. The uncertainties from both of these sources in the central data set were then added in quadrature.

The resulting uncertainties in the cross section values for the forward and central data sets are assumed to be uncorrelated, both within the rapidity bins and across the EMD classes.

The uncertainty in the correction for incoherent events in the forward data set is estimated using an alternative method to determine the value of the b_{pd} parameter in Eq. 4.9. This involves leaving the parameter free in a p_{T} fit applied to a data sample with sufficient statistics in the high p_{T} tail. This procedure is carried out for data sets integrated in neutron emission classes but differential in rapidity bins. The extracted b_{pd} parameters from these fits are then kept fixed within the p_{T} fits for the remaining data samples. The difference between the f_{I} values obtained by this method and the one described in Sec. 4.7 is taken as the uncertainty.

In the central data set, the uncertainty in the incoherent fraction is assessed by employing an alternative shape for the $\gamma\gamma$ contribution in the p_{T} fits. Rather than relying on the PDF template from STARlight, a data-driven method is used to estimate the p_{T} shape of this contribution. This involves selecting side bands around the J/ψ mass peak to obtain a data sample predominantly composed of the $\gamma\gamma$ process. The shape obtained from this sample is then utilized in the p_{T} fits.

The uncertainties in f_{I} discussed above are treated as uncorrelated. However, there is one correlated contribution to the uncertainty. The width of the p_{T} distribution for coherent J/ψ photoproduction in STARlight does not precisely match the observed shape in the data. To gauge the impact of this discrepancy on the f_{I} values, the generator-level p_{T} distribution from STARlight was used to fit the coherent peak, given its broader shape. Half of the observed difference was assigned as the uncertainty. It is worth noting that this effect is more pronounced in the central data set, as the resolution of the central barrel detectors surpasses that of the muon spectrometer.

The uncertainty arising from the determination of the feed-down contribution is assessed by varying the ratio of the raw ψ' to J/ψ yields, utilized in Sec. 4.6 for estimating this correction. The variation is carried out within the statistical uncertainty determined by the size of the available data sets. Since the ratio is independently measured for the central and forward data sets, this uncertainty is considered uncorrelated between the two data sets but fully correlated within the EMD classes and rapidity bins of one data set.

The experimental uncertainty in the branching ratio size, as reported in Ref. [109], is considered and treated as a correlated source.

The correlated uncertainty arising from the luminosity determination is primarily attributed to the precision with which the reference cross section is known and the stability of the detector calibration over time, crucial for the van der Meer scans [107]. In the central data set, an additional contribution to the uncertainty stems from the precision with which the live time of the `CCUP31` trigger is known. However, for the forward data set, where the `CMUP6` trigger is employed, the live time is measured with sufficient precision so that this contribution can be neglected.

In the central barrel, another source of correlated uncertainty arises from the ITS-TPC track matching efficiency. This uncertainty is evaluated in both data and MC by applying ITS-related cuts to tracks selected with only TPC requirements and vice versa.

An additional correlated uncertainty in the central barrel analysis arises from the TOF trigger efficiency. A dedicated study was conducted by TOF experts and for the decay channels considered in this analysis only a small uncertainty was assigned to the efficiency, primarily due to its dependence on the time selection range of the trigger. Similarly, the uncertainty associated with the SPD trigger efficiency was assessed by slightly modifying the conditions of the data-driven method used to compute this efficiency.

In the forward rapidity data set, the uncertainty assigned to the muon spectrometer tracking efficiency is evaluated by comparing the values obtained from MC simulations and a data-driven method. This method utilizes the redundancy in the number of signals coming from the tracking chambers [116]. Additionally, the uncertainty on the efficiency of the matching between the tracking chambers and the muon trigger chambers is also taken from studies conducted by muon spectrometer experts. Finally, the uncertainty on the muon trigger efficiency, as provided by the experts, is considered. It is determined by comparing the muon trigger efficiency computed in data and MC simulations and taking into account the difference between the trigger algorithm response in data and MC. The uncertainties above are considered as correlated across the forward rapidity data set.

The uncertainty on the $\varepsilon_{\mathrm{pu}}$ correction in the forward data set is computed by varying the correction factor within its uncertainty. In the central data set, this correction is more significant due to the presence of offline AD veto requirements, so another method is used to evaluate its uncertainty. The analysis is repeated without the offline AD and V0 vetoes. While the change in the J/ψ yield and the $\varepsilon_{\mathrm{pu}}$ value should cancel out to give the same value as with the vetoes present, the resulting value is slightly different. This difference is taken as the systematic uncertainty for the $\varepsilon_{\mathrm{pu}}$ in the central analysis. These uncertainties are considered correlated in their respective data sets.

Another correlated uncertainty for the respective data sets arises from the $\varepsilon_{\mathrm{emd}}$ correction. This is evaluated by varying the correction within its uncertainty and computing the resulting cross section value.

The uncertainty on the migration correction was estimated by individually varying the ZDC pileup and efficiency values $\varepsilon_{\mathrm{A}}, \varepsilon_{\mathrm{C}}, p_{\mathrm{A}}, p_{\mathrm{C}}$ within their respective uncertainties. The resulting systematic uncertainty was determined as the maximum difference between the central value and the value obtained with a modified parameter for each class. It is important to note that these uncertainties are negatively correlated among the EMD classes within a single rapidity bin.

The values for each source of the systematic uncertainties discussed above can be found in Tab. 4.6 and Tab. 4.7 for the forward and central data sets, respectively.

Source	Err.	$2.5 < \|y\| < 3.0$			$3.0 < \|y\| < 3.5$			$3.5 < \|y\| < 4.0$		
		0n0n	Xn0n	XnXn	0n0n	Xn0n	XnXn	0n0n	Xn0n	XnXn
Yield	U	0.2	1.3	0.8	0.1	0.6	0.7	0.5	0.5	0.9
f_{I}	U	0.4	0.6	1.6	0.4	0.9	3.3	0.4	0.5	2.2
Coh. sh.	C	0.1	0.1	0.1	0.1	0.1	0.1	0.1	0.1	0.1
f_{D}	C	0.7	0.7	0.7	0.7	0.7	0.7	0.7	0.7	0.7
Br. r.	C	0.6	0.6	0.6	0.6	0.6	0.6	0.6	0.6	0.6
Lumi.	C	2.5	2.5	2.5	2.5	2.5	2.5	2.5	2.5	2.5
Track.	C	3	3	3	3	3	3	3	3	3
Trig.	C	6.2	6.2	6.2	6.2	6.2	6.2	6.2	6.2	6.2
Match.	C	1	1	1	1	1	1	1	1	1
$\varepsilon_{\mathrm{pu}}$	C	0.2	0.2	0.2	0.2	0.2	0.2	0.2	0.2	0.2
$\varepsilon_{\mathrm{emd}}$	C	0	1.1	6	0	1.1	6	0	1.1	6
Migr.	A	−0.3	3.8	3.3	−0.2	3.6	3.6	−0.2	3.3	3.6

Table 4.6: Table displaying systematic uncertainties for the forward rapidity analysis. The uncertainty values, presented in percentage, are provided for each rapidity bin and EMD class. The correlation for each uncertainty source is indicated in the 'Err.' column as follows: U=uncorrelated, C=correlated, A=anticorrelated. The negative sign preceding the migration uncertainty value for the 0n0n class denotes its negative correlation with the other EMD classes in a given rapidity bin.

Source	Err.	$\|y\| < 0.2$			$0.2 < \|y\| < 0.8$		
		0n0n	0nXn+Xn0n	XnXn	0n0n	0nXn+Xn0n	XnXn
Yield	U	1.5	1.5	1.5	1.5	1.5	1.5
f_{I}	U	0.1	1.5	1.3	0.1	1.5	1.3
Coh. sh.	C	0.1	0.8	0.6	0.1	0.8	0.6
f_{D}	C	0.6	0.6	0.6	0.6	0.6	0.6
Br. r.	C	0.5	0.5	0.5	0.5	0.5	0.5
Lumi.	C	2.5	2.5	2.5	2.5	2.5	2.5
Trig. time	C	1.5	1.5	1.5	1.5	1.5	1.5
ITS-TPC	C	2.8	2.8	2.8	2.8	2.8	2.8
TOF trig.	C	0.7	0.7	0.7	0.7	0.7	0.7
SPD trig.	C	1	1	1	1	1	1
$\varepsilon_{\mathrm{pu}}$	C	3	3	3	3	3	3
$\varepsilon_{\mathrm{emd}}$	C	0	3.2	3.5	0	3.2	3.5
Migr.	A	−3.9	3.4	0.9	−3.6	3.1	1.1

Table 4.7: Table displaying systematic uncertainties for the central rapidity analysis. The uncertainty values, presented in percentage, are provided for each rapidity bin and EMD class. The correlation for each uncertainty source is indicated in the 'Err.' column as follows: U=uncorrelated, C=correlated, A=anticorrelated. The negative sign preceding the migration uncertainty value for the 0n0n class denotes its negative correlation with the other EMD classes in a given rapidity bin.

4.10 UPC cross section

The rapidity differential coherent J/ψ photoproduction cross sections for the neutron emission class j, including all the corrections discussed in this chapter, are computed using Eq. 4.26 as

$$\frac{\mathrm{d}\sigma^{j}_{\mathrm{PbPb}}}{\mathrm{d}y} = \frac{N^{i}(\mathrm{J}/\psi)}{(1+f_{\mathrm{I}}+f_{\mathrm{D}})} \cdot c_{ij}^{-1} \cdot \frac{1}{(\mathrm{A}\times\varepsilon)\cdot\varepsilon_{\mathrm{pu}}\cdot\varepsilon_{\mathrm{emd}}\cdot\mathrm{BR}\cdot\mathscr{L}\cdot\Delta\mathrm{y}}\,, \tag{4.26}$$

where $N^{i}(\mathrm{J}/\psi)$ represents the raw J/ψ yields obtained from the invariant mass fits. f_{I} and f_{D} are corrections for the incoherent and feed-down contributions to the yield, respectively. c_{ij}^{-1} is the inverted matrix used to correct for the effect of neutron class migration. $(\mathrm{A}\times\varepsilon)$ represents the detector acceptance times efficiency correction for J/ψ reconstruction. $\varepsilon_{\mathrm{pu}}$ is the correction for EMD pileup, and $\varepsilon_{\mathrm{emd}}$ is the correction factor for EMD veto losses. BR taken from Ref. [109] denotes the branching ratio value for the corresponding decay channel, $\mathscr{L}$ is the integrated luminosity of the analyzed data set, and Δy is the rapidity interval size.

Class	$\mathrm{d}\sigma_{\mathrm{PbPb}}/\mathrm{d}y$ (mb)
$\lvert y\rvert < 0.2$	
0n0n	$3.130 \pm 0.090 \pm 0.047 \pm 0.164 \mp 0.122$
0nXn+Xn0n	$0.730 \pm 0.050 \pm 0.015 \pm 0.045 \pm 0.025$
XnXn	$0.250 \pm 0.024 \pm 0.005 \pm 0.016 \pm 0.002$
$0.2 < \lvert y\rvert < 0.8$	
0n0n	$2.900 \pm 0.070 \pm 0.044 \pm 0.152 \mp 0.104$
0nXn+Xn0n	$0.800 \pm 0.040 \pm 0.017 \pm 0.050 \pm 0.025$
XnXn	$0.300 \pm 0.029 \pm 0.006 \pm 0.019 \pm 0.003$
$2.5 < \lvert y\rvert < 3.0$	
0n0n	$2.668 \pm 0.076 \pm 0.011 \pm 0.199 \mp 0.009$
Xn0n	$0.242 \pm 0.021 \pm 0.003 \pm 0.018 \pm 0.009$
XnXn	$0.256 \pm 0.024 \pm 0.005 \pm 0.024 \pm 0.009$
$3.0 < \lvert y\rvert < 3.5$	
0n0n	$2.322 \pm 0.033 \pm 0.010 \pm 0.173 \mp 0.005$
Xn0n	$0.172 \pm 0.010 \pm 0.002 \pm 0.013 \pm 0.006$
XnXn	$0.161 \pm 0.011 \pm 0.005 \pm 0.015 \pm 0.006$
$3.5 < \lvert y\rvert < 4.0$	
0n0n	$1.590 \pm 0.049 \pm 0.010 \pm 0.119 \mp 0.003$
Xn0n	$0.101 \pm 0.009 \pm 0.001 \pm 0.008 \pm 0.003$
XnXn	$0.079 \pm 0.011 \pm 0.002 \pm 0.008 \pm 0.003$

Table 4.8: Values of the coherent J/ψ photoproduction cross sections ($\mathrm{d}\sigma_{\mathrm{PbPb}}/\mathrm{d}y$) for each neutron emission class and rapidity bin, along with their uncertainties. The first uncertainty value is the statistical uncertainty, the second value is the uncorrelated systematic uncertainty, and the third value is the correlated systematic uncertainty. The last value includes the uncertainty given by the EMD class migration correction. Note the $\mp$ sign, indicating the negative correlation, used for the 0n0n EMD class values. This is done to emphasize the negative correlation between this uncertainty and the other migration uncertainties in the respective rapidity bin.

The resulting values for the coherent J/ψ photoproduction cross section measured in Pb–Pb UPCs at $\sqrt{s_{NN}} = 5.02$ TeV are summarized in Tab. 4.8 for each neutron emission class and rapidity bin, along with their uncertainties. These results together with the prediction from models discussed in Sec. 1.8 are plotted in Fig. 4.18.

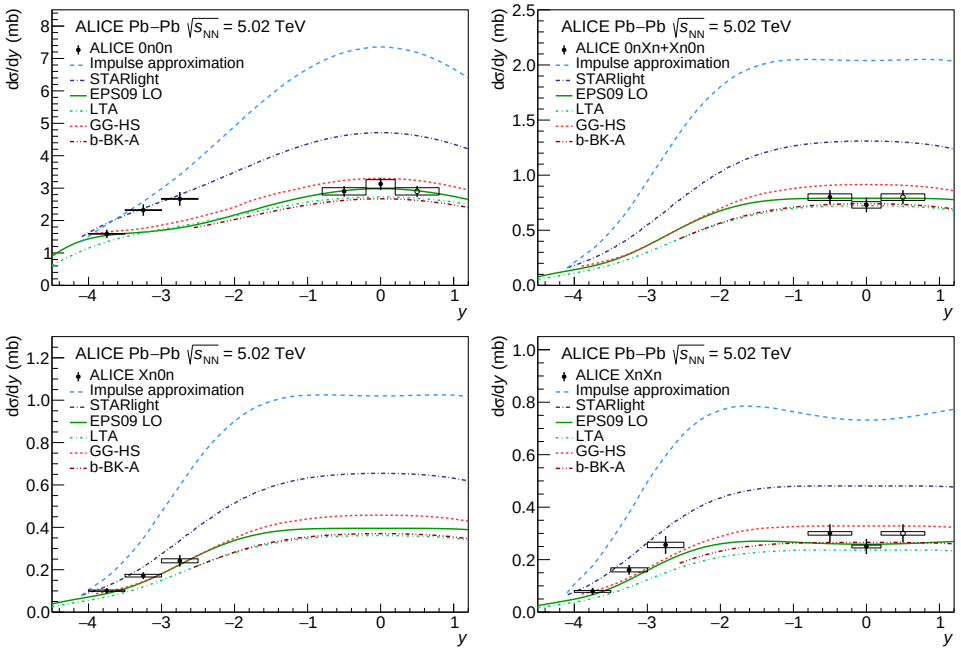

Figure 4.18: Coherent J/ψ photoproduction cross section measured in Pb–Pb UPCs at $\sqrt{s_{NN}} = 5.02$ TeV. Solid markers represent the measured values (values at $0.2 < |y| < 0.8$ are displayed at negative rapidities and reflected into positive rapidities with an open marker). The vertical line across a marker represents the sum in quadrature of the statistical and uncorrelated systematic uncertainties. The width of the boxes depicts the range in rapidity covered by each measurement, while the height of a box represents the sum in quadrature of the correlated systematic uncertainties and the effect of migrations across neutron classes. The lines depict the predictions of different models discussed in Sec. 1.8 [1].

The IA prediction is consistently above the measured results in all instances, highlighting the presence of shadowing effects. The STARlight model, which also does not include shadowing, overpredicts all the measurements, especially those at central rapidity, with the exception of two forward data points ($3.5 < |y| < 2.5$) in the 0n0n class. These two points are also the only ones severely underpredicted by the remaining four models. The EPS09 LO and the LTA models, both of which incorporate nuclear shadowing, as well as the GG-HS and b-BK-A models, which include saturation effects, provide fairly similar predictions and offer a good description of the measured data points within current uncertainties, except for the two points discussed above. This suggests that some QCD dynamic mechanism is necessary to describe the J/ψ photoproduction cross section at the available energies.

4.11 Photonuclear cross section

With the technique discussed in Sec. 1.6, which utilizes the measurements of UPC cross section in the same rapidity intervals but different EMD classes, the photonuclear cross section is extracted from the measurement presented above, see Tab. 4.8. The photon flux values used for the extraction are computed using the $\mathbf{n}^{\mathbf{O}}_{\mathbf{O}}\mathbf{n}$ model and can be found in Tab. 4.9, see Sec. 1.8 for details about the model.

Rapidity	n_γ(0n0n)	n_γ(0nXn+Xn0n)	n_γ(XnXn)
$3.5 < y < 4.0$	178.51	18.18	6.34
$3.0 < y < 3.5$	162.99	18.19	6.34
$2.5 < y < 3.0$	147.46	18.19	6.34
$0.2 < y < 0.8$	77.88	17.88	6.33
$-0.2 < y < 0.2$	62.86	17.47	6.27
$-0.8 < y < -0.2$	48.31	16.75	6.18
$-3.0 < y < -2.5$	3.91	4.97	2.78
$-3.5 < y < -3.0$	1.22	2.15	1.42
$-4.0 < y < -3.5$	0.26	0.61	0.48

Table 4.9: The photon flux values for the different rapidity bins and neutron emission classes as computed using the $\mathbf{n}^{\mathbf{O}}_{\mathbf{O}}\mathbf{n}$ model, see Sec. 1.8.

To accurately handle the uncertainties associated with the resulting photonuclear cross section, the extraction is performed using a χ^2 method that relies on relative values of the uncertainties and considers correlated uncertainties through the use of nuisance parameters. This χ^2 method was originally employed by the H1 collaboration for analyzing data from inclusive deeply inelastic scattering at HERA [117]. The same method was also utilized by the ALICE collaboration to extract the energy dependence of exclusive photoproduction of J/ψ in p–Pb collisions [118, 119]. The χ^2 formula is given by

$$\chi^2_{\text{exp}}\left(\vec{m},\vec{b}\right) = \sum_i \frac{\left(m^i - \sum_j \gamma^i_j m^i b_j - \mu^i\right)^2}{\delta^2_{i,\text{stat}}\mu^i\left(m^i - \sum_j \gamma^i_j m^i b_j\right) + \left(\delta_{i,\text{uncor}}\, m^i\right)^2} + \sum_j b_j^2, \qquad (4.27)$$

where μ^i represent the values of the measured UPC cross sections in rapidity interval i, corresponding to the left-hand side of Eq. 1.6. The quantities m^i are determined by the right-hand side of Eq. 1.6, utilizing flux values from Tab. 4.9. The unknown parameters $\sigma_{\gamma\text{Pb}}(\pm y)$ need to be extracted from the fit. It is noteworthy that, for the central rapidity measurement at $-0.2 < y < 0.2$, Eq. 1.6 simplifies to involve only one unknown parameter $\sigma_{\gamma\text{Pb}}$. The terms $\delta_{i,\text{stat}} = \Delta_{i,\text{stat}}/\mu^i$ and $\delta_{i,\text{uncor}} = \Delta_{i,\text{uncor}}/\mu^i$ represent relative statistical and relative uncorrelated systematic uncertainties, respectively. The matrix γ^i_j denotes relative correlated systematic uncertainties from source j in rapidity interval i, and b_j is the corresponding set of nuisance parameters.

The fit using Eq. 4.27 is performed several times, taking into account different types of uncertainties in the input values.

1. The fit is performed using statistical and systematic uncertainties, both uncorrelated and correlated, with the full form of Eq. 4.27. In addition to the systematic uncertainties listed in Tab. 4.6 and Tab. 4.7, another one is taken into account for the total value of the photon flux. This uncertainty is obtained by varying the nuclear radius in the Woods–Saxon distribution of the $\mathbf{n}^{\mathbf{O}}_{\mathbf{O}}\mathbf{n}$ model within the boundaries of the neutron skin width [120]. As a result, there is an additional 2% correlated uncertainty for all rapidity bins and EMD classes.

2. The fit is performed taking into account only the statistical and uncorrelated systematic uncertainties. This simplifies the form of Eq. 4.27 so that all terms containing the nuisance parameters b_j vanish.

3. The fit described in 1. is reiterated, with the UPC cross sections modified individually by their respective migration uncertainties. Each fit iteration involves changing one value at a time.

4. The fit described in 1. is repeated, incorporating modified photon flux values from the $\mathbf{n}^{\mathbf{O}}_{\mathbf{O}}\mathbf{n}$ model. The cross sections, used as input for the $\mathbf{n}^{\mathbf{O}}_{\mathbf{O}}\mathbf{n}$ model to compute the fractions of the total photon flux corresponding to each EMD class, are adjusted by $\pm 5\%$, see Ref. [121]. Consequently, the resulting flux fractions are altered by 1% to 8%, depending on the rapidity bin and EMD class. It is noteworthy that the resulting uncertainty exhibits negative correlation among the EMD classes within a given rapidity interval.

The uncertainties of the extracted photonuclear cross sections are determined from the results of these fits. The uncorrelated uncertainty is taken as the uncertainty returned by fit 2. The correlated uncertainty is taken as the square root of the difference between the squares of the uncertainties from fit 1. and fit 2. The uncertainty due to EMD class migration is determined as the largest difference between the results of fit 1. and fit 3., divided by $\sqrt{2}$. The uncertainty originating from the photon flux fraction variation is determined as the largest difference between the results of fit 1. and fit 4., also divided by $\sqrt{2}$. The extraction was also attempted using STARlight photon flux values instead of the $\mathbf{n}^{\mathbf{O}}_{\mathbf{O}}\mathbf{n}$ values. The difference in the results was below 1%, except for the two cross sections at the highest energies (633.21 GeV and 813.05 GeV), which were 2.6% and 7.7% higher, respectively. However, these differences are still well within the uncorrelated uncertainties of the results.

The extracted photonuclear cross section values, their associated uncertainties, and the corresponding center-of-mass energy per nucleon are provided in Tab. 4.10 and plotted in Fig. 4.19.

Rapidity	$W_{\gamma\mathrm{Pb,n}}$ (GeV)	$\sigma_{\gamma\mathrm{Pb}}$ (μb)
$3.5 < y < 4.0$	19.12	$8.84 \pm 0.30 \pm 0.68 \pm 0.02 \pm 0.04$
$-4.0 < y < -3.5$	813.05	$57.32 \pm 20.77 \pm 7.57 \pm 6.41 \pm 6.56$
$3.0 < y < 3.5$	24.55	$13.89 \pm 0.23 \pm 1.08 \pm 0.05 \pm 0.08$
$-3.5 < y < -3.0$	633.21	$46.58 \pm 6.61 \pm 5.73 \pm 3.77 \pm 3.63$
$2.5 < y < 3.0$	31.53	$16.89 \pm 0.59 \pm 1.32 \pm 0.11 \pm 0.18$
$-3.0 < y < -2.5$	493.14	$44.68 \pm 6.38 \pm 5.15 \pm 2.73 \pm 2.97$
$0.2 < y < 0.8$	97.11	$21.73 \pm 5.12 \pm 3.12 \pm 4.32 \pm 2.73$
$-0.8 < y < -0.2$	160.10	$25.00 \pm 7.33 \pm 4.88 \pm 5.43 \pm 3.91$
$-0.2 < y < 0.2$	124.69	$24.15 \pm 0.69 \pm 1.37 \pm 0.50 \pm 0.06$

Table 4.10: The extracted photonuclear cross section, $\sigma_{\gamma\mathrm{Pb}}$, and its corresponding center-of-mass energy per nucleon, $W_{\gamma\mathrm{Pb,n}}$. The first uncertainty is uncorrelated, the second is correlated, the third is due to the correction for migration across EMD classes, and the last one is due to flux fraction uncertainties for different neutron emission classes. Note that the two $\sigma_{\gamma\mathrm{Pb}}$ values extracted in the same rapidity interval, in absolute values, are anticorrelated.

These results span three orders of magnitude in Bjorken-x ($1.1 \times 10^{-5} < x < 3.3 \times 10^{-2}$) and extend the energy range of preceding measurements by over 300 GeV, encompassing $17 < W_{\gamma\mathrm{Pb,n}} < 920$ GeV. Alongside them are plotted the results derived from ALICE Run 1 data [26, 38], refer to Sec. 1.7 for detailed information. Subsequently to the publication of the new ALICE results, the CMS collaboration published a related analysis [122]. Employing the EMD technique and the Run 2 dataset, they extracted the coherent J/ψ photoproduction cross section within a complementary rapidity range, and therefore an energy range, to the analysis presented in this thesis, covering the intervals between the ALICE data points. In addition to these measurements, theoretical predictions from models discussed in Sec. 1.8 are also shown.

The results obtained by using ALICE Run 1 data [26, 38] agree well with the new results at energies $W_{\gamma\mathrm{Pb,n}} = 92$ GeV and 470 GeV, while they are less than 2 standard deviations lower at 18 GeV. The consistency of results obtained from measurements in peripheral and ultra-peripheral collisions during Run 1, when compared to data points from Run 2 measurements of UPCs in EMD classes, validates the use of these techniques. The results from Run 2 data, as measured by the CMS collaboration [122], are located between the ALICE data points and appear to smoothly follow the same trend.

The IA is in agreement with the measured cross sections below 40 GeV, but it systematically overpredicts all the data, with the difference increasing as the energy increases. The prediction from the STARlight model agrees with the available data below 60 GeV but overestimates the results at higher energies. At lower energies, the remaining models agree well with the measurement at 19 GeV (the LTA model slightly underpredicts the value, and the b-BK-A model does not provide predictions for energies lower than 35 GeV), but they all underestimate the available data points between 24 GeV and 60 GeV. For the ALICE data points, this energy range

corresponds to the rapidity range where the models also underpredict the UPC cross section, especially in the 0n0n EMD class. In the higher energy range, the EPS09 LO model agrees with the data between 90 GeV and 160 GeV but overestimates the available data above 160 GeV. For the most energetic data point at 813 GeV, it gives an even higher value than the STARlight model. The GG-HS model provides a better agreement with the available data above 160 GeV but nonetheless remains systematically above the data points. The best agreement with the data in the high-energy region is achieved by the LTA model and the b-BK-A model, which both give very similar predictions.

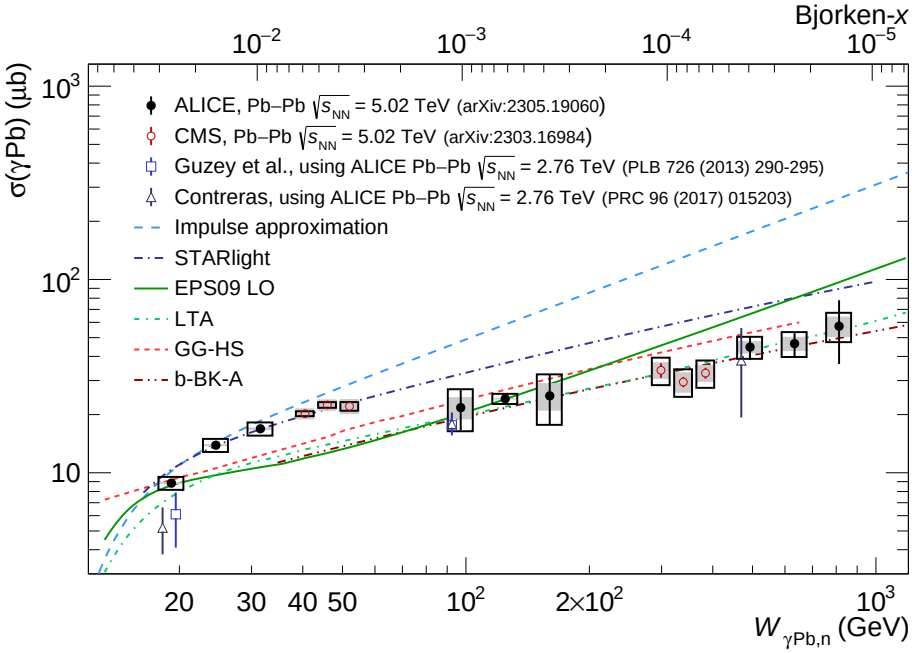

Figure 4.19: Photonuclear cross section for the $\gamma + \mathrm{Pb} \rightarrow \mathrm{J}/\psi + \mathrm{Pb}$ process as a function of $W_{\gamma \mathrm{Pb,n}}$ (lower axis) or Bjorken-x (upper axis). The solid markers represent the measured cross section using ALICE Run 2 data, where the vertical line across each solid marker indicates the uncorrelated uncertainty. The height of an empty box corresponds to the sum in quadrature of the correlated systematic uncertainties and the uncertainty given by migrations across neutron emission classes. The gray box represents the theoretical uncertainty arising from the computation of the photon flux fractions. The lines depict the predictions of different models discussed in Sec.1.8. The open triangular and square markers show the cross sections extracted in [26, 38] using ALICE Run 1 data. For CMS results [122], the vertical bars, and the shaded and open boxes represent the statistical, experimental, and theoretical (photon flux) uncertainties, respectively [1].

4.12 Nuclear suppression factor

The nuclear suppression factor can be computed using Eq. 1.19. The cross section values for the IA are computed in accordance with Ref. [38] and can be found in Tab. 4.11. The authors of Ref. [38] claim a 5% uncertainty for the IA prediction, attributed to the uncertainty of the input data and the model parametrization. This uncertainty has been considered as an additional source in the theoretical systematic uncertainties for the computed nuclear suppression factors, as depicted in Fig. 4.20, along with the model predictions discussed in Sec. 1.8. The results obtained from ALICE Run 1 data [26, 38], as well as the results from CMS [122], are also shown.

Rapidity	$\sigma^{\mathrm{IA}}_{\gamma\mathrm{Pb}}$ (μb)
$3.5 < y < 4.0$	10
$3.0 < y < 3.5$	14
$2.5 < y < 3.0$	19
$0.2 < y < 0.8$	48
$-0.2 < y < 0.2$	58
$-0.8 < y < -0.2$	71
$-3.0 < y < -2.5$	176
$-3.5 < y < -3.0$	215
$-4.0 < y < -3.5$	262

Table 4.11: Theoretical input needed to obtain the nuclear suppression factor. The last column shows the value of $\sigma^{\mathrm{IA}}_{\gamma\mathrm{Pb}}$ as computed in Ref. [38].

The nuclear suppression factor is generally used as a quantitative measure of nuclear shadowing, with the advantage that some types of theoretical uncertainties cancel out in the model predictions due to the ratio in Eq. 1.19. However, the authors of Ref. [38] stress that several types of uncertainties, namely the correction for the contribution of the real part of the amplitude and the skewness correction, remain. As a result, there is approximately a 10% uncertainty associated with the use of the nuclear suppression factor as a quantitative measure of nuclear gluon shadowing.

The comparison between the available data points and the theoretical predictions remains the same as in Fig. 4.19 and is discussed in the previous section. When looking at the S_{Pb} values in the region $W_{\gamma\mathrm{Pb,n}}$ of 300 GeV to 813 GeV, the combined results of ALICE and CMS could suggest a halt in the decreasing trend of the nuclear suppression factor value, establishing a flat trend. However, with the current precision of the data, the observation is also in good agreement with the model predictions, which show a continuous decrease. Further measurements with increased precision, or preferably at higher $W_{\gamma\mathrm{Pb,n}}$, could distinguish between the two scenarios.

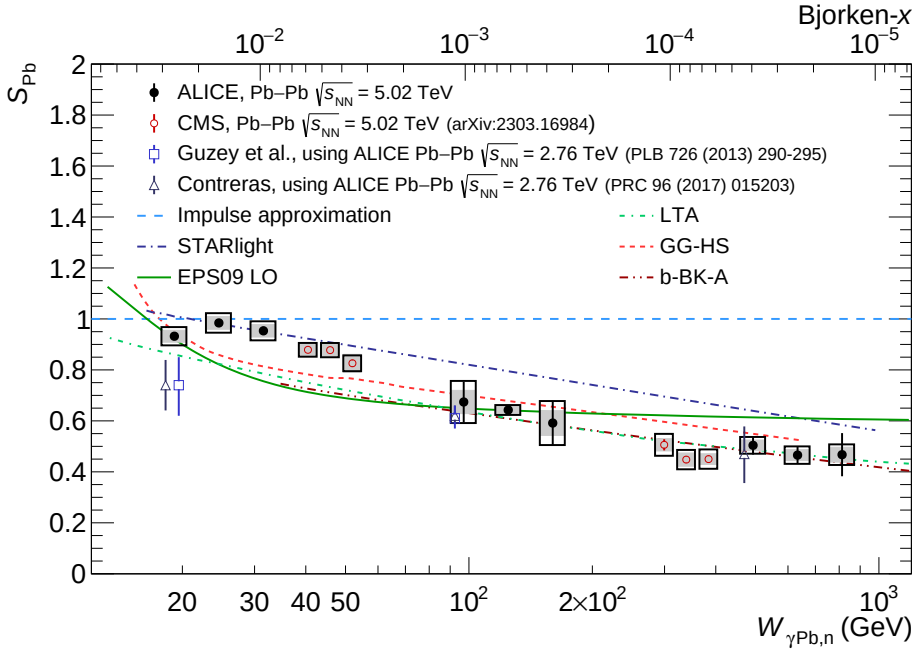

Figure 4.20: Nuclear suppression factor for the $\gamma + \mathrm{Pb} \to J/\psi + \mathrm{Pb}$ process as a function of $W_{\gamma \mathrm{Pb,n}}$ (lower axis) or Bjorken-x (upper axis). The solid markers represent the measurements using ALICE Run 2 data, with the vertical line across each marker indicating the uncorrelated uncertainty. The height of an empty box corresponds to the sum in quadrature of the correlated systematic uncertainties and the uncertainty given by migrations across neutron emission classes. A gray box represents the theoretical uncertainty arising from the computation of the photon flux fractions and the impulse approximation. The lines depict predictions from different models discussed in Sec.1.8. Open triangular and square markers show the nuclear suppression factor extracted in [26, 38] using ALICE Run 1 data. For CMS results [122], vertical bars, shaded and open boxes represent the statistical, experimental systematic, and theoretical systematic uncertainties, respectively [1].

Conclusion

An introduction to the physics of ultra-peripheral collisions was given in Chap. 1. It described the phenomena of saturation and shadowing, which affect the parton distribution functions of gluons at high energies. The cross section of coherent J/ψ photoproduction in heavy ions collisions, sensitive to the gluon PDFs, was also introduced, along with a procedure using the EMD process to disentangle the low and high Bjorken-x contributions in the J/ψ photoproduction cross section. Relevant previous measurements, together with the current theoretical models describing this process, were also discussed.

The ALICE detector and its subdetectors, crucial for obtaining the results presented in this thesis, were introduced in Chap. 2. The upgrades of the ALICE detector during LS 2, with a special emphasis on the MFT detector and the architecture of the new QC system of ALICE and its implementation for the MFT, were described in Chap. 3.

The measurement of the coherent J/ψ photoproduction cross section in Pb–Pb UPC events at a center-of-mass energy per nucleon pair of $\sqrt{s_{\mathrm{NN}}} = 5.02$ TeV, accompanied by neutron emission, was used to extract the energy dependence of the photonuclear cross section γPb. This analysis and its results were presented in Chap. 4, covering the kinematic region of $17 < W_{\gamma\mathrm{Pb,n}} < 920$ GeV, corresponding to a Bjorken-x range of three orders of magnitude, $1.1 \times 10^{-5} < x < 3.3 \times 10^{-2}$. These results represent the highest energy measurement of the γPb cross section and the nuclear suppression factor available to date, extending the accessible range by more than 300 GeV with respect to the previous measurements.

The results indicate that the data in the low-energy range of 25 to 35 GeV align well with the predictions of IA and STARlight, both of which lack QCD dynamical effects. However, these models prove inadequate at higher energies, which constitute the primary focus of this study. Theoretical predictions that incorporate nuclear shadowing or saturation effects exhibit the closest agreement with the high-energy data.

Bibliography

[1] **ALICE** Collaboration, S. Acharya *et al.*, "Energy dependence of coherent photonuclear production of J/ψ mesons in ultra-peripheral Pb-Pb collisions at $\sqrt{s_{NN}}$ = 5.02 TeV", *JHEP* **10** (2023) 119, arXiv:2305.19060 [nucl-ex].

[2] **ALICE** Collaboration, "ALICE upgrades during the LHC Long Shutdown 2", arXiv:2302.01238 [physics.ins-det].

[3] **ALICE** Collaboration, T. Herman, "J/ψ Photoproduction Results from ALICE", *Acta Phys. Polon. Supp.* **16** no. 1, (2023) 98.

[4] **ALICE** Collaboration, T. Herman, "Latest ALICE results on J/ψ photoproduction in ultra-peripheral collisions at the LHC", in *28th International Workshop on Deep Inelastic Scattering and Related Subjects*. 7, 2021. arXiv:2107.13284 [nucl-ex].

[5] **ALICE** Collaboration, T. Herman, "Latest ALICE results on coherent J/ψ photoproduction in ultra-peripheral Pb$-$Pb collisions at the LHC", *PoS* **LeptonPhoton2019** (2019) 145.

[6] **H1, ZEUS** Collaboration, H. Abramowicz *et al.*, "Combination of measurements of inclusive deep inelastic $e^{\pm}p$ scattering cross sections and QCD analysis of HERA data", *Eur. Phys. J. C* **75** (2015) 580, arXiv:1506.06042 [hep-ex].

[7] A. H. Mueller, "Small x Behavior and Parton Saturation: A QCD Model", *Nucl. Phys. B* **335** (1990) 115–137.

[8] A. Morreale and F. Salazar, "Mining for Gluon Saturation at Colliders", *Universe* **7** (2021) 312, arXiv:2108.08254 [hep-ph].

[9] K. J. Eskola, P. Paakkinen, H. Paukkunen, and C. A. Salgado, "EPPS21: a global QCD analysis of nuclear PDFs", *Eur. Phys. J. C* **82** no. 5, (2022) 413, arXiv:2112.12462 [hep-ph].

[10] N. Armesto, "Nuclear shadowing", *J. Phys. G* **32** (2006) R367–R394, arXiv:hep-ph/0604108.

[11] L. D. McLerran and R. Venugopalan, "Computing quark and gluon distribution functions for very large nuclei", *Phys. Rev. D* **49** (1994) 2233–2241, arXiv:hep-ph/9309289.

[12] A. Accardi *et al.*, "Electron Ion Collider: The Next QCD Frontier: Understanding the glue that binds us all", *Eur. Phys. J. A* **52** no. 9, (2016) 268, arXiv:1212.1701 [nucl-ex].

[13] M. G. Ryskin, "Diffractive J/ψ electroproduction in LLA QCD", *Z. Phys. C* **57** (1993) 89–92.

[14] V. Guzey, E. Kryshen, and M. Zhalov, "Coherent photoproduction of vector mesons in ultraperipheral heavy ion collisions: Update for run 2 at the CERN Large Hadron Collider", *Phys. Rev. C* **93** (2016) 055206, arXiv:1602.01456 [nucl-th].

[15] **ALICE** Collaboration, J. Adam *et al.*, "Measurement of an excess in the yield of J/ψ at very low p_{T} in Pb-Pb collisions at $\sqrt{s_{\mathrm{NN}}} = 2.76$ TeV", *Phys. Rev. Lett.* **116** (2016) 222301, arXiv:1509.08802 [nucl-ex].

[16] **STAR** Collaboration, J. Adam *et al.*, "Low-p_T e^+e^- pair production in Au+Au collisions at $\sqrt{s_{NN}} = 200$ GeV and U+U collisions at $\sqrt{s_{NN}} = 193$ GeV at STAR", *Phys. Rev. Lett.* **121** no. 13, (2018) 132301, arXiv:1806.02295 [hep-ex].

[17] **STAR** Collaboration, J. Adam *et al.*, "Observation of excess J/ψ yield at very low transverse momenta in Au+Au collisions at $\sqrt{s_{\mathrm{NN}}} = 200$ GeV and U+U collisions at $\sqrt{s_{\mathrm{NN}}} = 193$ GeV", *Phys. Rev. Lett.* **123** (2019) 132302, arXiv:1904.11658 [hep-ex].

[18] **ALICE** Collaboration, S. Acharya *et al.*, "Dielectron production at midrapidity at low transverse momentum in peripheral and semi-peripheral Pb–Pb collisions at $\sqrt{s}_{\mathrm{NN}} = 5.02$ TeV", *JHEP* **06** (2023) 024, arXiv:2204.11732 [nucl-ex].

[19] **ALICE** Collaboration, "Photoproduction of low-p_{T} J/ψ from peripheral to central Pb−Pb collisions at 5.02 TeV", arXiv:2204.10684 [nucl-ex].

[20] **LHCb** Collaboration, R. Aaij *et al.*, "J/ψ photoproduction in Pb-Pb peripheral collisions at $\sqrt{s_{NN}}$= 5 TeV", *Phys. Rev. C* **105** (2022) L032201, arXiv:2108.02681 [hep-ex].

[21] S. R. Klein and J. Nystrand, "Exclusive vector meson production in relativistic heavy ion collisions", *Phys. Rev.* **C60** (1999) 014903, arXiv:hep-ph/9902259 [hep-ph].

[22] A. J. Baltz *et al.*, "The Physics of Ultraperipheral Collisions at the LHC", *Phys. Rept.* **458** (2008) 1–171, arXiv:0706.3356 [nucl-ex].

[23] J. G. Contreras and J. D. Tapia Takaki, "Ultra-peripheral heavy-ion collisions at the LHC", *Int. J. Mod. Phys.* **A30** (2015) 1542012.

[24] S. R. Klein and H. Mäntysaari, "Imaging the nucleus with high-energy photons", *Nature Rev. Phys.* **1** (2019) 662–674, arXiv:1910.10858 [hep-ex].

[25] S. Klein and P. Steinberg, "Photonuclear and Two-photon Interactions at High-Energy Nuclear Colliders", *Ann. Rev. Nucl. Part. Sci.* **70** (2020) 323–354, arXiv:2005.01872 [nucl-ex].

[26] J. G. Contreras, "Gluon shadowing at small x from coherent J/ψ photoproduction data at energies available at the CERN Large Hadron Collider", *Phys. Rev. C* **96** (2017) 015203, arXiv:1610.03350 [nucl-ex].

[27] A. J. Baltz, S. R. Klein, and J. Nystrand, "Coherent vector meson photoproduction with nuclear breakup in relativistic heavy ion collisions", *Phys. Rev. Lett.* **89** (2002) 012301, arXiv:nucl-th/0205031.

[28] V. Guzey, M. Strikman, and M. Zhalov, "Disentangling coherent and incoherent quasielastic J/ψ photoproduction on nuclei by neutron tagging in ultraperipheral ion collisions at the LHC", *Eur. Phys. J. C* **74** (2014) 2942, arXiv:1312.6486 [hep-ph].

[29] I. A. Pshenichnov, "Electromagnetic excitation and fragmentation of ultrarelativistic nuclei", *Phys. Part. Nucl.* **42** (2011) 215–250.

[30] **ALICE** Collaboration, B. Abelev *et al.*, "Coherent J/ψ photoproduction in ultra-peripheral Pb-Pb collisions at $\sqrt{s_{\rm NN}} = 2.76$ TeV", *Phys. Lett. B* **718** (2013) 1273–1283, arXiv:1209.3715 [nucl-ex].

[31] **ALICE** Collaboration, E. Abbas *et al.*, "Charmonium and e^+e^- pair photoproduction at mid-rapidity in ultra-peripheral Pb-Pb collisions at $\sqrt{s_{\rm NN}}$=2.76 TeV", *Eur. Phys. J. C* **73** (2013) 2617, arXiv:1305.1467 [nucl-ex].

[32] **CMS** Collaboration, V. Khachatryan *et al.*, "Coherent J/ψ photoproduction in ultra-peripheral PbPb collisions at $\sqrt{s_{\rm NN}} = 2.76$ TeV with the CMS experiment", *Phys. Lett. B* **772** (2017) 489–511, arXiv:1605.06966 [nucl-ex].

[33] **LHCb** Collaboration, R. Aaij *et al.*, "Study of coherent J/ψ production in lead-lead collisions at $\sqrt{s_{\rm NN}}$ = 5 TeV", *JHEP* **07** (2022) 117, arXiv:2107.03223 [hep-ex].

[34] **ALICE** Collaboration, S. Acharya *et al.*, "Coherent J/ψ and ψ' photoproduction at midrapidity in ultra-peripheral Pb–Pb collisions at $\sqrt{s_{NN}}$ = 5.02 TeV", *Eur. Phys. J. C* **81** (2021) 712, arXiv:2101.04577 [nucl-ex].

[35] **ALICE** Collaboration, S. Acharya *et al.*, "First measurement of the $|t|$-dependence of coherent J/ψ photonuclear production", *Phys. Lett. B* **817** (2021) 136280, arXiv:2101.04623 [nucl-ex].

[36] **ALICE** Collaboration, S. Acharya *et al.*, "Coherent J/ψ photoproduction at forward rapidity in ultra-peripheral Pb-Pb collisions at $\sqrt{s_{\rm NN}} = 5.02$ TeV", *Phys. Lett. B* **798** (2019) 134926, arXiv:1904.06272 [nucl-ex].

[37] **ALICE** Collaboration, S. Acharya *et al.*, "Coherent photoproduction of ρ^0 vector mesons in ultra-peripheral Pb-Pb collisions at $\sqrt{s_{\rm NN}}$ = 5.02 TeV", *JHEP* **06** (2020) 035, arXiv:2002.10897 [nucl-ex].

[38] V. Guzey, E. Kryshen, M. Strikman, and M. Zhalov, "Evidence for nuclear gluon shadowing from the ALICE measurements of PbPb ultraperipheral exclusive J/ψ production", *Phys. Lett. B* **726** (2013) 290–295, arXiv:1305.1724 [hep-ph].

[39] **ATLAS** Collaboration, G. Aad *et al.*, "Exclusive dielectron production in ultraperipheral Pb+Pb collisions at $\sqrt{s_{\rm NN}}$ = 5.02 TeV with ATLAS", *JHEP* **2306** (2023) 182, arXiv:2207.12781 [nucl-ex].

[40] **ALICE** Collaboration, J. Adam *et al.*, "Coherent ρ^0 photoproduction in ultra-peripheral Pb-Pb collisions at $\sqrt{s_{\rm NN}} = 2.76$ TeV", *JHEP* **09** (2015) 095, arXiv:1503.09177 [nucl-ex].

[41] **ALICE** Collaboration, S. Acharya *et al.*, "First measurement of coherent $\rho 0$ photoproduction in ultra-peripheral Xe–Xe collisions at $\sqrt{s_{\rm NN}} = 5.44$ TeV", *Phys. Lett. B* **820** (2021) 136481, arXiv:2101.02581 [nucl-ex].

[42] **CMS** Collaboration, A. M. Sirunyan *et al.*, "Observation of Forward Neutron Multiplicity Dependence of Dimuon Acoplanarity in Ultraperipheral Pb-Pb Collisions at $\sqrt{s_{NN}}$=5.02 TeV", *Phys. Rev. Lett.* **127** (2021) 122001, arXiv:2011.05239 [hep-ex].

[43] **ATLAS** Collaboration, G. Aad *et al.*, "Exclusive dimuon production in ultraperipheral Pb+Pb collisions at $\sqrt{s_{\rm NN}} = 5.02$ TeV with ATLAS", *Phys. Rev. C* **104** (2021) 024906, arXiv:2011.12211 [nucl-ex].

[44] L. A. Harland-Lang, "Exciting ions: A systematic treatment of ultraperipheral heavy ion collisions with nuclear breakup", *Phys. Rev. D* **107** no. 9, (2023) 093004, arXiv:2303.04826 [hep-ph].

[45] S. R. Klein and J. Nystrand, "Interference in exclusive vector meson production in heavy ion collisions", *Phys. Rev. Lett.* **84** (2000) 2330–2333, arXiv:hep-ph/9909237.

[46] S. R. Klein, J. Nystrand, J. Seger, Y. Gorbunov, and J. Butterworth, "STARlight: A Monte Carlo simulation program for ultra-peripheral collisions of relativistic ions", *Comput. Phys. Commun.* **212** (2017) 258–268, arXiv:1607.03838 [hep-ph].

[47] M. Broz, J. G. Contreras, and J. D. Tapia Takaki, "A generator of forward neutrons for ultra-peripheral collisions: $\mathbf{n}^{\mathbf{O}}_{\mathbf{O}}\mathbf{n}$", *Comput. Phys. Commun.* (2020) 107181, arXiv:1908.08263 [nucl-th].

[48] A. Veyssiere, H. Beil, R. Bergere, P. Carlos, and A. Lepretre, "Photoneutron cross sections of 208 Pb and 197 Au", *Nucl. Phys. A* **159** (1970) 561–576.

[49] T. A. Armstrong *et al.*, "Total hadronic cross-section of gamma rays in hydrogen in the energy range 0.265-GeV to 4.215-GeV", *Phys. Rev. D* **5** (1972) 1640–1652.

[50] T. A. Armstrong *et al.*, "The total photon deuteron hadronic cross-section in the energy range 0.265-4.215 GeV", *Nucl. Phys. B* **41** (1972) 445–473.

[51] N. Bianchi *et al.*, "Total hadronic photoabsorption cross-section on nuclei in the nucleon resonance region", *Phys. Rev. C* **54** (1996) 1688–1699.

[52] T. Lappi and H. Mantysaari, "J/ψ production in ultraperipheral Pb+Pb and p+Pb collisions at energies available at the CERN Large Hadron Collider", *Phys. Rev. C* **87** (2013) 032201, arXiv:1301.4095 [hep-ph].

[53] J. Cepila, J. G. Contreras, and M. Krelina, "Coherent and incoherent J/ψ photonuclear production in an energy-dependent hot-spot model", *Phys. Rev. C* **97** (2018) 024901, arXiv:1711.01855 [hep-ph].

[54] H. Mäntysaari and B. Schenke, "Probing subnucleon scale fluctuations in ultraperipheral heavy ion collisions", *Phys. Lett. B* **772** (2017) 832–838, arXiv:1703.09256 [hep-ph].

[55] D. Bendova, J. Cepila, J. G. Contreras, and M. Matas, "Photonuclear J/ψ production at the LHC: Proton-based versus nuclear dipole scattering amplitudes", *Phys. Lett. B* **817** (2021) 136306, arXiv:2006.12980 [hep-ph].

[56] V. P. Gonçalves, D. E. Martins, and C. R. Sena, "Coherent and incoherent J/ψ photoproduction in Pb–Pb collisions at the LHC, HE-LHC and FCC", *Eur. Phys. J. A* **57** (2021) 82, arXiv:2007.13625 [hep-ph].

[57] K. J. Eskola, C. A. Flett, V. Guzey, T. Löytäinen, and H. Paukkunen, "Exclusive J/ψ photoproduction in ultraperipheral Pb+Pb collisions at the CERN Large Hadron Collider calculated at next-to-leading order perturbative QCD", *Phys. Rev. C* **106** (2022) 035202, arXiv:2203.11613 [hep-ph].

[58] G. F. Chew and G. C. Wick, "The Impulse Approximation", *Phys. Rev.* **85** (1952) 636.

[59] T. H. Bauer, R. D. Spital, D. R. Yennie, and F. M. Pipkin, "The Hadronic Properties of the Photon in High-Energy Interactions", *Rev. Mod. Phys.* **50** (1978) 261. [Erratum: Rev.Mod.Phys. 51, 407 (1979)].

[60] A. Pautz and G. Shaw, "Nuclear shadowing and ρ photoproduction", *Phys. Rev. C* **57** (May, 1998) 2648–2654. https://link.aps.org/doi/10.1103/PhysRevC.57.2648.

[61] M. G. Ryskin, R. G. Roberts, A. D. Martin, and E. M. Levin, "Diffractive J / psi photoproduction as a probe of the gluon density", *Z. Phys. C* **76** (1997) 231–239, arXiv:hep-ph/9511228.

[62] A. D. Martin, C. Nockles, M. G. Ryskin, and T. Teubner, "Small x gluon from exclusive J/psi production", *Phys. Lett. B* **662** (2008) 252–258, arXiv:0709.4406 [hep-ph].

[63] V. Guzey and M. Zhalov, "Exclusive J/ψ production in ultraperipheral collisions at the LHC: constrains on the gluon distributions in the proton and nuclei", *JHEP* **10** (2013) 207, arXiv:1307.4526 [hep-ph].

[64] K. J. Eskola, H. Paukkunen, and C. A. Salgado, "EPS09: A New Generation of NLO and LO Nuclear Parton Distribution Functions", *JHEP* **04** (2009) 065, arXiv:0902.4154 [hep-ph].

[65] L. Frankfurt, V. Guzey, and M. Strikman, "Leading Twist Nuclear Shadowing Phenomena in Hard Processes with Nuclei", *Phys. Rept.* **512** (2012) 255–393, arXiv:1106.2091 [hep-ph].

[66] D. Bendova, J. Cepila, J. G. Contreras, and M. Matas, "Solution to the Balitsky-Kovchegov equation with the collinearly improved kernel including impact-parameter dependence", *Phys. Rev. D* **100** (2019) 054015, arXiv:1907.12123 [hep-ph].

[67] J. Cepila, J. G. Contreras, and M. Matas, "Predictions for nuclear structure functions from the impact-parameter dependent Balitsky-Kovchegov equation", *Phys. Rev. C* **102** no. 4, (2020) 044318, arXiv:2002.11056 [hep-ph].

[68] A. G. Shuvaev, K. J. Golec-Biernat, A. D. Martin, and M. G. Ryskin, "Off diagonal distributions fixed by diagonal partons at small x and xi", *Phys. Rev.* **D60** (1999) 014015, arXiv:hep-ph/9902410 [hep-ph].

[69] V. N. Gribov, "Glauber corrections and the interaction between high-energy hadrons and nuclei", *Sov. Phys. JETP* **29** (1969) 483–487.

[70] N. Armesto, "A Simple model for nuclear structure functions at small x in the dipole picture", *Eur. Phys. J.* **C26** (2002) 35–43, arXiv:hep-ph/0206017 [hep-ph].

[71] M. L. Good and W. D. Walker, "Diffraction disssociation of beam particles", *Phys. Rev.* **120** (1960) 1857–1860.

[72] H. I. Miettinen and J. Pumplin, "Diffraction Scattering and the Parton Structure of Hadrons", *Phys. Rev. D* **18** (1978) 1696.

[73] S. R. Klein, "Challenges to the Good-Walker paradigm in coherent and incoherent photoproduction", *Phys. Rev. C* **107** no. 5, (2023) 055203, arXiv:2301.01408 [hep-ph].

[74] H. Mäntysaari, "Review of proton and nuclear shape fluctuations at high energy", *Rept. Prog. Phys.* **83** (2020) 082201, arXiv:2001.10705 [hep-ph].

[75] J. Cepila, J. G. Contreras, and J. D. Tapia Takaki, "Energy dependence of dissociative J/ψ photoproduction as a signature of gluon saturation at the LHC", *Phys. Lett.* **B766** (2017) 186–191, arXiv:1608.07559 [hep-ph].

[76] K. J. Golec-Biernat and M. Wusthoff, "Saturation effects in deep inelastic scattering at low Q**2 and its implications on diffraction", *Phys. Rev. D* **59** (1998) 014017, arXiv:hep-ph/9807513.

[77] N. Armesto, C. A. Salgado, and U. A. Wiedemann, "Relating high-energy lepton-hadron, proton-nucleus and nucleus-nucleus collisions through geometric scaling", *Phys. Rev. Lett.* **94** (2005) 022002, arXiv:hep-ph/0407018.

[78] H. Mäntysaari and B. Schenke, "Evidence of strong proton shape fluctuations from incoherent diffraction", *Phys. Rev. Lett.* **117** (2016) 052301, arXiv:1603.04349 [hep-ph].

[79] **ALICE** Collaboration, K. Aamodt *et al.*, "The ALICE experiment at the CERN LHC", *JINST* **3** (2008) S08002.

[80] **ALICE** Collaboration, B. Abelev *et al.*, "Performance of the ALICE Experiment at the CERN LHC", *Int. J. Mod. Phys.* **A29** (2014) 1430044, arXiv:1402.4476 [nucl-ex].

[81] A. Tauro, "ALICE Schematics." General Photo, May, 2017.

[82] **ALICE** Collaboration, K. Aamodt *et al.*, "Alignment of the ALICE Inner Tracking System with cosmic-ray tracks", *JINST* **5** (2010) P03003, arXiv:1001.0502 [physics.ins-det].

[83] J. Alme *et al.*, "The ALICE TPC, a large 3-dimensional tracking device with fast readout for ultra-high multiplicity events", *Nucl. Instrum. Meth.* **A622** (2010) 316–367, arXiv:1001.1950 [physics.ins-det].

[84] **ALICE** Collaboration, J. Adam *et al.*, "Determination of the event collision time with the ALICE detector at the LHC", *Eur. Phys. J. Plus* **132** (2017) 99, arXiv:1610.03055 [physics.ins-det].

[85] **ALICE** Collaboration, *ALICE dimuon forward spectrometer: Technical Design Report*. Technical design report. ALICE. CERN, Geneva, 1999. http://cds.cern.ch/record/401974.

[86] **ALICE** Collaboration, E. Abbas *et al.*, "Performance of the ALICE VZERO system", *JINST* **8** (2013) P10016, arXiv:1306.3130 [nucl-ex].

[87] M. Broz *et al.*, "Performance of ALICE AD modules in the CERN PS test beam", *JINST* **16** (2021) P01017, arXiv:2006.14982 [physics.ins-det].

[88] G. Herrera Corral, "Diffractive Physics with ALICE at the LHC: the control of quantum collisions", *J. Phys. Conf. Ser.* **624** no. 1, (2015) 012008.

[89] G. Puddu *et al.*, "The zero degree calorimeters for the ALICE experiment", *Nucl. Instrum. Meth. Phys. Res. Sect. A* **581** (2007) 397–401.

[90] C. Oppedisano *et al.*, "Physics performance of the ALICE zero degree calorimeter", *Nucl. Phys. B Proc. Suppl.* **197** (2009) 206–210.

[91] M. Schweizer, "One of the two Zero Degree Calorimeter installed in the LHC tunnel near the ALICE cavern.." `http://cds.cern.ch/record/1087658`, Jan, 2008.

[92] **ALICE TPC** Collaboration, J. Adolfsson *et al.*, "The upgrade of the ALICE TPC with GEMs and continuous readout", *JINST* **16** no. 03, (2021) P03022, `arXiv:2012.09518 [physics.ins-det]`.

[93] AliceO2Group, "QualityControl, GitHub repository." `https://github.com/AliceO2Group/QualityControl`, 2021. Cited 2021-08-30.

[94] **ALICE** Collaboration, J. Adam *et al.*, "Technical Design Report for the Muon Forward Tracker", tech. rep., CERN, Jan, 2015. `https://cds.cern.ch/record/1981898`.

[95] MFT, "MFT TWiki page." `https://twiki.cern.ch/twiki/bin/viewauth/ALICE/MuonForwardTracker`. Cited 2023-07-11.

[96] ALICE, "ALICE web page - MFT detector." `https://alice-collaboration.web.cern.ch/menu_proj_items/MFT`. Cited 2023-07-11.

[97] **ALICE** Collaboration, G. Aglieri Rinella, "The ALPIDE pixel sensor chip for the upgrade of the ALICE Inner Tracking System", *Nucl. Instrum. Meth. A* **845** (2017) 583–587.

[98] J. A. Ballin, J. P. Crooks, P. D. Dauncey, A.-M. Magnan, Y. Mikami, O. D. Miller, M. Noy, V. Rajovic, M. Stanitzki, K. Stefanov, R. Turchetta, M. Tyndel, E. G. Villani, N. K. Watson, and J. A. Wilson, "Monolithic active pixel sensors (maps) in a quadruple well technology for nearly 100factor and full cmos pixels", *Sensors* **8** no. 9, (2008) 5336–5351. `https://www.mdpi.com/1424-8220/8/9/5336`.

[99] S. Senyukov, J. Baudot, A. Besson, G. Claus, L. Cousin, A. Dorokhov, W. Dulinski, M. Goffe, C. Hu-Guo, and M. Winter, "Charged particle detection performances of CMOS pixel sensors produced in a 0.18νm process with a high resistivity epitaxial layer", *Nucl. Instrum. Meth. A* **730** (2013) 115–118, `arXiv:1301.0515 [physics.ins-det]`.

[100] M. Collaboration, "ALICE MFT operation Webpage." `https://alice-mft-operation.docs.cern.ch/`. Cited 2023-07-11.

[101] M. C. ALICE, "ALICE Muon Forward Tracker (MFT)", Dec, 2020. https://cds.cern.ch/record/2748310. General Photo.

[102] A. Caratelli, S. Bonacini, K. Kloukinas, A. Marchioro, P. Moreira, R. D. Oliveira, and C. Paillard, "The gbt-sca, a radiation tolerant asic for detector control and monitoring applications in hep experiments", *Journal of Instrumentation* **10** no. 03, (Mar, 2015) C03034. https://dx.doi.org/10.1088/1748-0221/10/03/C03034.

[103] M. Tkáčik, J. Jadlovský, S. Jadlovská, L. Koska, A. Jadlovská, and M. Donadoni, "Fred—flexible framework for frontend electronics control in alice experiment at cern", *Processes* **8** no. 5, (2020) . https://www.mdpi.com/2227-9717/8/5/565.

[104] T. Toffoli and N. Margolus, *Cellular Automata Machines: A New Environment for Modeling*. The MIT Press, 04, 1987. https://doi.org/10.7551/mitpress/1763.001.0001.

[105] I. Abt, I. Kisel, S. Masciocchi, and D. Emelyanov, "CATS: A cellular automaton for tracking in silicon for the HERA-B vertex detector", *Nucl. Instrum. Meth. A* **489** (2002) 389–405.

[106] R. Brun, F. Bruyant, F. Carminati, S. Giani, M. Maire, A. McPherson, G. Patrick, and L. Urban, *GEANT: Detector Description and Simulation Tool; Oct 1994*. CERN Program Library. CERN, Geneva, 1993. https://cds.cern.ch/record/1082634. Long Writeup W5013.

[107] **ALICE** Collaboration, "ALICE luminosity determination for Pb−Pb collisions at $\sqrt{s_{\mathrm{NN}}} = 5.02$ TeV", arXiv:2204.10148 [nucl-ex].

[108] J. E. Gaiser, *Charmonium Spectroscopy From Radiative Decays of the* J/ψ *and* ψ'. PhD thesis, SLAC, 1982. http://www-public.slac.stanford.edu/sciDoc/docMeta.aspx?slacPubNumber=slac-r-255.html.

[109] **Particle Data Group** Collaboration, R. L. Workman *et al.*, "Review of Particle Physics", *PTEP* **2022** (2022) 083C01.

[110] **ALICE** Collaboration, "First polarisation measurement of coherently photoproduced J/ψ in ultra-peripheral Pb−Pb collisions at $\sqrt{s_{\mathrm{NN}}}$ = 5.02 TeV", arXiv:2304.10928 [nucl-ex].

[111] H. Xing, C. Zhang, J. Zhou, and Y.-J. Zhou, "The cos 2ϕ azimuthal asymmetry in ρ^0 meson production in ultraperipheral heavy ion collisions", *JHEP* **10** (2020) 064, arXiv:2006.06206 [hep-ph].

[112] **STAR** Collaboration, M. Abdallah *et al.*, "Tomography of ultrarelativistic nuclei with polarized photon-gluon collisions", *Sci. Adv.* **9** (2023) eabq3903, arXiv:2204.01625 [nucl-ex].

[113] **H1** Collaboration, C. Alexa *et al.*, "Elastic and Proton-Dissociative Photoproduction of J/ψ Mesons at HERA", *Eur. Phys. J.* **C73** no. 6, (2013) 2466, arXiv:1304.5162 [hep-ex].

[114] I. Pshenichnov, I. Mishustin, J. Bondorf, A. Botvina, and A. Ilinov, "Particle emission following Coulomb excitation in ultrarelativistic heavy ion collisions", *Phys. Rev. C* **60** (1999) 044901, arXiv:nucl-th/9901061.

[115] **ALICE** Collaboration, "Neutron emission in ultraperipheral Pb-Pb collisions at $\sqrt{s_{\rm NN}} = 5.02$ TeV", arXiv:2209.04250 [nucl-ex].

[116] **ALICE** Collaboration, J. Adam *et al.*, "Differential studies of inclusive J/ψ and ψ(2S) production at forward rapidity in Pb-Pb collisions at $\sqrt{s_{\rm NN}} = 2.76$ TeV", *JHEP* **05** (2016) 179, arXiv:1506.08804 [nucl-ex].

[117] **H1** Collaboration, F. D. Aaron *et al.*, "Measurement of the Inclusive ep Scattering Cross Section at Low Q^2 and x at HERA", *Eur. Phys. J. C* **63** (2009) 625–678, arXiv:0904.0929 [hep-ex].

[118] **ALICE** Collaboration, S. Acharya *et al.*, "Energy dependence of exclusive J/ψ photoproduction off protons in ultra-peripheral p–Pb collisions at $\sqrt{s_{\rm NN}} = 5.02$ TeV", *Eur. Phys. J. C* **79** (2019) 402, arXiv:1809.03235 [nucl-ex].

[119] **ALICE** Collaboration, S. Acharya *et al.*, "Exclusive and dissociative J/ψ photoproduction, and exclusive dimuon production, in p-Pb collisions at sNN=8.16 TeV", *Phys. Rev. D* **108** no. 11, (2023) 112004, arXiv:2304.12403 [nucl-ex].

[120] S. Abrahamyan *et al.*, "Measurement of the Neutron Radius of ^{208}Pb Through Parity-Violation in Electron Scattering", *Phys. Rev. Lett.* **108** (2012) 112502, arXiv:1201.2568 [nucl-ex].

[121] A. J. Baltz, M. J. Rhoades-Brown, and J. Weneser, "Heavy ion partial beam lifetimes due to Coulomb induced processes", *Phys. Rev. E* **54** (1996) 4233–4239.

[122] **CMS** Collaboration, A. Tumasyan *et al.*, "Probing Small Bjorken-x Nuclear Gluonic Structure via Coherent J/ψ Photoproduction in Ultraperipheral Pb-Pb Collisions at sNN=5.02 TeV", *Phys. Rev. Lett.* **131** no. 26, (2023) 262301, arXiv:2303.16984 [nucl-ex].

Appendix A

Publications

Published for SISSA by Springer

Received: June 7, 2023
Revised: August 8, 2023
Accepted: October 4, 2023
Published: October 20, 2023

Energy dependence of coherent photonuclear production of J/ψ mesons in ultra-peripheral Pb-Pb collisions at $\sqrt{s_{NN}} = 5.02$ TeV

The ALICE collaboration

E-mail: ALICE-publications@cern.ch

Abstract: The cross section for coherent photonuclear production of J/ψ is presented as a function of the electromagnetic dissociation (EMD) of Pb. The measurement is performed with the ALICE detector in ultra-peripheral Pb-Pb collisions at a centre-of-mass energy per nucleon pair of $\sqrt{s_{NN}} = 5.02$ TeV. Cross sections are presented in five different J/ψ rapidity ranges within $|y| < 4$, with the J/ψ reconstructed via its dilepton decay channels. In some events the J/ψ is not accompanied by EMD, while other events do produce neutrons from EMD at beam rapidities either in one or the other beam direction, or in both. The cross sections in a given rapidity range and for different configurations of neutrons from EMD allow for the extraction of the energy dependence of this process in the range $17 < W_{\gamma\,\mathrm{Pb,n}} < 920$ GeV, where $W_{\gamma\,\mathrm{Pb,n}}$ is the centre-of-mass energy per nucleon of the γPb system. This range corresponds to a Bjorken-x interval spanning about three orders of magnitude: $1.1 \times 10^{-5} < x < 3.3 \times 10^{-2}$. In addition to the ultra-peripheral and photonuclear cross sections, the nuclear suppression factor is obtained. These measurements point to a strong depletion of the gluon distribution in Pb nuclei over a broad, previously unexplored, energy range. These results, together with previous ALICE measurements, provide unprecedented information to probe quantum chromodynamics at high energies.

Keywords: Heavy Ion Experiments, Quarkonium, Forward Physics

ArXiv ePrint: 2305.19060

https://doi.org/10.1007/JHEP10(2023)119

JHEP10(2023)119

Contents

JHEP10(2023)119

1 Introduction

One of the main research topics in quantum chromodynamics (QCD) today is the study of the hadronic structure when probed at high energies, corresponding to low values of the fraction of the hadron momentum carried by the colliding parton (Bjorken-x). The gluon distribution inside the proton has been observed to increase steeply at low values of x [1]. At some point, this growth must stop to preserve unitarity. In QCD this is achieved by a dynamic equilibrium of gluon splitting and annihilation processes. This

regime of the gluon distribution is known as saturation, see ref. [2] for a recent review. In a nucleus with A nucleons, the parton distributions would naively be A times those in a single nucleon, but modifications, known as nuclear shadowing, are observed at small x [3]. Similar considerations to those for a single nucleon regarding unitarity imply that saturation is expected to set in for large nuclei at lower energies (higher x values) than in protons, with this behaviour scaling roughly as $A^{1/3}$ [4].

Diffractive production of J/ψ vector mesons off nuclear targets is a powerful tool to study the energy evolution of the structure of heavy nuclei. The interaction can involve the full nucleus or only one nucleon; these cases are called coherent and incoherent production, respectively. The coherent process has a large experimental cross section, it is very sensitive to the gluon structure of hadrons, and it can be described within perturbative QCD owing to the large J/ψ mass, which provides a hard scale to justify the use of perturbative techniques. At the LHC, the coherent production of J/ψ can be measured in ultra-peripheral collisions (UPCs) where the incoming Pb nuclei pass each other at impact parameters larger than the sum of their radii, such that the interaction involves photons from the strong electromagnetic field of the incoming ions [5–8].

Previous measurements of this process at the LHC were performed at different centre-of-mass energies per nucleon pair ($\sqrt{s_{\rm NN}}$) and different rapidities of the J/ψ. Using data from LHC Run 1, where the Pb nuclei collided at $\sqrt{s_{\rm NN}} = 2.76\,\text{TeV}$, the ALICE Collaboration measured the coherent photoproduction of J/ψs in UPCs at forward rapidity [9] and midrapidity [10], while the CMS Collaboration provided a cross section for this process at an intermediate rapidity range [11]. For LHC Run 2, the energy of Pb-Pb collisions was raised to $\sqrt{s_{\rm NN}} = 5.02\,\text{TeV}$ and new measurements of this process were performed by the ALICE Collaboration at mid [12, 13] and forward rapidity [14] as well as by the LHCb Collaboration at forward rapidity [15].

The importance of a wide experimental rapidity coverage is that the rapidity of the J/ψ in this process is related to the centre-of-mass energy per nucleon in the $\gamma\,$Pb system by $(W_{\gamma\,\text{Pb,n}})^2 = m\sqrt{s_{\rm NN}}\exp(-y)$, where m is the mass of the J/ψ and y its rapidity in the laboratory frame measured with respect to the direction of the incoming Pb nucleus. (Natural units are used in all equations.) At the LHC, either of the two incoming Pb ions can be the source of the photon and, in this circumstance, the cross section for the coherent photoproduction of J/ψ in UPCs as a function of rapidity has two components [16]

$$\frac{\mathrm{d}\sigma_{\rm PbPb}}{\mathrm{d}y} = n_\gamma(y,\{b\})\sigma_{\gamma\,\rm Pb}(y) + n_\gamma(-y,\{b\})\sigma_{\gamma\,\rm Pb}(-y), \tag{1.1}$$

where $\sigma_{\gamma\,\rm Pb}(y)$ is the photonuclear cross section for the coherent production of a J/ψ at rapidity y, and $n_\gamma(y)$ is the photon flux which, in the equivalent photon approximation [5], quantifies the number of photons with energy $k = (m/2)\exp(-y)$. The notation $\{b\}$ signifies that the flux is obtained by integrating over a range on impact parameter b.

A study of the rapidity dependence of $\sigma_{\gamma\,\rm Pb}$ was performed in ref. [17] using ALICE Run 1 data at $\sqrt{s_{\rm NN}} = 2.76\,\text{TeV}$. The analysis is based on two facts: (1) at $y = 0$ both contributions in eq. (1.1) are equal, so that knowledge of the photon flux $n_\gamma(y = 0)$ yields $\sigma_{\gamma\,\rm Pb}$ at the corresponding $W_{\gamma\,\text{Pb,n}} = 92\,\text{GeV}$; (2) at the largest rapidities accessible to

JHEP10(2023)119

ALICE, the first term in the right-hand side of eq. (1.1) contributes only about 5% so that the UPC cross section is dominated by the second term in eq. (1.1) corresponding to interactions with low-energy photons at $W_{\gamma\,\mathrm{Pb,n}} = 20\,\mathrm{GeV}$ for the ALICE data used in the analysis. The extracted cross sections are discussed in section 6.2.

In order to extract the full energy dependence of $\sigma_{\gamma\,\mathrm{Pb}}$ from the UPC cross section, at least two measurements at the same rapidity but with different photon fluxes are needed. Up to now, there are two proposals on how to achieve this. Both utilise the fact that the photon flux also depends on the impact-parameter range where the $\gamma\,\mathrm{Pb}$ interaction takes place. One proposal, presented in ref. [18], makes use of the coherent production of J/ψ measured in *peripheral* collisions originally reported by the ALICE Collaboration [19] and later on confirmed by the STAR [20], ALICE [21], and LHCb [22] Collaborations. Applying this approach to ALICE data at $\sqrt{s_{\mathrm{NN}}} = 2.76\,\mathrm{TeV}$ for the coherent photonuclear production of J/ψ measured in peripheral collisions and in UPCs, in ref. [18] the cross sections for $\sigma_{\gamma\,\mathrm{Pb}}$ at three values of $W_{\gamma\,\mathrm{Pb,n}}$: 18 GeV, 92 GeV, and 470 GeV are obtained. The extracted cross sections are discussed in section 6.2. The other proposal, presented in refs. [23, 24], utilises the fact that the electromagnetic fields of the incoming nuclei are so strong that there is a sizeable probability of a second photon exchange between the colliding nuclei, which may result in the electromagnetic dissociation (EMD) of at least one of the interacting nuclei [25]. The presence of neutrons from EMD of one or both nuclei, which can be determined using zero-degree calorimeters, can be used to tag specific ranges of the impact parameter. This is so because high energy photons are emitted at smaller impact parameters than low energy photons and in order to induce the dissociation of a nucleus a photon needs a minimum energy of the order of 10 MeV. This means that events where EMD has occurred select a photon flux with $\{b\}$ covering smaller impact parameters than events without EMD. In this way, the measurement of coherent J/ψ photoproduction in UPCs with no, single, or mutual EMD can be used to disentangle the two different $\sigma_{\gamma\,\mathrm{Pb}}$ contributions in eq. (1.1) [24]. The tagging of single and mutual EMD has been successfully tested; first, in the measurement of coherent ρ^0 photoproduction at midrapidity by the ALICE Collaboration [26–28], and later in the measurement of $\gamma\gamma \to \mu^+\mu^-$ and $\gamma\gamma \to e^+e^-$ in UPCs by the CMS and ATLAS Collaborations [29–31]. These ATLAS and CMS measurements have been successfully described by the newest version of the SuperChic Monte Carlo generator [32]. More recently, the CMS Collaboration submitted results on the coherent photoproduction of J/ψ accompanied by EMD in a rapidity range complementary to the one explored in this analysis [33].

In this article, the cross section for the coherent photoproduction of J/ψ accompanied by nuclear EMD is presented (section 6.1). The measurement is carried out in five rapidity regions covering the intervals $|y| < 0.8$ and $2.5 < |y| < 4.0$. These measurements are used to extract the photonuclear cross section $\sigma_{\gamma\,\mathrm{Pb}}$ in the range $17 < W_{\gamma\,\mathrm{Pb,n}} < 920\,\mathrm{GeV}$, which corresponds to a Bjorken-x in the range $1.1\times10^{-5} < x < 3.3\times10^{-2}$, where $x = m^2/W^2_{\gamma\,\mathrm{Pb,n}}$ (section 6.2). In addition, the nuclear suppression factor is obtained in this kinematic region (section 6.3). The measurements are compared to theoretical models covering a wide spectrum of approaches going from models assuming no nuclear dynamics, to state-of-the-art computations based on perturbative QCD.

JHEP10(2023)119

2 Theoretical models

Many different models provide predictions for the coherent photoproduction of J/ψ in UPCs; for example, those presented in refs. [16, 34–40]. Predictions for this process when accompanied by EMD of the incoming nuclei exist for only a few of the models, which are discussed in section 2.2. All the models are based on the computation of the two elements shown in eq. (1.1): the photon flux $n_\gamma(y)$ and the photonuclear cross section $\sigma_{\gamma\,\mathrm{Pb}}(y)$. There is also an interference term [41], but its effect, when the cross section is integrated over the transverse momentum of the J/ψ as for the results presented here, can be neglected.

2.1 The photon flux

The predictions and the experimental results discussed below utilise photon fluxes based on the approach of the STARlight [16, 42] and $\mathbf{n^{O}_{O}n}$ models [43]. There are two steps to compute the photon fluxes: obtaining the total flux, and computing the fractions of the flux that are assigned to the different EMD classes presented in section 4.3.

The total flux as implemented in both STARlight and $\mathbf{n^{O}_{O}n}$ is computed in the semi-classical approximation (for details see, e.g. ref. [5]). In this approach, the form factor of the Pb ion is modelled with a Woods-Saxon distribution, while the coherence condition is supplemented by the requirement of no hadronic interactions, as obtained with a Poissonian model based on the nuclear overlap function and the total nucleon-nucleon cross section.

Both STARlight [23] and $\mathbf{n^{O}_{O}n}$ [43] compute the fractions of the total fluxes for each EMD scenario based on photoproduction data measured at lower energies and extrapolations to LHC energies. There are two relevant differences between STARlight and $\mathbf{n^{O}_{O}n}$. First, STARlight uses the Lorentz-line parameterisation of the giant-dipole resonance data described in ref. [44], while $\mathbf{n^{O}_{O}n}$ uses the data directly; the numerical difference between them is negligible. Second, $\mathbf{n^{O}_{O}n}$ uses photonuclear Pb data in the nucleon resonance region [45], while STARlight uses data from photon-nucleon interactions [46, 47] in this region. Both models provide similar fluxes apart from the most forward rapidity region. In this kinematic range, the fluxes differ by up to 20%. As $\mathbf{n^{O}_{O}n}$ uses experimental data on $\gamma\,\mathrm{Pb}$ collisions, the fluxes from this model are used in section 6.2 to extract the photonuclear cross section.

2.2 The photonuclear cross section

The photonuclear cross section can be computed using various theoretical approaches. The impulse approximation (IA) assumes that the nuclear scattering is given by the superposition of the scattering on the individual nucleons [48]. In the context of the coherent production of J/ψ, a nuclear suppression factor can be defined using IA, and the associated cross section $\sigma^{\mathrm{IA}}_{\gamma\,\mathrm{Pb}}$. This factor quantifies the difference between the nucleus being a set of independent nucleons and a real nucleus:

$$S_{\mathrm{Pb}}(W_{\gamma\,\mathrm{Pb,n}}) = \sqrt{\frac{\sigma_{\gamma\,\mathrm{Pb}}}{\sigma^{\mathrm{IA}}_{\gamma\,\mathrm{Pb}}}}. \tag{2.1}$$

JHEP10(2023)119

The square root in eq. (2.1) is motivated by the fact that the diffractive photoproduction of J/ψ is proportional to the square of the gluon distribution of the target within the leading log approximation of QCD [49].

The model for the photonuclear cross section by Klein and Nystrand [16], implemented in STARlight, is based on the following steps. A parameterisation of HERA data on the exclusive forward production of J/ψ is converted, using the vector dominance model (VDM) [50], into the forward cross section for $J/\psi + p \to J/\psi + p$; using the optical theorem, this cross section yields the total $J/\psi + p$ cross section, which is introduced into a classical Glauber prescription to produce the total cross section for $J/\psi + Pb$. Finally, the optical theorem and VDM are used again to obtain the forward $\sigma_{\gamma\,Pb}$. The nuclear form factor is used to obtain the total $\sigma_{\gamma\,Pb}$.

The model by Guzey, Kryshen, and Zhalov [34] is based on the leading logarithmic approximation of perturbative QCD [49] for the exclusive production of J/ψ at zero momentum transfer for $\gamma\,p$ collisions. This cross section is scaled to the nuclear case using the square of the ratio of the gluon distribution in the Pb nucleus to the gluon distribution in the proton scaled by the Pb mass number. The computation is performed for two cases. The first one is based on the EPS09-LO parameterisation of nuclear parton density functions [51]. The second one relies on the leading twist approximation (LTA) of gluon shadowing [52]. This model includes the nuclear form factor computed with a Woods-Saxon prescription. The photon fluxes needed to compute the UPC cross section are obtained from the flux fractions given by STARlight. The theoretical uncertainties explored in this model originate in the spread of predictions from the nuclear parton distribution functions (PDFs) for the EPS09-LO case, and in the uncertainty on the parameters of LTA obtained by fits to HERA diffractive data. For the LTA case, the uncertainty on the predicted cross sections reaches up to 30%, while for EPS09-LO it can be as large as a factor of 2. The authors of the LTA computations provided the upper and lower limits of their predictions. The average of these numbers is depicted in the figures shown in section 6. These figures also show the predictions for the EPS09-based model, using the central value of the EPS09 parameterisation.

The model by Bendova et al. [38] is based on the solution of the impact-parameter dependent Balitsky-Kovchegov (b-BK) equation, as discussed in ref. [53] and references therein. There are two models presented in ref. [38]. One uses the b-BK equation to evolve the amplitude for the interaction of a colour dipole with a proton towards higher energies, and then uses this amplitude to compute the $\gamma\,p$ cross section at the given energy followed by the application of the Glauber-Gribov approach [54], in order to obtain the photonuclear cross section. The second model, shown in the figures below with the notation b-BK-A, starts with a nuclear initial condition for the b-BK equation whose solutions at higher energies can then be directly used to obtain the photonuclear cross section without the need of a Glauber-Gribov prescription. The photon fluxes needed to compute the UPC cross section are given by the $\mathbf{n}^{\mathbf{O}}_{\mathbf{O}}\mathbf{n}$ model. There are some theoretical uncertainties associated with this type of model [55]. The main two uncertainties are related to the use of the Glauber-Gribov approach instead of a nuclear initial condition, and to the approach used to compute the J/ψ wave function. The first uncertainty changes the cross section

JHEP10(2023)119

for coherent production of J/ψ up to 30% [38], while the J/ψ wave function produces an uncertainty up to about 20% [37, 56]. This model is valid only at small Bjorken-x, so the cross section in UPCs for $|y|$ larger than about three cannot be predicted as these rapidities are dominated by contributions with Bjorken-x larger than 0.01.

The model by Cepila et al. [36] is based on the colour-dipole approach to QCD, including gluon saturation effects, framed within the Good-Walker formalism for diffraction [57–59]. In this model, hadrons are constituted by hot spots with the hadronic structure fluctuating event by event. For a recent review, see ref. [60]. This type of model describes HERA data [61, 62]. In the model by Cepila et al. the number of hot spots increases as Bjorken-x decreases and the transition from proton to nuclear targets is based on the Glauber-Gribov prescription. The theoretical uncertainties coming from the wave function of the J/ψ are the same as described above. Other uncertainties related to the fluctuation of the colour fields were explored in ref. [61] and found to be small with respect to the current precision of the experimental data. The uncertainty on the modelling of the nuclear case was explored in ref. [36] by comparing the Glauber-Gribov prescription with results based on a geometric-scaling approach. Differences of up to 30% were found, with recent data [12] clearly preferring the Glauber-Gribov prescription, which is shown in the figures below with the notation GG-HS. Also in this case, the photon fluxes needed to compute the UPC cross section are given by the $\mathbf{n}^{\mathbf{O}}_{\mathbf{O}}\mathbf{n}$ model.

3 Experimental set-up

The results presented here are based on a data sample collected with the ALICE detector in 2018, when the LHC provided collisions of Pb nuclei at $\sqrt{s_{\rm NN}} = 5.02$ TeV. The experimental signature of the events of interest for this analysis consists of a pair of leptons, from the J/ψ decay, the potential presence of neutrons emitted at beam rapidities by EMD, and no other signal above the noise threshold recorded in the detector. The two tracks produced by the leptons are measured with the central barrel detectors (dimuon and dielectron decay channels of the J/ψ) to obtain the results for $|y| < 0.8$, discussed in section 3.1, or with the muon spectrometer (dimuon channel only) to obtain the results for $2.5 < |y| < 4.0$, described in section 3.2. Forward detectors located in the A and C sides of the experiment[1] are used to record the neutrons and to veto other activity; they are introduced in section 3.3. The triggers used in this analysis, and the associated luminosity, are presented in section 3.4. The full description of the ALICE detector and its performance can be found in refs. [63, 64].

3.1 Central barrel detectors

Three central barrel detectors, the Inner Tracking System (ITS), the Time Projection Chamber (TPC), and the Time-of-Flight (TOF) were used to record data for this analysis. These detectors are surrounded by a large solenoid magnet producing a magnetic field of $B = 0.5$ T. Their common pseudorapidity acceptance is $|\eta| < 0.9$.

[1]The A and C nomenclature is used LHC wide and refers to the direction of flight of the beams in the accelerator as being anti- or clockwise when the LHC is seen from the top.

JHEP10(2023)119

The ITS [65] consists of six cylindrical layers of silicon detectors. The innermost layer is at a radius of 3.9 cm with respect to the beam axis, while the outermost layer is at 43 cm. The two layers closest to the beam form the Silicon Pixel Detector (SPD) and cover the range in pseudorapidity $|\eta| < 1.4$. The SPD is a fine granularity detector with about 10 million pixels. It serves as a tracking device and can also be used to issue triggers. Surrounding the SPD there are two layers of silicon drift chambers and then two layers of silicon microstrips. These four outer layers of the ITS are used in this analysis exclusively for tracking.

The TPC [66] is a five metre long cylindrical chamber separated into two drift volumes by a 100 kV central electrode. The two end-plates are 250 cm away from the central electrode along the beam direction; they are instrumented with multi-wire proportional chambers that are readout by about 560 000 pads allowing for high precision tracking in the transverse plane. The longitudinal coordinate is given by the drift time of ionisation electrons in the TPC electric field. For each individual track, the TPC provides up to 159 track points, which also provide energy-loss measurements that are used for particle identification (PID). In the momentum range of the tracks considered in this analysis (from 1 to 2 GeV/c) the PID from the TPC allows for a clean separation of electrons from muons. The TPC covers the range $|\eta| < 0.9$.

The TOF detector consists of a barrel of multi-gap resistive plate chambers that provide a high precision timing for tracks traversing TOF [67]. It surrounds the TPC and has a pseudorapidity coverage of $|\eta| < 0.9$. The TOF readout channels are arranged into 18 azimuth sectors that can provide topological trigger decisions [68].

3.2 The muon spectrometer

The muon spectrometer, located in the C side of the experiment, covers the pseudorapidity interval $-4 < \eta < -2.5$. The composition of the muon spectrometer, when seen from the nominal interaction point (IP), is as follows. First, there is a ten hadronic interaction-length absorber — made of carbon, concrete, and steel — with the task of filtering out hadrons produced in the collisions. The absorber is followed by five tracking stations, each made of two planes of cathode pad chambers. The third station is inside a dipole magnet producing a 3 T m integrated magnetic field. The next element is an iron wall with a thickness of 7.2 hadronic interaction lengths, which is followed by the muon trigger system consisting of two stations, each instrumented with two layers of resistive plate chambers. In addition, a conical absorber made of tungsten, lead, and steel surrounds the beam pipe at small polar angles (less than 2°) with the mission of shielding the spectrometer from secondary particles. Muon tracks detected in the trigger stations are used by the trigger and matched offline to the tracks reconstructed in the five tracking stations. The trigger system provides single-muon and dimuon triggers for tracks above a programmable transverse-momentum threshold. For the 2018 data used in this analysis the threshold was set to 1 GeV/c. The trigger efficiency for tracks measured with both the trigger and the tracking chambers increases with transverse momentum and it is approximately 50% at 1 GeV/c.

JHEP10(2023)119

3.3 Forward detectors

The zero-degree neutron calorimeters, ZNA and ZNC, are two 8.7 interaction-length calorimeters made of a tungsten alloy with embedded quartz fibres [69, 70]. They are located ± 112.5 m, respectively, from the IP along the beam direction. They detect neutral particles produced at a pseudorapidity $|\eta| > 8.8$. Each calorimeter is segmented into four towers. Half the optical fibres, which are uniformly distributed in the calorimeter, are read out by four photomultipliers (PMTs) and the other half are read out by a single fifth photomultiplier common to all towers. The signals collected from the PMTs are used to determine the energy deposition. The relative energy resolution for one neutron is about 20% [71]. In addition, each calorimeter provides timing information obtained with a TDC (time-to-digital converter). The detectors can also provide a trigger signal.

Two systems, V0 [72] and AD [73], are used to veto other activity in the events. Both V0 and AD are based on plastic scintillators and wave-length shifters; the light is captured using PMTs. Each system has two counters that are placed at both sides of the IP along the beam direction. The V0 counters have 32 scintillator tiles each. They cover the pseudorapidity ranges $2.8 < \eta < 5.1$ (V0A) and $-3.7 < \eta < -1.7$ (V0C) and are located at 340 cm and 90 cm from the interaction point, respectively. The AD system consists of two arrays, each of 8 scintillator modules. The arrays are arranged in two layers of four modules. The AD arrays cover the pseudorapidity ranges $4.7 < \eta < 6.3$ (ADA) and $-6.9 < \eta < -4.9$ (ADC), and are located 17 m and 19.5 m from the IP, respectively. Both V0 and AD have a timing resolution well below 1 ns, and both can be used to veto hadronic interactions at the trigger level.

3.4 Triggers and luminosity

The analysis is based on two triggers: one to select candidate events with the two leptons from the decay of the J/ψ detected by the central barrel detectors (denoted as CBtrig below) and the other to select candidate events where the muons are measured by the muon spectrometer (denoted as MStrig below). They use trigger inputs from AD, V0, TOF, SPD and the muon trigger system.

AD and V0 provide triggers based on the timing of the signal. Two time windows are defined: one to trigger by events compatible with an interaction at the IP (beam-beam window) and another compatible with interactions happening behind one of the two counters of each system (beam-gas window). In the triggers described below, the requested input is the logical negation of a trigger in the beam-beam window. For the V0 the following nomenclature is used: notVBA (notVBC) for the veto of activity in V0A (V0C). The corresponding triggers for AD are notUBA and notUBC.

The SPD is read out by 400 (800) chips in the inner (outer) layer with each of the readout chips providing a trigger signal if at least one of its pixels is fired. When projected into the transverse plane, the chips are arranged in 20 (40) azimuth regions in the inner (outer) layer allowing for a topological selection of events at the trigger level. In particular, a trigger element, denoted by STG below, requires at least two pairs of chips where each

JHEP10(2023)119

pair has a trigger signal in the inner and in the outer layer in the same azimuth region and the pairs are back-to-back in azimuth.

A similar trigger, called OMU, is based on the trigger signals from TOF where between 2 and 6 signals from TOF are required, such that at least two of them are back-to-back in azimuth.

Using these elements CBtrig is the logical AND of: notVBA, notVBC, notUBA, notUBC, STG, and OMU. MStrig is given by the logical AND of MUL and notVBA, where MUL stands for a dimuon with the tracks having opposite electric charge and each of them is above the transverse-momentum threshold of 1 GeV/c as measured by the trigger chambers of the muon spectrometer.

The integrated luminosity (L_{int}) of the samples selected by the central barrel and the muon spectrometer triggers just described is determined using reference cross sections measured in van der Meer scans [74] and amounts to $233 \pm 7\,\mu\mathrm{b}^{-1}$ and $533 \pm 13\,\mu\mathrm{b}^{-1}$, respectively.

4 Data samples

4.1 Event selection with the central barrel detectors

The event selection is the same as that of ref. [12]. Events are kept for further analysis if:

- CBtrig is fired.
- There is a reconstructed primary vertex, determined using at least two reconstructed tracks, and having a position within 15 cm of either side of the IP along the beam direction.
- There are, in the central barrel, exactly two good reconstructed tracks of opposite electric charge. Good reconstructed tracks are made of signals from the ITS and the TPC. Each track has to cross at least 70 (out of a maximum of 159) TPC pad rows and it also has to include signals from both SPD layers. Each track must have a distance of closest approach to the primary vertex, in the direction along the beam line, of less than 2 cm.
- The transverse momentum of the pair fulfils $p_{\mathrm{T}} < 0.2\,\mathrm{GeV}/c$, in order to select a data sample enriched with coherently produced events.
- Events have to pass the offline selection using the reconstructed information from V0 and AD. The offline selection in these detectors is more precise than vetoes at the trigger level, because it relies on larger time windows than the trigger electronics and on a more refined algorithm to quantify the signal.

The PID capabilities of the TPC are used to determine the mass to be associated with a track according to the proximity of the energy lost by ionisation to that expected by an electron or muon hypothesis. The selected events are distributed into two rapidity intervals, $|y| < 0.2$ and $0.2 < |y| < 0.8$. They are the input for the midrapidity analysis described below.

JHEP10(2023)119

4.2 Event selection with the muon spectrometer

The event selection follows closely that used in ref. [14]; the difference being that in 2015 the trigger included, in addition to a veto in V0A as in 2018, vetoes in ADA, ADC, and V0C. The 2018 data sample, which has less vetoes, is used for this analysis. As the data sample is smaller in this analysis than for the results presented in ref. [14], the integrated luminosity is correspondingly reduced. Note also, that after the publication of ref. [14], the luminosity determination was better understood [74] which reflects in a substantially smaller uncertainty for the luminosity in the present work. Events are kept for further analysis if:

- MStrig is fired.
- There are, in the muon spectrometer, exactly two good reconstructed tracks of opposite electric charge. Good reconstructed tracks have a pseudorapidity $-4 < \eta < -2.5$; their radial position at the exit of the absorber lies within 17.5 cm and 89.5 cm to ensure that they pass through the homogeneous region of the absorber; the information of the trigger chambers matches that from the tracking chambers; the track momentum multiplied by the distance of closest approach of the track to the interaction point is below a set threshold to remove beam-induced background.
- The four-momentum of the track pair, constructed using the muon mass, has to have a rapidity in the range $2.5 < |y| < 4$. The transverse momentum of the pair is less than $0.25\,\mathrm{GeV}/c$.
- The event passes an offline veto, which is applied using the reconstructed information from V0A. At most two tiles in V0C have a signal in the beam-beam window, in order to allow for a maximum of two muons crossing this counter.

The selected events are distributed into three rapidity intervals, $2.5 < |y| < 3.0$, $3.0 < |y| < 3.5$, and $3.5 < |y| < 4.0$. They are the input for the forward rapidity analysis described below.

4.3 Event classification using ZNA and ZNC

The selected events are classified into three neutron classes depending on the presence of signals in the neutron zero-degree calorimeters. The presence of a neutron is determined using the timing capabilities of the calorimeter. If the TDC registers a signal that has an energy over a threshold around 500 GeV, then the event is tagged as having at least one neutron emitted near beam rapidities. The following classes can be formed:

- No neutrons are registered either in ZNA or in ZNC. This class is denoted as 0n0n below.
- At least one neutron is observed in one of the calorimeters, but not in the other. There are two cases: (*i*) ZNA detects at least one neutron and ZNC shows no neutron activity, or (*ii*) ZNC detects neutron(s) and ZNA does not. They are denoted as 0nXn

JHEP10(2023)119

or Xn0n, respectively. For the data sample at midrapidity, both cases are combined in one class: 0nXn+Xn0n. For the data sample at forward rapidity, the 0nXn sample has a large contamination from incoherent J/ψ production [24], so only the class Xn0n is considered for further analysis.

- Both ZNA and ZNC detect at least one neutron. This case is denoted as XnXn.

4.4 Monte Carlo samples

The STARlight Monte Carlo (MC) [42] (version: r299) is used to generate event samples for the following five processes in Pb-Pb UPC: coherent and incoherent production of both J/$\psi \to l^+l^-$ and $\psi' \to$ J/$\psi + X$ as well as $\gamma\gamma \to l^+l^-$, where l denotes a lepton. The generated particles are propagated through a model of the ALICE experimental set-up implemented in GEANT 3.21 [75]. The simulation matches the time evolution of the detector conditions during the data-taking period. The simulated data sets are passed through the same analysis chain as the real data, which allows for using the coherent MC sample to compute the acceptance and efficiency of the detector for signal, and all samples to be used to determine the background.

5 Analysis procedure

The cross section for coherent J/ψ photoproduction in UPC for a given neutron class and rapidity interval is given by

$$\frac{\mathrm{d}\sigma_{\mathrm{PbPb}}}{\mathrm{d}y} = \frac{N_{\mathrm{J}/\psi}}{(\mathrm{A}\times\epsilon)\times \mathrm{BR}(\mathrm{J}/\psi \to l^+l^-)\times L_{\mathrm{int}}\times \Delta y}, \tag{5.1}$$

where $N_{\mathrm{J}/\psi}$ represents the J/ψ yield, (A$\times\epsilon$) takes into account the acceptance and efficiency of the detector, BR(J/$\psi \to l^+l^-$) is the branching ratio, L_{int} stands for the integrated luminosity of the corresponding data sample, and Δy is the width of the rapidity interval.

5.1 Yield extraction

In order to make the best use of the limited amount of data at midrapidity, specially for the XnXn neutron class, the data samples for the two decay channels (J/$\psi \to e^+e^-$ and J/$\psi \to \mu^+\mu^-$) are joined and analysed together. Note that in our previous analysis [12], it was demonstrated that both decay channels produce compatible cross sections for coherent J/ψ production, justifying our decision to join the samples.

The extraction of the J/ψ yield involves three steps: a fit to the invariant mass distribution of the lepton pairs; the subtraction of contributions from ψ' feed-down and from incoherent J/ψ production; and a correction to account for the migration across the different neutron classes.

The invariant mass distribution is modelled with two Crystal Ball [76] functions, to describe the J/ψ and ψ' signals, and a term to take into account the background, mostly from two-photon production of dilepton pairs. For the analysis at midrapidity, this background is represented by an exponential distribution, while for the analysis at forward rapidity it

JHEP10(2023)119

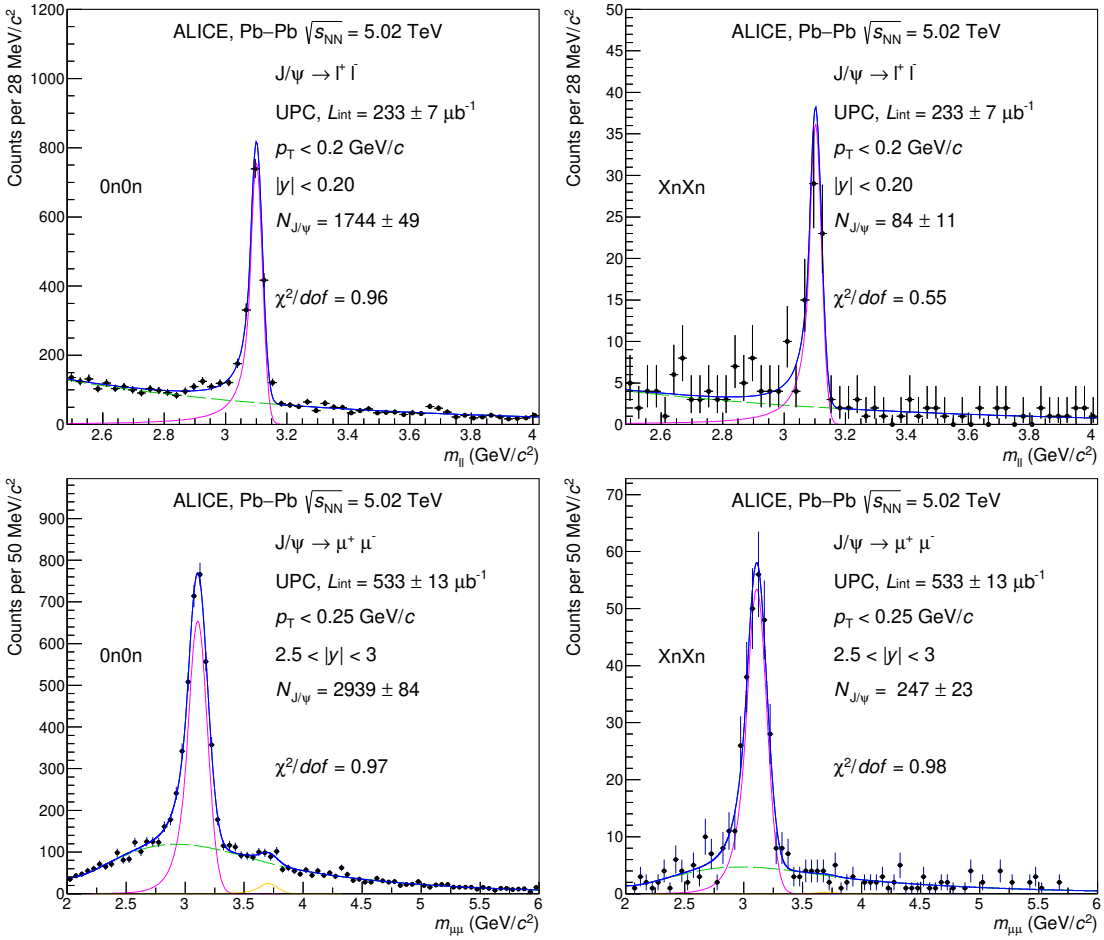

Figure 1. Invariant-mass distributions for events in the 0n0n (left) and XnXn (right) neutron classes measured at mid (top) and forward rapidity (bottom). The solid black markers represent data, the vertical line through each of them is the associated statistical uncertainty. The blue lines depict the fit models, described in the text, which are composed of a signal (shown in magenta) and a background (shown in green) contribution. In the lower left plot the contribution from ψ' is clearly visible (shown in yellow).

is parameterised using a fourth-order polynomial that turns smoothly into an exponential tail for masses larger than 4 GeV/c^2. The tail parameters of the Crystal Ball functions are fixed to the values found by fits to the MC samples. The mass difference between the ψ' and the J/ψ is fixed according to the values from ref. [77]. The width parameter for the ψ' is fixed to the width parameter of the J/ψ multiplied by the ratio of the widths of the ψ' to the J/ψ obtained from fits to the MC samples. The J/ψ pole mass and width are left free. At forward rapidity, the polynomial parameters for the background are fixed to the values from a fit to the MC samples of the $\gamma\gamma \to \mu^+\mu^-$ process. The slope of the exponential is left free. The main output of the fit is the number of J/ψ candidates ($N_{\rm fit}$) and its associated uncertainty. Examples of the fit to the invariant mass distribution for the mid and forward rapidity analyses for two different neutron classes are shown in figure 1.

JHEP10(2023)119

The number of candidates from the fit contains contributions from coherent and incoherent processes as well as from feed-down from ψ'. The number of coherent candidates is given by:

$$N_{\rm coh} = \frac{N_{\rm fit}}{1 + f_{\rm I} + f_{\rm D}}, \tag{5.2}$$

where the fractions $f_{\rm I} = N_{\rm incoh}/N_{\rm coh}$ and $f_{\rm D} = N_{\text{feed-down}}/N_{\rm coh}$ correct for the number of J/ψ coming from the incoherent process ($N_{\rm incoh}$) and from decays of ψ' ($N_{\text{feed-down}}$). The fraction $f_{\rm D}$ is obtained directly from data as explained in ref. [12] for the midrapidity and in ref. [14] for the forward rapidity analysis. The values found are $f_{\rm D} = 0.039 \pm 0.006$ and $f_{\rm D} = 0.055 \pm 0.010$, respectively.

The fraction $f_{\rm I}$, see table 3, is obtained from a fit to the transverse momentum distribution of lepton pairs in a restricted range of the invariant mass of the pair around the J/ψ pole mass ($2.9 < m < 3.2\,{\rm GeV}/c^2$ and $2.85 < m < 3.35\,{\rm GeV}/c^2$ for the analysis at mid and at forward rapidities, respectively). This fit uses MC templates from STARlight for coherent and incoherent J/ψ production, J/ψ from decays of coherent and incoherent ψ' production, and from the $\gamma\gamma \to l^+l^-$ process. In addition, incoherent J/ψ production with nucleon dissociation, a process not included in the STARlight MC but present in data, is taken into account, to describe the large transverse momentum region, with a template based on the H1 parameterisation of this process [78]. The normalisation of the templates from feed-down is constrained by the value of $f_{\rm D}$, while the normalisation of the $\gamma\gamma \to l^+l^-$ template is fixed by the fits to the invariant mass distribution. The three free parameters of the fit are the normalisation of both incoherent templates and of the coherent template. Examples of the fit to the transverse momentum distributions for the mid and forward rapidity analyses for two different neutron classes are shown in figure 2.

The last step to extract the J/ψ yield in a given class is to take into account the possibility of misclassification of events. There are two potential effects: that a neutron is not measured (ZNA, ZNC efficiency) which could move an event, for example, from the Xn0n into the 0n0n class; and, that a neutron from a collision of an independent pair of Pb ions is detected (pile-up), which may then shift an event, for example, from the 0n0n to the Xn0n class. The pile-up probability is determined using a special data sample collected with an unbiased trigger; it amounts to 0.0237 ± 0.0005 and 0.0238 ± 0.0006 for ZNA and ZNC, respectively. The efficiency of detecting at least one neutron in a Xn event is determined as explained in ref. [79] and amounts to 0.933 ± 0.017 for ZNA and 0.931 ± 0.017 for ZNC. The effects of pile-up and inefficiencies give rise to a migration matrix which is applied to the $N_{\rm coh}$ values of the different classes to obtain the $N_{\rm J/\psi}$ values. Note that migration does not change the total number of J/ψ candidates, so this correction introduces anti-correlated uncertainties.

5.2 Corrections

The term $({\rm A} \times \epsilon)$, in eq. (5.1) is the product of three factors: $({\rm A} \times \epsilon)_{\rm det}$, $\epsilon_{\rm pu}$, and $\epsilon_{\rm emd}$. $({\rm A} \times \epsilon)_{\rm det}$ accounts for the acceptance and efficiency of the detector, including the trigger system, to measure the decay products of the coherently produced J/ψ; it is obtained from the data sample of MC simulated events. These events were produced under the assumption of

JHEP10(2023)119

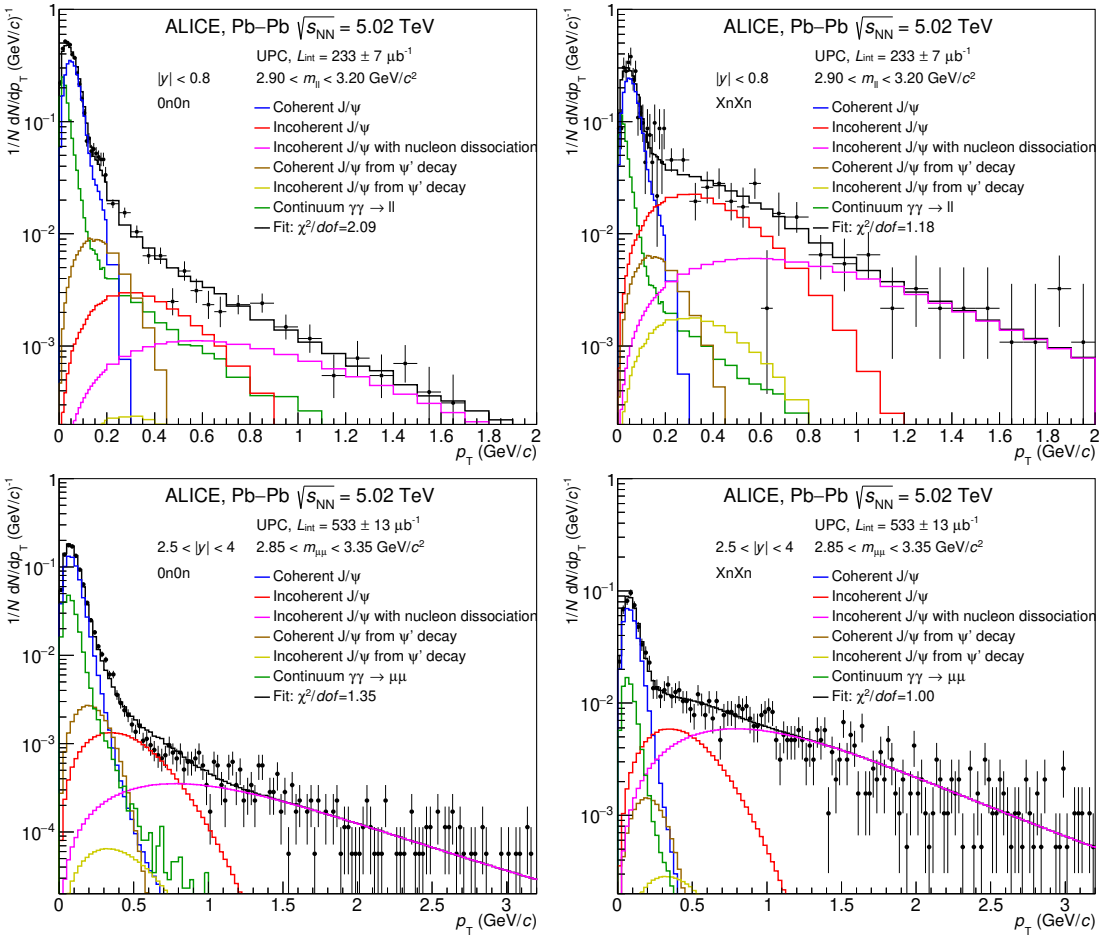

Figure 2. Transverse momentum distributions for events of the 0n0n (left) and XnXn (right) neutron classes measured at mid (top) and forward rapidity (bottom). The solid black markers represent data, the vertical line through each of them is the associated statistical uncertainty. The black lines depict the fit model described in the text.

transverse polarisation as expected for the case of photoproduction and recently confirmed by the ALICE Collaboration [80]. Polarisation could also play a role at midrapidity due to the interference of the two possible photon sources. As the incoming photon is linearly polarised, the interference causes an azimuthal anisotropy that can be observed in the final state [81, 82]. Interference effects appear at low values of transverse momenta and at midrapidity where both amplitudes are similar [41]. As the measurements presented here are integrated over transverse momentum, the potential impact of the interference is suppressed. Furthermore, the interference contributes mainly at small impact parameters, that is in the XnXn class, where our data sample has the largest statistical uncertainty and the contribution of interference effects is not visible.

The other two terms, $\epsilon_{\rm pu}$, and $\epsilon_{\rm emd}$, take into account the effects of pile-up. The first one, $\epsilon_{\rm pu}$, accounts for cases where, in addition to the coherent production of J/ψ, another independent collision leaves signals in V0 or AD causing the event to be rejected at the

JHEP10(2023)119

trigger level. The pile-up probability is measured using data selected with an unbiased trigger based on the timing of bunches crossing the IP. For the midrapidity analysis $\epsilon_{\rm pu} = 0.920 \pm 0.002$, while for the forward rapidity sample $\epsilon_{\rm pu} = 0.962 \pm 0.001$; the uncertainty comes from the size of the unbiased data sample. The second pile-up factor, $\epsilon_{\rm emd}$, takes into account events where the dissociation of the incoming nucleus produces, in addition to neutrons, charged particles that leave a signal in AD or V0. These extra particles come from EMD events with the neutron emission accompanied by the emission of protons or pions. According to ref. [83], the corresponding cross sections are expected to be large. This factor is determined with a data sample triggered by an energy deposition over the threshold in either ZNA or ZNC; this sample is populated by EMD events [79]. For the 0n0n events $\epsilon_{\rm emd} = 1.0$ as there is no nuclear dissociation. For the analysis at midrapidity $\epsilon_{\rm emd} = 0.74 \pm 0.04$ and $\epsilon_{\rm emd} = 0.57 \pm 0.05$ for the 0nXn+Xn0n and XnXn classes, respectively. For the analysis at forward rapidity $\epsilon_{\rm emd} = 0.88 \pm 0.01$ and $\epsilon_{\rm emd} = 0.84 \pm 0.05$ for the Xn0n and XnXn classes, respectively. The uncertainty reflects the size of the data sample used to determine these factors.

5.3 Systematic uncertainties

A number of studies were undertaken to estimate potential systematic uncertainties. Their effect on the measured cross sections is summarised in tables 1 and 2.

To study the uncertainty on the model used for the signal extraction at midrapidity, the yield according to the Crystal Ball function is compared to counting the events under the peak region after the background is subtracted using the exponential shape from the fit. The model based on the Crystal Ball function is used as the baseline and half of the difference, amounting to 1.5%, is assigned as the systematic uncertainty. Another contribution to the uncertainty on the signal extraction comes from the description of the background. This was estimated by varying the fit range which produces a 0.3% effect which is added in quadrature to the uncertainty on the modelling of the signal. For the analysis at forward rapidity the uncertainty is estimated by varying the values of the tail parameters of the Crystal Ball function in the ranges found by fits to the signal in the simulated MC samples. This uncertainty varies from 0.1% to 1.3% and is considered uncorrelated across rapidity and neutron classes.

There is an uncorrelated source of uncertainty for the determination of $f_{\rm I}$ that originates in the modelling of the different templates needed for the fit to the transverse momentum distribution described in section 5.1. For the midrapidity analysis, it is estimated by using for the template of the $\gamma\gamma \to l^+l^-$ process either the transverse momentum distribution obtained at either side of the J/ψ peak in the invariant mass distribution or the template from the STARlight MC. For the forward analysis, the shape of the incoherent distribution is obtained either from the fit described in section 5.1 or it is constrained by fitting the transverse momentum distribution of the 0nXn sample with the requirement of activity in the ADC detector; this sample is dominated by incoherent production. The uncorrelated uncertainty for $f_{\rm I}$ varies from a fraction of a percent to a few percent.

There is also a correlated uncertainty related to the extraction of the incoherent contamination. It is known that the STARlight MC does not describe correctly the shape of

JHEP10(2023)119

		$\|y\| < 0.2$			$0.2 < \|y\| < 0.8$		
Source	Type	0n0n	0nXn+Xn0n	XnXn	0n0n	0nXn+Xn0n	XnXn
Signal extraction	U	1.5	1.5	1.5	1.5	1.5	1.5
Incoherent fraction	U	0.1	1.5	1.3	0.1	1.5	1.3
Coherent shape	C	0.1	0.8	0.6	0.1	0.8	0.6
Feed-down	C	0.6	0.6	0.6	0.6	0.6	0.6
Branching ratio	C	0.5	0.5	0.5	0.5	0.5	0.5
Luminosity	C	2.5	2.5	2.5	2.5	2.5	2.5
Trigger live time	C	1.5	1.5	1.5	1.5	1.5	1.5
ITS-TPC matching	C	2.8	2.8	2.8	2.8	2.8	2.8
TOF trigger	C	0.7	0.7	0.7	0.7	0.7	0.7
SPD trigger	C	1	1	1	1	1	1
ϵ_{pu}	C	3	3	3	3	3	3
ϵ_{emd}	C	0	3.2	3.5	0	3.2	3.5
Migrations	A	−3.9	3.4	0.9	−3.6	3.1	1.1

Table 1. Summary of the systematic uncertainties, given in percent, related to the measurements performed with the central barrel detectors. The minus sign in the entry for migrations in the 0n0n class signifies that this uncertainty is anti-correlated with those from migrations in the 0nXn+Xn0n and XnXn classes. The second column identifies the type of uncertainty (U=uncorrelated, C=correlated, A=anticorrelated) as used in eq. (6.1).

		$2.5 < \|y\| < 3.0$			$3.0 < \|y\| < 3.5$			$3.5 < \|y\| < 4.0$		
Source	Type	0n0n	Xn0n	XnXn	0n0n	Xn0n	XnXn	0n0n	Xn0n	XnXn
Signal extraction	U	0.2	1.3	0.8	0.1	0.6	0.7	0.5	0.5	0.9
Incoherent fraction	U	0.4	0.6	1.6	0.4	0.9	3.3	0.4	0.5	2.2
Coherent shape	C	0.1	0.1	0.1	0.1	0.1	0.1	0.1	0.1	0.1
Feed-down	C	0.7	0.7	0.7	0.7	0.7	0.7	0.7	0.7	0.7
Branching ratio	C	0.6	0.6	0.6	0.6	0.6	0.6	0.6	0.6	0.6
Luminosity	C	2.5	2.5	2.5	2.5	2.5	2.5	2.5	2.5	2.5
Tracking	C	3	3	3	3	3	3	3	3	3
Trigger	C	6.2	6.2	6.2	6.2	6.2	6.2	6.2	6.2	6.2
Matching	C	1	1	1	1	1	1	1	1	1
ϵ_{pu}	C	0.2	0.2	0.2	0.2	0.2	0.2	0.2	0.2	0.2
ϵ_{emd}	C	0	1.1	6	0	1.1	6	0	1.1	6
Migrations	A	−0.3	3.8	3.3	−0.2	3.6	3.6	−0.2	3.3	3.6

Table 2. Summary of the systematic uncertainties, given in percent, related to the measurements performed with the muon spectrometer. The minus sign in the entry for migrations in the 0n0n class signifies that this uncertainty is anti-correlated with those from migrations in the 0nXn+Xn0n and XnXn classes. The second column identifies the type of uncertainty (U=uncorrelated, C=correlated, A=anticorrelated) as used in eq. (6.1).

the transverse momentum distribution for the coherent production of J/ψ [13]. A different shape for the transverse momentum dependence of coherent production was used in the fit and half the difference in the results is assigned as an uncertainty. The effect is below 1% and it is larger for the midrapidity analysis since the resolution of the muon spectrometer is not as good as for the central barrel detectors, so it is not so sensitive to this effect.

JHEP10(2023)119

The uncertainty on feed-down is estimated by varying f_{D} within its uncertainty. As the determination of feed-down is independently done using the central barrel detectors and the muon spectrometer, this uncertainty is correlated only across the corresponding measurements and it is uncorrelated between the results obtained at mid and forward rapidities. It amounts to 0.6% and 0.7%, respectively.

Two other sources of uncertainties are also considered as correlated: the uncertainty on the branching ratios is obtained from ref. [77]; the uncertainty on the determination of the luminosity, coming from the measurement of the reference cross sections and from the stability of the calibration over time, is taken from ref. [74] and amounts to 2.5%. For CBtrig there is another source of uncertainty related to the luminosity of the data sample, namely the precision to which the live time of the trigger is known, which is 1.5%. The live time of MStrig is known with a very good precision and produces a negligible uncertainty.

For the central barrel analysis there are four uncertainty sources that are correlated across the corresponding measurements. A systematic uncertainty on the tracking efficiency of 2% per track is estimated by comparing, in data and in MC, the matching efficiency for track segments reconstructed in the TPC and in the ITS. This leads to a 2.8% systematic uncertainty for two tracks. The uncertainty of the TOF trigger efficiency due to the spread of the arrival times of various particle species to TOF is evaluated as 0.5% per track (1% in total). The uncertainty associated with the determination of the trigger efficiency of the SPD is obtained directly from data by varying the requirements to select the tracks used to measure this efficiency. This uncertainty amounts to 1%.

There are three correlated uncertainties associated with the muon spectrometer. The uncertainty on the tracking efficiency amounts to 3%. It is estimated by comparing the single-muon tracking efficiency values obtained in MC and data, with a procedure that exploits the redundancy of the information from the tracking chambers [84]. The systematic uncertainty on the dimuon trigger efficiency has two contributions. The uncertainty on the intrinsic efficiencies of the muon trigger chambers is determined by varying them in the MC by an amount equal to the statistical uncertainty on their measurement with a data-driven method and amounts to 1.5%. The uncertainty on the response of the trigger algorithm is obtained by comparing the trigger response function between data and MC; it amounts to 6.0%. These two contributions are added in quadrature. There is also a 1% uncertainty on the matching efficiency of tracks reconstructed with the tracking and the trigger chambers.

The uncertainty on ϵ_{pu} for the forward rapidity analysis is obtained by varying this factor within its uncertainty. It amounts to 0.2%. As there are more detector systems contributing to ϵ_{pu} in the CBtrig case, the uncertainty for the midrapidity measurements is estimated by repeating the analysis without the offline veto from AD and V0, which increases both the yield and ϵ_{pu}. These increases do not compensate exactly and the ensuing difference of 3% is assigned as a systematic uncertainty. The uncertainty on ϵ_{emd} is obtained by varying it within its uncertainty. It is of the order of a few percent, differing among the neutron classes and rapidity intervals.

The uncertainty on migrations across the different neutron classes is obtained by varying the pile-up in ZNA and ZNC as well as the efficiencies of these detectors within their uncertainties. At midrapidity the efficiency is the leading uncertainty for the XnXn neu-

JHEP10(2023)119

Class	N_{fit}	f_{I}	$(\text{A} \times \epsilon)_{\text{det}}$	$\text{d}\sigma_{\text{PbPb}}/\text{d}y$ (mb)
$\lvert y\rvert < 0.2$				
0n0n	1744 ± 49	0.014 ± 0.002	0.053	$3.130 \pm 0.090 \pm 0.047 \pm 0.164 \mp 0.122$
0nXn+Xn0n	412 ± 23	0.179 ± 0.011	0.053	$0.730 \pm 0.050 \pm 0.015 \pm 0.045 \pm 0.025$
XnXn	84 ± 11	0.144 ± 0.021	0.053	$0.250 \pm 0.024 \pm 0.005 \pm 0.016 \pm 0.002$
$0.2 < \lvert y\rvert < 0.8$				
0n0n	2179 ± 54	0.014 ± 0.002	0.024	$2.900 \pm 0.070 \pm 0.044 \pm 0.152 \mp 0.104$
0nXn+Xn0n	597 ± 28	0.179 ± 0.011	0.024	$0.800 \pm 0.040 \pm 0.017 \pm 0.050 \pm 0.025$
XnXn	134 ± 13	0.144 ± 0.021	0.024	$0.300 \pm 0.029 \pm 0.006 \pm 0.019 \pm 0.003$
$2.5 < \lvert y\rvert < 3.0$				
0n0n	2939 ± 84	0.0140 ± 0.0038	0.069	$2.668 \pm 0.076 \pm 0.011 \pm 0.199 \mp 0.009$
Xn0n	318 ± 28	0.070 ± 0.0061	0.069	$0.242 \pm 0.021 \pm 0.003 \pm 0.018 \pm 0.009$
XnXn	247 ± 23	0.1180 ± 0.0159	0.069	$0.256 \pm 0.024 \pm 0.005 \pm 0.024 \pm 0.009$
$3.0 < \lvert y\rvert < 3.5$				
0n0n	7102 ± 102	0.0130 ± 0.0041	0.194	$2.322 \pm 0.033 \pm 0.010 \pm 0.173 \mp 0.005$
Xn0n	638 ± 37	0.0480 ± 0.0090	0.194	$0.172 \pm 0.010 \pm 0.002 \pm 0.013 \pm 0.006$
XnXn	450 ± 32	0.1590 ± 0.0332	0.194	$0.161 \pm 0.011 \pm 0.005 \pm 0.015 \pm 0.006$
$3.5 < \lvert y\rvert < 4.0$				
0n0n	2403 ± 74	0.0070 ± 0.0037	0.097	$1.590 \pm 0.049 \pm 0.010 \pm 0.119 \mp 0.003$
Xn0n	189 ± 16	0.0270 ± 0.0053	0.097	$0.101 \pm 0.009 \pm 0.001 \pm 0.008 \pm 0.003$
XnXn	111 ± 16	0.1650 ± 0.0223	0.097	$0.079 \pm 0.011 \pm 0.002 \pm 0.008 \pm 0.003$

Table 3. Values for the number of J/ψ candidates (N_{fit}), the incoherent fraction (f_{I}), correction for the detector acceptance and efficiency ($(\text{A} \times \epsilon)_{\text{det}}$) and the measured cross section ($\text{d}\sigma_{\text{PbPb}}/\text{d}y$) for the different neutron classes and rapidity ranges. The first uncertainty in the last column is statistical, the rest are systematic. The second uncertainty is uncorrelated, the third correlated, and the fourth originates from migrations across neutron classes. Note that for each rapidity range the 0n0n uncertainty related to migrations is preceded by a $\mp$, while the other neutron classes have a $\pm$; this means that these uncertainties are anti-correlated.

tron class, while pile-up dominates the other two neutron classes. At forward rapidities the efficiency is the leading uncertainty. The largest difference, with respect to the nominal measurement, from all variations is taken as the uncertainty. As mentioned above, these uncertainties are anti-correlated across the neutron classes within one rapidity range.

6 Results

6.1 Cross section in UPC

Using the analysis strategy described in section 5, the cross section for the coherent production of J/ψ vector mesons in UPCs of Pb nuclei at $\sqrt{s_{\text{NN}}} = 5.02\,\text{TeV}$ is obtained. The measurements are reported in table 3 along with other numerical values needed in eq. (5.1) and (5.2).

The results are compared to the predictions from different models in figure 3. The theoretical uncertainties associated to each model are discussed in section 2. In all cases the IA calculation is well above the data signalling important shadowing effects that have a similar magnitude in each of the different neutron emission classes. The STARlight model

JHEP10(2023)119

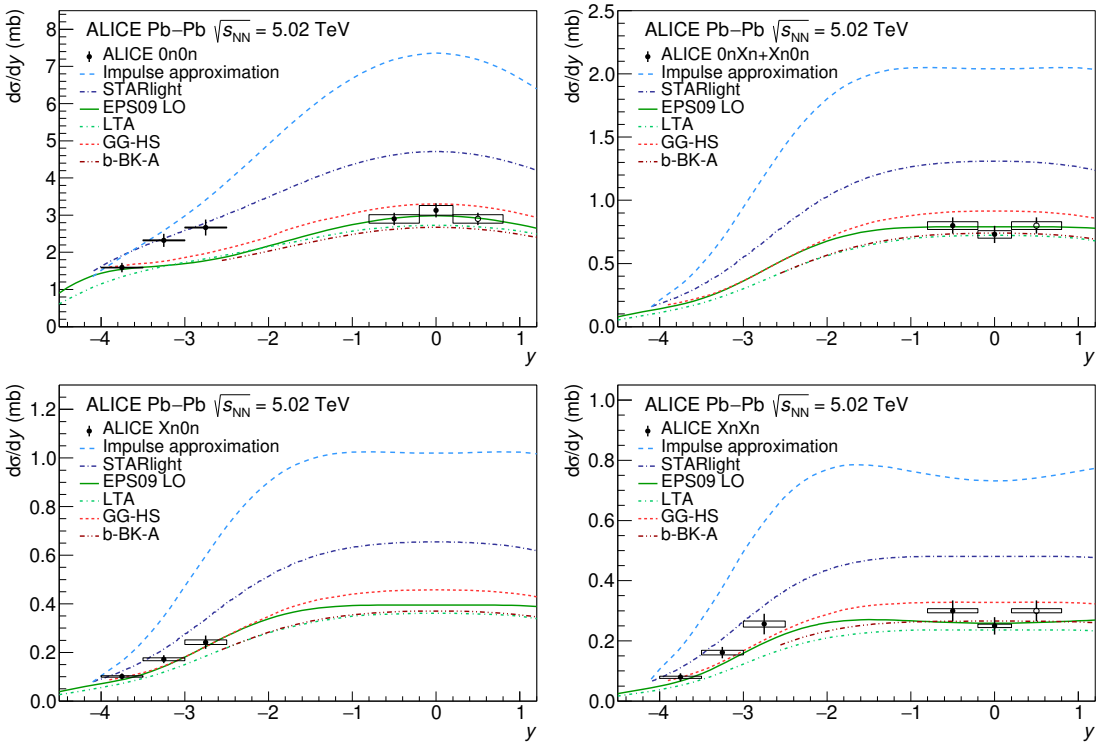

Figure 3. Measured cross section for the coherent production of J/ψ in UPCs at $\sqrt{s_{\rm NN}} = 5.02$ TeV. The solid markers represent the measured cross section (the measurement at $0.2 < |y| < 0.8$ is shown at negative rapidities and reflected into positive rapidities with an open marker). The vertical line across a marker is the sum in quadrature of the statistical and uncorrelated systematic uncertainty. The width of the boxes depicts the range in rapidity covered by each measurement, while the height of a box is the sum in quadrature of the correlated systematic uncertainties and the effect of migrations across neutron classes. Note that the uncertainties from migrations are anti-correlated between the 0n0n and the other two neutron classes in each rapidity interval. The lines depict the prediction of the different models discussed in section 2.

describes well the data at forward rapidity in the 0n0n class, while overestimating the data in all the other classes. At midrapidity, this model does not describe the data in any of the neutron classes. The predictions of the other four models — EPS09-LO, LTA, b-BK-A, and GG-HS — are qualitatively similar, while quantitatively they differ with the maximum spread given by the GG-HS and b-BK-A models, whose predictions differ by up to about 20%. These four models describe the data reasonably well, except for the rapidity range $3.5 < |y| < 2.5$ in the 0n0n class, where the data are clearly above the predictions. For the XnXn neutron class the data at forward rapidity are systematically slightly above the predictions.

The IA and STARlight models do not include gluon shadowing or saturation effects. The EPS09-LO and LTA models do not include explicitly gluon saturation, while the b-BK-A and GG-HS predictions do not include explicitly shadowing effects beyond saturation. The data indicate that the IA and STARlight predictions are disfavoured, implying the need of some QCD dynamic effect, beyond what is included in these models, to describe the

JHEP10(2023)119

y	n_γ(0n0n)	n_γ(0nXn+Xn0n)	n_γ(XnXn)	$\sigma^{\mathrm{IA}}_{\gamma\,\mathrm{Pb}}$ (μb)
$3.5 < y < 4$	178.51	18.18	6.34	10
$3 < y < 3.5$	162.99	18.19	6.34	14
$2.5 < y < 3$	147.46	18.19	6.34	19
$0.2 < y < 0.8$	77.88	17.88	6.33	48
$-0.2 < y < 0.2$	62.86	17.47	6.27	58
$-0.8 < y < -0.2$	48.31	16.75	6.18	71
$-3 < y < -2.5$	3.91	4.97	2.78	176
$-3.5 < y < -3$	1.22	2.15	1.42	215
$-4 < y < -3.5$	0.26	0.61	0.48	262

Table 4. Theoretical input needed to obtain the photonuclear cross section and the nuclear suppression factor. Photon fluxes, see eq. (1.1), computed with $\mathbf{n^{O}_{O}n}$ for the different neutron classes and rapidity ranges. The last column shows the value of $\sigma^{\mathrm{IA}}_{\gamma\,\mathrm{Pb}}$ as computed in ref. [17].

measurements. Within the experimental precision and the large theoretical uncertainties mentioned in section 2, models that include either shadowing or gluon saturation give an equally good description of the data.

6.2 Extraction of the photonuclear cross section

Having several independent UPC measurements allows for the extraction of the two photonuclear cross sections in each rapidity interval. A χ^2 minimisation is applied to the three measurements in each y range. The used χ^2 approach incorporates the correlated uncertainties through nuisance parameters and the uncorrelated and statistical ones utilising relative uncertainties. This method has already been used by the ALICE Collaboration to extract the energy dependence of exclusive photoproduction of J/ψ in p-Pb collisions [85, 86] and it was originally used by the H1 Collaboration for the measurement of the inclusive deeply inelastic cross section at HERA [87]. The χ^2 definition is given by

$$\chi^2_{\mathrm{exp}}\left(\vec{m},\vec{b}\right) = \sum_i \frac{\left(m^i - \sum_j \gamma^i_j m^i b_j - \mu^i\right)^2}{\delta^2_{i,\mathrm{stat}}\mu^i\left(m^i - \sum_j \gamma^i_j m^i b_j\right) + \left(\delta_{i,\mathrm{uncor}}\, m^i\right)^2} + \sum_j b_j^2. \tag{6.1}$$

Here, μ^i is the measured central value at a point i, m^i are given by the right-hand side of eq. (1.1) with the fluxes computed with the $\mathbf{n^{O}_{O}n}$ program [43] (see section 2.1 and table 4 for the flux values), and $\sigma_{\gamma\,\mathrm{Pb}}(\pm y)$ the two parameters to be extracted from the fit. Note that for the rapidity range $|y| < 0.2$ there is only one photonuclear cross section. The relative statistical and uncorrelated systematic uncertainties for each rapidity range (see tables 1 and 2) are given by $\delta_{i,\mathrm{stat}} = \Delta_{i,\mathrm{stat}}/\mu^i$ and $\delta_{i,\mathrm{uncor}} = \Delta_{i,\mathrm{uncor}}/\mu^i$, respectively. Finally, γ^i_j is the matrix of the correlated systematic uncertainty for the source of type j at the point i, where b_j is the associated set of nuisance parameters.

The uncertainties for the measurement of $\sigma_{\gamma\,\mathrm{Pb}}(y)$ are obtained as follows. A fit including the statistical as well as the correlated and uncorrelated systematic uncertainties is performed. Another fit including only the statistical and uncorrelated systematic uncertainties is performed. The uncertainty from this second fit is quoted as the uncorrelated

JHEP10(2023)119

y	$W_{\gamma\,\mathrm{Pb,n}}$ (GeV)	$\sigma_{\gamma\,\mathrm{Pb}}$ (μb)	unc. (μb)	corr. (μb)	mig. (μb)	flux frac. (μb)
$3.5 < y < 4$	19.12	8.84	0.30	0.68	0.02	0.04
$-4 < y < -3.5$	813.05	57.32	20.77	7.57	6.41	6.56
$3 < y < 3.5$	24.55	13.89	0.23	1.08	0.05	0.08
$-3.5 < y < -3$	633.21	46.58	6.61	5.73	3.77	3.63
$2.5 < y < 3$	31.53	16.89	0.59	1.32	0.11	0.18
$-3 < y < -2.5$	493.14	44.68	6.38	5.15	2.73	2.97
$0.2 < y < 0.8$	97.11	21.73	5.12	3.12	4.32	2.73
$-0.8 < y < -0.2$	160.10	25.00	7.33	4.88	5.43	3.91
$-0.2 < y < 0.2$	124.69	24.15	0.69	1.37	0.50	0.06

Table 5. Photonuclear cross sections extracted from the UPC measurements using the procedure described in the text. The quoted uncertainties are uncorrelated (unc.), correlated (corr.), caused by migrations across neutron classes (mig.) and by variations of the flux fractions in the different classes (flux frac.). The lines separate the different ranges in $|y|$. Note that two photonuclear cross sections in each rapidity interval are anti-correlated.

uncertainty. The difference between the uncertainties from the first and second fit, taken in quadrature, are quoted.

There are two contributions to the uncertainty associated to the photon fluxes. One is related to the total flux and the other to the fractions of the total flux in each neutron class. The first contribution is obtained by varying the parameter of the nuclear radius in the Woods-Saxon distribution according to neutron-skin measurements [88]; this uncertainty amounts to 2% correlated over all rapidity intervals and neutron classes. This factor is already taken into account in the correlated uncertainties mentioned in the previous paragraph. The second contribution is estimated by varying by ±5% all cross sections used as input in $\mathbf{n^{O}_{O}n}$ for the computation of the photon flux fractions (see also ref. [89]). The relative change in the photon fluxes goes from 1% to 8% depending on rapidity and neutron class. These changes are anti-correlated in neutron classes for each rapidity interval. To compute the associated uncertainties, fits — including the statistical, correlated and uncorrelated systematic uncertainties — are performed using the modified fluxes. The largest difference, divided by $\sqrt{2}$, between these fits and the fit with the default photon-flux values from $\mathbf{n^{O}_{O}n}$ is taken as the uncertainty originating from the photon flux. If the fluxes of STARlight were used, instead of those from $\mathbf{n^{O}_{O}n}$, then the results would vary by less than one percent, except for the two largest energies, where the cross sections would be larger by 2.6% and 7.7% at $W_{\gamma\,\mathrm{Pb,n}} = 633\,\mathrm{GeV}$ and $W_{\gamma\,\mathrm{Pb,n}} = 813\,\mathrm{GeV}$, respectively. This is well within the uncorrelated uncertainties of the measurement.

Uncertainties caused by the migrations across neutron classes are treated in a similar way to those associated with the photon flux. The input UPC cross sections are modified by the migration uncertainties, new fits are performed and the largest difference, divided by $\sqrt{2}$, with respect to the fit that uses the unmodified UPC cross sections is taken as the systematic uncertainty due to migration effects.

The results obtained by following this procedure are listed in table 5 and shown in figure 4, where they are compared to the predictions of the different models. Note that

JHEP10(2023)119

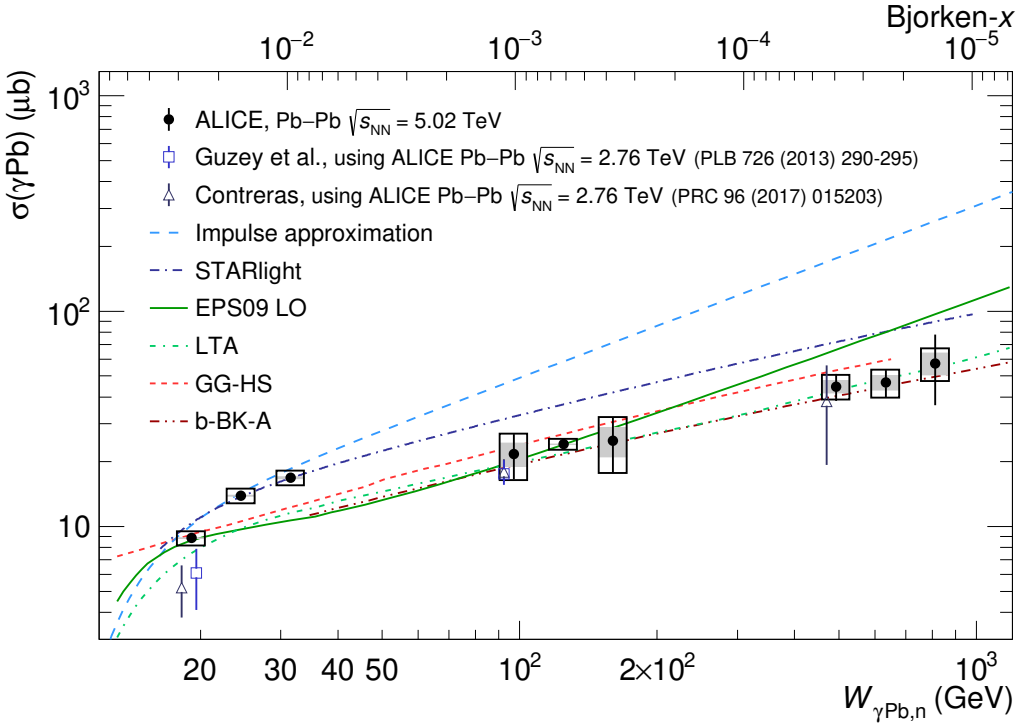

Figure 4. Photonuclear cross section for the $\gamma + \mathrm{Pb} \to \mathrm{J}/\psi + \mathrm{Pb}$ process as a function of $W_{\gamma\,\mathrm{Pb,n}}$ (lower axis) or Bjorken-x (upper axis). The solid markers represent the measured cross section. The vertical line across a marker is the uncorrelated uncertainty. The height of an empty box is the sum in quadrature of the correlated systematic uncertainties and the effect of migrations across neutron classes. The gray box represents the theoretical uncertainty coming from the computation of the photon flux. The lines depict the prediction of the different models discussed in section 2. The open triangular and square markers show the cross sections extracted in refs. [17, 18] using ALICE Run 1 data.

according to eq. (1.1) the results for the cross section at low and high $W_{\gamma\,\mathrm{Pb,n}}$ in one rapidity interval are anti-correlated. Note that the uncertainties for the high $W_{\gamma\,\mathrm{Pb,n}}$ region are large, reaching about 30% at $W_{\gamma\,\mathrm{Pb,n}} = 813\,\mathrm{GeV}$. The predictions obtained with IA [17] are consistent with the data for the energy region below 40 GeV, although systematically above the data; at all other energies the predictions from IA are well above the measurements with the difference increasing with energy. STARlight predictions describe the data for energies below 40 GeV, but overestimate the measurements at all other energies. None of the EPS09-LO, LTA, b-BK-A, and GG-HS models describe the data in the $W_{\gamma\,\mathrm{Pb,n}}$ range from about 25 to 35 GeV. The EPS09-LO model describes the measurements at the lowest energy and at intermediate energies, but overestimates the measurements at the highest energies. The GG-HS model does not include the reduction of phase space at low $W_{\gamma\,\mathrm{Pb,n}}$, but it describes the data, except for the mentioned energy range, for all other measurements, with the predictions systematically on the higher side of the measurements. The predictions of the LTA and b-BK-A models are very similar and describe the data fairly well at all energies, except for the energy range from about 25 to 35 GeV.

JHEP10(2023)119

The photonuclear cross sections extracted in refs. [17, 18] using ALICE Run 1 data are also shown in figure 4. The cross sections at the two highest $W_{\gamma\,\mathrm{Pb,n}}$, namely 92 GeV and 470 GeV, agree with the new measurements presented here, while the two cross sections at low $W_{\gamma\,\mathrm{Pb,n}}$ are below the new measurements by around 1.5 standard deviations. The fact that the cross sections extracted using the peripheral and ultra-peripheral results from Run 1 and the new measurements presented here agree reasonably well is remarkable, because they involve a different set of systematic uncertainties. It is also worth noting that the new measurements extend the range in $W_{\gamma\,\mathrm{Pb,n}}$ by about 350 GeV, up to $W_{\gamma\,\mathrm{Pb,n}} = 813$ GeV, with respect to the maximum energy reached by ALICE Run 1 data.

As mentioned above, the CMS Collaboration submitted results on this process [33]. The CMS data cover the ranges around 40 GeV to 50 GeV and 300 to 400 GeV in $W_{\gamma\,\mathrm{Pb,n}}$. These ranges lie in between the ranges covered by the ALICE forward and midrapidity analyses. The results of the CMS Collaboration smoothly follow the same trend as the cross sections measured by ALICE. At low energies the measurements are compatible with the STARlight predictions and at high energies with the LTA and b-BK-A predictions.

6.3 Nuclear suppression factor

The nuclear suppression factor is defined in eq. (2.1). To obtain it, the measured photonuclear cross sections are divided by the IA values, where we use the implementation from ref. [17]. The corresponding values of IA are listed in table 4. According to ref. [17] the computation of IA has an uncertainty of about 5%, which reflects the uncertainties related to the experimental input data and its parameterisation. This uncertainty is taken into account in the results shown below.

The nuclear suppression factor is important because it provides a quantitative measure of shadowing in this process and several theoretical uncertainties, e.g. that associated to the J/ψ wave function, should largely cancel in the ratio. Not all uncertainties cancel out completely; for example, in ref. [17] it is argued that the interpretation of the nuclear suppression factor in terms of the gluon shadowing factor has a theoretical uncertainty due to corrections, amounting to about 10%, that account for the skewedness and the real part of the amplitude.

The nuclear suppression factor is shown in figure 5, where the measurement is compared with the predictions of the different models. The nuclear suppression factor at low energies is about 0.94, decreases to values slightly above 0.64 at intermediate energies, and decreases further down to about 0.47 at the highest measured energies. The STARlight model describes only the $W_{\gamma\,\mathrm{Pb,n}}$ range from about 25 to 35 GeV. The other four models do not describe this energy range, but provide a fair description at higher energies, except for the EPS09-LO model, which predicts a nuclear suppression factor that remains constant with increasing $W_{\gamma\,\mathrm{Pb,n}}$, while the data and the other models exhibit a decreasing trend. The predictions of LTA and b-BK-A are quite close to each other and follow the behaviour of data at all energies, except for the range from about 25 to 35 GeV.

JHEP10(2023)119

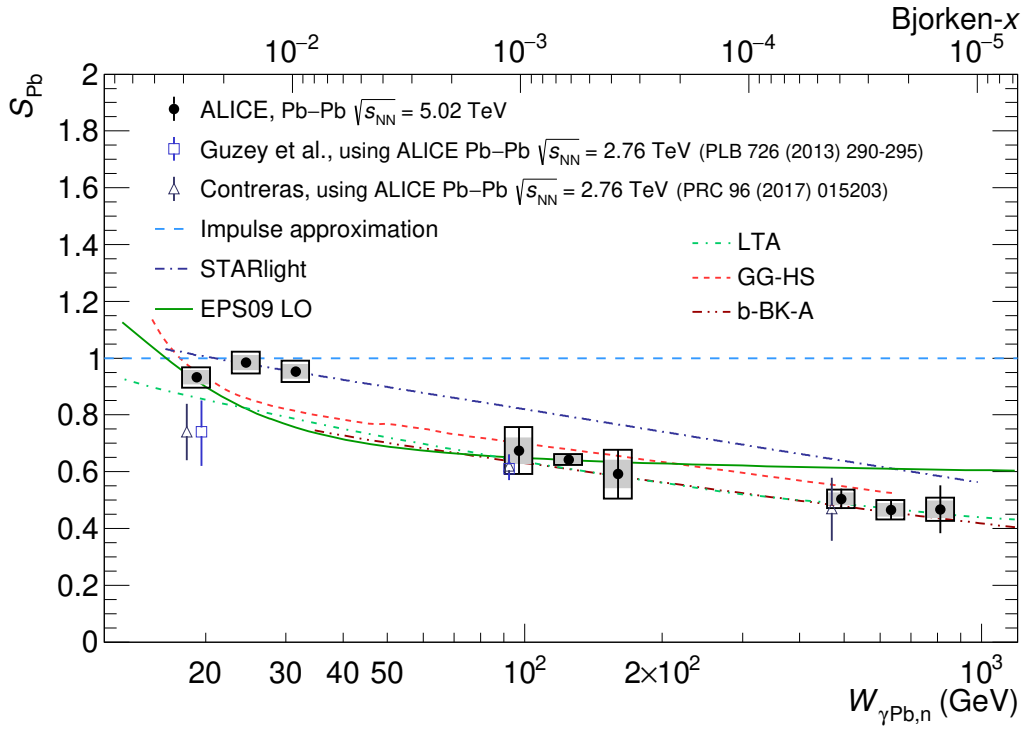

Figure 5. Nuclear suppression factor for the $\gamma + \mathrm{Pb} \to \mathrm{J}/\psi + \mathrm{Pb}$ process as a function of $W_{\gamma\,\mathrm{Pb,n}}$ (lower axis) or Bjorken-x (upper axis). The solid markers represent the measurement. The vertical line across a marker is the uncorrelated uncertainty. The height of an empty box is the sum in quadrature of the correlated systematic uncertainties and the effect of migrations across neutron classes. A gray box represents the theoretical uncertainty coming from the computation of the photon flux and of the impulse approximation. The lines depict the prediction of the different models discussed in section 2. The open triangular and square markers show the nuclear suppression factor extracted in refs. [17, 18] using ALICE Run 1 data.

7 Summary and outlook

The coherent photonuclear production of J/ψ accompanied by electromagnetic dissociation (EMD) was measured in a wide kinematic domain. Cross sections are reported for five rapidity intervals and three EMD classes. These measurements are used to extract the photonuclear cross section $\sigma_{\gamma\,\mathrm{Pb}}$ in the kinematic range $17 < W_{\gamma\,\mathrm{Pb,n}} < 920\,\mathrm{GeV}$, which corresponds to a Bjorken-x interval of about three orders of magnitude: $1.1 \times 10^{-5} < x < 3.3 \times 10^{-2}$. In addition, the nuclear suppression factor was measured in the same energy range. These results, together with previous ALICE measurements, provide unprecedented information to probe quantum chromodynamics at high energies.

The results are compared to cross sections and nuclear suppression factors obtained from ALICE Run 1 data. The new measurements agree with the lower energy results, provide a large improvement in precision, and extend the reach of ALICE data in $W_{\gamma\,\mathrm{Pb,n}}$, by about 350 GeV, up to $W_{\gamma\,\mathrm{Pb,n}} = 813\,\mathrm{GeV}$.

The results are also compared with different theoretical models. At low energies, predictions from IA are consistent with data, albeit systematically above them, while with

JHEP10(2023)119

increasing energies IA overestimates data more and more, signalling important energy-dependent shadowing effects. The STARlight model describes the low energy data, but overestimates the measurements at large energies. As neither IA nor STARlight include shadowing or saturation effects, their comparison with data points to the presence of nuclear QCD phenomena at high energies beyond what is included in these two predictions. All other models considered — based on EPS09-LO, the leading-twist approximation, solutions of the impact-parameter dependent BK equation, and an energy-dependent hot-spot approach — describe correctly the data at high energy, correspondingly small Bjorken-x, but underpredict the data in the $W_{\gamma\,\mathrm{Pb,n}}$ range from about 25 to 35 GeV. Within the uncertainties, both saturation or shadowing models give a reasonable description of data. The nuclear suppression factor varies from about 0.95 to 0.47 as the energy (Bjorken-x) increases (decreases).

New data to be collected during Run 3 and 4 at the LHC will provide substantially larger data samples [90], and the ALICE detector has been upgraded to fully exploit the new data sets [91]. These improvements should allow for more detailed studies and a reduction of the size of uncertainties. Furthermore, the measurement of the coherent photoproduction of J/ψ in peripheral Pb-Pb collisions will provide an alternative set of measurements, with different uncertainty sources, to extract the energy dependence of this process. Under these circumstances, a global analysis of all data promises a measurement of the photonuclear cross section $\sigma_{\gamma\,\mathrm{Pb}}$ over three orders of magnitude in Bjorken-x with a small experimental uncertainty.

Acknowledgments

The ALICE Collaboration would like to thank all its engineers and technicians for their invaluable contributions to the construction of the experiment and the CERN accelerator teams for the outstanding performance of the LHC complex. The ALICE Collaboration gratefully acknowledges the resources and support provided by all Grid centres and the Worldwide LHC Computing Grid (WLCG) collaboration. The ALICE Collaboration acknowledges the following funding agencies for their support in building and running the ALICE detector: A. I. Alikhanyan National Science Laboratory (Yerevan Physics Institute) Foundation (ANSL), State Committee of Science and World Federation of Scientists (WFS), Armenia; Austrian Academy of Sciences, Austrian Science Fund (FWF): [M 2467-N36] and Nationalstiftung für Forschung, Technologie und Entwicklung, Austria; Ministry of Communications and High Technologies, National Nuclear Research Center, Azerbaijan; Conselho Nacional de Desenvolvimento Científico e Tecnológico (CNPq), Financiadora de Estudos e Projetos (Finep), Fundação de Amparo à Pesquisa do Estado de São Paulo (FAPESP) and Universidade Federal do Rio Grande do Sul (UFRGS), Brazil; Bulgarian Ministry of Education and Science, within the National Roadmap for Research Infrastructures 2020-2027 (object CERN), Bulgaria; Ministry of Education of China (MOEC) , Ministry of Science & Technology of China (MSTC) and National Natural Science Foundation of China (NSFC), China; Ministry of Science and Education and Croatian Science Foundation, Croatia; Centro de Aplicaciones Tecnológicas y Desarrollo Nuclear (CEADEN),

JHEP10(2023)119

Cubaenergía, Cuba; Ministry of Education, Youth and Sports of the Czech Republic, Czech Republic; The Danish Council for Independent Research | Natural Sciences, the VILLUM FONDEN and Danish National Research Foundation (DNRF), Denmark; Helsinki Institute of Physics (HIP), Finland; Commissariat à l'Energie Atomique (CEA) and Institut National de Physique Nucléaire et de Physique des Particules (IN2P3) and Centre National de la Recherche Scientifique (CNRS), France; Bundesministerium für Bildung und Forschung (BMBF) and GSI Helmholtzzentrum für Schwerionenforschung GmbH, Germany; General Secretariat for Research and Technology, Ministry of Education, Research and Religions, Greece; National Research, Development and Innovation Office, Hungary; Department of Atomic Energy Government of India (DAE), Department of Science and Technology, Government of India (DST), University Grants Commission, Government of India (UGC) and Council of Scientific and Industrial Research (CSIR), India; National Research and Innovation Agency - BRIN, Indonesia; Istituto Nazionale di Fisica Nucleare (INFN), Italy; Japanese Ministry of Education, Culture, Sports, Science and Technology (MEXT) and Japan Society for the Promotion of Science (JSPS) KAKENHI, Japan; Consejo Nacional de Ciencia (CONACYT) y Tecnología, through Fondo de Cooperación Internacional en Ciencia y Tecnología (FONCICYT) and Dirección General de Asuntos del Personal Academico (DGAPA), Mexico; Nederlandse Organisatie voor Wetenschappelijk Onderzoek (NWO), Netherlands; The Research Council of Norway, Norway; Commission on Science and Technology for Sustainable Development in the South (COMSATS), Pakistan; Pontificia Universidad Católica del Perú, Peru; Ministry of Education and Science, National Science Centre and WUT ID-UB, Poland; Korea Institute of Science and Technology Information and National Research Foundation of Korea (NRF), Republic of Korea; Ministry of Education and Scientific Research, Institute of Atomic Physics, Ministry of Research and Innovation and Institute of Atomic Physics and University Politehnica of Bucharest, Romania; Ministry of Education, Science, Research and Sport of the Slovak Republic, Slovakia; National Research Foundation of South Africa, South Africa; Swedish Research Council (VR) and Knut & Alice Wallenberg Foundation (KAW), Sweden; European Organization for Nuclear Research, Switzerland; Suranaree University of Technology (SUT), National Science and Technology Development Agency (NSTDA), Thailand Science Research and Innovation (TSRI) and National Science, Research and Innovation Fund (NSRF), Thailand; Turkish Energy, Nuclear and Mineral Research Agency (TENMAK), Turkey; National Academy of Sciences of Ukraine, Ukraine; Science and Technology Facilities Council (STFC), United Kingdom; National Science Foundation of the United States of America (NSF) and United States Department of Energy, Office of Nuclear Physics (DOE NP), United States of America. In addition, individual groups or members have received support from: European Research Council, Strong 2020 - Horizon 2020 (grant nos. 950692, 824093), European Union; Academy of Finland (Center of Excellence in Quark Matter) (grant nos. 346327, 346328), Finland.

JHEP10(2023)119

References

[1] H1 and ZEUS collaboration, *Combination of measurements of inclusive deep inelastic $e^{\pm}p$ scattering cross sections and QCD analysis of HERA data*, *Eur. Phys. J. C* **75** (2015) 580 [arXiv:1506.06042] [INSPIRE].

[2] A. Morreale and F. Salazar, *Mining for Gluon Saturation at Colliders*, *Universe* **7** (2021) 312 [arXiv:2108.08254] [INSPIRE].

[3] N. Armesto, *Nuclear shadowing*, *J. Phys. G* **32** (2006) R367 [hep-ph/0604108] [INSPIRE].

[4] L.D. McLerran and R. Venugopalan, *Computing quark and gluon distribution functions for very large nuclei*, *Phys. Rev. D* **49** (1994) 2233 [hep-ph/9309289] [INSPIRE].

[5] A.J. Baltz, *The Physics of Ultraperipheral Collisions at the LHC*, *Phys. Rept.* **458** (2008) 1 [arXiv:0706.3356] [INSPIRE].

[6] J.G. Contreras and J.D. Tapia Takaki, *Ultra-peripheral heavy-ion collisions at the LHC*, *Int. J. Mod. Phys. A* **30** (2015) 1542012 [INSPIRE].

[7] S.R. Klein and H. Mäntysaari, *Imaging the nucleus with high-energy photons*, *Nature Rev. Phys.* **1** (2019) 662 [arXiv:1910.10858] [INSPIRE].

[8] S. Klein and P. Steinberg, *Photonuclear and Two-photon Interactions at High-Energy Nuclear Colliders*, *Ann. Rev. Nucl. Part. Sci.* **70** (2020) 323 [arXiv:2005.01872] [INSPIRE].

[9] ALICE collaboration, *Coherent J/ψ photoproduction in ultra-peripheral Pb-Pb collisions at $\sqrt{s_{NN}} = 2.76$ TeV*, *Phys. Lett. B* **718** (2013) 1273 [arXiv:1209.3715] [INSPIRE].

[10] ALICE collaboration, *Charmonium and e^+e^- pair photoproduction at mid-rapidity in ultra-peripheral Pb-Pb collisions at $\sqrt{s_{\rm NN}} = 2.76$ TeV*, *Eur. Phys. J. C* **73** (2013) 2617 [arXiv:1305.1467] [INSPIRE].

[11] CMS collaboration, *Coherent J/ψ photoproduction in ultra-peripheral PbPb collisions at $\sqrt{s_{NN}} = 2.76$ TeV with the CMS experiment*, *Phys. Lett. B* **772** (2017) 489 [arXiv:1605.06966] [INSPIRE].

[12] ALICE collaboration, *Coherent J/ψ and ψ' photoproduction at midrapidity in ultra-peripheral Pb-Pb collisions at $\sqrt{s_{\rm NN}} = 5.02$ TeV*, *Eur. Phys. J. C* **81** (2021) 712 [arXiv:2101.04577] [INSPIRE].

[13] ALICE collaboration, *First measurement of the $|t|$-dependence of coherent J/ψ photonuclear production*, *Phys. Lett. B* **817** (2021) 136280 [arXiv:2101.04623] [INSPIRE].

[14] ALICE collaboration, *Coherent J/ψ photoproduction at forward rapidity in ultra-peripheral Pb-Pb collisions at $\sqrt{s_{\rm NN}} = 5.02$ TeV*, *Phys. Lett. B* **798** (2019) 134926 [arXiv:1904.06272] [INSPIRE].

[15] LHCb collaboration, *Study of coherent J/ψ production in lead-lead collisions at $\sqrt{s_{\rm NN}} = 5$ TeV*, *JHEP* **07** (2022) 117 [arXiv:2107.03223] [INSPIRE].

[16] S. Klein and J. Nystrand, *Exclusive vector meson production in relativistic heavy ion collisions*, *Phys. Rev. C* **60** (1999) 014903 [hep-ph/9902259] [INSPIRE].

[17] V. Guzey, E. Kryshen, M. Strikman and M. Zhalov, *Evidence for nuclear gluon shadowing from the ALICE measurements of PbPb ultraperipheral exclusive J/ψ production*, *Phys. Lett. B* **726** (2013) 290 [arXiv:1305.1724] [INSPIRE].

JHEP10(2023)119

[18] J.G. Contreras, *Gluon shadowing at small x from coherent* J/ψ *photoproduction data at energies available at the CERN Large Hadron Collider*, *Phys. Rev. C* **96** (2017) 015203 [arXiv:1610.03350] [INSPIRE].

[19] ALICE collaboration, *Measurement of an excess in the yield of* J/ψ *at very low* $p_{\rm T}$ *in Pb-Pb collisions at* $\sqrt{s_{\rm NN}} = 2.76$ *TeV*, *Phys. Rev. Lett.* **116** (2016) 222301 [arXiv:1509.08802] [INSPIRE].

[20] STAR collaboration, *Observation of excess* J/ψ *yield at very low transverse momenta in Au+Au collisions at* $\sqrt{s_{\rm NN}} = 200$ *GeV and U+U collisions at* $\sqrt{s_{\rm NN}} = 193$ *GeV*, *Phys. Rev. Lett.* **123** (2019) 132302 [arXiv:1904.11658] [INSPIRE].

[21] ALICE collaboration, *Photoproduction of low-*$p_{\rm T}$ J/ψ *from peripheral to central Pb-Pb collisions at 5.02 TeV*, *Phys. Lett. B* **846** (2023) 137467 [arXiv:2204.10684] [INSPIRE].

[22] LHCb collaboration, J/ψ *photoproduction in Pb-Pb peripheral collisions at* $\sqrt{s_{NN}} = 5$ *TeV*, *Phys. Rev. C* **105** (2022) L032201 [arXiv:2108.02681] [INSPIRE].

[23] A.J. Baltz, S.R. Klein and J. Nystrand, *Coherent vector meson photoproduction with nuclear breakup in relativistic heavy ion collisions*, *Phys. Rev. Lett.* **89** (2002) 012301 [nucl-th/0205031] [INSPIRE].

[24] V. Guzey, M. Strikman and M. Zhalov, *Disentangling coherent and incoherent quasielastic* J/ψ *photoproduction on nuclei by neutron tagging in ultraperipheral ion collisions at the LHC*, *Eur. Phys. J. C* **74** (2014) 2942 [arXiv:1312.6486] [INSPIRE].

[25] I.A. Pshenichnov, *Electromagnetic excitation and fragmentation of ultrarelativistic nuclei*, *Phys. Part. Nucl.* **42** (2011) 215 [INSPIRE].

[26] ALICE collaboration, *Coherent* ρ^0 *photoproduction in ultra-peripheral Pb-Pb collisions at* $\sqrt{s_{\rm NN}} = 2.76$ *TeV*, *JHEP* **09** (2015) 095 [arXiv:1503.09177] [INSPIRE].

[27] ALICE collaboration, *Coherent photoproduction of* ρ^0 *vector mesons in ultra-peripheral Pb-Pb collisions at* $\sqrt{s_{\rm NN}} = 5.02$ *TeV*, *JHEP* **06** (2020) 035 [arXiv:2002.10897] [INSPIRE].

[28] ALICE collaboration, *First measurement of coherent* ρ^0 *photoproduction in ultra-peripheral Xe-Xe collisions at* $sNN = 5.44$ *TeV*, *Phys. Lett. B* **820** (2021) 136481 [arXiv:2101.02581] [INSPIRE].

[29] CMS collaboration, *Observation of Forward Neutron Multiplicity Dependence of Dimuon Acoplanarity in Ultraperipheral Pb-Pb Collisions at* $\sqrt{s_{NN}} = 5.02$ *TeV*, *Phys. Rev. Lett.* **127** (2021) 122001 [arXiv:2011.05239] [INSPIRE].

[30] ATLAS collaboration, *Exclusive dimuon production in ultraperipheral Pb+Pb collisions at* $\sqrt{s_{\rm NN}} = 5.02$ *TeV with ATLAS*, *Phys. Rev. C* **104** (2021) 024906 [arXiv:2011.12211] [INSPIRE].

[31] ATLAS collaboration, *Exclusive dielectron production in ultraperipheral Pb+Pb collisions at* $\sqrt{s_{NN}} = 5.02$ *TeV with ATLAS*, *JHEP* **2306** (2023) 182 [arXiv:2207.12781] [INSPIRE].

[32] L.A. Harland-Lang, *Exciting ions: A systematic treatment of ultraperipheral heavy ion collisions with nuclear breakup*, *Phys. Rev. D* **107** (2023) 093004 [arXiv:2303.04826] [INSPIRE].

[33] CMS collaboration, *Probing small Bjorken-x nuclear gluonic structure via coherent* J/ψ *photoproduction in ultraperipheral PbPb collisions at* $\sqrt{s_{\rm NN}} = 5.02$ *TeV*, arXiv:2303.16984 [INSPIRE].

JHEP10(2023)119

[34] V. Guzey, E. Kryshen and M. Zhalov, *Coherent photoproduction of vector mesons in ultraperipheral heavy ion collisions: Update for run 2 at the CERN Large Hadron Collider*, *Phys. Rev. C* **93** (2016) 055206 [arXiv:1602.01456] [INSPIRE].

[35] T. Lappi and H. Mantysaari, *J/|psi production in ultraperipheral Pb+Pb and p+Pb collisions at energies available at the CERN Large Hadron Collider*, *Phys. Rev. C* **87** (2013) 032201 [arXiv:1301.4095] [INSPIRE].

[36] J. Cepila, J.G. Contreras and M. Krelina, *Coherent and incoherent* J/ψ *photonuclear production in an energy-dependent hot-spot model*, *Phys. Rev. C* **97** (2018) 024901 [arXiv:1711.01855] [INSPIRE].

[37] H. Mäntysaari and B. Schenke, *Probing subnucleon scale fluctuations in ultraperipheral heavy ion collisions*, *Phys. Lett. B* **772** (2017) 832 [arXiv:1703.09256] [INSPIRE].

[38] D. Bendova, J. Cepila, J.G. Contreras and M. Matas, *Photonuclear J/ψ production at the LHC: Proton-based versus nuclear dipole scattering amplitudes*, *Phys. Lett. B* **817** (2021) 136306 [arXiv:2006.12980] [INSPIRE].

[39] V.P. Gonçalves, D.E. Martins and C.R. Sena, *Coherent and incoherent J/Ψ photoproduction in $Pb-Pb$ collisions at the LHC, HE-LHC and FCC*, *Eur. Phys. J. A* **57** (2021) 82 [arXiv:2007.13625] [INSPIRE].

[40] K.J. Eskola, C.A. Flett, V. Guzey, T. Löytäinen and H. Paukkunen, *Exclusive J/ψ photoproduction in ultraperipheral Pb+Pb collisions at the CERN Large Hadron Collider calculated at next-to-leading order perturbative QCD*, *Phys. Rev. C* **106** (2022) 035202 [arXiv:2203.11613] [INSPIRE].

[41] S.R. Klein and J. Nystrand, *Interference in exclusive vector meson production in heavy ion collisions*, *Phys. Rev. Lett.* **84** (2000) 2330 [hep-ph/9909237] [INSPIRE].

[42] S.R. Klein, J. Nystrand, J. Seger, Y. Gorbunov and J. Butterworth, *STARlight: A Monte Carlo simulation program for ultra-peripheral collisions of relativistic ions*, *Comput. Phys. Commun.* **212** (2017) 258 [arXiv:1607.03838] [INSPIRE].

[43] M. Broz, J.G. Contreras and J.D. Tapia Takaki, *A generator of forward neutrons for ultra-peripheral collisions: $n^O_O n$*, *Comput. Phys. Commun.* **253** (2020) 107181 [arXiv:1908.08263] [INSPIRE].

[44] A. Veyssiere, H. Beil, R. Bergere, P. Carlos and A. Lepretre, *Photoneutron cross sections of 208 Pb and 197 Au*, *Nucl. Phys. A* **159** (1970) 561 [INSPIRE].

[45] N. Bianchi et al., *Total hadronic photoabsorption cross-section on nuclei in the nucleon resonance region*, *Phys. Rev. C* **54** (1996) 1688 [INSPIRE].

[46] T.A. Armstrong et al., *Total hadronic cross-section of gamma rays in hydrogen in the energy range 0.265-GeV to 4.215-GeV*, *Phys. Rev. D* **5** (1972) 1640 [INSPIRE].

[47] T.A. Armstrong et al., *The total photon deuteron hadronic cross-section in the energy range* 0.265−4.215 *GeV*, *Nucl. Phys. B* **41** (1972) 445 [INSPIRE].

[48] G.F. Chew and G.C. Wick, *The Impulse Approximation*, *Phys. Rev.* **85** (1952) 636 [INSPIRE].

[49] M.G. Ryskin, *Diffractive J/ψ electroproduction in LLA QCD*, *Z. Phys. C* **57** (1993) 89 [INSPIRE].

JHEP10(2023)119

[50] T.H. Bauer, R.D. Spital, D.R. Yennie and F.M. Pipkin, *The Hadronic Properties of the Photon in High-Energy Interactions*, *Rev. Mod. Phys.* **50** (1978) 261 [*Erratum ibid.* **51** (1979) 407] [INSPIRE].

[51] K.J. Eskola, H. Paukkunen and C.A. Salgado, *EPS09: A New Generation of NLO and LO Nuclear Parton Distribution Functions*, *JHEP* **04** (2009) 065 [arXiv:0902.4154] [INSPIRE].

[52] L. Frankfurt, V. Guzey and M. Strikman, *Leading Twist Nuclear Shadowing Phenomena in Hard Processes with Nuclei*, *Phys. Rept.* **512** (2012) 255 [arXiv:1106.2091] [INSPIRE].

[53] D. Bendova, J. Cepila, J.G. Contreras and M. Matas, *Solution to the Balitsky-Kovchegov equation with the collinearly improved kernel including impact-parameter dependence*, *Phys. Rev. D* **100** (2019) 054015 [arXiv:1907.12123] [INSPIRE].

[54] V.N. Gribov, *Glauber corrections and the interaction between high-energy hadrons and nuclei*, *Sov. Phys. JETP* **29** (1969) 483 [INSPIRE].

[55] J. Cepila, J. Nemchik, M. Krelina and R. Pasechnik, *Theoretical uncertainties in exclusive electroproduction of S-wave heavy quarkonia*, *Eur. Phys. J. C* **79** (2019) 495 [arXiv:1901.02664] [INSPIRE].

[56] M. Krelina, J. Nemchik, R. Pasechnik and J. Cepila, *Spin rotation effects in diffractive electroproduction of heavy quarkonia*, *Eur. Phys. J. C* **79** (2019) 154 [arXiv:1812.03001] [INSPIRE].

[57] M.L. Good and W.D. Walker, *Diffraction disssociation of beam particles*, *Phys. Rev.* **120** (1960) 1857 [INSPIRE].

[58] H.I. Miettinen and J. Pumplin, *Diffraction Scattering and the Parton Structure of Hadrons*, *Phys. Rev. D* **18** (1978) 1696 [INSPIRE].

[59] S.R. Klein, *Challenges to the Good-Walker paradigm in coherent and incoherent photoproduction*, *Phys. Rev. C* **107** (2023) 055203 [arXiv:2301.01408] [INSPIRE].

[60] H. Mäntysaari, *Review of proton and nuclear shape fluctuations at high energy*, *Rept. Prog. Phys.* **83** (2020) 082201 [arXiv:2001.10705] [INSPIRE].

[61] H. Mäntysaari and B. Schenke, *Evidence of strong proton shape fluctuations from incoherent diffraction*, *Phys. Rev. Lett.* **117** (2016) 052301 [arXiv:1603.04349] [INSPIRE].

[62] J. Cepila, J.G. Contreras and J.D. Tapia Takaki, *Energy dependence of dissociative J/ψ photoproduction as a signature of gluon saturation at the LHC*, *Phys. Lett. B* **766** (2017) 186 [arXiv:1608.07559] [INSPIRE].

[63] ALICE collaboration, *The ALICE experiment at the CERN LHC*, 2008 *JINST* **3** S08002 [INSPIRE].

[64] ALICE collaboration, *Performance of the ALICE Experiment at the CERN LHC*, *Int. J. Mod. Phys. A* **29** (2014) 1430044 [arXiv:1402.4476] [INSPIRE].

[65] ALICE collaboration, *Alignment of the ALICE Inner Tracking System with cosmic-ray tracks*, 2010 *JINST* **5** P03003 [arXiv:1001.0502] [INSPIRE].

[66] J. Alme et al., *The ALICE TPC, a large 3-dimensional tracking device with fast readout for ultra-high multiplicity events*, *Nucl. Instrum. Meth. A* **622** (2010) 316 [arXiv:1001.1950] [INSPIRE].

[67] ALICE collaboration, *Determination of the event collision time with the ALICE detector at the LHC*, *Eur. Phys. J. Plus* **132** (2017) 99 [arXiv:1610.03055] [INSPIRE].

JHEP10(2023)119

[68] A. Akindinov et al., *A topological trigger based on the Time-of-Flight detector for the ALICE experiment*, *Nucl. Instrum. Meth. A* **602** (2009) 372 [INSPIRE].

[69] R. Arnaldi et al., *The Zero degree calorimeters for the ALICE experiment*, *Nucl. Instrum. Meth. A* **581** (2007) 397 [*Erratum ibid.* **604** (2009) 765] [INSPIRE].

[70] C. Oppedisano et al., *Physics performance of the ALICE zero degree calorimeter*, *Nucl. Phys. B Proc. Suppl.* **197** (2009) 206 [INSPIRE].

[71] ALICE collaboration, *Measurement of the Cross Section for Electromagnetic Dissociation with Neutron Emission in Pb-Pb Collisions at* $\sqrt{s_{NN}} = 2.76$ *TeV*, *Phys. Rev. Lett.* **109** (2012) 252302 [arXiv:1203.2436] [INSPIRE].

[72] ALICE collaboration, *Performance of the ALICE VZERO system*, 2013 *JINST* **8** P10016 [arXiv:1306.3130] [INSPIRE].

[73] M. Broz et al., *Performance of ALICE AD modules in the CERN PS test beam*, 2021 *JINST* **16** P01017 [arXiv:2006.14982] [INSPIRE].

[74] ALICE collaboration, *ALICE luminosity determination for Pb−Pb collisions at* $\sqrt{s_{\rm NN}} = 5.02$ *TeV*, arXiv:2204.10148 [INSPIRE].

[75] R. Brun et al., *GEANT Detector Description and Simulation Tool*, https://doi.org/10.17181/CERN.MUHF.DMJ1 W-5013; CERN-W5013 (1994) [INSPIRE].

[76] M. Oreglia, *A Study of the Reactions* $\psi' \to \gamma\gamma\psi$, Ph.D. thesis, Stanford University, Stanford, U.S.A. (1980) [INSPIRE].

[77] Particle Data Group collaboration, *Review of Particle Physics*, *PTEP* **2022** (2022) 083C01 [INSPIRE].

[78] H1 collaboration, *Elastic and Proton-Dissociative Photoproduction of J/psi Mesons at HERA*, *Eur. Phys. J. C* **73** (2013) 2466 [arXiv:1304.5162] [INSPIRE].

[79] ALICE collaboration, *Neutron emission in ultraperipheral Pb-Pb collisions at* $\sqrt{s_{NN}} = 5.02$ *TeV*, *Phys. Rev. C* **107** (2023) 064902 [arXiv:2209.04250] [INSPIRE].

[80] ALICE collaboration, *First polarisation measurement of coherently photoproduced* J/ψ *in ultra-peripheral Pb-Pb collisions at* $\sqrt{s_{\rm NN}} = 5.02$ *TeV*, arXiv:2304.10928 [INSPIRE].

[81] H. Xing, C. Zhang, J. Zhou and Y.-J. Zhou, *The* $\cos 2\phi$ *azimuthal asymmetry in* ρ^0 *meson production in ultraperipheral heavy ion collisions*, *JHEP* **10** (2020) 064 [arXiv:2006.06206] [INSPIRE].

[82] STAR collaboration, *Tomography of ultrarelativistic nuclei with polarized photon-gluon collisions*, *Sci. Adv.* **9** (2023) eabq3903 [arXiv:2204.01625] [INSPIRE].

[83] I.A. Pshenichnov, I.N. Mishustin, J.P. Bondorf, A.S. Botvina and A.S. Ilinov, *Particle emission following Coulomb excitation in ultrarelativistic heavy ion collisions*, *Phys. Rev. C* **60** (1999) 044901 [nucl-th/9901061] [INSPIRE].

[84] ALICE collaboration, *Differential studies of inclusive* J/ψ *and* $\psi(2S)$ *production at forward rapidity in Pb-Pb collisions at* $\sqrt{s_{\rm NN}} = 2.76$ *TeV*, *JHEP* **05** (2016) 179 [arXiv:1506.08804] [INSPIRE].

[85] ALICE collaboration, *Energy dependence of exclusive* J/ψ *photoproduction off protons in ultra-peripheral p-Pb collisions at* $\sqrt{s_{\rm NN}} = 5.02$ *TeV*, *Eur. Phys. J. C* **79** (2019) 402 [arXiv:1809.03235] [INSPIRE].

JHEP10(2023)119

[86] ALICE collaboration, *Exclusive and dissociative J/ψ photoproduction, and exclusive dimuon production, in p-Pb collisions at $\sqrt{s_{\rm NN}} = 8.16$ TeV*, arXiv:2304.12403 [INSPIRE].

[87] H1 collaboration, *Measurement of the Inclusive ep Scattering Cross Section at Low Q^2 and x at HERA*, *Eur. Phys. J. C* **63** (2009) 625 [arXiv:0904.0929] [INSPIRE].

[88] S. Abrahamyan et al., *Measurement of the Neutron Radius of ^{208}Pb Through Parity-Violation in Electron Scattering*, *Phys. Rev. Lett.* **108** (2012) 112502 [arXiv:1201.2568] [INSPIRE].

[89] A.J. Baltz, M.J. Rhoades-Brown and J. Weneser, *Heavy ion partial beam lifetimes due to Coulomb induced processes*, *Phys. Rev. E* **54** (1996) 4233 [INSPIRE].

[90] Z. Citron et al., *Report from Working Group 5: Future physics opportunities for high-density QCD at the LHC with heavy-ion and proton beams*, *CERN Yellow Rep. Monogr.* **7** (2019) 1159 [arXiv:1812.06772] [INSPIRE].

[91] ALICE collaboration, *ALICE upgrades during the LHC Long Shutdown 2*, arXiv:2302.01238 [INSPIRE].

JHEP10(2023)119

EUROPEAN ORGANIZATION FOR NUCLEAR RESEARCH

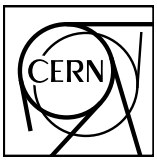

CERN-EP-2023-009
27 January 2023

ALICE upgrades during the LHC Long Shutdown 2

ALICE Collaboration

Abstract

A Large Ion Collider Experiment (ALICE) has been conceived and constructed as a heavy-ion experiment at the LHC. During LHC Runs 1 and 2, it has produced a wide range of physics results using all collision systems available at the LHC. In order to best exploit new physics opportunities opening up with the upgraded LHC and new detector technologies, the experiment has undergone a major upgrade during the LHC Long Shutdown 2 (2019–2022). This comprises the move to continuous readout, the complete overhaul of core detectors, as well as a new online event processing farm with a redesigned online-offline software framework. These improvements will allow to record Pb–Pb collisions at rates up to 50 kHz, while ensuring sensitivity for signals without a triggerable signature.

Contents

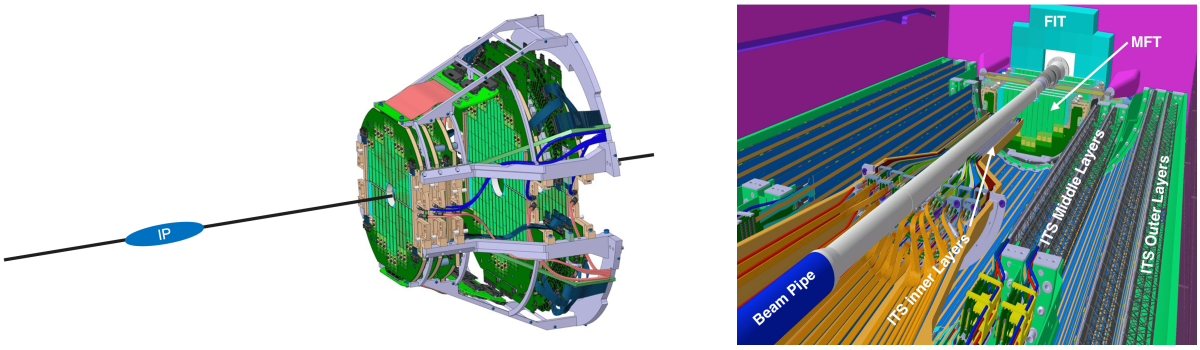

Figure 35: Schematic view of the Muon Forward Tracker (left) and its integration with the central barrel (right).

3.3 Muon Forward Tracker

The Muon Forward Tracker detector (MFT), see Fig. 35, is a high position resolution silicon detector, which has been designed to extend the physics program of the muon spectrometer (see Sec. 3.6). Its primary goal is to improve the pointing resolution of muons by matching the tracks reconstructed downstream of the hadron absorber to those reconstructed inside the MFT upstream of the absorber [23]. This approach allows the removal of multiple scattering effects in the hadron absorber and improves the pointing resolution of muon tracks down to about 100 µm. The MFT is located between the interaction point and the front absorber and surrounds the beam pipe at the closest possible distance. It provides charged particle tracking in the pseudorapidity interval $-3.6 < \eta < -2.45$, which covers most of the muon spectrometer acceptance. The acceptance boundaries are defined on one side by the size of the beam pipe, and on the other side by the volume and position of the ITS2, the FIT-C and the beam pipe support, as shown in Fig. 35.

3.3.1 Detector layout

The MFT has a projective geometry (see Fig. 35) based on five disks, coaxial with the beam pipe and labelled D00 (innermost) to D04 (outermost), the first two (D00 and D01) being identical and the others (D02, D03 and D04) having their diameters increasing with the distance from the interaction point. To ease assembly and insertion, the detector is divided into two identical halves, labelled H0 for the bottom part and H1 for the top part. The MFT is composed of a total of 936 ALPIDE silicon sensors (see Sec. 2.3) distributed on both sides faces of the ten half-disks, and arranged in detection modules called ladders. Each ladder is a hybrid integrated circuit with two to five sensors (depending on the position within the disk), which are glued and interconnected on a flexible printed circuit (FPC) board to provide the power and readout connections. In order to minimize the material budget, the silicon-pixel sensors constituting the MFT are thinned down to the same thickness of 50 µm as the ITS2 inner barrel sensors (see Sec. 3.2), and the FPC to which they are connected are made of polyamide with two layers of aluminum on either side. Each ladder is connected to a PCB that is located outside the acceptance, external to each half face. The MFT contains 240 ladders whose positions were defined to ensure an 85% overlap of the sensors between the two faces of each disk. The face of the half-disks is subdivided into four zones (each containing between three and five ladders) which yields a total of 80 zones for the full MFT.

The ten half-disks are then assembled into half-cones. The first three half-disks are connected to a set of motherboards that provide the connection of the readout lines with 6.5 m long copper cables, which run alongside the whole absorber towards the front-end electronics boards. For the two larger half-disks, the same type of copper cables is used, connected directly to the PCBs. Each half-cone also houses a Power Supply Unit (PSU), which controls and monitors the powering of the zones to guarantee the ladder safety and is located outside the acceptance between the last two half-disks. The disks and the PSU are water-cooled and air ventilation is used to ensure temperature homogeneity inside the confined space where the

MFT is mounted. Figure 36 shows an exploded view of the different elements composing the detector. The two half-cones are fixed to two end-cap patch-panels which in turn are fixed to large carbon fibre composite structures, called half-barrels, that are used to insert and position the MFT within the ALICE internal cage, see Sec. 3.5. The services are routed along the half-barrels and through the patch-panels to reach the detector. The patch-panels are mechanical pieces used also to support the FIT-C detector and to interconnect the readout cables from the half-cones to the readout units, which are located 6 m away beside the front absorber. Figure 37 shows a fully assembled half-cone and the MFT in its final position.

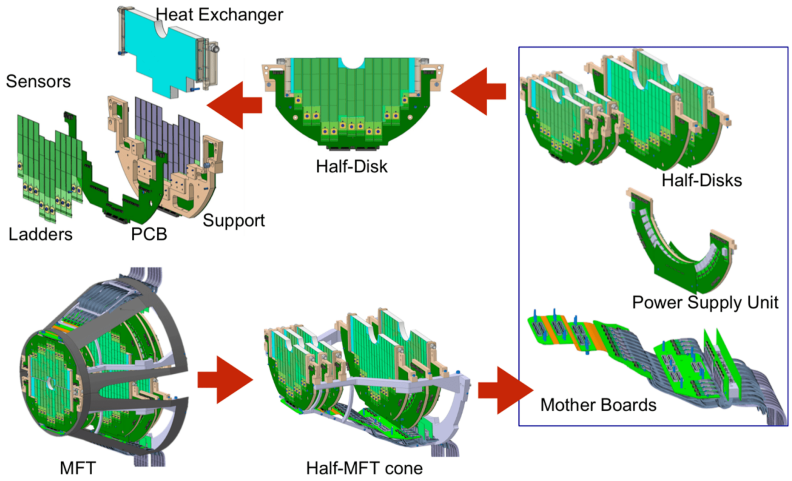

Figure 36: Detailed view of the elements composing the MFT detector.

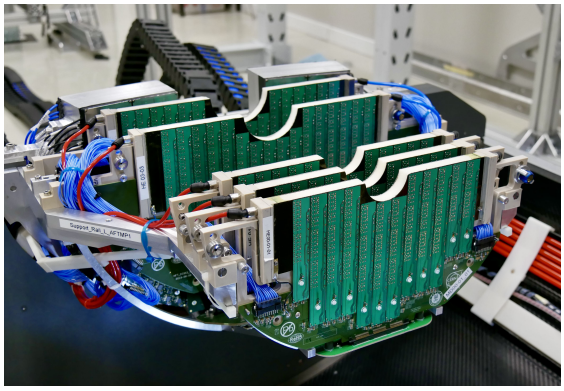

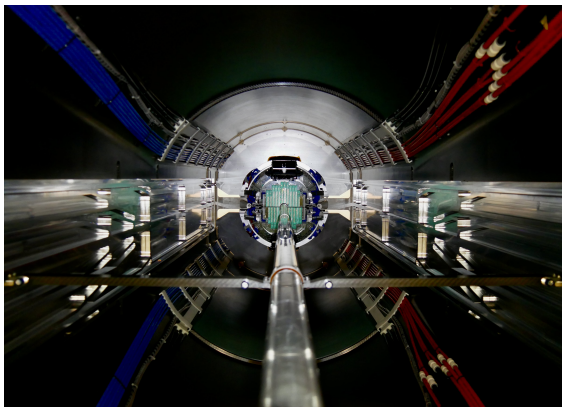

Figure 37: Left-hand panel: fully assembled half-cone of the MFT with patch-panel and the FIT-C detector. Right-hand panel: the MFT in its final position; the cooling and power services can be seen along the half-barrels.

3.3.2 Ladder assembly and testing

The basic element of the MFT detector, called ladder, is composed of an aluminum FPC on which silicon-pixels sensors are glued and interconnected. The length of the ladders varies from 2 to 5 chips each to match the size of the half-layers. Each FPC is equipped on one side with footprints for placing the sensors and a 70-pin connector for powering the chips and transmitting the high-speed readout signals, and on the other side with microelectronic components (resistors and capacitors) that decouple the power supply (analog and digital) of the sensors and adapt the impedance of the data lines. Given their variable length, the FPC design was optimized in order to reduce the maximum voltage drop to 100 mV and to ensure the best transmission of the high-speed data lines.

The ladder assembly took place in the clean room of the CERN EP/DT Departmental Silicon Facility using a three-axis digitally controlled placement machine, called ALICIA (ALICE Integrated Circuit

Inspection and Assembly machine), which places the chips with a precision of 5 µm on a specially machined stainless steel support with a lattice of very small holes to hold the chips in position by suction. At the same time, the FPC is positioned on a suction support which also keeps it perfectly flat and positioned with a precision better than 300 µm. Small dots of Araldite-type two-component glue are applied to the FPC using a stainless-steel stencil with conical holes. The FPC is flipped and positioned opposite to the chips with the help of precision centering pins. The weight of the FPC carrier provides sufficient pressure to spread out the glue and a spacer between the FPC and the chips ensures that the final thickness of the glue layer is around 50 µm. After curing of the glue, the assembly is removed from ALICIA, visually inspected and brought to the CERN bond-lab, where the connection between the FPC and the chips is realized by ultrasonic micro-wire bonding on the metallized pads of the FPC. Each micro-interconnection consists of 3 wires with 25 µm diameter that pass through the vias of the FPC to be connected to the 74 pads on the surface of the sensors. The assembly of the ladder is then completed and a final visual inspection verifies the quality of the interconnections. Figure 38 shows a picture of an assembled ladder.

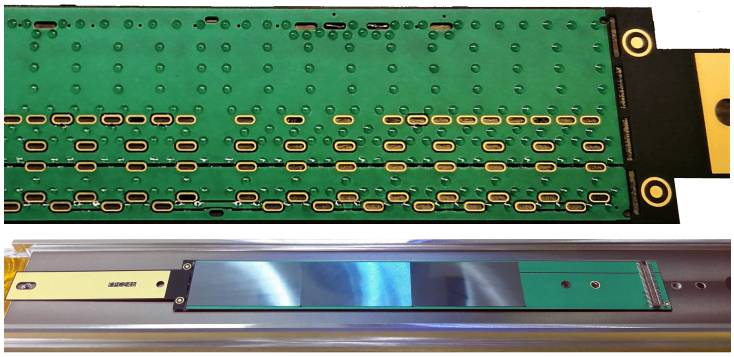

Figure 38: Example of an assembled MFT ladder. Upper picture: back side of the FPC with the glue spots on which the sensor are glued. Bottom picture: front view of assembled ladder.

Once the ladder is assembled, it is transferred to the MFT laboratory where it undergoes a battery of tests to qualify its performance. In the laboratory, two test benches allow each ladder to be qualified from an electrical and functional point of view. First of all, the ladder is gradually powered with analog and digital voltage and its power consumption is checked. Then, the ladder is connected to an acquisition system developed specifically for the ITS2 and the MFT projects, which allows its functionality to be tested in terms of electronic noise, number of dead or defective pixels, and transmission speed of the digitized data. Each test is associated with a qualification grade which is a function of the performance measured against the expected specifications and automatically determined by the qualification software. At the end of these tests, the ladder is qualified according to four grades:

- "Gold" for a ladder that works perfectly and whose pixels and circuitry respond exactly as expected.
- "Silver" when the number of pixels which do not respond correctly is between 0.1 and 4‰ and the ladder can be used without any problem.
- "Bronze" when the number of defective pixels is between 0.4 and 1% and the ladder, although functional, is used as spare rather than for equipping the MFT detector.
- "non-compliant" when a ladder does not pass the tests because of, for example, damaged chips, a defect of the FPC or improper handling. This ladder is discarded.

To fully equip the MFT (including one additional half detector and 20% spares modules), 500 ladders were manufactured, tested, qualified and mounted on the disks in one year with a rate of gold and silver qualified ladders of around 91%.

3.3.3 Half-Disks

As shown in Fig. 39, each half-disk is composed of a support to which a heat exchanger is glued and two PCBs are screwed. The ladders are glued onto each face of the heat exchanger, screwed to the support, and connected to the PCBs. Four different types of half-disks were designed since the first two disks (D00 and D01) are identical.

The half-disk supports, which form the mechanical interface between the elements of the half-disk and the cone structure, were also designed to ease integration of services (cooling pipes and power cables). To minimise the material budget, the support structures are made of PEEK (PolyEtherEtherKetone plastic).

The ladders are connected to a PCB to route the readout, slow control, and clock signals from the ladders to connectors located at the periphery of the half-disk. The PCBs of half-disks D00, D01 and D02 are connected to motherboards that relocate the connection to readout cables for integration reasons. For half-disks D03 and D04, the readout cables are directly connected to the PCBs. The PCB also distributes the different voltages (analog, digital, and reverse bias) to the ladders. Two connectors are located on the left and right sides, one for zones 0 and 1, and the other for zones 2 and 3. The PCB is equipped with decoupling capacitors located close to the ladder and power connectors. In addition, a temperature sensor (PT100) allows the measurement of the local temperature and the acquisition of a reference for the temperature information given by the ALPIDE chips. The temperature signal is sent to the PSU on a dedicated line of the power cables.

The heat exchanger was designed to keep the ALPIDE sensors at a temperature below 30°C using water cooling and to have a total material budget per half-disk below 0.7% of a radiation length. It is composed of two K13D2U carbon fiber cold plates glued to each side of a 14 mm thick core made of Rohacell foam. To circulate cooling water under each sensor, 3 or 4 kapton tubes of 1 mm diameter are glued and covered by a carbon fleece. Two manifolds made of PEEK are glued on each side of each heat exchanger to distribute water through the kapton pipes.

The heat exchangers are qualified in several steps. First, the internal structure is inspected using X-ray tomography in order to check the quality of the gluing and the integrity of the cooling pipes. Before closing the second manifold, the water flow exiting each pipe is measured in order to verify that none of the pipes are pinched. Finally, cooling tests are performed by using resistive patches to simulate the heat generated by the sensors. The temperature is monitored with PT100 sensors located on the heat exchanger and a thermal camera. The goal is to check the homogeneity of the cooling.

The ladders are glued to half-disks using the Dow Corning SE4445-CV silicon glue. The pattern of glue deposition was studied to avoid any flow outside the area of each sensor (see Fig. 40). The planarity of the heat exchanger is around 50 µm and the final thickness of the glue is around 50 µm. The ladders are positioned using a gantry and plugged into the disk PCB. Electrical and communication tests of the sensors are performed to check their proper functioning. In case of failure in the electrical and functional tests, the ladder can be replaced before the glue is fully cured. The remaining glue is removed and a new ladder can be glued.

3.3.4 Cone and Barrel

Each MFT half-cone is supported by a mechanical structure on which three motherboards for the readout are mounted (see Sec. 3.3.6). The different half-disks and the PSUs (see Sec. 3.3.5) with their support are mounted on this structure and the different services (readout cables, power cables, and cooling pipes) are routed inside this structure. The environment of the MFT, in particular the presence of the very fragile beam pipe, imposed several constraints on the design of the cone. As the MFT cone is supported from the side close to disk D04, the displacement due to gravity is the largest at disk D00. This displacement has to be kept below 100 µm to avoid interference with the beam pipe support flanges which are positioned very close to the detector. The cone support structure was produced from aluminum. In order to homogenise

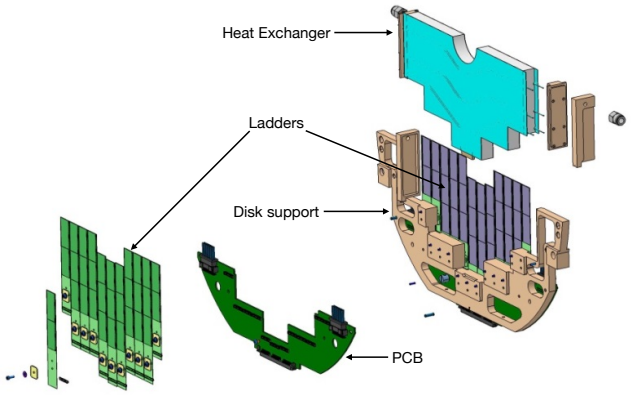

Figure 39: Exploded view of a half-disk (D00-01).

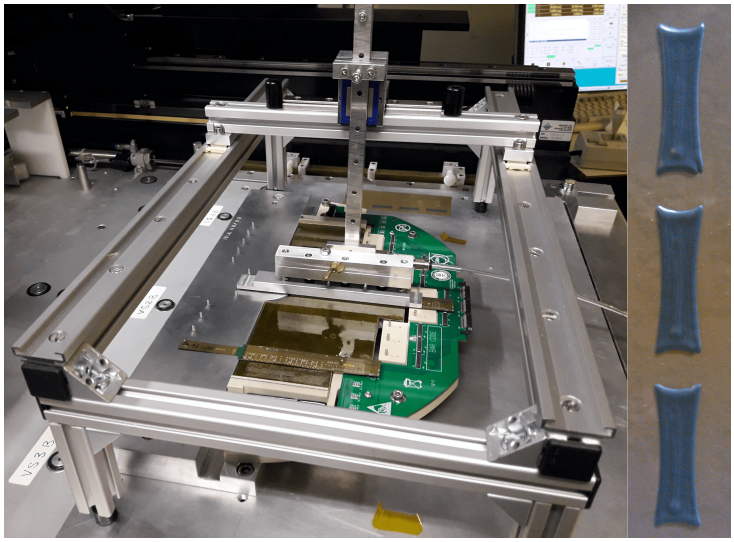

Figure 40: Left: Half-disk during ladder gluing. Right: Glue deposition pattern.

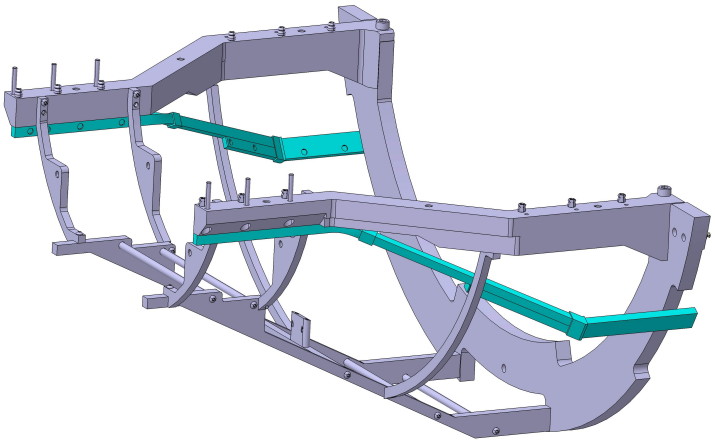

Figure 41: Half-cone structure with air ducts in light blue.

the temperature inside the cone, air guides produced by a 3D-printer were added, see Fig. 41. Reference targets can be fixed to the support structure for the purpose of geometry surveys.

Each half-cone is fixed onto a half-barrel which is built from composite material along which the services (power cables, water pipes, and air ducts) are run as shown in the right-hand panel of Fig. 37. On the A-side, a patch-panel (PP2) is mounted to guide these services. On the C-side, the patch-panel has the following functions:

- position and support a half-cone
- connect and guide the services from/to the half-cone (this is where the filter boards are fixed, see Sec. 3.3.5)
- position and support the FIT-C detector.

Finally, the half-barrels are equipped with wheels that run on guide rails for the insertion of the half-cones into their final position.

3.3.5 Services

The ALPIDE sensors require three different voltage supplies (analog, digital and reverse bias) which are locally generated via DC-DC converters in a PSU in order to minimize the material budget in the barrel by reducing the number of copper power lines and moving the fine power distribution as close as possible to the active detector area. The MFT is equipped with four PSUs, each powering one face of the five half-disks of the same half-MFT. Each PSU is composed of two boards (see Fig. 42): a main board ensures power distribution from the DC-DC converters and a mezzanine board controls the main board and is equipped with one GBT-SCA to send measurements to the DCS (voltages, currents, temperatures, humidity, and status of zones). The different functionalities of the PSU are:

- Conversion of the eternal power supply for the analog and digital circuitry of the sensors by FEASTMP-CLP DC-DC converters [1]. One DC-DC converter is used to power two zones of the same half-disk face (0-1 or 2-3) with analog voltage. For digital voltage, one DC-DC converter is also used to power two zones for half-disks 00-01-02 and one zone for half-disks 03 and 04 since they have more sensors per zone and the output current is limited to 4 A. The voltage drop from the PSU to the sensors is taken into account and the output voltages of the DC-DC converters are adjusted accordingly.

[1] A DC-DC converter is an electronics circuit that converts a continuous current from one voltage level to another.

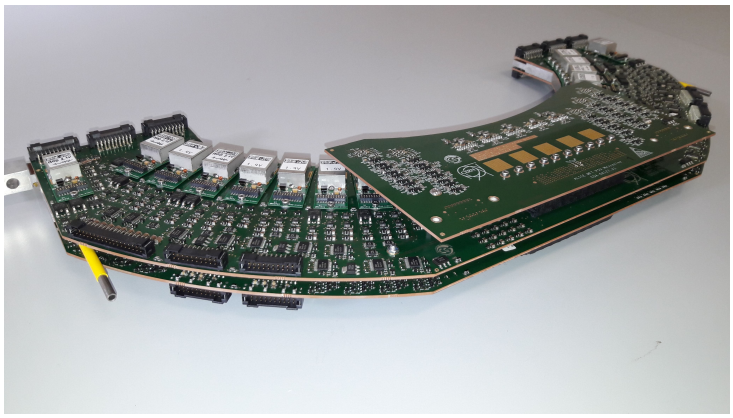

Figure 42: MFT PSU boards with mezzanine assembled on their support.

– Detection of latch-up events through the measurement of currents per zone (analog, digital, and reverse bias). In case of latch-up, all voltages of the zone are switched off and the information of the line that has generated this event is encoded and transmitted.

– Communication with DCS is realised by the use of GBT-SCAs to control DC-DC converters, reset zones, adjust reverse bias voltage and thresholds on analog, digital and reverse bias currents. It is also used to send the measurements of voltages, currents, and temperatures of the half-disks, of the inlet and outlet of cooling of the PSU, of the ambient temperature (two sensors on the mezzanine board), and finally of the humidity (sensor located on the mezzanine board). The status of zones and the latch-up information are also sent to DCS.

– Fail-safe procedure: in case of a loss of communication with the DCS for more than 6 s, all voltages are automatically switched off and the DC-DC converters are disabled.

All the PSUs are controlled through a dedicated CRU via four intermediate boards, called PSU-Interfaces (one per PSU), equipped with GBTx ASICs.

3.3.6 Readout

The MFT readout is based on the same general architecture used for the ITS2 detector (based on the Readout Unit front-end board, see Sec. 3.2.4) arranged with an implementation specifically designed for the MFT geometry. In particular, the 50 Ω differential pairs connecting the sensors to the external readout are routed from the disk to the cone section, then to the patch panel, and finally along the sides of the ALICE front absorber to the readout crates. This requires a specific design of the routing elements and cables in order to provide a reliable connection quality, in particular for the high speed data link at 1.2 Gb/s used for data transmission over a distance of several meters. The design and development of the MFT readout architecture contains a larger number of connections and passive elements than the ITS2, due to constraints on the number of cables that can be routed through the barrel detectors. All signals are instead routed through the limited space between the absorber and the TPC, requiring a sequence of passive dispatching elements, each one inducing specific constraints in terms of impedance adaption, which is a crucial parameter for the high-speed signal transmission quality.

3.3.7 Detector commissioning

The two halves of the MFT detector, together with a third spare half, were assembled by the end of 2019. Over almost one year, the detector was fully qualified and commissioned in the laboratory in order to assess and optimize its operation in terms of powering, cooling, and readout. A detailed study of the noise rates was performed and summarised in Fig. 43, which shows the fake-hit rate as a function of the

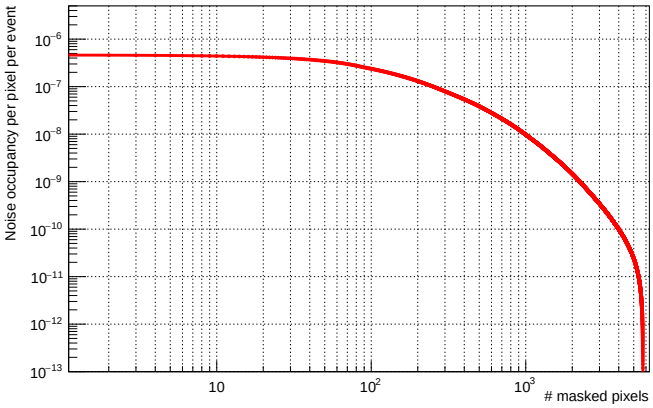

Figure 43: Noise occupancy, measured in hit/pixel/event as a function of the number of masked pixels over the whole MFT detector.

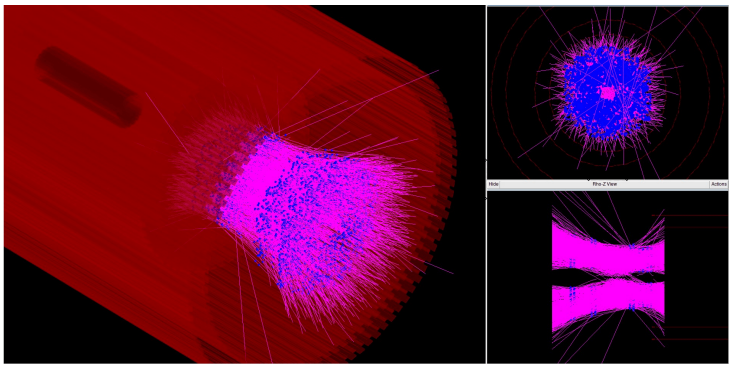

Figure 44: Display of the reconstructed muon tracks in the MFT from a TED shot event.

number of masked pixels. A noise occupancy below 10^{-7} hits per pixel and per event is obtained by masking only 138 pixels out of a total of 490 millions pixels. This result is well within the specifications for the detector.

The installation of the MFT into the ALICE experiment took place in December 2020 and required several months of activity to route all the services and integrate this new detector within the ALICE central systems. A detailed commissioning phase confirmed that the noise levels measured in the laboratory were unchanged after the complex installation inside the ALICE cavern. Moreover, the MFT was ready to take data in October 2021 during the commissioning of the LHC injection lines, using proton beams injected into the transfer line, which are dumped on the Target Extraction Dump (TED). Interactions of the proton beam with the TED, which is located around 30 m upstream from the ALICE cavern, produce a shower of muons traversing the ALICE detector. As shown in the event display in Fig. 44, the MFT detector was able to detect and reconstruct these muon showers, proving its readiness for data taking in Run 3.

7 Conclusions and outlook

After the successful conclusion of data taking in the LHC Runs 1 and 2, the ALICE detector has undergone a major upgrade in order to enable new or more precise measurements in Runs 3 and 4. The inner tracking system was completely replaced and is now fully instrumented with silicon pixel sensors, which provide a much better pointing resolution and support continuous readout. The muon forward tracker uses the same pixel sensors and provides for the first time precise pointing information for forward-rapidity muons reconstructed in the muon chambers and the muon identifier. The time projection chamber is now read out using new detectors based on gas electron multiplication foils that reduce ion backflow and enable continuous readout at much higher interaction rates. The new fast interaction trigger system provides the interaction trigger, as well as multiplicity measurements and time measurements for offline analysis. All other detector systems have undergone consolidation work and several systems have been equipped with upgraded readout electronics and/or new firmware to increase the readout speed or support continuous readout.

All upgrades were completed on schedule and have been commissioned with standalone runs as well as global commissioning runs in 2021 and 2022. The systems have been been tested with pilot beams in October 2021 before the official start of Run 3 and are being operated successfully for routine data taking with proton-proton collisions at $\sqrt{s} = 13.6\,\text{TeV}$ since July 2022. High-rate tests are being performed to qualify the systems for the high data rates in Pb–Pb collisions. The upgraded detectors will strongly extend the physics reach of the experiment, in particular in the sector of open and hidden heavy-flavour probes, measurements of thermal radiation from the quark–gluon plasma, as well as measurements of light nuclear states, final-state interactions of hadrons, and the internal structure of jets.

Two additional upgrades are in preparation for Long Shutdown 3 (2026–2028), with the goal of further enhancing the physics reach of the experiment in Run 4: new inner layers for the inner tracking system (ITS3 [150]) and a forward calorimeter with high-granularity readout (FoCal [157]).

The ITS3 upgrade consists in the replacement of the three innermost layers of the ITS2 with three ultra-light truly-cylindrical layers made with curved large-area MAPS sensors [158]. The innermost layer will have a radius of 18 mm and will surround a new beam pipe with reduced radius (16 mm) and thickness. The pointing resolution will be better than that of the ITS2 by a factor of two up to a transverse momentum of 5 GeV/c, reaching down to about 12 µm at $p_{\mathrm{T}} = 1$ GeV/c. The low-p_{T} tracking efficiency will also improve. The ITS3 will strongly enhance the low-mass dielectron, heavy-flavour meson, and baryon production measurements.

The FoCal consists of an electromagnetic calorimeter with high-granularity readout for optimal separation of direct-photon showers from those of neutral pions at forward pseudorapidity ($3.4 < \eta < 5.8$), coupled to a hadronic calorimeter for additional hadron rejection. The required granularity is achieved using a combination of MAPS silicon pixel readout planes and silicon pad readout planes. The main physics goal of the FoCal is the study of gluon parton distribution functions in the lead nucleus at Bjorken x values down to 10^{-6} using the nuclear modification factor of forward direct photons with transverse momentum $2 < p_{\mathrm{T}} < 20$ GeV/c in p–Pb collisions.

For the LHC Runs 5 and 6, a completely new apparatus, named ALICE 3, is proposed [159]. The ALICE 3 detector consists of a vertexing and tracking system with unique pointing resolution over a large pseudorapidity range ($-4 < \eta < +4$), complemented by multiple sub-detector systems for particle identification, including silicon time-of-flight layers, a ring-imaging Cherenkov detector with high-resolution readout, a muon identification system, and an electromagnetic calorimeter. Unprecedented pointing resolution of 10 µm at $p_{\mathrm{T}} = 200$ MeV/c at midrapidity in both the transverse and longitudinal directions can be achieved by placing the first layers as close as possible to the interaction point, on a retractable structure to leave sufficient aperture for the beams at injection energy. This next-generation apparatus will, on the one hand, enable novel studies of the QGP and, on the other hand, open up important

physics opportunities in other areas of QCD and beyond. The main new studies in the QGP sector focus on low-p_{T} heavy-flavour production, including beauty hadrons, multi-charm baryons and charm–charm correlations, as as well as on precise multi-differential measurements of dielectron emission to probe the mechanism of chiral-symmetry restoration and the time-evolution of the QGP temperature. Besides QGP studies, ALICE 3 can uniquely contribute to hadronic physics, for example with femtoscopic studies of the interaction potentials between charm mesons and searches for nuclei with charm, to fundamental physics, with tests of the Low theorem for ultra-soft photon emission, and to searches for physics beyond the Standard Model, for example in the sector of axion-like particles and the anomalous magnetic moment of τ leptons. The programme aims to collect an integrated luminosity of about 35 nb^{-1} with Pb–Pb collisions and 18 fb^{-1} with pp collisions at top LHC energy. The potential to further increase the luminosity for ion running in the LHC by using smaller ions (e.g. ^{84}Kr or ^{128}Xe), as well as further runs with small collision systems to explore the approach to thermal equilibrium, are being explored.

References

[1] **ALICE** Collaboration, K. Aamodt *et al.*, "The ALICE experiment at the CERN LHC", *JINST* **3** (2008) S08002.

[2] **ALICE** Collaboration, B. B. Abelev *et al.*, "Performance of the ALICE Experiment at the CERN LHC", *Int. J. Mod. Phys. A* **29** (2014) 1430044, arXiv:1402.4476 [nucl-ex].

[3] **ALICE** Collaboration, "The ALICE experiment – A journey through QCD", arXiv:2211.04384 [nucl-ex].

[4] **RD12 Collaboration** Collaboration, B. G. Taylor, "Timing distribution at the LHC",. https://cds.cern.ch/record/592719.

[5] E. B. S. Mendes, S. Baron, D. M. Kolotouros, C. Soos, and F. Vasey, "The 10G TTC-PON: challenges, solutions and performance", *JINST* **12** (2017) C02041.

[6] https://espace.cern.ch/GBT-Project/default.aspx.

[7] **ALICE, ATLAS** Collaboration, A. Borga *et al.*, "The C-RORC PCIe card and its application in the ALICE and ATLAS experiments", *JINST* **10** (2015) C02022.

[8] J. Cachemiche *et al.*, "The PCIe-based readout system for the LHCb experiment", *JINST* **11** (2016) P02013.

[9] O. Bourrion *et al.*, "Versatile firmware for the Common Readout Unit (CRU) of the LHC ALICE experiment", *JINST* **16** (2021) P05019.

[10] G. Aglieri Rinella, "The ALPIDE pixel sensor chip for the upgrade of the ALICE Inner Tracking System", *Nuclear Instruments and Methods in Physics Research Section A: Accelerators, Spectrometers, Detectors and Associated Equipment* **845** (2017) 583 – 587. http://www.sciencedirect.com/science/article/pii/S0168900216303825. Proceedings of the Vienna Conference on Instrumentation 2016.

[11] W. Snoeys, "CMOS monolithic active pixel sensors for high energy physics", *Nuclear Instruments and Methods in Physics Research Section A: Accelerators, Spectrometers, Detectors and Associated Equipment* **765** (2014) 167 – 171. HSTD-9 2013 - Proceedings of the 9th International Hiroshima Symposium on Development and Application of Semiconductor Tracking Detectors, International Conference Center, Hiroshima, Japan, 2-5 September 2013.

[12] S. Senyukov, J. Baudot, A. Besson, G. Claus, L. Cousin, A. Dorokhov, W. Dulinski, M. Goffe, C. Hu-Guo, and M. Winter, "Charged particle detection performances of CMOS pixel sensors produced in a process with a high resistivity epitaxial layer", *Nuclear Instruments and Methods in Physics Research Section A: Accelerators, Spectrometers, Detectors and Associated Equipment* **730** (2013) 115 – 118. Proceedings of the 9th International Conference on Radiation Effects on Semiconductor Materials Detectors and Devices, October 9-12 2012, Dipartimento di Fisica e Astronomia, Firenze.

[13] H. Hernandez, *et al.*, "A monolithic 32-channel front end and dsp asic for gaseous detectors", *IEEE TRANSACTIONS ON INSTRUMENTATION AND MEASUREMENT* **69** (2020) 2686–2697.

[14] M. van Elzakker, E. van Tuijl, P. Geraedts, D. Schinkel, E. A. M. Klumperink, and B. Nauta, "A 10-bit charge-redistribution adc consuming 1.9 μw at 1 ms/s", *IEEE Journal of Solid-State Circuits* **45** (2010) 1007–1015.

[15] **ALICE TPC** Collaboration, J. Adolfsson *et al.*, "The upgrade of the ALICE TPC with GEMs and continuous readout", *JINST* **16** (2021) P03022, arXiv:2012.09518 [physics.ins-det].

[16] **ALICE** Collaboration, B. Abelev *et al.*, "Technical Design Report for the Upgrade of the ALICE Inner Tracking System", *J. Phys. G* **41** (2014) 087002.

[17] **ALICE** Collaboration, M. Mager, "The Monolithic Active Pixel Sensor for the ALICE ITS upgrade", *Nucl. Instrum. Meth. A* **848** (2016) 434–438.

[18] **ALICE** Collaboration, A. Szczepankiewicz, "Readout of the upgraded ALICE-ITS", *Nucl. Instrum. Meth. A* **824** (2016) 465–469.

[19] **ALICE** Collaboration, J. Schambach *et al.*, "A Radiation-Tolerant Readout System for the ALICE Inner Tracking System Upgrade", *NSS/MIC* (2018) 1–6.

[20] L. Amaral *et al.*, "The versatile link, a common project for super-LHC", *JINST* **4** (2009) P12003.

[21] "Two-wire bus-system comprising a clock wire and a data wire for interconnecting a number of stations." https://patents.google.com/patent/US4689740A/en.

[22] **ALICE** Collaboration, F. Reidt, "Upgrade of the alice its detector", *Nuclear Instruments and Methods in Physics Research Section A: Accelerators, Spectrometers, Detectors and Associated Equipment* **1032** (2022) 166632. https://arxiv.org/abs/2111.08301.

[23] **ALICE** Collaboration, J. Adam *et al.*, "Technical Design Report for the Muon Forward Tracker", Tech. Rep. CERN-LHCC-2015-001. ALICE-TDR-018, May, 2015. https://cds.cern.ch/record/1981898.

[24] **ALICE** Collaboration, "Upgrade of the ALICE Time Projection Chamber", Tech. Rep. CERN-LHCC-2013-020, ALICE-TDR-16, CERN, Geneva, 2013. https://cds.cern.ch/record/1622286.

[25] **ALICE TPC** Collaboration, "The ALICE TPC, a large 3-dimensional tracking device with fast readout for ultra-high multiplicity events", *Nucl. Instr. Meth. A* **622** (2010) 316–367.

[26] F. Sauli, "Gem: A new concept for electron amplification in gas detectors", *Nuclear Instruments and Methods in Physics Research Section A: Accelerators, Spectrometers, Detectors and Associated Equipment* **386** (1997) 531–534. https://www.sciencedirect.com/science/article/pii/S0168900296011722.

[27] A. Deisting, C. Garabatos, A. Szabo, and D. Vranic, "Measurements of ion mobility in argon and neon based gas mixtures", *Nucl. Instrum. Meth. A* **845** (2017) 215–217, arXiv:1603.07638 [physics.ins-det].

[28] M. Villa, S. Duarte Pinto, M. Alfonsi, I. Brock, G. Croci, E. David, R. de Oliveira, L. Ropelewski, H. Taureg, and M. van Stenis, "Progress on large area gems", *Nuclear Instruments and Methods in Physics Research Section A: Accelerators, Spectrometers, Detectors and Associated Equipment* **628** (2011) 182–186. https://www.sciencedirect.com/science/article/pii/S0168900210015020. VCI 2010.

[29] M. Ball, B. Ketzer, J. Ottnad, V. Ratza, and S. Urban, "Quality assurance of GEM foils for the upgrade of the ALICE TPC", *JINST* **12** (Jan, 2017) C01081–C01081. https://doi.org/10.1088%2F1748-0221%2F12%2F01%2Fc01081.

[30] E. Brucken and T. Hilden, "The GEM QA protocol of the ALICE TPC upgrade project", *PoS* **MPGD2017** (2019) 073.

[31] E. Brucken and T. Hilden, "GEM foil quality assurance for the ALICE TPC upgrade", *EPJ Web Conf.* **174** (2018) 03004. https://doi.org/10.1051/epjconf/201817403004.

[32] T. E. Hilden, J. E. Brucken, D. VARGA, and M. Vargyas, "GEM foil gain prediction", *PoS* **MPGD2017** (2019) 010.

[33] M. Capeáns-Garrido, R. Fortin, L. Linssen, M. Moll, and C. Rembser, "A GIF++ Gamma Irradiation Facility at the SPS H4 Beam Line", Tech. Rep. CERN-SPSC-2009-029. SPSC-P-339, CERN, Geneva, 2009. https://cds.cern.ch/record/1207380.

[34] M. R. Jäkel, M. Capeáns, I. Efthymiopoulos, A. Fabich, R. Guida, G. Maire, M. Moll, D. Pfeiffer, F. Ravotti, and H. Reithler, "CERN-GIF^{++}: a new irradiation facility to test large-area particle detectors for the high-luminosity LHC program", *PoS* **TIPP2014** (2014) 102.

[35] P. Moreira, *et al.*, "The GBT Project", *Proceedings of the TWEPP09* **2** (2009) 342. https://cds.cern.ch/record/1235836.

[36] **ALICE** Collaboration, W. H. Trzaska, "New Fast Interaction Trigger for ALICE", *Nucl. Instrum. Meth.* **A845** (2017) 463–466.

[37] **ALICE** Collaboration, M. Bondila *et al.*, "ALICE T0 Detector", *IEEE Trans. Nucl. Sc.* **52** (2005) 1705.

[38] **ALICE** Collaboration, E. Abbas *et al.*, "Performance of the ALICE VZERO system", *JINST* **8** (2013) P10016, arXiv:1306.3130 [nucl-ex].

[39] M. Broz *et al.*, "Performance of ALICE AD modules in the CERN PS test beam", *JINST* **16** (2021) P01017, arXiv:2006.14982 [physics.ins-det].

[40] D. Finogeev, T. Karavicheva, D. Serebryakov, A. Tikhonov, W. Trzaska, and N. Vozniuk, "Readout system of the ALICE Fast Interaction Trigger", *JINST* **15** (2020) C09005.

[41] **ALICE** Collaboration, W. H. Trzaska, "New ALICE detectors for Run 3 and 4 at the CERN LHC", *Nucl. Instrum. Meth. A* **958** (2020) 162116.

[42] **ALICE** Collaboration, Y. Melikyan, "Performance of Planacon MCP-PMT photosensors under extreme working conditions", *Nucl. Instrum. Meth. A* **952** (2020) 161689.

[43] T. Sjöstrand, "The PYTHIA Event Generator: Past, Present and Future", *Comput. Phys. Commun.* **246** (2020) 106910, arXiv:1907.09874 [hep-ph].

[44] R. Brun, F. Bruyant, M. Maire, A. C. McPherson, and P. Zanarini, "GEANT3, CERN-DD-EE-84-1", tech. rep., 9, 1987.

[45] V. Grabski, "New fiber readout design for the large area scintillator detectors: providing good amplitude and time resolutions", arXiv:1909.01184 [physics.ins-det].

[46] **ALICE** Collaboration, S. Rojas-Torres, "The Forward Diffractive Detector for ALICE", *PoS* **LHCP2020** (2020) 221.

[47] R. Arnaldi *et al.*, "Front-end electronics for the rpcs of the alice dimuon trigger", *IEEE Transactions on Nuclear Science* **52** (2005) 1176–1181.

[48] P. Dupieux *et al.*, "Upgrade of the ALICE muon trigger electronics", *Journal of Instrumentation* **9** (2014) C09013–C09013.

[49] M. Marchisone, "Performance of a resistive plate chamber equipped with a new prototype of amplified front-end electronics in the ALICE detector", *Journal of Physics: Conference Series* **889** (2017) 012011.

[50] A. Bianchi *et al.*, "Characterization of tetrafluoropropene-based gas mixtures for the resistive plate chambers of the ALICE muon spectrometer", *Journal of Instrumentation* **14** (2019) P11014–P11014.

[51] B. Joly *et al.*, "Production readiness review for the upgrade of the muon trigger front-end electronics", 2016. `https://edms.cern.ch/document/1728246/1`, accessed 2016-10-24.

[52] G. Blanchard *et al.*, "The local trigger electronics of the alice dimuon trigger", 2003. `https://edms.cern.ch/ui/file/406309/1/ALICE-EN-2003-010.pdf`, accessed 2003-12-10.

[53] C. Renard *et al.*, "Mid readout electronics documentation on the web", 2019. `https://www-subatech.in2p3.fr/~electro/projets/alice/dimuon/trigger/upgrade`, accessed 2019-12-11.

[54] P. Dupieux *et al.*, "Mid data format and content", 2020. `https://twiki.cern.ch/twiki/pub/ALICE/MIDRO/MID-DataFormat-150520.pdf`, accessed 2020-05-15.

[55] **ALICE** Collaboration, S. Acharya *et al.*, "The ALICE Transition Radiation Detector: construction, operation, and performance", *Nucl. Instrum. Meth. A* **881** (2018) 88–127, `arXiv:1709.02743 [physics.ins-det]`.

[56] J. Jadlovsky *et al.*, "Communication Architecture of the Detector Control System for the Inner Tracking System", in *Proc. of International Conference on Accelerator and Large Experimental Control Systems (ICALEPCS'17), Barcelona, Spain, 8-13 October 2017*, no. 16 in International Conference on Accelerator and Large Experimental Control Systems, pp. 1930–1933. JACoW, 2018.

[57] **ALICE** Collaboration, G. Dellacasa *et al.*, "ALICE technical design report of the time-of-flight system (TOF)", *CERN-LHCC-2000-012* (2000) .

[58] **ALICE** Collaboration, G. Dellacasa *et al.*, "ALICE Addendum to the technical design report of the time-of-flight system (TOF)", *CERN-LHCC-2002-016* (2000) .

[59] A. Akindinov *et al.*, "Design aspects and prototype test of a very precise TDC system implemented for the multigap RPC of the ALICE-TOF", *Nucl. Instrum. Meth. A* **533** (2004) 178–182.

[60] **ALICE** Collaboration, P. Antonioli, A. Kluge, and W. e. Riegler, "Upgrade of the ALICE Readout & Trigger System", *CERN-LHCC-2013-019, ALICE-TDR-015* (2013) .

[61] **ALICE** Collaboration, D. Falchieri, "DRM2: the readout board for the ALICE TOF upgrade", *PoS* **TWEPP-17** (2018) 081.

[62] **ALICE** Collaboration, F. Costa *et al.*, "DDL, the ALICE data transmission protocol and its evolution from 2 to 6 Gb/s", *JINST* **10** (2015) C04008.

[63] **ALICE** Collaboration, D. Falchieri, "Radiation tests and production test strategy for the ALICE TOF readout upgrade board", *PoS* **TWEPP2018** (2019) 025.

[64] D. Falchieri, P. Antonioli, C. Baldanza, F. Giorgi, A. Mati, and C. Tintori, "Design and Test of a GBTX-Based Board for the Upgrade of the ALICE TOF Readout Electronics", *IEEE Trans. Nucl. Sci.* **64** (2017) 1357–1362.

[65] CAEN, "CAENVME Library and VME-PCI optical bridges", *https://www.caen.it/products/caenvmelib-library/* .

[66] D. Falchieri, P. Antonioli, C. Baldanza, M. Giacalone, and A. Mati, "Readout board validation setup for the ALICE Time of Flight detector upgrade", in *2019 IEEE Nuclear Science Symposium (NSS) and Medical Imaging Conference (MIC)*, pp. 1–3. 2019.

[67] **ALICE** Collaboration, S. Beole *et al.*, "ALICE technical design report: Detector for high momentum PID", *CERN-LHCC-98-19* (8, 1998) .

[68] **ALICE** Collaboration, P. Cortese *et al.*, "ALICE electromagnetic calorimeter technical design report", *CERN-LHCC-2008-014, CERN-ALICE-TDR-014* (2008) .

[69] J. Allen *et al.*, "ALICE DCal: An Addendum to the EMCal Technical Design Report for Di-Jet and Hadron-Jet correlation measurements in ALICE", *CERN-LHCC-2010-011, ALICE-TDR-14-add-1* (2010) .

[70] **ALICE** Collaboration, "Performance of the ALICE Electromagnetic Calorimeter", `arXiv:2209.04216 [physics.ins-det]`.

[71] **ALICE** Collaboration, H. Muller, R. Pimenta, Z.-B. Yin, D.-C. Zhou, X. Cao, Q.-X. Li, Y.-Z. Liu, F.-F. Zou, B. Skaali, and T. Awes, "Configurable electronics with low noise and 14-bit dynamic range for photodiode-based photon detectors", *Nucl. Instrum. Meth. A* **565** (2006) 768–783.

[72] R. Esteve Bosch, A. Jimenez de Parga, B. Mota, and L. Musa, "The ALTRO chip: A 16-channel A/D converter and digital processor for gas detectors", *IEEE Trans. Nucl. Sci.* **50** (2003) 2460–2469.

[73] F. Zhang, H. Muller, T. C. Awes, S. Martoiu, J. Kral, D. Silvermyr, A. Tarazona Martinez, G. Huang, and D. Zhou, "Point-to-point readout for the ALICE EMCal detector", *Nucl. Instrum. Meth. A* **735** (2014) 157–162.

[74] J. Christiansen, A. Marchioro, P. Moreira, and A. Sancho, "Receiver ASIC for timing, trigger and control distribution in LHC experiments", *IEEE Trans. Nucl. Sci.* **43** (1996) 1773–1777.

[75] J. Kral, T. Awes, H. Muller, J. Rak, and J. Schambach, "L0 trigger for the EMCal detector of the ALICE experiment", *Nucl. Instrum. Meth. A* **693** (2012) 261–267.

[76] **ALICE EMCal** Collaboration, O. Bourrion, N. Arbor, G. Conesa-Balbastre, C. Furget, R. Guernane, and G. Marcotte, "The ALICE EMCal L1 trigger first year of operation experience", *JINST* **8** (2013) C01013, `arXiv:1210.8078 [physics.ins-det]`.

[77] **ALICE** Collaboration, G. Dellacasa *et al.*, "ALICE technical design report of the photon spectrometer (PHOS)",. `http://cds.cern.ch/record/381432`.

[78] H. Muller, D. Budnikov, M. Ippolitov, Q. Li, V. Manko, R. Pimenta, D. Rohrich, I. Sibiryak, B. Skaali, and A. Vinogradov, "Front-end electronics for PWO-based PHOS calorimeter of ALICE", *Nucl. Instrum. Meth. A* **567** (2006) 264–267.

[79] O. Bourrion, R. Guernane, B. Boyer, J. Bouly, and G. Marcotte, "Level-1 jet trigger hardware for the ALICE electromagnetic calorimeter at LHC", *JINST* **5** (2010) C12048, arXiv:1010.2670 [physics.ins-det].

[80] **ALICE PHOS calorimeter** Collaboration, D. Aleksandrov *et al.*, "A high resolution electromagnetic calorimeter based on lead-tungstate crystals", *Nucl. Instrum. Meth. A* **550** (2005) 169–184.

[81] **ALICE** Collaboration, C. W. Fabjan *et al.*, "ALICE: Physics performance report, volume II", *J. Phys.* **G32** (2006) 1295–2040.

[82] **ALICE** Collaboration, S. Acharya *et al.*, "Calibration of the photon spectrometer PHOS of the ALICE experiment", *JINST* **14** (2019) P05025, arXiv:1902.06145 [physics.ins-det].

[83] I. A. Pshenichnov, J. P. Bondorf, I. N. Mishustin, A. Ventura, and S. Masetti, "Mutual heavy ion dissociation in peripheral collisions at ultrarelativistic energies", *Physical Review C* **64** (Aug, 2001) 249031–2490319, 0101035. http://link.aps.org/doi/10.1103/PhysRevC.64.024903.

[84] I. Pshenichnov, "Electromagnetic excitation and fragmentation of ultrarelativistic nuclei", *Phys. Part. Nucl.* **42** (Mar, 2011) 215–250. http://link.springer.com/10.1134/S1063779611020067.

[85] **ALICE** Collaboration, B. Abelev *et al.*, "Measurement of the Cross Section for Electromagnetic Dissociation with Neutron Emission in Pb-Pb Collisions at $\sqrt{s_{NN}}$ = 2.76 TeV", *Phys. Rev. Lett.* **109** (2012) 252302, arXiv:1203.2436 [nucl-ex].

[86] IOxOS Technologies SA, "ADC_3112 Four Channel 900 Msps 12-bit ADC", 2018. https://www.ioxos.ch/wp-content/uploads/2018/02/ADC_3112_DS_A1.pdf, accessed 2020-09-30.

[87] Texas Instruments Inc, "Dual Channel 12-Bit 900Msps Analog-to-Digital Converter, ADS5409", 2014. https://www.ti.com/lit/ds/symlink/ads5409.pdf, accessed 2020-09-30.

[88] IOxOS Technologies SA, "IFC_1211 Intelligent FPGA Controller." https://www.ioxos.ch/wp-content/uploads/2018/02/IFC_1211_DS_A2.pdf, accessed 2020-09-30.

[89] P. Buncic, M. Krzewicki, and P. Vande Vyvre, "Technical Design Report for the Upgrade of the Online-Offline Computing System", Tech. Rep. CERN-LHCC-2015-006. ALICE-TDR-019, Apr, 2015. https://cds.cern.ch/record/2011297.

[90] A. Peters, E. Sindrilaru, and G. Adde, "EOS as the present and future solution for data storage at CERN", *Journal of Physics: Conference Series* **664** (Dec, 2015) 042042. https://doi.org/10.1088/1742-6596/664/4/042042.

[91] G. Eulisse, P. Konopka, M. Krzewicki, M. Richter, D. Rohr, and S. Wenzel, "Evolution of the alice software framework for run 3", *EPJ Web Conf.* **214** (2019) 05010. https://doi.org/10.1051/epjconf/201921405010.

[92] A. Rybalchenko, D. Klein, M. Al-Turany, and T. Kollegger, "Shared Memory Transport for ALFA", *EPJ Web Conf.* **214** (2019) 05029.

[93] M. Richter *et al.*, "Data Handling in the ALICE O2 Event Processing", in *Proceedings of the conference Computing in High Energy Physics (CHEP'18) in Sofia, Bulgaria*. Nov., 2018.

[94] R. Brun and F. Rademakers, "ROOT: An object oriented data analysis framework", *Nucl. Instrum. Meth. A* **389** (1997) 81–86.

[95] "A cross-language development platform for in-memory analytics." https://arrow.apache.org.

[96] **ALICE** Collaboration, M. Lettrich, "Fast and Efficient Entropy Compression of ALICE Data using ANS Coding", *EPJ Web Conf.* **245** (2020) 01001.

[97] D. Rohr, "Usage of GPUs in ALICE online and offline processing during LHC run 3", *EPJ Web of Conferences* **251** (2021) 04026. https://doi.org/10.1051%2Fepjconf%2F202125104026.

[98] J. Duda, "Asymmetric numeral systems as close to capacity low state entropy coders", *CoRR* **abs/1311.2540** (2013) , 1311.2540. http://arxiv.org/abs/1311.2540.

[99] F. Costa *et al.*, "Assessment of the ALICE O^2 readout servers", in *Proceedings of the conference Computing in High Energy Physics (CHEP'19) in Adelaide, Australia*. Nov., 2019.

[100] D. Eschweiler and V. Lindenstruth, "The portable driver architecture", in *Proceedings 16th Real-Time Linux Workshop*. Open Source Automation Development Lab (OSADL), Oct., 2014.

[101] D. Eschweiler, *Efficient device drivers for supercomputers*. PhD thesis, Goethe University Frankfurt, Frankfurt am Main, Germany, 2015. http://d-nb.info/1120712483.

[102] **ALICE** Collaboration, K. Alexopoulos and F. Costa, "The ReadoutCard Userspace Driver for the New Alice O2 Computing System", *IEEE Trans. Nucl. Sci.* **68** (2021) 1876–1883, arXiv:2010.16327 [physics.ins-det].

[103] **ALICE** Collaboration, P. Konopka and B. von Haller, "The ALICE O2 data quality control system", vol. 245, p. 01027. 2020.

[104] R. Brun and F. Rademakers, "ROOT: An object oriented data analysis framework", *Nucl. Instrum. Meth. A* **389** (1997) 81–86.

[105] T. Mrnjavac, K. Alexopoulos, V. Chibante Barroso, and G. Raduta, "AliECS: a New Experiment Control System for the ALICE Experiment", vol. 245, p. 01033. 2020.

[106] "Apache mesos", 2020. http://mesos.apache.org/, accessed 2020-10-10.

[107] M. Al-Turany, A. Rybalchenko, D. Klein, M. Kretz, D. Kresan, R. Karabowicz, A. Lebedev, A. Manafov, T. Kollegger, and F. Uhlig, "ALFA: A framework for building distributed applications", vol. 245, p. 05021. 2020.

[108] "Consul by hashicorp", 2020. https://www.consul.io/, accessed 2020-10-10.

[109] "The go programming language", 2020. https://golang.org/, accessed 2020-10-10.

[110] G. Vino *et al.*, "A Monitoring System for the New ALICE O^2 Farm", in *Proceedings of the International Conference on Accelerator and Large Experimental Physics Control Systems (ICALEPCS'19) in New York, USA*. Oct., 2019.

[111] V. Barroso *et al.*, "Towards the integrated ALICE Online-Offline (O^2) monitoring subsystem", in *Proceedings of the conference Computing in High Energy Physics (CHEP'18) in Sofia, Bulgaria*. Nov., 2018.

[112] "Telegraf", 2020. https://www.influxdata.com/time-series-platform/telegraf/, accessed 2020-01-23.

[113] "Apache kafka", 2018. https://kafka.apache.org/, accessed 2018-11-18.

[114] "Influxdb - downsampling and data retention", 2020. https://docs.influxdata.com/influxdb/v1.8/guides/downsample~_~and~_~retain, accessed 2020-09-02.

[115] "Grafana - the open platform for analytics and monitoring", 2020. https://grafana.com/, accessed 2020-01-12.

[116] **ALICE** Collaboration, S. Chapeland *et al.*, "The ALICE DAQ infoLogger", *J.Phys.Conf.Ser.* **513** (2014) 012005.

[117] M. Teitsma, V. C. Barosso, P. Boeschoten, and P. Hendriks, "Jiskefet, a bookkeeping application for ALICE", vol. 245, p. 04023. 2020. arXiv:2003.05756 [cs.HC].

[118] S. Wenzel, "A scalable and asynchronous detector simulation system based on alfa", *EPJ Web Conf.* **214** (2019) 02029. https://doi.org/10.1051/epjconf/201921402029.

[119] M. Al-Turany, D. Bertini, R. Karabowicz, D. Kresan, P. Malzacher, T. Stockmanns, and F. Uhlig, "The FairRoot framework", *J. Phys. Conf. Ser.* **396** (2012) 022001.

[120] J. Allison *et al.*, "Recent developments in Geant4", *Nucl. Instrum. Meth. A* **835** (2016) 186–225.

[121] F. Carminati and A. Morsch, "Simulation in ALICE", *eConf* **C0303241** (2003) TUMT004, arXiv:physics/0306092.

[122] I. Hrivnacova, D. Adamova, V. Berejnoi, R. Brun, F. Carminati, A. Fasso, E. Futo, A. Gheata, I. Gonzalez Caballero, and A. Morsch, "The Virtual Monte Carlo",. https://cds.cern.ch/record/619573. Talk from the 2003 Computing in High Energy and Nuclear Physics (CHEP03), La Jolla, Ca, USA, March 2003, 8 pages, LaTeX, 6 eps figures. PSN THJT006. See http://root.cern.ch/root/vmc/VirtualMC.html.

[123] G. Battistoni *et al.*, "Overview of the FLUKA code", *Annals Nucl. Energy* **82** (2015) 10–18.

[124] B. Volkel, A. Morsch, I. Hřivnáčová, J. Grosse-Oetringhaus, and S. Wenzel, "Using multiple engines in the virtual monte carlo package", *EPJ Web of Conferences* **245** (01, 2020) 02008.

[125] A. Alkin, G. Eulisse, J. F. Grosse-Oetringhaus, P. Hristov, and M. Kabus, "ALICE Run 3 Analysis Framework", *EPJ Web Conf.* **251** (2021) 03063.

[126] R. Quishpe, J. F. Grosse-Oetringhaus, R. Cruceru, and C. Grigoras, "Hyperloop – The ALICE analysis train system for Run 3", *PoS* **LHCP2021** (2021) 250, arXiv:2109.09594 [physics.ins-det].

[127] Wes McKinney, "Data Structures for Statistical Computing in Python", in *Proceedings of the 9th Python in Science Conference*, Stéfan van der Walt and Jarrod Millman, eds., pp. 56 – 61. 2010.

[128] M. Zaharia, *et al.*, "Apache spark: A unified engine for big data processing", *Communications of the ACM* **59** (11, 2016) 56–65.

[129] J. Kvapil *et al.*, "ALICE Central Trigger System for LHC Run 3", *EPJ Web Conf.* **251** (2021) 04022.

[130] C. Ghabrous Larrea, K. Harder, D. Newbold, D. Sankey, A. Rose, A. Thea, and T. Williams, "IPbus: a flexible Ethernet-based control system for xTCA hardware", *JINST* **10** (2015) C02019.

[131] A. Augustinus, P. Chochula, G. d. Cataldo, L. Jirdén, A. Kurepin, M. Lechman, O. Pinazza, P. Rosinský, and A. Moreno, "The wonderland of operating the alice experiment", *ICALEPCS 2011* . http://accelconf.web.cern.ch/accelconf/icalepcs2011/papers/thbhaust02.pdf.

[132] P. Chochula, A. Augustinus, P. Bond, A. Kurepin, M. Lechman, J. Lang, and O. Pinazza, "Challenges of the alice detector control system for the lhc run3", *16th International Conference on Accelerator and Large Experimental Physics Control Systems* (2017) . https://doi.org/10.18429/JACoW-ICALEPCS2017-TUMPL09,2018.

[133] "Wincc open architecture",. https://winccoa.com/.

[134] H. Boterenbrood and B. Hallgren, "The development of embedded local monitor board (elmb)", *9th Workshop on Electronics for LHC Experiments, Amsterdam, The Netherlands* (2003) .

[135] C. Gaspar, M. Dönszelmann, and P. Charpentier, "Dim, a portable, light weight package for information publishing, data transfer and inter-process communication", *Computer Physics Communications* **140** (2001) . https://doi.org/10.1016/S0010-4655(01)00260-0.

[136] W. Salter *et al.*, "LHC Data Interchange Protocol (DIP) Definition." https://edms.cern.ch/file/457113/2/DIPDescription.doc.

[137] B. Franek and C. Gaspar, "Smi++-object oriented framework for designing control systems", *IEEE Nuclear Science Symposium Conference Record* (1997) . https://ieeexplore.ieee.org/document/672515/.

[138] https://www.oracle.com/database/data-guard.

[139] https://www.can-cia.org/can-knowledge.

[140] https://www.anagate.de/products/can-ethernet-gateways.php.

[141] https://opcfoundation.org/about/opc-technologies/opc-ua.

[142] M. Tkáčik, J. Jadlovský, S. Jadlovská, L. Koska, A. Jadlovská, and M. Donadoni, "Fred—flexible framework for frontend electronics control in alice experiment at cern", *Processes* **8** (2020) . https://www.mdpi.com/2227-9717/8/5/565.

[143] P. Chochula, A. Augustinus, P. Bond, A. Kurepin, M. Lechman, J. Lang, and O. Pinazza, "Adapos: An architecture for publishing alice dcs conditions data", *16th International Conference on Accelerator and Large Experimental Physics Control Systems* (2017) . https://accelconf.web.cern.ch/icalepcs2017/doi/JACoW-ICALEPCS2017-TUPHA042.html.

[144] **ALICE** Collaboration, B. Abelev *et al.*, "Upgrade of the ALICE Experiment: Letter Of Intent", *J. Phys. G* **41** (2014) 087001.

[145] Z. Citron *et al.*, *Report from Working Group 5: Future physics opportunities for high-density QCD at the LHC with heavy-ion and proton beams*, vol. 7, pp. 1159–1410. 12, 2019. arXiv:1812.06772 [hep-ph].

[146] Y. Oh, C. M. Ko, S. H. Lee, and S. Yasui, "Heavy baryon/meson ratios in relativistic heavy ion collisions", *Phys. Rev. C* **79** (2009) 044905, arXiv:0901.1382 [nucl-th].

[147] S. Plumari, V. Minissale, S. K. Das, G. Coci, and V. Greco, "Charmed Hadrons from Coalescence plus Fragmentation in relativistic nucleus-nucleus collisions at RHIC and LHC", *Eur. Phys. J. C* **78** (2018) 348, arXiv:1712.00730 [hep-ph].

[148] M. He and R. Rapp, "Hadronization and Charm-Hadron Ratios in Heavy-Ion Collisions", *Phys. Rev. Lett.* **124** (2020) 042301, arXiv:1905.09216 [nucl-th].

[149] R. Rapp, "Dilepton Spectroscopy of QCD Matter at Collider Energies", *Adv. High Energy Phys.* **2013** (2013) 148253, arXiv:1304.2309 [hep-ph].

[150] **ALICE** Collaboration, "Letter of Intent for an ALICE ITS Upgrade in LS3, CERN-LHCC-2019-018", tech. rep., CERN, Geneva, 2019. https://cds.cern.ch/record/2703140.

[151] A. Andronic, P. Braun-Munzinger, K. Redlich, and J. Stachel, "Decoding the phase structure of QCD via particle production at high energy", *Nature* **561** (2018) 321–330, arXiv:1710.09425 [nucl-th].

[152] X. Du and R. Rapp, "Sequential Regeneration of Charmonia in Heavy-Ion Collisions", *Nucl. Phys. A* **943** (2015) 147–158, arXiv:1504.00670 [hep-ph].

[153] **ALICE** Collaboration, "ALICE physics projections for a short oxygen-beam run at the LHC, ALICE-PUBLIC-2021-004",. https://cds.cern.ch/record/2765973.

[154] **ALICE** Collaboration, "Future high-energy pp programme with ALICE, ALICE-PUBLIC-2020-005",. http://cds.cern.ch/record/2724925.

[155] **ALICE** Collaboration, S. Acharya *et al.*, "Constraints on jet quenching in p-Pb collisions at $\sqrt{s_{\rm NN}}$ = 5.02 TeV measured by the event-activity dependence of semi-inclusive hadron-jet distributions", *Phys. Lett. B* **783** (2018) 95–113, arXiv:1712.05603 [nucl-ex].

[156] **ALICE** Collaboration, J. Adam *et al.*, "Measurement of jet quenching with semi-inclusive hadron-jet distributions in central Pb-Pb collisions at $\sqrt{s_{\rm NN}} = 2.76$ TeV", *JHEP* **09** (2015) 170, arXiv:1506.03984 [nucl-ex].

[157] **ALICE** Collaboration, "Letter of Intent: A Forward Calorimeter (FoCal) in the ALICE experiment, CERN-LHCC-2020-009", tech. rep., CERN, Geneva, Jun, 2020. https://cds.cern.ch/record/2719928.

[158] **ALICE ITS project** Collaboration, G. A. Rinella *et al.*, "First demonstration of in-beam performance of bent Monolithic Active Pixel Sensors", *Nucl. Instrum. Meth. A* **1028** (2022) 166280, arXiv:2105.13000 [physics.ins-det].

[159] **ALICE** Collaboration, "Letter of intent for ALICE 3: A next-generation heavy-ion experiment at the LHC", arXiv:2211.02491 [physics.ins-det].

J/ψ PHOTOPRODUCTION RESULTS FROM ALICE*

T. Herman

for the ALICE Collaboration

Faculty of Nuclear Sciences and Physical Engineering
Czech Technical University in Prague, Czech Republic

Received 15 August 2022, accepted 7 September 2022, published online 14 December 2022

Diffractive photoproduction of J/ψ vector mesons is studied at the LHC with the ALICE detector in p–Pb and Pb–Pb ultra-peripheral collisions (UPCs), where the Pb ions act as powerful sources of quasi-real photons. In this contribution, the first measurement at the LHC of dissociative photoproduction of J/ψ off protons is presented; this process is sensitive to quantum fluctuations of the structure of the target at the subnucleon level. In addition, cross sections for the exclusive channel and for continuum dimuon production at small masses were obtained in the same kinematic region. This latter process probes our simultaneous understanding, in a new kinematic region, of the photon flux emitted by protons and by lead ions. The transverse momentum dependence of J/ψ photoproduction on lead targets in Pb–Pb collisions at midrapidity, which is sensitive to the gluonic structure of Pb in the impact-parameter plane, is also presented. The measurement of J/ψ photoproduction off hadrons sheds light onto the initial state of QCD targets and provides important constraints on the initial conditions used in hydrodynamical models of heavy-ion collisions.

DOI:10.5506/APhysPolBSupp.16.1-A98

1. Introduction

At low Bjorken-x, the parton composition of nucleons and nuclei is expected to reach the saturation regime [1], where the number of observed partons stops growing. In addition, there is the nuclear shadowing effect, where the ratio of the gluon distribution function extracted from a nucleon and from a nucleus does not scale linearly with the atomic mass number. The saturation scale should depend on the atomic mass number and saturation may be one of the contributions to the observed nuclear shadowing effects.

* Presented at the 29$^{\text{th}}$ International Conference on Ultrarelativistic Nucleus–Nucleus Collisions: Quark Matter 2022, Kraków, Poland, 4–10 April, 2022.

Ultra-peripheral collisions (UPCs), with impact parameters larger than the sum of the radii of the colliding particles, allow for the suppression of hadronic interactions and provide photon-induced reactions at the LHC, which are sensitive to the parton distributions of the colliding particles. Vector meson photoproduction can be studied with the ALICE detector in several different collision systems (Pb–Pb, Xe–Xe, p–Pb). It is possible to study the Bjorken-x evolution of the parton distributions, the dependency on the center-of-mass energy of the photon-target system, and the transverse plane distribution of the partons.

2. ALICE detector

Starting from the interaction point the charged particles from collisions at central rapidities are first measured using the Inner Tracking System (ITS), a silicon detector used for event triggering and particle tracking. Further away, the tracks are detected by the Time Projection Chamber (TPC) that is composed of a gaseous drift volume with multiwire proportional chamber end caps. The TPC is used for particle tracking and identification. Finally, the tracks go through the Time-of-Flight (TOF) detector. TOF is a multigap resistive plate chamber detector used for event triggering and particle identification. All of the central rapidity detectors are enclosed in a 0.5 T solenoidal magnet.

To measure particles at forward rapidity, there is the muon spectrometer. It starts with an absorber stopping all particles except muons. These are tracked in five planes of cathode pad chambers with the third plane enclosed in a dipole magnet. Then there is an iron wall protecting two planes of resistive plate chambers used for event triggering.

To enforce the exclusivity condition for the vector meson photoproduction events, two sets of scintillator counters are used, the V0 and AD detectors. The V0 is also used for luminosity determination.

3. Results

Pb–Pb UPC results

The $|t|$ dependence of the coherent J/ψ photoproduction cross section measured by ALICE in Pb–Pb UPCs at $\sqrt{s_{NN}} = 5.02$ TeV [2] via the dimuon decay channel can be seen in Fig. 1. This measurement allows probing of the transverse partonic structure of the nucleus at low x. Comparison to STARlight [3], which is driven by the nuclear form factor, shows a difference in both the shape and magnitude. This demonstrates the presence of $|t|$-dependent QCD dynamical effects. Comparison to the LTA [4] model based on the leading twist approximation of nuclear shadowing data and the b-BK [5] model based on the color dipole approach coupled with the impact-

parameter-dependent Balitsky–Kovchegov equation shows agreement with the data within current uncertainties. Future measurements should differentiate between the two predictions.

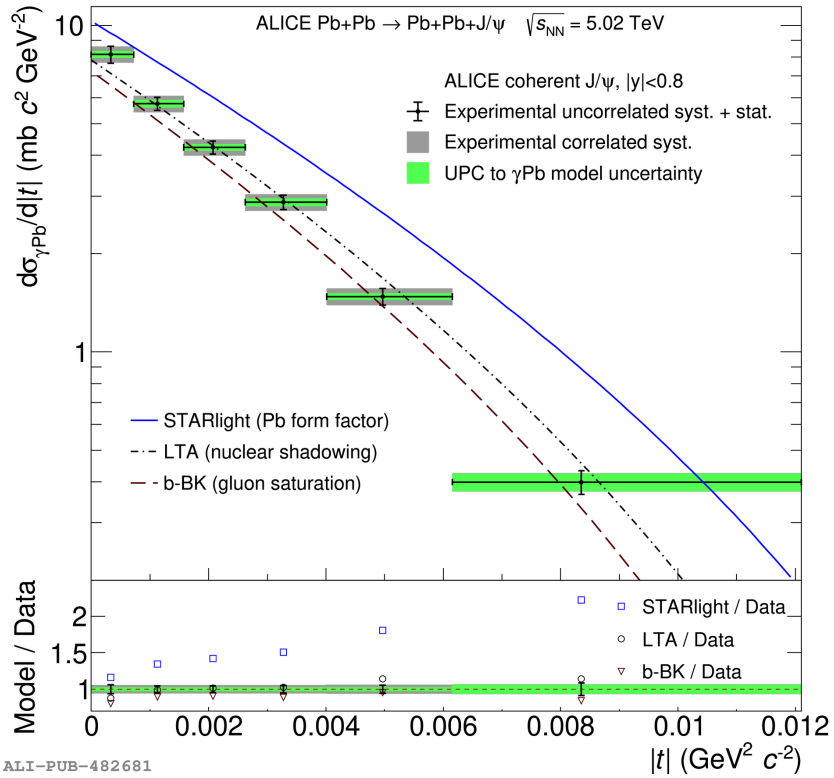

Fig. 1. $|t|$ dependence of the photonuclear cross section for the coherent J/ψ photoproduction compared with model predictions (top panel). Model-to-data ratio for each prediction in each measured point (bottom panel). The uncertainties are split between those originating from the experiment and those originating from the correction to go from the UPC to the photonuclear cross section [2].

p–Pb UPC results

The cross section for the $\gamma\gamma \to \mu\mu$ process in the low invariant mass region was measured in the p–Pb UPCs at $\sqrt{s_{NN}} = 8.16$ TeV. The ALICE results for two rapidity regions in three invariant mass intervals can be seen in Fig. 2 together with predictions from the STARlight [3] model. This model is based on LO QED calculations without final-state radiation effects or other NLO effects. STARlight also does not take into account possible interactions within the radius of the colliding particles which might explain the reason for the slight excess observed in the data. However, the difference is still within 3σ. This result can be utilized to improve current modes which are used to fix background in vector meson or jet photoproduction measurements and improve predictions for light-by-light scattering.

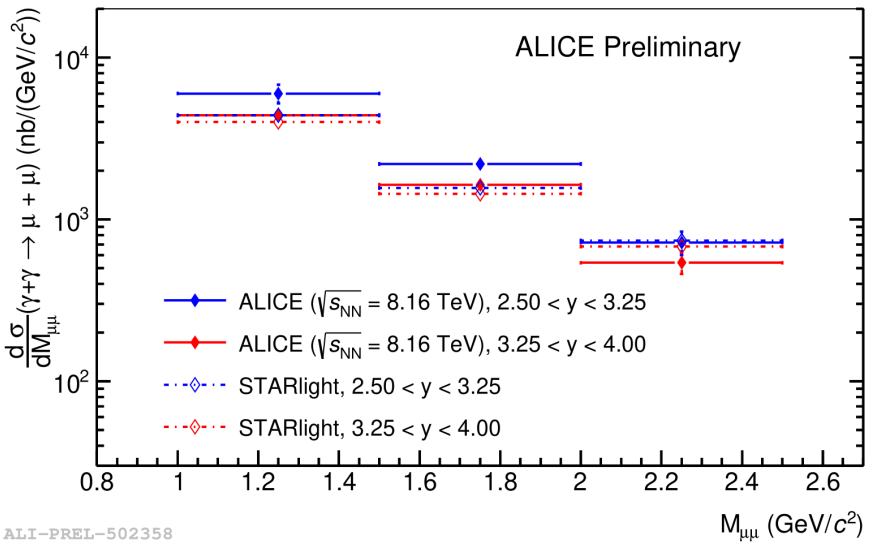

Fig. 2. The differential cross sections for exclusive $\gamma\gamma \to \mu\mu$ production for p–Pb UPCs at $\sqrt{s_{NN}} = 8.16$ TeV as a function of $M_{\mu\mu}$. The vertical error bars represent the statistical and systematic uncertainties summed in quadrature. The results are compared with predictions by STARlight for the same kinematic domain.

The center-of-mass energy dependence of the exclusive J/ψ photoproduction cross section (measured via the dimuon decay channel) can be seen in Fig. 3. A power law fit to the ALICE data gives the exponent value

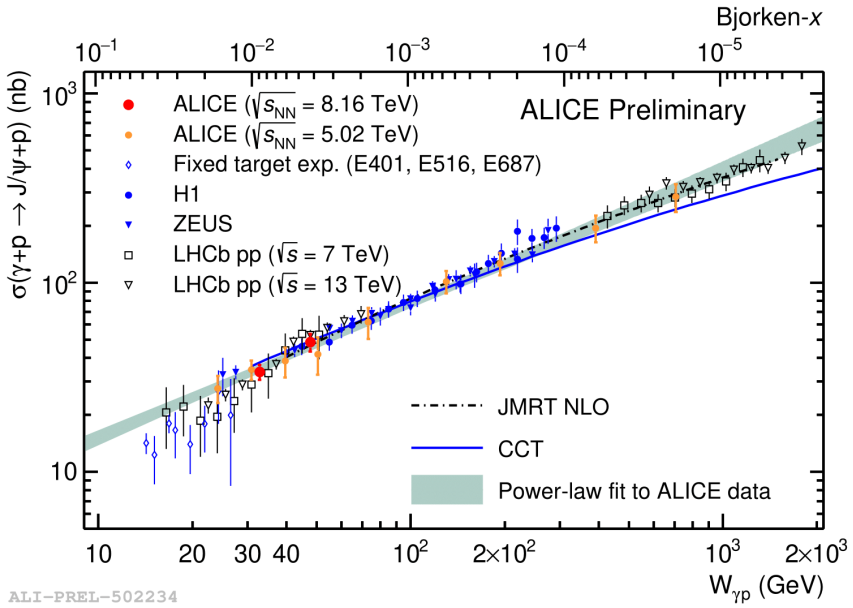

Fig. 3. Exclusive J/ψ photoproduction cross section on proton targets measured by ALICE and compared to previous measurements. Comparisons to the next-to-leading-order JMRT model as well as to the CCT model are shown. The power law fit to the ALICE data is also shown.

$\delta = 0.70 \pm 0.04$. There is no change observed between the results from HERA and the LHC. Also the LHCb and ALICE results are compatible. Two model predictions are also shown, the JMRT NLO [6] model which is based on the DGLAP formalism with main NLO contributions and the CCT [7] model which includes saturation in an energy-dependent hot-spot model. Both models agree with the data.

For the first time the center-of-mass energy dependence of the dissociative J/ψ photoproduction cross section (characterized by a higher average p_{T}) has been measured by ALICE and can be seen in Fig. 4. The data are in agreement with both the H1 results and the CCT [7] model prediction. During the LHC Run 3, ALICE will be able to measure this cross section at the center-of-mass energy where the CCT model predicts a maximum.

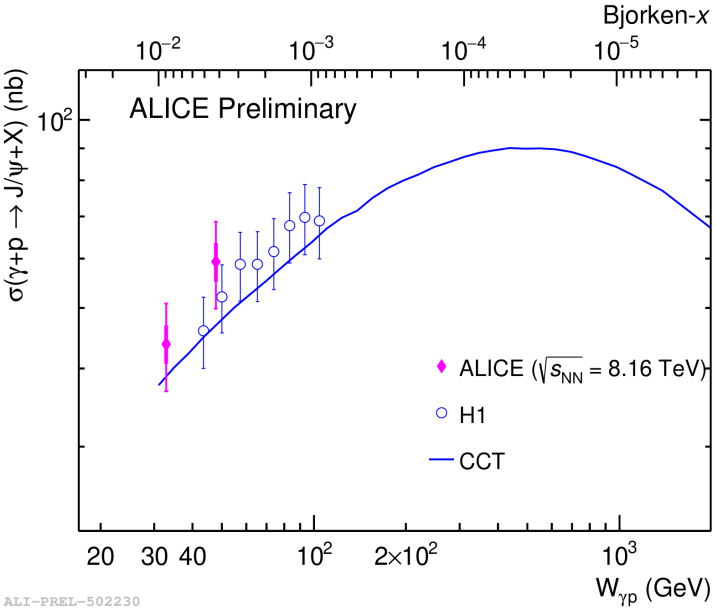

Fig. 4. Dissociative J/ψ photoproduction cross section on proton targets measured by ALICE and compared to H1 data. Comparison to the CCT model is shown. For ALICE points, thick lines represent statistical errors, while the thin line shows statistical and systematic errors summed in quadrature.

4. Conclusion and outlook

In summary, the measurement of the $|t|$ dependence of the coherent J/ψ photoproduction cross section measured in Pb–Pb UPCs shows sensitivity to the parton distribution in the transverse plane. Models with shadowing or saturation describe the data within uncertainties. The cross section for the $\gamma\gamma \to \mu\mu$ process in the low invariant mass region was measured in the p–Pb UPCs and compared to STARlight predictions. The model slightly underestimates the data. The measurement of the exclusive J/ψ photopro-

duction cross section has been found to be in agreement with the previous LHC results as well as the HERA results and theoretical predictions. For the first time, the center-of-mass energy dependence of the dissociative J/ψ photoproduction cross section has been measured at the LHC. The results are in agreement with H1 results and the CCT [7] model.

During LHC Runs 3 and 4, the integrated luminosity will increase by a factor of 13 with respect to Run 2. In addition, ALICE underwent major detector and electronics upgrades during LS2 as well as a transition to a completely new data acquisition system allowing a switch to a continuous data collection policy. These changes will yield much higher data collection efficiency. This will lead to an increase in the precision of all the previous measurements. It will also be possible to make new multi-differential measurements or to study the angular dependencies between dileptons. Completely new observables will also become available, *e.g.* the $\Upsilon(1S)$ production which will allow the probing of a kinematic region with a hard scale ten times larger than that of J/ψ [8].

REFERENCES

[1] A. Morreale, F. Salazar, *Universe* **7**, 312 (2021).
[2] ALICE Collaboration (S. Acharya *et al.*), *Phys. Lett. B* **817**, 136280 (2021).
[3] S.R. Klein *et al.*, *Comput. Phys. Commun.* **212**, 258 (2017).
[4] L. Frankfurt, V. Guzey, M. Strikman, *Phys. Rep.* **512**, 255 (2012).
[5] D. Bendova, J. Cepila, J. G. Contreras, M. Matas, *Phys. Lett. B* **817**, 136306 (2021).
[6] S.P. Jones, A.D. Martin, M.G. Ryskin, T. Teubner, *J. Phys. G: Nucl. Part. Phys.* **44**, 03LT01 (2017).
[7] J. Cepila, J.G. Contreras, J.D. Tapia Takaki, *Phys. Lett. B* **766**, 186 (2017).
[8] Z. Citron *et al.*, *CERN Yellow Rep. Monogr.* **7**, 1159 (2019).

Latest ALICE results on J/ψ photoproduction in ultra-peripheral collisions at the LHC

T. Herman[1⋆] for the ALICE Collaboration

1 Faculty of Nuclear Sciences and Physical Engineering, Czech Technical University in Prague, Prague, Czech Republic
⋆ tomas.herman@cern.ch

July 29, 2021

Proceedings for the XXVIII International Workshop on Deep-Inelastic Scattering and Related Subjects, Stony Brook University, New York, USA, 12-16 April 2021
doi:10.21468/SciPostPhysProc.?

Abstract

Ultra-peripheral collisions (UPCs), studied using the ALICE detector, allow us to investigate the low-x behavior of the gluon distribution of the colliding particles.

Two new measurements of coherent J/ψ photoproduction cross section from Pb–Pb UPCs at $\sqrt{s_{\mathrm{NN}}} = 5.02$ TeV are presented: the first measurement of the |t|-dependence of the cross section providing a new tool to investigate the transverse gluonic structure at low Bjorken-x and a rapidity-differential measurement at midrapidity allowing us to provide stringent constraints on nuclear gluon shadowing and saturation models.

In addition, prospects for heavy vector meson photoproduction measurements in LHC Run 3 and 4 are presented.

1 Introduction

At low Bjorken-x the gluon content of free nucleons or nucleons within nuclei is predicted to reach a saturation regime [1], where the gluon distribution is expected to stop growing, which has not been conclusively observed yet. So far, there have been only hints of possible onset of saturation. Ultra-peripheral collisions allow us to investigate, using photon-induced interactions, processes sensitive to the low-x behavior of the gluon distribution and they are a promising tool to provide important constraints on the initial stages of the collision. With increasing atomic number A of the studied nucleus, there are stronger nuclear shadowing effects on the gluon PDFs at low x. The onset of saturation is expected to depend on A and it may by one of the contributing factors to nuclear shadowing.

In UPCs, the impact parameter b of the colliding particles is larger than the sum of their radii R. Hence the short-range hadronic interactions are suppressed. This enables photon-induced reactions to be measured. It should be noted that photon-induced reactions also contribute at $b < R_1 + R_2$ as demonstrated by the J/ψ excess at very low p_{T} reported by ALICE [2] or by the dilepton excess at low p_{T} by STAR [3].

Coherent photoproduction of J/ψ at the LHC is measured at the highest available energies with the Bjorken-x of the probed gluon distribution depending on parameters of the collision as

$$x = \frac{M_{J/\psi}}{\sqrt{s_{NN}}} e^{\pm y}, \tag{1}$$

where y is the rapidity of the produced vector meson with mass $M_{J/\psi}$ coming from a collision with given center of mass energy per nucleon pair $\sqrt{s_{NN}}$. Thus by measuring the cross section at different rapidities the gluon distribution at different Bjorken-x can be explored. To study also the transverse-plane distribution of the gluons in the colliding particles one can look at the $|t|$ ($\sim p_T^2$) dependence of the cross section which is related by a 2D Fourier transform to the impact parameter.

2 ALICE detector

The silicon Inner Tracking System (ITS) is used to trigger events and measure particle tracks in the central rapidity region of the ALICE detector nearest to the beam pipe. To identify particles and measure tracks further from the interaction point, a Time Projection Chamber (TPC) consisting of a drift volume with multi-wire proportional chambers is used. To improve particle identification and assist in triggering, a multigap resistive plate chamber Time-of-Flight (TOF) detector is used as well. These detectors cover the midrapidity region and are enclosed in a solenoid magnet with magnetic field intensity $B = 0.5$ T.

In the forward rapidity region there is an absorber stopping the majority of the produced charged particles except muons. These are then measured using five planes of a Muon Tracker with cathode pad chambers. The third plane is enclosed in a dipole magnet used for the momentum measurement. For triggering there is a Muon Trigger with resistive plate chambers protected by an additional Muon Wall absorber.

To enforce the exclusivity condition implicit in coherent photoproduction, the following detectors covering forward rapidities are used to impose activity vetoes: the V0 scintillator counter and the ALICE Diffractive (AD) scintillator counter. In addition, the V0 detector is used in luminosity measurement.

3 Results

3.1 Rapidity differential cross section

The studied data sample consists of Pb–Pb UPCs at $\sqrt{s_{NN}} = 5.02$ TeV. The coherent J/ψ cross section at midrapidity is computed as a weighted average of the results obtained considering three decay channels: $\mu^+\mu^-, e^+e^-, p\bar{p}$. The new midrapidity measurement of the cross section [4] can be seen in Fig. 1 (left) complementing the previously published forward rapidity values [5].

The ALICE results are compared to several theoretical predictions. First is the Impulse approximation (IA) based on photoproduction data from protons not including nuclear effects except coherence. Then there is the STARlight model also based on photoproduction data from protons but incorporating a vector meson dominance model to include multiple scattering, however without gluon shadowing. Next are the EPS09 LO prediction, which is a parametrization of nuclear shadowing data, and the Leading Twist Approximation (LTA) of nuclear shadowing. There is also

a group of models based on the color dipole approach coupled to the Color Glass Condensate (CGC) formalism with different assumptions on the dipole-proton scattering amplitude (IIM BG, IPsat, BGK-I). Further there is the GG-HS prediction which is a color dipole model with hot-spot nucleon structure. And finally the b-BK model utilizing solutions of the impact-parameter dependent Balitsky-Kovchegov equation.

By taking the ratio of the measured cross section and the IA prediction the nuclear suppression factor S_{Pb} can be extracted for $x \in (0.3, 1.4) \times 10^{-3}$ as

$$S_{\mathrm{Pb}} = \sqrt{\left(\frac{\mathrm{d}\sigma}{\mathrm{d}y}\right)_{\mathrm{data}} \Big/ \left(\frac{\mathrm{d}\sigma}{\mathrm{d}y}\right)_{\mathrm{IA}}} = 0.65 \pm 0.03. \tag{2}$$

Models with shadowing (EPS09, LTA) and saturation (GG-HS) describe central and forward data but underestimate semi-forward data. Other models describe either the central or the forward rapidity region. None of the models describes the full rapidity dependence.

The ψ' cross section [4] is measured using the same data sample. In Fig. 1 (right) the weighted average computed from three decay channels, $\mu^+\mu^-\pi^+\pi^-, e^+e^-\pi^+\pi^-$, l^+l^-, is shown. The nuclear suppression factor for the ψ' cross section for $x \in (0.3, 1.6) \times 10^{-3}$ is computed to be $S_{\mathrm{Pb}} = 0.66 \pm 0.06$. This results is consistent with the value for J/ψ.

Theoretical predictions which include shadowing (EPS09, LTA) agree with the measured cross section. Among the models involving saturation, the b-BK agrees with the observed data, while the GG-HS overpredicts it. The rest of the models overpredict the ALICE data point.

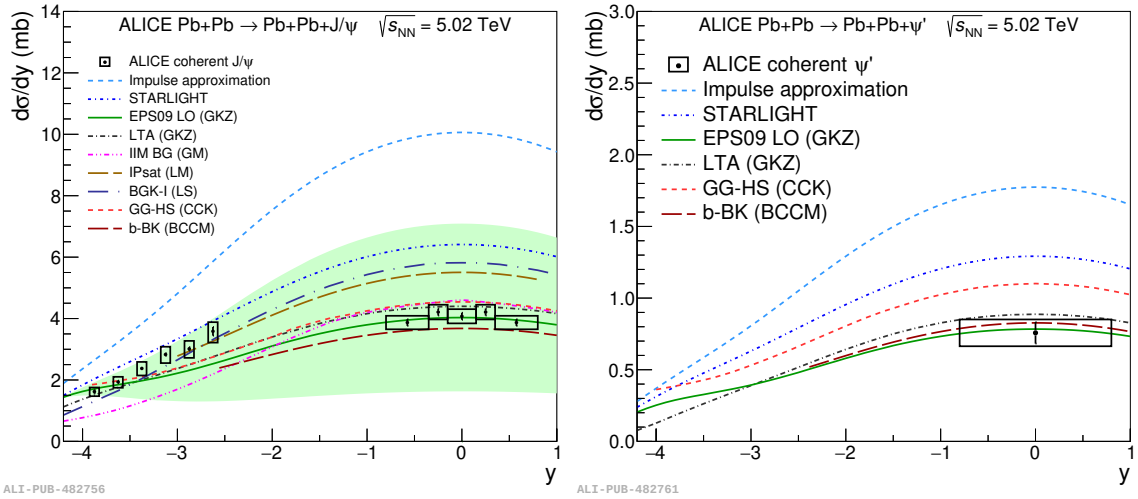

Figure 1: Rapidity differential cross section of the coherent J/ψ (left) and ψ' (right) photoproduction in Pb–Pb UPC events measured by ALICE. The error bars (boxes) show the statistical (systematic) uncertainties. Several theoretical models are also shown [4].

3.2 $|t|$-differential cross section

The first measurement of the $|t|$-dependence of the coherent J/ψ photonuclear cross section [6] was obtained at midrapidity from Pb–Pb UPCs at $\sqrt{s_{\mathrm{NN}}} = 5.02$ TeV and it is shown in Fig. 2. In this measurement only the dimuon decay channel was used as it has the smallest uncertainties.

First, the p_{T}^2-dependent UPC cross section was measured. To go from the measured p_{T}^2 cross section distribution to the $|t|$-dependent UPC cross section, the p_{T}^2 contribution of the photon was extracted using an unfolding technique. Further, the cross sections were corrected for the interference of the photon sources. Finally, to go from UPC to desired photonuclear cross section the photon fluxes were computed and used as follows, see e.g., [7] for details,

$$\left.\frac{\mathrm{d}^2\sigma^{\mathrm{coh}}_{\mathrm{J}/\psi}}{\mathrm{d}y\,\mathrm{d}p_{\mathrm{T}}^2}\right|_{y=0} = 2n_{\gamma\mathrm{Pb}}(y=0)\frac{\mathrm{d}\sigma_{\gamma\mathrm{Pb}}}{\mathrm{d}|t|}. \tag{3}$$

The difference between the ALICE results and the STARlight prediction (driven by the nuclear form factor) in both shape and magnitude demonstrates the presence of QCD dynamical effects in the $|t|$-dependence of the cross section. Models based on pQCD (LTA:nuclear shadowing, b-BK:gluon saturation) describe the data within the current uncertainties. Future measurements should allow us to distinguish between the two predictions.

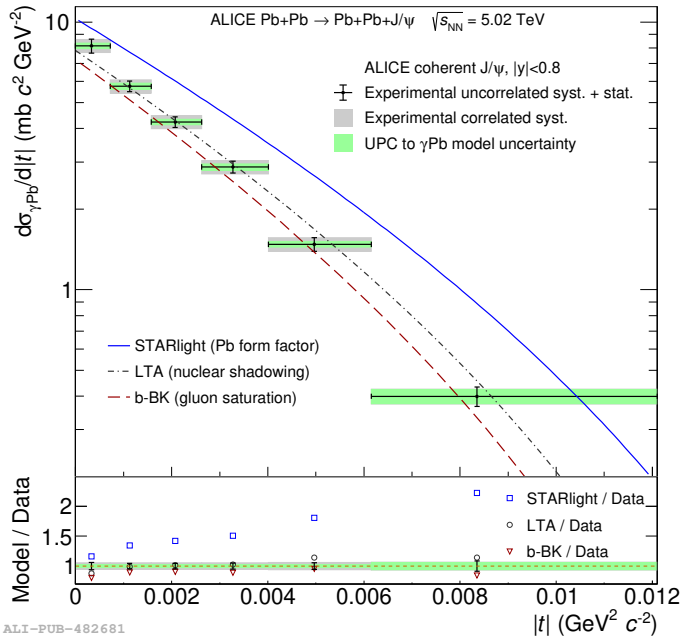

Figure 2: $|t|$ dependence of the photonuclear cross section for the coherent J/ψ photoproduction compared with model predictions (top panel). Model to data ratio for each prediction in each measured point (bottom panel). The uncertainties are split between those originating from experiment and those originating from the correction to go from the UPC to the photonuclear cross section [6].

4 Conclusion and outlook

The gluon content of nucleons in Pb nuclei at Bjorken-$x \in (0.3, 1.4) \times 10^{-3}$ has been probed using ALICE data by measuring coherent charmonium photoproduction in Pb–Pb UPCs at $\sqrt{s_{\mathrm{NN}}} = 5.02$ TeV. The nuclear suppression factor has been found to be $S_{\mathrm{Pb}} \approx 0.65$. The $|t|$ dependence of the

cross section is observed to be sensitive to gluon distribution in the transverse plane. Models incorporating shadowing using the LTA [8] or saturation using the b-BK equation [9] describe all data at midrapidity within the current uncertainties. Results from the LHC might decrease the EPPS16 uncertainties as indicated in Ref. [10] where a reweighing of the EPPS16 nPDFs was implemented.

In the Run 3 and 4 of the LHC the integrated luminosity will increase by a factor 13 with respect to the previous Run 2. Moreover, ALICE will run in continuous readout mode with higher data collection efficiency. There are also significant detector upgrades. All of this will result in millions of J/ψ to be recorded by ALICE [11]. Thus a larger data sample, smaller systematic uncertainties and a better efficiency will lead to increased precision on all previous measurements as well as enabling to make new differential measurements, e.g., $\mathrm{d}^2\sigma/\mathrm{d}y\mathrm{d}|t|$, and angular dependencies between the decay products. In addition, completely new measurements will become possible, e.g., photoproduction of Υ [11], which occurs at a 10 times larger scale that the J/ψ, and measurement of interference effects [12] between the two source-target configurations of the heavy ions.

Funding information This work has been partially supported by the grant 18-07880S of the Czech Science Foundation (GACR).

References

[1] A. H. Mueller, *Small x Behavior and Parton Saturation: A QCD Model*, Nucl. Phys. B **335**, 115 (1990), doi:10.1016/0550-3213(90)90173-B.

[2] J. Adam *et al.*, *Measurement of an excess in the yield of J/ψ at very low p_{T} in Pb-Pb collisions at $\sqrt{s_{\mathrm{NN}}} = 2.76$ TeV*, Phys. Rev. Lett. **116**(22), 222301 (2016), doi:10.1103/PhysRevLett.116.222301, 1509.08802.

[3] J. Adam *et al.*, *Low-p_T e^+e^- pair production in Au+Au collisions at $\sqrt{s_{NN}} = 200$ GeV and U+U collisions at $\sqrt{s_{NN}} = 193$ GeV at STAR*, Phys. Rev. Lett. **121**(13), 132301 (2018), doi:10.1103/PhysRevLett.121.132301, 1806.02295.

[4] S. Acharya *et al.*, *Coherent J/ψ and ψ' photoproduction at midrapidity in ultra-peripheral Pb-Pb collisions at $\sqrt{s_{\mathrm{NN}}} = 5.02$ TeV* (2021), 2101.04577.

[5] S. Acharya *et al.*, *Coherent J/ψ photoproduction at forward rapidity in ultra-peripheral Pb-Pb collisions at $\sqrt{s_{\mathrm{NN}}} = 5.02$ TeV*, Phys. Lett. B **798**, 134926 (2019), doi:10.1016/j.physletb.2019.134926, 1904.06272.

[6] S. Acharya *et al.*, *First measurement of the $|t|$-dependence of coherent J/ψ photonuclear production*, Phys. Lett. B **817**, 136280 (2021), doi:10.1016/j.physletb.2021.136280, 2101.04623.

[7] J. G. Contreras, *Gluon shadowing at small x from coherent J/ψ photoproduction data at energies available at the CERN Large Hadron Collider*, Phys. Rev. C **96**(1), 015203 (2017), doi:10.1103/PhysRevC.96.015203, 1610.03350.

[8] L. Frankfurt, V. Guzey and M. Strikman, *Leading Twist Nuclear Shadowing Phenomena in Hard Processes with Nuclei*, Phys. Rept. **512**, 255 (2012), doi:10.1016/j.physrep.2011.12.002, 1106.2091.

[9] D. Bendova, J. Cepila, J. G. Contreras and M. Matas, *Photonuclear J/ψ production at the LHC: Proton-based versus nuclear dipole scattering amplitudes*, Phys. Lett. B **817**, 136306 (2021), doi:10.1016/j.physletb.2021.136306, 2006.12980.

[10] V. Guzey, E. Kryshen, M. Strikman and M. Zhalov, *Nuclear suppression from coherent J/ψ photoproduction at the Large Hadron Collider*, Phys. Lett. B **816**, 136202 (2021), doi:10.1016/j.physletb.2021.136202, 2008.10891.

[11] Z. Citron *et al.*, *Report from Working Group 5: Future physics opportunities for high-density QCD at the LHC with heavy-ion and proton beams*, CERN Yellow Rep. Monogr. **7**, 1159 (2019), doi:10.23731/CYRM-2019-007.1159, 1812.06772.

[12] S. R. Klein and J. Nystrand, *Interference in exclusive vector meson production in heavy ion collisions*, Phys. Rev. Lett. **84**, 2330 (2000), doi:10.1103/PhysRevLett.84.2330, hep-ph/9909237.

PROCEEDINGS OF SCIENCE

Latest ALICE results on coherent J/ψ photoproduction in ultra-peripheral Pb–Pb collisions at the LHC

Tomas Herman* **(on behalf of the ALICE collaboration)**
Czech Technical University in Prague - Faculty of Nuclear Sciences and Physical Engineering
E-mail: tomas.herman@cern.ch

The high flux of photons from lead ions at the LHC allows us to study photon-induced reactions in ultra-peripheral collisions (UPC) of Pb–Pb nuclei in a new kinematic regime. The study of these collisions, where projectiles do not overlap and hence hadronic interactions are suppressed, provides information about the initial state of nuclei. Coherent charmonium photoproduction is of particular interest since it is sensitive to poorly known gluon shadowing effects in target Pb ions.

The newest ALICE results on vector meson photoproduction in UPC Pb–Pb collisions from LHC Run 2 are presented and are compared to current models describing nuclear gluon shadowing.

XXIX International Symposium on Lepton Photon Interactions at High Energies - LeptonPhoton2019
August 5-10, 2019
Toronto, Canada

*Speaker.

PoS(LeptonPhoton2019)145

1. Proton and nucleus structure

The structure of the proton can be described by parton distribution functions (PDF). At low x the main component is the gluon distribution function which is steeply rising due to gluon splitting. Eventually, the process of gluon recombination will stop this rise and saturation of the gluon PDF will be reached. This has been predicted by perturbative Quantum Chromodynamics (pQCD), but not yet conclusively observed.

It is known that the structure of nuclei is not a simple coherent sum of the structure of its nucleons. It has been measured that at small x, the structure function of lead is smaller than what is expected from the above-mentioned sum. This phenomenon is called shadowing. One of the possible origins of shadowing is saturation.

2. Coherent J/ψ photoproduction in ultra-peripheral collisions

The coherent photonuclear production of a J/ψ is a sensitive probe of shadowing at low x and small scales, where shadowing is poorly known. A diagram of this process is shown in Fig. 1 (left). The lead ions at the LHC are a very intense source of high energy photons where the photon flux intensity is proportional to Z^2 while the maximum energy of the photons is given by the Lorentz boost of the lead ion. Due to the large mass of the produced J/ψ vector meson the measurements can be compared with perturbative calculations, and due to its small decay width and sizeable branching ratio into dileptons the experimental signal is clean. The leading order cross section for this process in collinear pQCD is proportional to the gluon density squared and thus particularly sensitive to potential saturation and shadowing effects.

To measure this process at the LHC, hadronic interactions must be suppressed. This is achieved in ultra-peripheral collisions (UPC) which are interactions at an impact parameter b larger than the sum of the radii of the colliding particles $R_1 + R_2$. This requirement suppresses the short-range strong interaction and leaves a clean sample of events which involve at least one exchanged photon, see Fig. 1 (right). The previous ALICE measurements can be found in Ref. [1]. For a recent review of UPC at the LHC see Ref. [2] and references therein.

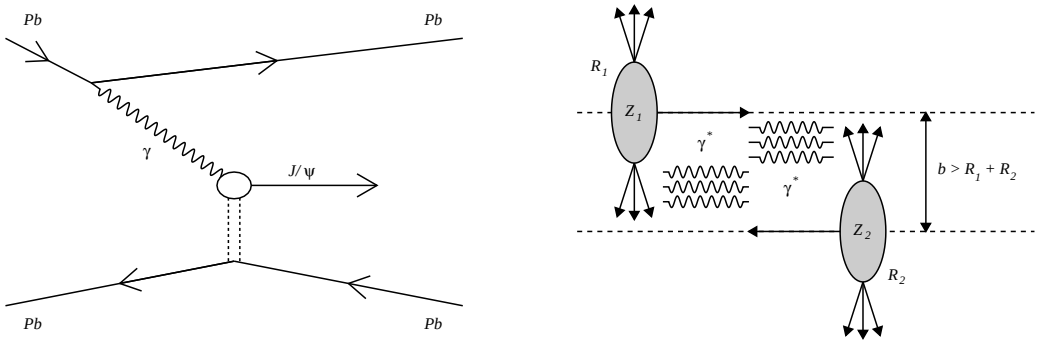

Figure 1: Diagram of the photoproduction of a J/ψ vector meson in a Pb–Pb UPC (left) and diagram of an UPC of two nuclei at an impact parameter b with charge $Z_i \cdot e$ and radii R_i, surrounded by a cloud of virtual photons γ^* (right).

3. The analysis procedure

The analysed data sample of Pb–Pb UPC at $\sqrt{s_{\mathrm{NN}}}$ = 5.02 TeV was recorded during the LHC Run 2 with the ALICE detector [3] in the rapidity range $-4.0 < y < -2.5$. The J/ψ is measured in the dimuon decay channel. The key subdetectors used in this analysis are the muon spectrometer for muon track reconstruction and the AD and V0 scintillators, which cover a large rapidity range, used as vetoes to reject background events.

The raw J/ψ yield and the feed-down contribution from ψ' decays were extracted from the invariant mass spectra (Fig. 2 (left)), while the transverse momentum distribution was used to estimate the contribution from the incoherent process (Fig. 2 (right)).

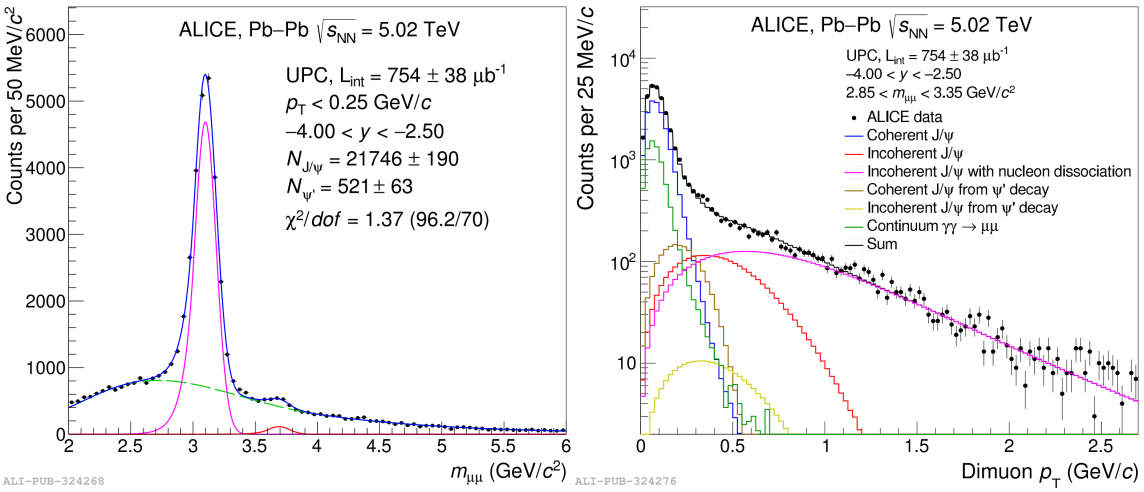

Figure 2: Invariant mass distribution (left) and the transverse momentum distribution (right) of unlike-sign dimuons in the full rapidity range measured with the ALICE detector at $\sqrt{s_{\mathrm{NN}}}$ = 5.02 TeV. In the invariant mass plot the magenta line describes the J/ψ peak, the red line describes the ψ' peak, the green line describes the background from $\gamma\gamma \to \mu^+\mu^-$, and the blue line describes the full fit function [4].

4. Results

Figure 3 shows the measured rapidity dependence of the cross section for coherent photoproduction of J/ψ off Pb nuclei. Data is compared with different models for this process. The IPSat (LM) [5] and BGK-I (LS) [6] predictions, based on the colour dipole model, describe best the data. The difference between the Impulse Approximation, which does not consider any nuclear effects, and the measured cross section signals moderate gluon shadowing. The GG-HS (CCK) [7, 8] describes data at forward rapidities and underestimates the measurement at semi-forward rapidities, similar behaviour is observed for EPS09 (GKZ) [9]. Starlight [10], which assumes no gluon shadowing, slightly overshoots data at all rapidities.

Acknowledgments

This work has been partially supported by the grant 18-07880S of the Czech Science Foundation (GACR).

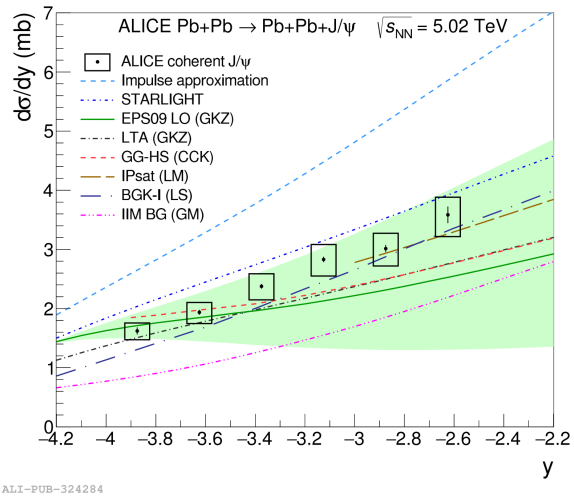

Figure 3: Rapidity dependence of the cross section for coherent photoproduction of J/ψ off Pb nuclei in ultra-peripheral Pb–Pb collisions at $\sqrt{s_{\rm NN}}$ = 5.02 TeV. The error bars represent the statistical uncertainties, the boxes around the points the systematic uncertainties. The results are compared with theoretical calculations, see text and Ref. [4] for details.

References

[1] ALICE collaboration, *Coherent J/ψ photoproduction in ultra-peripheral Pb-Pb collisions at $\sqrt{s_{NN}} = 2.76$ TeV*, *Phys. Lett.* **B718** (2013) 1273 [1209.3715].

[2] J. G. Contreras and J. D. Tapia Takaki, *Ultra-peripheral heavy-ion collisions at the LHC*, *Int. J. Mod. Phys.* **A30** (2015) 1542012.

[3] ALICE collaboration, *The ALICE experiment at the CERN LHC*, *JINST* **3** (2008) S08002.

[4] ALICE collaboration, *Coherent J/ψ photoproduction at forward rapidity in ultra-peripheral Pb-Pb collisions at $\sqrt{s_{\rm NN}} = 5.02$ TeV*, 1904.06272.

[5] T. Lappi and H. Mantysaari, *J/ψ production in ultraperipheral Pb+Pb and p+Pb collisions at energies available at the CERN Large Hadron Collider*, *Phys. Rev.* **C87** (2013) 032201 [1301.4095].

[6] A. Łuszczak and W. Schäfer, *Coherent photoproduction of J/ψ in nucleus-nucleus collisions in the color dipole approach*, *Phys. Rev.* **C99** (2019) 044905 [1901.07989].

[7] J. Cepila, J. G. Contreras and J. D. Tapia Takaki, *Energy dependence of dissociative J/ψ photoproduction as a signature of gluon saturation at the LHC*, *Phys. Lett.* **B766** (2017) 186 [1608.07559].

[8] J. Cepila, J. G. Contreras and M. Krelina, *Coherent and incoherent J/ψ photonuclear production in an energy-dependent hot-spot model*, *Phys. Rev.* **C97** (2018) 024901 [1711.01855].

[9] V. Guzey, E. Kryshen and M. Zhalov, *Coherent photoproduction of vector mesons in ultraperipheral heavy ion collisions: Update for run 2 at the CERN Large Hadron Collider*, *Phys. Rev.* **C93** (2016) 055206 [1602.01456].

[10] S. R. Klein, J. Nystrand, J. Seger, Y. Gorbunov and J. Butterworth, *STARlight: A Monte Carlo simulation program for ultra-peripheral collisions of relativistic ions*, *Comput. Phys. Commun.* **212** (2017) 258 [1607.03838].

Appendix B

List of good runs for the forward rapidity measurement

Good runs for period LHC18q - NanoAOD 425 20190111-1316 - muon_calo_pass2:

```
295585, 295586, 295587, 295588, 295589, 295612, 295615,
295665, 295666, 295667, 295668, 295671, 295673, 295675,
295676, 295677, 295714, 295716, 295717, 295718, 295719,
295723, 295725, 295753, 295754, 295755, 295758, 295759,
295762, 295763, 295786, 295788, 295791, 295816, 295818,
295819, 295822, 295825, 295826, 295829, 295831, 295854,
295855, 295856, 295859, 295860, 295861, 295863, 295881,
295908, 295909, 295910, 295913, 295936, 295937, 295941,
295942, 295943, 295945, 295947, 296061, 296062, 296063,
296065, 296066, 296068, 296123, 296128, 296132, 296133,
296134, 296135, 296142, 296143, 296191, 296192, 296194,
296195, 296196, 296197, 296198, 296241, 296242, 296243,
296244, 296246, 296247, 296269, 296270, 296273, 296279,
296280, 296303, 296304, 296307, 296309, 296312, 296377,
296378, 296379, 296380, 296381, 296383, 296414, 296419,
296420, 296423, 296424, 296433, 296472, 296509, 296510,
296511, 296514, 296516, 296547, 296548, 296549, 296550,
296551, 296552, 296553, 296615, 296616, 296618, 296619,
296622, 296623
```

Good runs for period LHC18r - NanoAOD 426 20190111-1316 - muon_calo_pass2:

```
296690, 296691, 296694, 296749, 296750, 296781, 296784,
296785, 296786, 296787, 296791, 296793, 296794, 296799,
296836, 296838, 296839, 296848, 296849, 296850, 296851,
296852, 296890, 296894, 296899, 296900, 296903, 296930,
296931, 296932, 296934, 296935, 296938, 296941, 296966,
296967, 296968, 296969, 296971, 296975, 296976, 296979,
297029, 297031, 297035, 297085, 297117, 297118, 297119,
```

```
297123, 297124, 297128, 297129, 297132, 297133, 297193,
297194, 297196, 297218, 297219, 297221, 297222, 297278,
297310, 297312, 297315, 297317, 297363, 297366, 297367,
297372, 297379, 297380, 297405, 297408, 297413, 297414,
297415, 297441, 297442, 297446, 297450, 297451, 297452,
297479, 297481, 297483, 297512, 297537, 297540, 297541,
297542, 297544, 297558, 297588, 297590, 297595
```

Appendix C

List of good runs for the central rapidity measurement

Good runs for periodLHC18q pass1 ESD:

```
295585, 295586, 295588, 295589, 295610, 295611, 295612,
295615, 295666, 295667, 295668, 295673, 295675, 295676,
295712, 295714, 295717, 295718, 295719, 295721, 295723,
295725, 295754, 295755, 295758, 295759, 295762, 295763,
295786, 295788, 295791, 295816, 295818, 295819, 295822,
295825, 295826, 295829, 295831, 295853, 295854, 295855,
295856, 295859, 295860, 295861, 295909, 295910, 295913,
295936, 295937, 295941, 295942, 296016, 296060, 296062,
296063, 296065, 296066, 296123, 296132, 296133, 296134,
296135, 296142, 296143, 296191, 296192, 296194, 296195,
296196, 296197, 296198, 296240, 296241, 296242, 296243,
296244, 296246, 296247, 296269, 296270, 296273, 296279,
296280, 296303, 296304, 296309, 296312, 296377, 296378,
296379, 296380, 296381, 296383, 296414, 296415, 296419,
296420, 296423, 296424, 296433, 296472, 296509, 296510,
296511, 296512, 296516, 296547, 296548, 296549, 296550,
296551, 296552, 296553, 296594, 296615, 296616, 296618,
296619, 296621, 296622, 296623
```

Good runs for periodLHC18r pass1 ESD:

```
296690, 296691, 296693, 296694, 296781, 296784, 296785,
296786, 296787, 296790, 296793, 296794, 296799, 296835,
296836, 296838, 296839, 296848, 296850, 296851, 296852,
296894, 296899, 296900, 296903, 296930, 296931, 296932,
296934, 296935, 296938, 296941, 296966, 297031, 297035,
297085, 297117, 297118, 297119, 297123, 297124, 297128,
297129, 297132, 297133, 297193, 297195, 297196, 297218,
297221, 297222, 297278, 297310, 297311, 297317, 297332,
```

```
297333, 297335, 297336, 297363, 297366, 297367, 297372,
297379, 297380, 297405, 297406, 297413, 297414, 297415,
297441, 297442, 297446, 297450, 297451, 297452, 297479,
297481, 297483, 297512, 297537, 297540, 297541, 297542,
297544, 297558, 297588, 297590, 297595, 297219, 297194,
297029, 296890, 296849, 296750, 296749
```